Year : 2021

Novel insights into direct translocation and endocytosis of cell-penetrating peptides

Trofimenko Evgeniya

UNIL | Université de Lausanne
Faculté de biologie et de médecine

Département des Sciences Biomédicales

Novel insights into direct translocation and endocytosis of cell-penetrating peptides

Thèse de doctorat ès sciences de la vie (PhD)

présentée à la

Faculté de biologie et de médecine
de l'Université de Lausanne

par

Evgeniya Trofimenko

Maîtrise Universitaire ès Sciences en Sciences Moléculaires du Vivant
de l'Université de Lausanne

Jury

Prof. Dr. Manuel Mameli, Président
Prof. Dr. Christian Widmann, Directeur de thèse
Prof. Dr. Sandrine Sagan, Experte
Prof. Dr. Andreas Mayer, Expert

Lausanne
(2021)

UNIL | Université de Lausanne
Faculté de biologie et de médecine

Département des Sciences Biomédicales

Novel insights into direct translocation and endocytosis of cell-penetrating peptides

Thèse de doctorat ès sciences de la vie (PhD)

présentée à la

Faculté de biologie et de médecine
de l'Université de Lausanne

par

Evgeniya Trofimenko

Maîtrise Universitaire ès Sciences en Sciences Moléculaires du Vivant
de l'Université de Lausanne

Jury

Prof. Dr. Manuel Mameli, Président
Prof. Dr. Christian Widmann, Directeur de thèse
Prof. Dr. Sandrine Sagan, Experte
Prof. Dr. Andreas Mayer, Expert

Lausanne
(2021)

UNIL | Université de Lausanne
Faculté de biologie et de médecine

Ecole Doctorale
Doctorat ès sciences de la vie

Imprimatur

Vu le rapport présenté par le jury d'examen, composé de

Président·e	Monsieur	Prof.	Manuel	**Mameli**
Directeur·trice de thèse	Monsieur	Prof.	Christian	**Widmann**
Expert·e·s	Madame	Prof.	Sandrine	**Sagan**
	Monsieur	Prof.	Andreas	**Mayer**

le Conseil de Faculté autorise l'impression de la thèse de

Madame Evgeniya Trofimenko

Maîtrise universitaire ès Sciences en sciences moléculaires du vivant, Université de Lausanne

intitulée

Novel insights into direct translocation and endocytosis of cell-penetrating peptides

Date de l'examen : 23 avril 2021

Date d'émission de l'imprimatur : Lausanne, le 3 juin 2021

pour le Doyen
de la Faculté de biologie et de médecine

Prof. Niko GELDNER
Directeur de l'Ecole Doctorale

"Success is not final, failure is not fatal: it is the courage to continue that counts."

Winston Churchill

ACKNOWLEDGEMENTS

I am deeply grateful to my supervisor and mentor Prof. Christian Widmann for accepting me in his laboratory as a doctoral student and for giving me the opportunity to be part of exiting scientific research. His extensive knowledge, experience, invaluable advice, open mindedness encouraged me all along my doctoral work to become a better, more rounded and curious researcher with a soft spot for unexpected results. I am also thankful to my thesis committee: Prof. Sagan, Prof. Mayer and Prof. Mameli for their knowledge, helpful insight and interest towards my work. I would like to thank all members of the lab for their help and support that created a great friendly atmosphere in a day to day life. I am also thankful to all the collaborators, especially the laboratory of Prof. Francesca Amati at Department of Biomedical Sciences, Prof. Anita Luthi and Dr. Julien Puyal at the Department of Fundamental Neurosciences, Prof. Andrea Danani at Dalle Molle Institute for Artificial Intelligence Research, Ticino and Prof. Mitsunori Fukuda, Tohoku University, Japan for their expertise and plentiful knowledge. Finally, I would like to offer my special thanks to my family, especially to my mom, for their unwavering support, inspiration and belief in me all my life.

TABLE OF CONTENTS

SUMMARY

Cell-penetrating peptides (CPPs), are short, non-toxic molecules that carry positively charged amino acids within their sequences. CPPs, such as TAT, polyarginine (R9) and Penetratin allow delivery of bioactive cargo across cellular membranes. Even though this property has been discovered and studied in fundamental and applied biology since the end of 1980's, our understanding of the way CPPs enter cells is still incomplete. This knowledge gap halts further development and improvement of CPP-derived compounds and therapeutics, some of which are currently in phase II and III clinical trials.

CPPs enter cells through direct translocation and endocytosis. Direct translocation is an entry mechanism, which allows CPPs to cross the cell membrane and gain direct access to the cytosol, independently of endocytic pathways. Our work supports the following model: CPPs directly translocate into cells by crossing the plasma membrane through ~2 nm wide water pores that they contribute to create by locally megapolarizing cells (-150 mV). Water pores are created by a combination of lipid head group reorientation coupled to intrusion of a water column in the membrane bilayer. Water pores can spontaneously form if cells are sufficiently hyperpolarized. The mild hyperpolarization achieved through the movement of potassium ions through their channels or mere presence of CPPs is not sufficient to trigger efficient formation of such pores. This is achieved only in combination of these two phenomena. The movement of the positive charges carried by the CPPs into the cell, as well as the transport of extracellular cations, dissipates the membrane potential, resulting in the collapse of the water pores and sealing of the plasma membrane. Formation of water pores is therefore transient and does not affect cell viability.

CPPs additionally enter cells through endosocytosis, a vesicular type of entry, used by cells to take up a variety of extracellular substances. The current evidence indicates that all endocytosed substances follow a single endocytic maturation pathway towards lysosomes that is characterized molecularly by the presence of Rab5 and Rab7 on early and late endosomes, respectively. We provide evidence that there is a second endolysomal pathway that is Rab14-dependent, but does not involve Rab5 or Rab7. We have discovered this pathway by studying how CPPs are endocytosed. However, this endocytic route is taken by other, physiological, cationic cargos such as polyamines or homeoproteins. Both homeoproteins and polyamines are of fundamental importance in biology and medicine. How they are endocytosed had been unresolved until now. Our study may therefore open new avenues of research and may help understanding how cargos of translational interest are taken up by cells.

RESUME

Les peptides de pénétration cellulaire (CPP) sont des molécules courtes et non toxiques qui portent des acides aminés chargés positivement au sein de leurs séquences. Les CPPss, tels que TAT, polyarginine (R9) et Penetratin permettent la livraison des molécules bioactive à travers les membranes cellulaires. Même si cette propriété a été découverte et étudiée en biologie fondamentale et appliquée depuis la fin des années 1980, notre compréhension de la manière dont les CPPs entrent dans les cellules est encore incomplète. Le manque de connaissances ralenti le développement et l'amélioration des composés thérapeutiques dérivés des CPPs. Par ailleurs, certaines molécules dérivées des CPPs sont actuellement en phase II et III d'essais cliniques.

Les CPPs pénètrent dans les cellules par translocation directe et endocytose. La translocation directe est un mécanisme d'entrée qui permet aux CPPs de traverser la membrane cellulaire et d'accéder directement au cytosol, indépendamment des voies d'endocytose. Notre travail soutient le modèle suivant : les CPPs traversent directement la membrane cytoplasmique grâce à des pores d'eau de ~ 2 nm de large. Les CPPs contribuent à la formation de ces portes en mégapolarisantes localement la membrane cellulaire (-150 mV). Les pores d'eau sont créés par une réorientation des têtes lipidiques couplée à l'intrusion d'une colonne d'eau dans la bicouche lipidique. Les pores d'eau peuvent se former spontanément si les cellules sont suffisamment hyperpolarisées. L'hyperpolarisation obtenue par le mouvement des ions potassium au travers des canaux ou la présence de CPP n'est pas suffisante pour déclencher une formation efficace de tels pores. La réalisation de cet evenement n'est réalisé qu'en combinaison de ces deux phénomènes. La création de pores d'eau n'est possible que lorsque les deux phénomènes coïncident. Le mouvement des charges positives portées par les CPPs entrant dans la cellule, ainsi que le transport des cations extracellulaires, dissipe le potentiel membranaire, entraînant l'effondrement des pores d'eau et le scellement de la membrane plasmique. La formation de pores d'eau est donc transitoire et n'affecte pas la viabilité cellulaire.

Les CPPs pénètrent également dans les cellules par endocytose, un type d'entrée vésiculaire, utilisé par les cellules pour absorber une variété de substances extracellulaires. Les preuves actuelles indiquent que toutes les substances endocytosées suivent une seule voie de maturation endocytique aboutissant à leur fusion avec des lysosomes. Cette voie est caractérisée au niveau moléculaire par la présence de Rab5 et Rab7 sur les endosomes précoces et tardifs respectivement. Nous apportons la preuve qu'il existe une deuxième voie endolysomale qui dépend de Rab14, mais qui n'implique pas Rab5 ou Rab7. Nous avons découvert cette voie en étudiant comment les CPPs sont endocytosés. Cependant, cette voie endocytaire est empruntée par d'autres molécules physiologiques cationiques telles que les polyamines ou les homéoprotéines. Ces derniers sont d'une importance fondamentale en biologie et en médecine. La façon dont ils sont endocytés n'avait jusqu'à présent jamais été élucidée. Notre étude permet donc d'ouvrir de nouvelles voies de recherche et d'aider à comprendre comment les molécules d'intérêt translationnel (Homéoprotéines et polyamines) sont prises en charge par les cellules.

ABBREVIATIONS

AP2	Adaptor protein 2
Cas9	Crispr associated protein 9
CS	Chondroitin sulfate
CLIC/GEEK	clathrin-independent carrier/glycosylphosphotidylinositol-anchored protein enriched endocytic compartment
CPPs	Cell-penetrating peptides
CRISPR	Clustered Regularly Interspaced Short Palindromic Repeat
DMEM	Dulbecco's modified Eagle Medium
EGF	Epidermal growth factor
F-actin	Filamentous actin
FBS	Fetal bovine serum
GAG	Glycosaminoglycan
GPI	Glycosylphosphatidylinositol
GEF	Guanine exchange factor
HD	Homeodomains
HS	Heparan sulfate
HP	Homeoproteins
IAA	Indole-3-acetic acid
ITC	Isothermal titration calorimetry
i.p.	intraperitoneal
i.v.	intravenous
K9	Nanomeric lysine
LCMV	Lymphocytic choriomeningitis virus
LLOME	L-leucyl-L-leucine methyl ester
NEM	N-Ethylmaleimide
PBS	Phosphate-buffered saline
PI	Propidium iodide
PI(3)P	Phosphatidylinositol 3-phosphate
PI(3,4)P2	Phosphatidylinositol 3,4-biphosphate
PI(3,5)P2	Phosphatidylinositol 3,5-biphosphate
PI(4,5)P2	Phosphatidylinositol 4,5-biphosphate
PI(3,4,5)P3	Phosphatidylinositol 3,4,5-triphosphate
R9	Nanomeric arginine, polyarginine

RasGAP	RasGTPase-activating protein
SMAC	Second mitochondria-derived activator of caspases
sgRNA	single guide RNA
TAT	Trans-activator of transcription
Vm	Membrane potential

INTRODUCTION

1. CELL-PENETRATING PEPTIDES AND APPLICATIONS

Cell penetrating peptides (CPPs) are non-toxic molecules of 5-30 amino acids that can translocate into living cells. CPPs can be hooked to a variety of cargos to allow their transport into cells for therapeutic or experimental purposes[1-16]. The origin of CPPs is diverse. For example, TAT_{48-57} is a 10 amino-acid fragment derived from the trans-activator of transcription (TAT) HIV-1 protein[17,18], penetratin is a 16 amino-acid peptide derived from the Antennapedia *Drosophila melanogaster* protein[19], and MAP (model amphipatic peptide) is a synthetic alanine/leucine/lysine-rich peptide[20]. CPPs can be subdivided into three classes, based on their physico-chemical properties (reviewed in[21]). Cationic CPPs, such as TAT, R9 and penetratin, are positively charged and arginine- and lysine-rich. Amphipathic CPPs, such as MAP, contain both hydrophobic and hydrophilic regions. Hydrophobic CPPs (such as Pep-7[22]), as their name implies, are predominantly made up of hydrophobic residues and have a low net charge. In addition, CPPs can be fused through covalent bonds or non-covalent interactions to various types of cargos such as siRNAs, DNA, liposomes, peptides, proteins and nanoparticles (Figure 1). This allows to increase the intracellular drug concentration in a tissue of interest or in a given cell compartment and thereby expand compound efficacy.

Recently, a number of CPP-conjugated compounds made it to clinical trials (reviewed in[1-3,15]). Applications of these compounds are only limited by the cargo related function, not by CPPs themselves. Currently, there are two compounds that are evaluated in phase III clinical trials. AM-111[23] and XG-102[24] that correspond to a TAT-hooked JNK inhibitor tested in the context of hearing loss, and intraocular inflammation and pain, respectively. Other CPP-derived therapeutics are currently being evaluated at earlier clinical trial phases targeting Crohn's disease, central nervous system tumors, other types tumors, as well as tumor imaging[15].

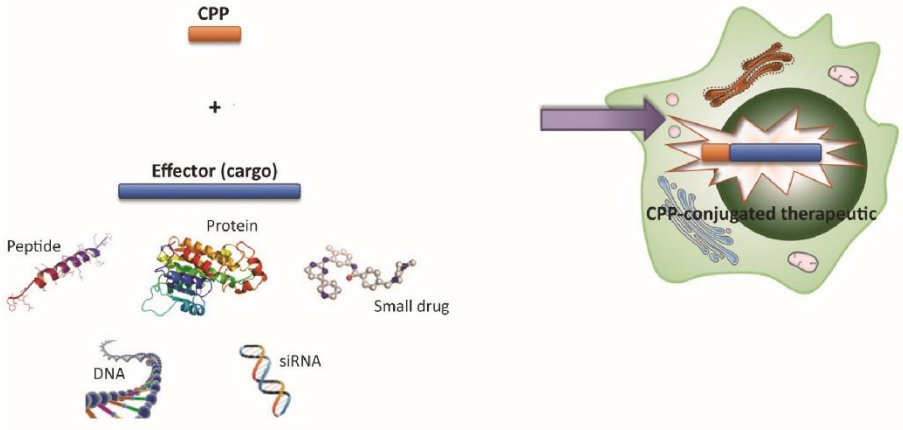

Figure 1. Scheme depicting cell-penetrating peptide-based application and various types of cargos that can be carried into the cells. *Adapted from Guidotti et al., Trends in Pharmacological Sciences, 2017.*

Therefore, CPPs represent a significant therapeutic potential, however one of the bottle necks in CPP-related research is that there is no consensus on their mode of entry (reviewed in[1-12,16]) due to the fact that CPP internalization depends on numerous factors, among which are CPP sequence, structure, concentration, time of incubation, bound cargo and local lipid composition of a cell membrane.

2. CELL-PENETRATING PEPTIDE INTERACTIONS WITH CELL MEMBRANE

To enter cells, CPPs have to cross the protective cell barrier, the plasma membrane, which is composed of a lipid bilayer made of phospholipids and cholesterols (Figure 2). Phospholipid diversity is based on the composition of (1) polar head group (choline, serine, inositol, ethanolamine, etc.), (2) backbone (glycerol or sphingolipid), (3) type of fatty acid (palmitic, oleic, stearic, etc.) and (4) grade of fatty acid unsaturation. Further diversity within the lipid bilayer comes from the localization of various lipids within inner and outer cell membrane layers. As such phosphatidylserine and phosphoinositol phosphates that are found in the inner layer of the plasma membrane. On the other hand, lipids such as glycolipids and sphingomyelins are mainly present in the outer layer of the plasma membrane. This corresponds to vertical segregation of the lipid bilayer. Additionally, lateral segregation occurs in heterogenous nanodomains enriched in cholesterol and sphingolipids called lipid rafts[25,26].

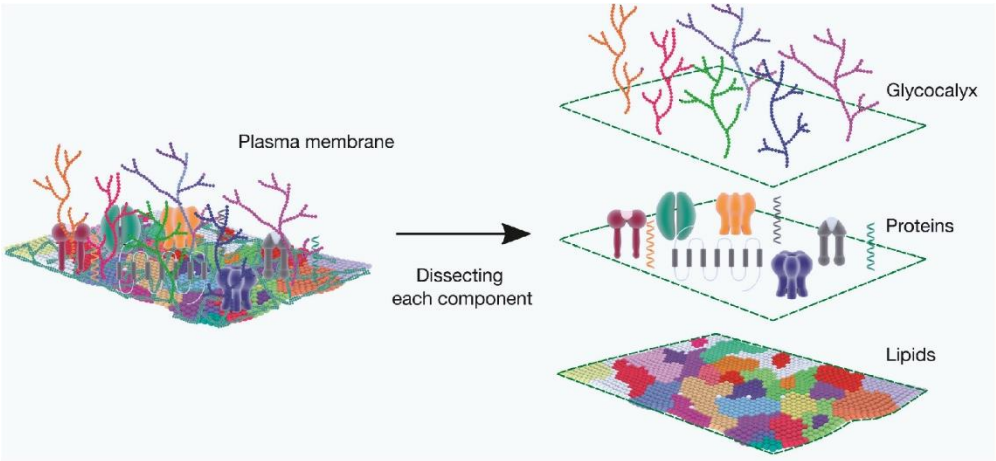

Figure 2. Illustration of cell membrane components. *Addapted from FEBS, 2020*

Glycolipids and glycoproteins (glycocalyx) present in the outer leaflet of the plasma membrane often contain sialic acid, which is found within terminal saccharide branches of N-glycans, O-glycans, and glycosphingolipids and occasionally capping side chains of glycosylphosphatidylinositol (GPI) anchors. The main characteristic of sialic acids is that they are negatively charged at physiological pH[27]. Proteoglycans, found on the outer leaflet of the plasma membrane, can either also be anchored to GPI or can have a transmembrane conformation, in that case proteoglycans are referred to as syndecans. Syndecans ensure interactions with cytosolic proteins including filamentous actin (F-actin) and actin-binding proteins. Proteoglycans consist of a core protein covalently attached to polysaccharides, glycosaminoglycans (GAGs), either heparan sulfate (HS) or chondroitin sulfate (CS). To further increase the plasma membrane complexity sulfate groups can be added to polysaccharides at various positions. Under physiological pH, the sulfate groups are negative charged[28-31]. Therefore, both sialic acid and GAGs represent potential electrostatic interaction sites for CPPs. Additionally, interaction with acid sphingomyelinase[32], local membrane deformation[33], as well as calcium fluxes[34] have been suggested to play a role in CPP direct translocation into cells.

2.1 Role of extracellular sialic acid

The role of sialic acid in CPP internalization is concentration-dependent and the lack of sialic acid appears to favor Penetratin and WR6 peptide uptake[35-37]. On the other hand, fluorescently labeled TAT and TAT-Cre internalization was reduced in CHO-lec2 and A-745 cells deficient in sialic acid[38]. TAT-Cre-induced GFP expression in a Lox-STOP-Lox-EGFP system was not affected by the lack of sialic acid could be due to the fact that such experimental system is leaky in the sense that only one TAT-Cre molecule could be necessary to trigger GFP expression. Therefore, sialic acid interactions may have a dual effect on CPP internalization, dependent on the nature and sequence composition of the CPP. Furthermore, electrostatic interactions between CPPs and extracellular components of the plasma membrane on its own is not sufficient to trigger CPP internalization.

2.2 Role of extracellular glycosaminoglycans

Cationic CPPs as TAT, R9 and Penetratin interact electrostatically with negatively charged extracellular GAGs[35,39-49]. Based on isothermal titration calorimetry (ITC) experiments such interactions are dependent on the content of sulfate groups within GAGs and the most likely interactions occur with heparin, structurally similar to HS[35,50]. Penetratin shows higher capacity than TAT or polyarginines to form stable interactions with heparin[40,45,47]. It is therefore, hypothesized that in addition to interactions with cationic residues, amphipathicity carried by Penetratin, but not by TAT or R9, is necessary to trigger GAG clustering at the site of CPP internalization. Studies based on heparinase treatments (enzymatic GAG digestion), the addition of GAG-binding competitors (heparin, HS and CS), as well as CHO cells deficient in GAGs (A-745 and D-677, CHO-lec2), show that cationic CPPs (TAT, R8, R9 and Penetratin) entry is diminished in the absence of GAGs[35-37,46,51-61]. On the other hand, overexpression of syndecans, increases the cellular uptake of TAT, R8 and penetratin[61,62].

Additionally, GAGs have been implicated in TAT and R8 endocytosis through Rac1 phosphorylation and F-actin remodeling, involved in macropinocytosis[38,47,61,63,64]. TAT internalization lead to increased uptake of dextran, which was rendered less efficient in the absence of GAG and sialic acid[38]. Furthermore, TAT bound to 7-nm quantum dots entry is dependent on the presence of GAGs, which can then trigger Rac1 activation and actin polymerization.

These data indicate that GAGs play an important role in the regulation of CPP interactions with cell membrane and therefore their subsequent internalization.

2.3 Role of guanidinium group within cell-penetrating peptide sequence

The nature of cationic amino acids in peptides determines their translocation abilities. It is known for example that peptides made of 9 lysines (K9) poorly reaches the cytosol and that replacing arginine by lysine in Penetratin[44,65,66] and TAT[55] significantly diminishes their internalization. Additionally,

guanidinium groups play a role in the internalization of R9 and its translocation across octanol/water medium[67]. Arginine substitution for hydrophobic leucine, also led to reduced R9 uptake[58].

Both arginine and lysine are basic, positively charged amino acids, that contain guanidinium and lysyl groups, respectively. Guanidinium, as opposed to lysyl groups can form two hydrogen bonds[68], which allow for more stable electrostic interactions. It has been determined that, once embedded into membranes, lysine residues tend to lose protons[69,70]. Furthermore, CPP interaction with GAGs appears to occur through guanidinium groups found within CPP sequence, as demonstrated for Penetratin in CHO cells (A-745) deficient in GAGs[17].

In conclusion, the presence of guanidinium groups within the CPP sequence ensures for more stable electrostatic interactions with the extracellular plasma membrane components as polyasaccharides or negatively charged lipid head groups, which in turn facilitates CPP insertion and translocation across the lipid bilayer.

2.4 Role of tryptophane within cell-penetrating peptide sequence

Besides electrostatic interactions between the CPPs and the cell membrane the presence of aromatic residues, as tryptophane is also involved in the CPP internalization. Through tryptophane substitution for phenylalanine, at positions 48 and 56, it has been demonstrated that Penetratin uptake has been decreased[71]. However, substitution of arginines to tryptophane within R9 peptide, had no effect on the CPP internalization[60,72,73]. Circular dichroism and NMR studies showed that tryptophane residues promote β-sheet conformation stabilizing the interactions with HS, CS and heparin[35]. The role of tryptophane in CPP/membrane interactions has been confirmed through a substitution experiment of three tryptophane for phenylalanines[74]. In this situation, as the secondary structure was not affected by the substitution, membrane binding has been preserved, even though CPP uptake was decreased. This could be due to apparently higher capability of insertion into lipid bilayer of tryptophan, as opposed to phenylalanine[74-76]. Tryptophane interplay with plasma membrane occurs through interactions with GAGs[35,73]. In fact, there is a positive correlation between the number of tryptophane residues within the CPP sequence (R9, R6W3, R6L3, Penetratin, Penetratin(W48F) and TAT) and the efficiency of interactions with the GAGs[35,73]. As expected CPP/membrane binding for CPPs that contain arginine and tryptophane residues in their sequence was diminished in the absence of GAGs[35,58].

Together these data suggest that the lack of guanidinium groups that form electrostatic interactions with negatively charged components of plasma membrane can be compensated by the presence of aromatic residues through adaptation of a more stable B-sheet conformation of CPP to ensure stable GAG binding.

Concluding remarks

The interaction between CPPs and cellular membranes represent the initial step of CPP internalization. At the plasma membrane electrostatic interactions occur between the basic amino acids and negatively charges sialic acids, GAGs and phospholipids. Interplay between CPPs and sialic acid, although less investigated than GAGs, appears to be beneficial in the context of TAT internalization as opposed to amphipathic Penetratin. CPP/GAG interactions, less discriminatory, play a role in the internalization of many CPPs. Furthermore, CPP sequence composition, more specifically guanidinium carried by arginine, forming electrostatic interactions with phospholipids and other negatively charged membrane components, as well as tryptophan, which facilitates CPP membrane insertion, are crucial for efficient peptide membrane binding and internalization. As for both endocytosis and direct translocation the initial step of CPP internalization is dependent on the CPP/cell membrane interactions, the regulators of such interactions can be involved in both CPP uptake mechanisms.

3. CELL-PENETRATING PEPTIDE DIRECT TRANSLOCATION

CPPs enter cells through direct translocation. Direct translocation is an entry mechanism, which allows CPPs to cross the cell membrane and gain direct access to the cytoplasm, independent of endocytic pathways. How does this process occur? Due to current technical limitations, the answer to this question in the majority of cases is based on acellular analysis, primarily NMR studies and coarse-grained *in silico* modeling experiments. Such approaches describe inverse micelles[77-80], carpet model[81,82], barrel-stave and toroidal pores[83-89], as well as membrane potential-dependent pores[87-90] as prospective mechanisms of CPP direct translocation. Even though these studies offer insight into visualization of CPP entry mechanisms, they are performed under non-physiological conditions where membrane compositions are simplified (lacking various lipids and membrane proteins), and certain approximations are employed in *in silico* studies [91,92], such 'all or none' CPP delivery in the extracellular space, which would be diffuse and progressive in intracellular studies. In addition, chemical cellular fixation prior to image acquisition, which is a step that is often employed, can induce CPP release from endosomes and from the cell membrane into the cytoplasm[93-96], leading to artefactual CPP intracellular localization. As direct translocation is not exclusive and is often accompanied by endocytosis (reviewed in[1,3,4,8-16,97,98]), the most reliable approach to distinguish between these two pathways with certainty is through confocal time-lapse experiments in live cells[99-101]. Therefore, acellular experiments, fixed or lysed cell-based approaches should be performed in combination with live cell visualization.

3.1 Inverted micelles

Inverted micelle model consists of electrostatic, as well as of peptide-lipid interactions between the CPP and the cell membrane that leads to lipid bilayer rearrangement and membrane curvature to the

point where the CPP will be englobed by the cell membrane lipids in a micelle-like structure[77]. The micelle will then be destabilized and the CPP released into to the cytosol, without ever being in contact with hydrophobic environment. CPP entry through inverted micelles was first suggested for Penetratin[77]. NMR studies on model membranes showed lipid bilayer destabilization in the presence of Penetratin[78] and TAT[79] and confirmed the importance of initial interactions between the CPP and the membrane, suggesting an active role of CPP in the internalization process. Visual interpretations from transmission electron microscopy[79] and *in silico* coarse-grained approach[80] confirmed the inverted micelle structures that occur through the interaction between guanidinium groups carried within the CPP sequence and the negatively charged phospholipids within the plasma membrane[80], that would be compatible with amphiphatic CPPs that carry a relatively small cargo. Additionaly, substitution of tryptophate residues within Penetratin sequence, prevented inverted micelle formation[78]. These data suggest that CPP/membrane interactions may depend on other factors beyond charge-dependent electrostatic bonds. Studies showing no membrane permeabilisation induced by TAT[102] or Penetratin[103] are in accordance with the inverted micelles model. However, this model is based on interpretations of acellular experiments and not direct assessment in physiological conditions. The authors mention that the observed data could in addition correspond to pinosome formation[77] or an unusual uni- or multilamellar structure[79] , potentially reminiscent of fusion pore described below[33,104]. In addition, later studies show that TAT can indeed translocate through pores[89,99,101,105]. *In silico* modelling also suggests that inverted micelle structure could represent the initial step of a pore formed across the membrane to allow CPP translocation[101]. This could explain the discrepancy with a study showing Penetratin entry through toroidal pore based on coarse-grained simulations[88].

3.2 Membrane destabilization due to cell-penetrating peptide cooperativity

Based on currently proposed mechanisms, partial and local membrane destabilization is key to CPP translocation across the cell membrane. Whole cell electrophysiology recordings of smooth muscle cells showed increased ion flow, as well as current jumps in the presence of R9 in a concentration dependent manner[87]. Such recordings indicate membrane destabilization and permeabilization induced by the CPP over time. However not all cells responded to similar extent. Lack of response in cells could be due to the potentially decreased CPP entry at a temperature below 37°C[99,106-108], as well as to heterogeneous CPP uptake within the cell population[99-101]. Calcium addition to liposomes restored the current increase induced by the CPP to its original state[87], suggesting that membrane repair can be achieved through calcium influx[109]. Authors suggest that CPPs induce toroidal pore formation within the plasma membrane[87]. Essentially, these pore structures describe cooperativity between the oligomerized CPPs at the cell surface through the electrostatic and peptide-lipid

interactions with the lipid bilayer. Such oligomerization imposes a strain on the lipid bilayer and leads to its curvature. Barrel stave pore is made of amphipathic CPP hydrophobic interactions with lipids creating a hydrophilic centre, with no or minimal phospholipid heads reorientations[85]. Toroidal pore is triggered by reorientation of phospholipid groups upon interaction with several CPPs that remain bound to the bilayer and thereby create a pore[86]. The barrel-stave and toroidal pore models postulate that a more efficient interaction can be achieved between the cell membrane and several CPP molecules working together as opposed to a single CPP[110]. The CPP translocation through toroidal pores is based on *in silico* modeling data and was initially described for antimicrobial CPPs[83-86]. Even though initially described for antimicrobial CPP, other arginine-rich peptides were shown to take advantage of toroidal pores[87-89] that require a minimum of six interactions between guanidinium groups carried by the CPP and phosphate groups on the cell membrane[87].

The pore size was estimated to 0.5-1 nm[85] and later to 6 nm in diameter[110] based on modeling experiments. However, the size of the pore, CPP orientation (parallel or perpendicular to the membrane) and CPP oligomerization could depend on peptide to lipid ratio, membrane fluidity, hydration and level of interactions between the CPPs and the membranes[83,110].

Described as such, the toroidal pore model does not address the directionality of pore formation and more importantly, its transiency. Earlier studies suggest that that CPP could travel both ways in and out of the membrane by forming a toroidal pore[86], however this is not consistent with cellular observations of CPP accumulation within cells and low cytotoxicity. The time-dependent increase in membrane destabilization in live cells[87] does not support the idea of a transient mechanism, which could reflect on cell viability due to patch clamp procedure and/or incubation with R9, which we cannot formally ruled out as the level of CPP-induced cytotoxicity over time was not confirmed in smooth muscle cells[87]. Membrane repair can be achieved through calcium influx, followed by exocytosis to patch the membrane[109], however this has not been tested routinely in the studies mentioned here. Therefore, an additional stage of the cooperative pore mechanism is still missing.

3.3 Fusion pore

CPP direct translocation can originate from specific areas at the cell surface suggesting discrete structures within the cell membrane[33,56,99,100,104,111]. In fact, electron microscopy experiments revealed that these are multilamenar structures, which are formed specifically in the presence of mono-arginine CPPs [33,104]. The initial interaction between the CPP and the cell membrane leads to membrane ruffling or protrusions that eventually fold on themselves and leading to CPP capture between two layers of the membrane. Fusion between the two lipid bilayers then occurs in a manner similar to calcium-assisted vesicle fusion and results in CPP penetration[104]. However, these structures appear to originate from the interactions between the cell membrane and the hydrophobic tag carried by the CPP, such

as AlexaFluor488, HA or fluorescein[33], which makes this entry mechanism irrelevant for non-tagged, purely cationic CPP. However, we could imagine that similar mode of entry could be taken by amphipathic CPP or cationic CPPs carrying a hydrophobic cargo for example TAT-RasGAP$_{317-326}$[99], as well as others. TAT may also enter through a similar mechanism[56], where TAT aggregates may reveal to be similar multi-laminar structures if visualized at higher resolution. Once these structures are formed, the fusion pore model suggests that additional CPPs can translocate through such pores[104]. In the proposed model, this will eventually lead to cell lysis and high cytotoxicity, which is not observed. In live cells, the fusion pore should therefore be transient, however currently there is no mechanism suggesting the pore closure or membrane repair in this context. We could imagine that such multilamenar structures are seen as endosomes by the cells and can then be degraded in lysosomes as they advance in endocytic pathway; however, this remains to be tested.

3.4 pH-dependent cell-penetrating peptide uptake

It has been suggested that the difference of pH across the cell membrane plays a role in CPP uptake. Authors postulate that pH gradient determines the state of protonation of the fatty acids within the cell membrane[101]. More specifically, high pH would lead to fatty acid deprotonation, which allows for binding of CPPs to the negatively charged membrane. This subsequently, leads to fatty acid protonation, which results in CPP release into the cytosol. Such CPP transfer occurs only from high to low pH[101], which could explains the lack of CPP release from acidic endosomes. The authors posit that the pH gradient is sufficient to induce cationic CPP direct translocation[101].

Based on experimental evidence in live cells, incubation at pH 9, significantly improves TAT uptake in comparison to physiological pH (pH 7.5) or pH 6 in several species[101]. However, this data is contradictory to the previously reported increased membrane destabilization at low pH in the presence of R9[87], which would lead to increased CPP uptake. Reduced CPP uptake at low pH can also be a result of inefficient CPP binding to the cell membrane, as is the case of TAT which binding decreased by 85% at pH 5.0-6.5 in comparison to physiological pH[112]. In addition, when TAT is linked to a cargo, RasGAP$_{317-326}$, variations in pH no longer have an effect on the CPP-cargo uptake[99]. Unfortunately, no conclusions can be drawn from the pH-dependent uptake experiments of FITC-tagged CPPs[101], as FITC fluorescence is quenched at low pH. Therefore, pH as a trigger of CPP direct translocation remains controversial.

Even though, fatty acid (oleic acid) enrichment in the media of live cells ensures better binding and more efficient uptake over time at various CPP concentrations[101], the cell membrane is composed of only trace amounts of free fatty acids[113,114]. Moreover, free fatty acids cannot be replaced by phospholipids, as the latter remain deprotonated at physiological pH values. Additionally, the pH difference across the cell membrane is of 0.2 on average[115], which is unlikely to represent the driving

force for CPP internalization. Therefore, the pH-dependent mechanism would not account for CPP uptake in physiological conditions.

3.5 Membrane potential-dependent cell-penetrating peptide uptake

Differences in ion concentrations across the cell membrane create an ion gradient, resulting in a membrane potential. Electrophysiological and pharmacological membrane potential modulations have revealed that depolarization blocks CPP uptake and hyperpolarization improves the uptake of cationic CPP. In fact, this mechanism postulates that membrane potential in itself is sufficient to trigger CPP direct translocation based on live cell experiments[67,99,100,112], as well as *in silico* studies[99,116-119].

Potassium channels are required to establish a basal low membrane potential, subsequently permissive for CPP direct translocation[99]. Hyperpolarizing drugs, such as valinomycin, enhance permissiveness in live cells[67,99,100]. This is mimicked in *in silico* simulations, where the electric field pushes that CPP into the membrane[116], which explains very minimal interactions between the cell membrane and the CPP in the absence of membrane potential in modeling studies[99]. When CPPs bind the plasma membrane, through electrostatic and peptide-lipid interactions, they further decrease the membrane potential, resulting in a locally hyperpolarized membrane, which we have recently estimated at around -150 mV[99]. This dramatically increases the likelihood of water pore formation. CPPs can then use these water pores to enter cells according to their electrochemical gradient.

Water pores of 2-nm diameter are created by a combination of lipid head group reorientation coupled to intrusion of a column of water in the membrane bilayer[99]. However, larger molecules of up to 5-nm in diameter bound to CPP (Cre[99], carbonic anhydrase and myoglobin[120], which are 5, 3.5 x 5.3 and 2.6 x 4.4 nm in diameter, respectively) can translocate across the cell membrane as well, but with reduced efficiency, confirmed by intracellular and *in silico* experiments[99]. The 2-nm pore is in addition compatible with conductance data obtained from oocytes in presence of Pep-1, an amphipathic CPP[121]. Though unable to be measured in living cells[122], water movement likely plays an active role in the formation of the pore and is not merely occurring once the pores are formed[99]. The movement of the positive charges carried by the CPPs into the cell dissipates the membrane potential, resulting in the collapse of the water pores and sealing of the plasma membrane[99,116]. CPP-mediated formation of water pores is therefore transient and does not affect cell viability[99].

Multiple rounds of CPP-driven water pore formation and CPP translocation into cells can lead to intracellular accumulation of the CPP[99,100]. Initial CPP binding to the cell membrane is independent of membrane potential[99,123]. Nevertheless, cell membrane composition and fluidity can affect CPP direct translocation. Membrane potential is therefore secondary to peptide-lipid interactions.

Based on *in silico* modeling, a single CPP molecule[99], as well as cooperative interactions between several CPPs can trigger membrane potential-dependent pore formation[112,116-119], which could be

reminiscent of the previously described toroidal pores. We can imagine that if the CPP-cargo complex is bigger than 5-nm, or if the CPP does not carry a sufficient amount of positive charges (or the cargo is highly hydrophobic), the CPP-cargo complex can be blocked within the pore. This can potentially lead to further membrane destabilization and formation of inverted micelle-like structures.

Concluding remarks

All of the CPP direct translocation models, described above, state that initial interaction between the CPP and the plasma membrane is sufficient to trigger direct translocation. However various factors, such as charge of the CPP, charge of the cargo, size of the cargo, CPP/lipid ratio, membrane potential, strength of interaction between the CPP and the phospholipid head groups of the cell membrane, angle of CPP orientation to the cell surface can modulate the CPP internalization.

Any proposed mechanism of CPP direct translocation has to explain the following intracellular observations:

i) unidirectional entry, which leads to apparent accumulation/concentration of CPP within cells over time

ii) lipid bilayer destabilization has to be transient to account for low CPP cytotoxicity

iii) the translocation mechanism across the cell membrane must differ from the mechanism of endosomal escape, more specifically CPP translocation across endosomal membranes.

The membrane potential-dependent CPP translocation mechanism based on live cell experiments fulfills the above criteria. However, this model is constricted to the passage of the cargo of up to 5-nm in diameter. The mechanism for the entry of a larger cargo, whether it is based on CPP cooperativity for a formation of a larger pore or any other approach, remains to be described.

4. CELL-PENETRATING PEPTIDE ENDOCYTOSIS

Endocytosis is a major entry route used by cells to take up a variety of extracellular substances ranging from nutrients to pathogens to CPPs. Various non-exclusive mechanisms of CPP endocytosis have been proposed. However, there is no consensus and clarity in the field regarding the precise nature of the endosomal pathway used by CPPs and its underlying mechanisms. Similar to direct translocation (described above), numerous components can affect CPP endocytosis, including initial CPP-cell membrane interactions, time of incubation, the nature of the cargo hooked to CPPs, as well as cell lines used.

4.1 Cell-penetrating peptide response to endocytic inhibitors

Pharmacological inhibitors of different stages of endocytosis often provide valuable insight and help determine which endosomal pathway is used by the endocytosed material or a pathogen. This approach has been employed in the study of CPP endocytosis. In Table 1 we can see that, depending on the type of inhibitor used, the uptake of a given CPP can be either decreased, unaffected or even increased in some studies especially for TAT, R8 and R9 peptides, as opposed to WRAP peptide, which is consistently unaffected by any of the endocytosis inhibitors used. Combinations of several inhibitors, for example chlorpromazine with Methyl-β-cyclodextrin or EIPA, appear to abolish the CPP cytoplasmic accumulation with no apparent effect on endocytosis[124]. The effect is often inconsistent between the studies (see Table 1, the results for TAT and R9), cell lines and the fluorophore used to label the CPP[125,126]. Most surprisingly, in some studies, the endocytic inhibitors appear to have an effect on CPP accumulation within the cytoplasm[106,124,127], which can potentially correspond to either increased direct translocation, favored endosomal escape or cell membrane damage. Time-dependent cell visualization as well as viability assays are required to distinguish with certainty between these possibilities. Rendering therefore, static images or flow cytometry data provided by the authors insufficient.

Unfortunately, no general conclusion can be made based on these studies, since different CPP (even closely related families) exhibit different behavior. The nature of the CPP and cell type used may influence the CPP response to various endocytic inhibitors, as demonstrated in a comparative study using 22 CPPs in 4 cell lines[128]. Furthermore, many of pharmacological endocytosis inhibitors lack specificity and, on their own, may generate data that will not be sufficient to tell unambiguously whether a given pathway is used in CPP endocytosis. Therefore, several endocytosis inhibitors should be used (alone or in combination) with appropriate controls: the use of endocytosed material, whose uptake is known to be affected by that inhibitor. Inhibitor-based studies should be complemented with genetic and biochemical approaches, as we can imagine that by blocking one endocytic route, another may be activated. In addition, flow cytometry[51,55,124,126,127,129-132] as well as experiments performed on lysed cells[123,133] are inappropriate for such studies, as they do not allow the distinction between the potential effect of the inhibitor on endocytosis, direct translocation and surface bound CPP. Time-lapse microscopy would be better suited, as we can imagine that even if there is no effect on CPP endocytosis of a given inhibitor, it could affect the movement of vesicles[134], as well as their maturation and these potential effects would become obvious by time-lapse microscopy.

Table 1. Effect of endocytosis inhibitors on CPP uptake. This table lists frequently used endocytosis inhibitors and their effect on the intracellular uptake of various CPP molecules.

Reagent	Function	Decreased uptake	No effect	Increased uptake
Amiloride	Na^+/H^+ exchange inhibition[135]	TAT-Cre-488[51]		
Amonium chloride	Endosome acidification inhibitor	RI-TAT[112]		
Brefeldin A	Trans-Golgi transport inhibitor		TAT[133], REV[133], R8[133], TAT-Technitium[123]	
Chloroquine	Endosomal acidification inhibitor		TAT[133], REV[133], R8[133], TAT-Technitium[123]	
Colchicin	Microtubule polymerization inhibitor		TAT[133], REV[133], R8[133]	
Chlorpromazine	Translocation of clathrin and AP2 from the cell surface[136]	TAT[124,131] and R9[124]	Penetratin[124], WRAP[137]	
Cytochalasin D	Depolymerizes F-actin[138,139]	TAT[55], TAT-Cre[51]	TAT[133,134], REV[133], R8[133], TAT-Technitium[123], TAT-$RasGAP_{317-326}$[99]	
Dynasore	Dynamin inhibitor[140]	R9 and TAT[141]		
EIPA	Na^+/H^+ exchange inhibition[135]	R8[127], R9[141], R16[130], TAT[55,141], Penetratin[130]	R8[130], WRAP[137], TAT-$RasGAP_{317-326}$[99]	TAT[124]
Filipin	Cholesterol sequestration[142]		R8[127]	
IPA3	Inhibitor of PAK1[143,144]	R8[127]	TAT-$RasGAP_{317-326}$[99]	
Methyl-β-cyclodextrin	Cholesterol depletion[145-147]	TAT[141,148], TAT-Cre[51]	Trf[148], Penetratin[124], WRAP[137]	R9[141], R9 and TAT[124]
MSD	Chlathrin-mediated endocytosis inhibitor	RI-TAT[112]		

NEM	Caveolin-dependent endocytosis inhibitor	TAT[132]		
Nocadazole	Disruption of microtubule assembly/disassembly [149]		R8[130], full TAT[134], TAT[133], REV[133], R8[133], TAT-Technitium[123]	
Nystatin	Cholesterol sequestration[150]	TAT-Cre[51]	TAT[131,133], REV[133], R8[133]	R8[127], R8-Cre[127]
Okadaic acid	Caveolin-dependent endocytosis inhibitor	TAT[132]		
Pitstop	Interferes with binding of proteins to N-terminus of clathrin[151]	R8[127]		
Sucrose	Clathrin-mediated endocytosis inhibitor	RI-TAT[112]		
Taxol	Microtubule polymerization stabilizer		TAT[133], REV[133], R8[133], TAT-Technitium[123]	
Wortmannin	pan-PI3K inhibitor[152]	R8[127]	WRAP[137], TAT[133], REV[133], R8[133], TAT-Technitium[123]	

4.2 Cell-penetrating peptide colocalization with endosomal markers

Various forms of endocytosis have been described, and the main endocytic routes are clathrin-mediated endocytosis, macropinocytosis, and CLIC/GEEC[153-155]. Transferrin, dextran and cholera toxin B enter through clathrin-mediated endocytosis, macropinocytosis and clathrin-independent endocytic pathways, respectively and are often used to study such entry routes. Colocalization experiments between transferrin and various CPPs, show partial colocalization between transferrin and R8[127,141], R8-Cre[127], TAT[94,106,112,134,141,148], Penetratin[124,148] and WRAP-siRNA, a tryptohane- and arginine-rich molecule[137]. Dextran appears to colocalize with Penetratin[124], as well as minimally with WRAP[137]. In fact, CPPs appear to stimulate dextran uptake[55]. In turn, cholera toxin B partially colocalizes with Penetratin[124] and TAT[134,148], but not with full size TAT protein[134] or WRAP[137]. Conditional clathrin heavy chain knock out or caveolin-1 knock out had no effect on TAT uptake[156]. Taken together these studies

suggest that CPPs have a somewhat promiscuous endocytic behavior, especially when it comes to TAT or Penetratin.

The early endocytic vesicles (endosomes) are formed by membrane invaginations, actin-driven membrane protrusions (in the case of macropinocytosis for example), or ruffling. Early endosomes mature into multivesicular bodies (MVBs), late endosomes and finally lysosomes, where degradation of the endocytosed material occurs[157,158]. In some circumstances, the endocytosed material can be recycled back to the plasma membrane or towards other cellular compartments such as the Golgi[157-159]. During maturation and trafficking, endosomes are decorated with telltale markers that can be traced back to a given stage of endocytosis. Rab5 and Rab7 are such markers that correspond to early and late endosomes, respectively (Figure 3). Based on visual inspection of representative images in literature, R8 and TAT colocalizes partially with Rab5A[141]. However, a trypthophane-, arginine- rich CPP, WRAP linked to siRNA cargo shows no colocalization with aforementioned markers or lysotracker (labels lysosomes in a pH-dependent manner)[137]. In addition, no colocalization was observed between trans-Golgi network and TAT or R8[141]. Arginine-rich peptides (R4, R8, R16) were not found in mitochondria either[130]. These studies confirm that CPP vesicles correspond to endosomes. However, the difference within the CPP sequences (even between R8 and R16 there is only partial colocalization)[130], as well as the presence of the cargo may influence the type of endocytic route taken by the CPPs.

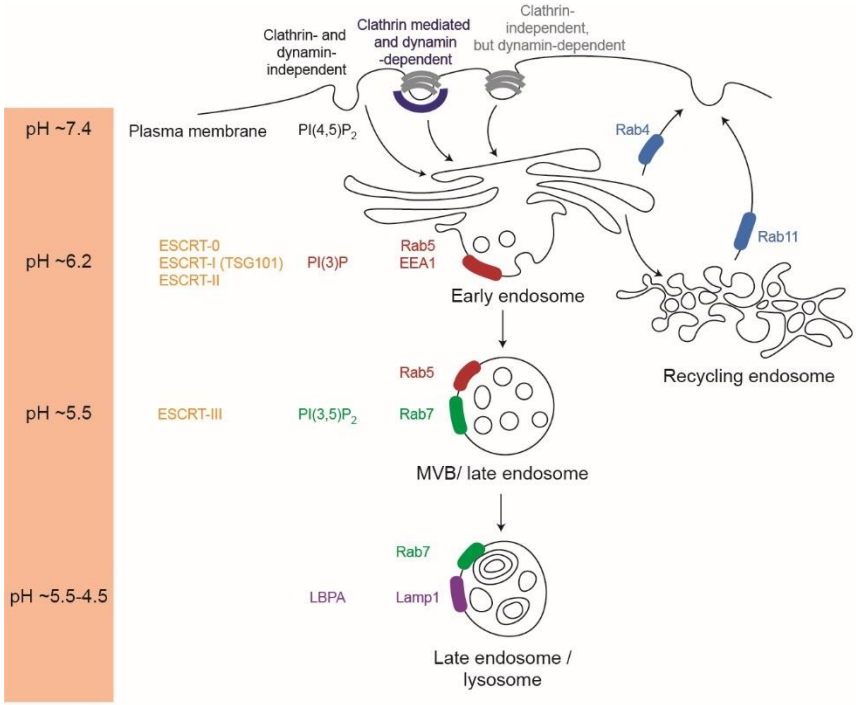

Figure 3. Hallmarks of endocytosis and endosomal maturation.
Endocytosis occurs in clathrin- and/or dynamin-dependent or independent manners. The resulting endosomes first acquire Rab5 and EEA1 on their membranes, then Rab7 and finally Lamp1. The figure also depicts other markers associated with early and late endosomes/lysosomes. Endosomes can be routed to destinations other than lysosomes like the trans-Golgi network or back to the plasma membrane. This involves specific Rab proteins (e.g. Rab4). See text for additional information.

More exotic endocytic markers such as CXCR4[129] and SDC4[127], a co-receptor for HIV-1 infection and a member of cell membrane proteoglycans, respectively, have also been identified. Photocrosslinking experiments revealed partial colocalization between R8 and SDC4[127], which was not observed for CXCR4[129]. siRNA knock down of SDC4 lead to a decrease of total R8 and R8-Cre uptake, with no additional effect in the presence endocytosis inhibitors[127]. However, CXCR4 appears to colocalize to a certain extent with R12[129]. siRNA

knock-down of CXCR4 had no effect on the uptake of TAT, R8 or Transferrin[129], suggesting a specific role of CXCR4 in the uptake of R12.

Taken together, microscopy-based colocalization studies show that cationic CPPs may enter through several endocytic pathways. Some specificity could be observed for peptides that carry a high number of positive charges that potentially can stabilize the initial interaction between the CPP and the cell membrane. Experiments showing qualitative actin rearrangement in the presence of R8 and Penetratin support the importance of initial CPP interaction with the cell membrane to induce CPP endocytosis and potentially direct translocation[130].

Concluding remarks

However, no concrete conclusions can be drawn from these studies. One of the reasons is that not all of the studies use a confocal microscope[141]. Confocal microscopy improves spatial resolution and allows a better distinction between closely positioned vesicles both along the vertical and horizontal planes, which can otherwise lead to false positives in colocalization quantitation. The type of quantification procedure used to measure colocalization, as well as image quality can also impact the results. The typically used software for studying colocalization splits the image into pixels and then considers two channels separately by checking the point of overlap for the single pixels of equal intensity. This methodology does not take into consideration the morphology of endosomes and in a situation where two endosomes are close together or one signal is brighter than the other, the researcher will obtain a false positive result for colocalization. In other studies, there is no rigorous quantification of colocalization and only a few representative images are shown[106,112,124,129,130,134,137,148]. We suggest that visual assessment of representative images as well as the use of Mander's coefficient calculations would be extremely helpful and much more appropriate in the assessment of colocalization[160]. Time of incubation in the presence of the cargo may also play a role, especially in the case when trafficking is halted. This will lead to overestimation of colocalization in comparison to pulse chase experiments at earlier time points. In addition, cell line used, as well as the choice of the fluorophore carried by the CPP may lead to inconsistent results[125,126].

5. DISTINCTION BETWEEN DIRECT TRANSLOCATION AND ENDOCYTOSIS

5.1 Temperature and energy dependence

Endocytosis is considered as an energy-dependent process, which can be blocked by lowering the incubation temperature to 16-20°C to halt endosomal maturation or to 4°C to block endocytosis altogether. Therefore, by evaluating cellular CPP content at 4°C, investigators claim to be able to study direct translocation mechanism in the absence of endocytosis[36,58,60,161]. Previously published data show

that CPPs as Penetratin, TAT, polyarginines (over 8 arginines) are able to enter cells at 4°C through direct translocation in the absence of endosomes[60,162-165]. Furthermore, unlike at 37°C, CPPs accumulate on the cell surface at 4°C independently of GAGs[55,58,60]. These CPP/membrane interactions seem to require CPP accumulation in certain membrane foci leading to membrane protrusion and multi-lamellarity prior to internaliaztion[164,165]. According to several other studies CPP endocytosis and direct translocation are both temperature-dependent processes that are virtually blocked at 4°C[94,106-108,166]. It has been further demonstrated in a comparative study of 22 CPPs in 4 cell lines, that CPP response to temperature decrease and endocytic inhibitor treatment is cell type- and CPP-dependent[128]. Therefore, the effect of temperature on CPP internalization cannot be applied as a general rule to distinguish endocytosis and direct translocation.

5.2 CPP availability

Different CPP/lipid ratio might prompt one mode of entry over the other. CPP/lipid ratio is determined by several factors, among which are CPP concentration in the media and cell number, which may reflect on CPP/membrane binding efficiency. It has been reported by imaging that at lower ratios endocytosis is favored since only vesicular pattern is observed [56,107,111,162,163]. However, the prevalence of residual direct translocation has not been experimentally evaluated and could depend on the sensitivity of the experimental setup. Moreover, serum presence in the media affects the CPP availability. Cationic CPPs interact with proteins present in serum[56,163], which results in lower CPP availability in the media. On the other hand, serum removal sensitized cells to TAT-RasGAP$_{317-326}$-induced death[167]. Therefore, CPP concentrations, more specifically CPP/lipid ratios would have to be adapted for the experiments performed with or without serum to reach a similar biological activity and CPP uptake in cells.

5.3 Size of cell-penetrating peptide-bound cargo

The nature of the cargo carried by the CPP, such as hydrophobicity, secondary structure and size may also influence the internalization efficiency of the CPP-cargo complex. Internalization of the large size (not only molecular weight, but also the volume in space occupied by the secondary structure) cargo bound to TAT, such as ubiquitin and mCherry enter cells predominantly through endocytosis[168-171]. Similar results were observed with R8-bound to EGFP[125], as well as R9-SMAC complex, a caspase activator[124]. Unfortunately, no endosomal escape has been observed in functional assays, among which cytosolic deubiquitination of TAT-ubiquitin or SMAC-induced apoptosis, for the above-mentioned cargo, indicating that the CPP-cargo complexes was trapped in the endosomes. Whether the lack of cytosolic access is specific to the CPP-large cargo internalization or a general feature of CPP-related endocytosis remains to be determined.

5.4 Membrane polarization

Differences in ion concentrations across the cell membrane set an ion gradient, resulting in a membrane potential. Electrophysiological and pharmacological membrane potential modulations have revealed that depolarization blocks CPP uptake[67,112] and hyperpolarization improves the uptake of CPPs that carry positive residues[67,100,119,172,173] (see Introduction section 3). In fact, the membrane potential itself appears sufficient to trigger CPP direct translocation based on live cell experiments[67,100,112], as well as *in silico* studies[116-118]. We have additionally showed that while blocking direct translocation, depolarization has no effect on endocytosis of transferrin[99], vesicular stomatitis virus[174], as well as various CPPs[99]. The fact that decrease in temperature does affect the plasma membrane potential[167] is in line with the observation that R12 uptake that was not inhibited at 4°C[163], was blocked by a potassium rich buffer. These results suggest that membrane potential modulation, more specifically pharmacological depolarization may represent a more efficient strategy to study CPP endocytosis and endosomal escape in the absence of direct translocation (Serulla, et al., manuscript in preparation).

Concluding remarks

As CPPs enter cells through both direct translocation and endocytosis[1,4,175,176], it is very difficult to distinguish between these two processes as both provide two independent strategies for CPP cytosolic access. The most efficient approach appears to be visualization of CPP uptake with a high enough temporal resolution[166,177], however even this is technically challenging. Furthermore, CPP uptake is dependent on numerous factors as structure, size, hydrophobicity, charge, presence or absence of serum, temperature, membrane potential and others. Each of these factors should be considered while studying the CPP internalization and each can potentially be used to study a specific entry mechanism. While some approaches show some controversial results, others demonstrated that membrane potential modulation is an efficient method that allows to selectively regulate the direct translocation of cationic CPPs, up to the point where only endocytosis would take place[67,100,112,119,167,172,173]. However, as many factors, may affect the internalization it is difficult to have a generalized approach and therefore numerous factors must be considered in a case by case manner.

RESULTS PART I:

Genetic, cellular and structural characterization of the membrane potential-dependent cell-penetrating peptide translocation pore

CONTRIBUTIONS

I performed all the experiments except for those listed hereafter. CRISPR/Cas9 screening as well as candidate validation on Raji and SKW6.4 cells were performed by Dr. Mathieu Heulot and Dr. Nadja Chevalier, respectively. *In silico* modeling was performed by Dr. Gianvito Grasso in collaboration with Prof. Andrea Danani laboratory at Dalle Molle Institute for Artificial Intelligence Research, Ticino, Switzerland. TAT-Cre and TAT-PNA uptake experiments were performed by Dr. Mathieu Heulot and Dr. Sebastien Michel, respectively. Mouse injections were performed by Gilles Dubuis and zebrafish injections by Dr. Yoan Arribat at Prof. Francesca Amati laboratory. Pyrene butyrate experiments were performed by Marc Serulla. Quantitation of uptake of several CPPs was done by Florine Ory and CPP/lipid ratio was determined by Lihn Chi Dam. Electrophysiology experiments were performed by me at the laboratory of Prof. Anita Luthi, Department of Fundamental Neurosciences. All under the supervision of Prof. Christian Widmann.

ABSTRACT

Cell-penetrating peptides (CPPs) allow intracellular delivery of cargo molecules. They provide efficient methodology to transfer bioactive molecules in cells, in particular in conditions when transcription or translation of cargo-encoding sequences is not desirable or achievable. The mechanisms allowing CPPs to enter cells are ill-defined. Using a CRISPR/Cas9-based screening, we discovered that KCNQ5, KCNN4, and KCNK5 potassium channels positively modulate cationic CPP direct translocation into cells by decreasing the transmembrane potential (V_m). These findings provide the first unbiased genetic validation of the role of Vm in CPP translocation in cells. *In silico* modeling and live cell experiments indicate that CPPs, by bringing positive charges on the outer surface of the plasma membrane, decrease the V_m to very low values (-150 mV or less), a situation we have coined megapolarization that then triggers formation of water pores used by CPPs to enter cells. Megapolarization lowers the free energy barrier associated with CPP membrane translocation. Using dyes of varying sizes, we assessed the diameter of the water pores in living cells and found that they readily accommodated the passage of 2 nm-wide molecules, in accordance with the structural characteristics of the pores predicted by *in silico* modeling. Pharmacological manipulation to lower transmembrane potential boosted CPPs cellular internalization in zebrafish and mouse models. Besides identifying the first proteins that regulate CPP translocation, this work characterized key mechanistic steps used by CPPs to cross cellular membrane. This opens the ground for strategies aimed at improving the ability of cells to capture CPP-linked cargos *in vitro* and *in vivo*.

INTRODUCTION

Cell penetrating peptides (CPPs) are short non-toxic sequences of 5-30 amino acids present in proteins able to cross membranes such as homeoproteins and some viral components. CPPs can also be used to deliver bioactive cargo (siRNAs, DNA, polypeptides, liposomes, nanoparticles and others) in cells for therapeutic or experimental purposes[1,3,4,8-14,16]. Even though they differ in their origin[17-20] and physico-chemical properties, the majority of CPPs carry positive charges in their sequence[1,4,10,11]. Poly-arginine (e.g. R9), HIV-1 TAT_{47-57}, Penetratin ($Antennapedia_{43-58}$), and Transportan are among the most used and studied CPPs.

CPPs enter cells through a combination of two non-mutually exclusive mechanisms[9,10]: endocytosis and direct translocation[1,3,4,8-12,16]. The nature of these entry mechanisms is debated and not fully understood at the molecular level. The vesicular internalization of CPPs may occur through clathrin-dependent endocytosis, macropinocytosis, and caveolin-1-mediated endocytosis[1,4,8-12]. In this case, access to the cytoplasm requires that the CPPs break out of endosomes through a poorly understood process called endosomal escape.

Direct translocation allows the CPPs to access the cytosol through their ability to cross the plasma membrane. There is currently no unifying model to explain mechanistically how direct translocation proceeds and no genes have yet been identified to modulate the manner by which CPPs cross cellular membranes. There is a general consensus though that an adequate plasma membrane potential (V_m) is required for direct translocation to occur. Electrophysiological and pharmacological V_m modulations have revealed that depolarization blocks CPP internalization[67,112] and hyperpolarization improves the internalization of cationic CPPs[67,100,119,172,173]. By itself, a sufficiently low V_m (i.e. hyperpolarization) appears to trigger CPP direct translocation in live cells[67,100,112]. *In silico* modeling has provided evidence that membrane hyperpolarization leads to the formation of transient water pores, allowing CPP translocation into cells[87,90,116-118] but the free energy landscape governing CPP translocation has not been determined. Moreover, the nature and the structural characteristics of the pores used by CPPs to cross the plasma membrane have not been investigated in live cells.

Here, we provide the first genetic evidence that validates the importance of V_m for CPP direct translocation and we characterize the size of the water pores used by CPPs to enter live cells. We also determined the role of the V_m in modulating the free energy barrier associated with membrane translocation and the impact of the V_m on CPP translocation kinetics.

RESULTS

TAT-RasGAP$_{317-326}$ enters cells via endocytosis and direct translocation, but only direct translocation mediates its biological activity

In the present work, we have used TAT-RasGAP$_{317-326}$ as a model compound to investigate the molecular basis of CPP cellular internalization. This peptide is made up of the TAT$_{48-57}$ CPP and a 10 amino-acid sequence derived from the SH3 domain of p120 RasGAP[178]. TAT-RasGAP$_{317-326}$ sensitizes cancer cells to chemo-, radio- and photodynamic therapies[179-182] and prevents cell migration and invasion[183]. This peptide also exhibits antimicrobial activity[184]. Some cancer cell lines, such as Raji (Burkitt's lymphoma), SKW6.4 (transformed B-lymphocytes) and HeLa (cervix carcinoma), are directly killed by this peptide in a necrotic-like manner[185]. TAT-RasGAP$_{317-326}$ kills cells by physical disruption of the plasma membrane once it has reached the cytosol by direct translocation and interacted with specific phospholipids found on the cytosolic side of the plasma membrane[186]. To characterize the mode of entry of TAT-RasGAP$_{317-326}$, Raji, SKW6.4 and HeLa cells were incubated with a FITC-labelled version of the peptide and visualized over time. Peptide-cell interaction and internalization occurred through the following pattern: binding to the plasma membrane (Supplementary Movie 1), internalization leading to vesicular staining and/or diffuse cytosolic staining, and eventually cell death characterized by membrane disruption (Supplementary Fig. 1a-d and Supplementary Movie 1). Only in a minority of Raji and SKW6.4 cells, was the peptide solely found in vesicular structures (i.e. in the absence of cytosolic staining) (Supplementary Fig. 1b). Most of the cells acquired the peptide rapidly in their cytoplasm without any detectable presence of labelled vesicles (Supplementary Fig. 1a-b and Supplementary Movies 1-2). Even though labelled vesicles might be masked by the intense cytosolic staining (when present), these results nevertheless demonstrate that at the concentrations used here the main mode of entry of TAT-RasGAP$_{317-326}$ in Raji and SKW6.4 cell lines occurs via a non-vesicular direct plasma membrane translocation mechanism. This entry can be visualized in living cells prior to the saturation of the cytosolic signal (Supplementary Movies 1-2). In the case of TAT-RasGAP$_{317-326}$ uptake in HeLa cells, direct translocation and the vesicular mode of entry appeared to occur equally frequently (Supplementary Fig. 1a-b and Supplementary Movie 3). Direct translocation across the plasma membrane often seemed to originate from specific areas of the cells (Supplementary Fig. 1e-f), suggesting discrete structures on the plasma membrane involved in CPP entry[18,36-39]. Laser illumination-induced damage to cell integrity[187-190] was ruled out as a mechanism of fluorescent dye-labelled CPP cellular internalization (Supplementary Fig. 1g). Cells were able to concentrate the CPP in their cytoplasm (Supplementary Fig. 1h). TAT-RasGAP$_{317-326}$ internalization was found to be temperature-dependent (Supplementary Fig. 1i). The contribution of the peptide surface binding to the overall cell-associated signal only accounted to about 20% (Supplementary Fig. 1j-k); hence, the

majority of the cell-associated peptide signal comes from within cells. Despite intensity differences, the kinetics of appearance of the two populations with vesicular and diffuse cytosolic staining was similar (Supplementary Fig. 2a-b). There was an almost perfect correlation between i) the percentage of cells with low intensity peptide fluorescence and the percentage of cells with predominant vesicular staining (Supplementary Fig. 2c), ii) the percentage of cells with high intensity peptide fluorescence and the percentage of cells with marked cytosolic staining (Supplementary Fig. 2d). Cell death induced by TAT-RasGAP$_{317-326}$ was mostly recorded in cells from the high-intensity fluorescent population (Supplementary Fig. 2e), which can only be achieved through direct translocation of the peptide through the cell membrane as cell death was not seen in cells where only vesicular CPP entry had occurred. Hence, direct translocation of the peptide is what allows TAT-RasGAP$_{317-326}$ to kill HeLa cells. In Raji and SKW6.4 cells incubated with TAT-RasGAP$_{317-326}$, only one fluorescence intensity peak was observed at a given time point that progressively shifted towards higher fluorescence intensities (Supplementary Fig. 2f). As little vesicular staining was detected in Raji and SKW6.4 cells incubated with TAT-RasGAP$_{317-326}$ (Supplementary Fig. 1a-b), the peak seen in Supplementary Fig. 2f mostly corresponds to cells that have acquired the peptide through direct translocation. As in HeLa cells therefore, it is the direct translocation of the peptide in Raji and SKW6.4 cells that eventually induces their death. Together these results show that even though two modes of entry can be used by TAT-RasGAP$_{317-326}$ to penetrate cells, it is direct translocation that is necessary for its biological activity.

Identification of potassium channels as mediators of CPP direct translocation into cells

The mode of CPP cellular entry is still debated and no proteins have been identified that regulate this process. The CPP entry process starts after the initial electrostatic interactions between the positively charged CPP and the negatively charged components of the cell membrane[1,3,4,8-12,16]. Interaction with acid sphingomyelinase[32], local membrane deformation[33], as well as calcium fluxes[34] have been suggested to play a role in CPP direct translocation into cells. To screen for genes that control CPP internalization, we performed a CRISPR/Cas9 screen using TAT-RasGAP$_{317-326}$ as a selective agent (Supplementary Fig. 3a). In Raji and SKW6.4 cell lines, among the most highly significantly differentially modulated genes were specific potassium channels or genes coding for proteins known to regulate such channels indirectly (e.g. PIP5K1A[191]) (Fig. 1a and Supplementary Fig. 3b). KCNQ5, identified in Raji cells, is a voltage-dependent potassium channel. KCNN4 and KCNK5, identified in SKW6.4 cells, are calcium-activated channels and belong to the two-pore (voltage-independent) potassium channel family[192], respectively.

These potassium channels were pharmacologically or genetically inactivated (Fig. 1b and Supplementary Fig. 4a-c) to validate their involvement in TAT-RasGAP$_{317-326}$ cellular internalization and the resulting death induction. The KCNQ family inhibitor, XE-991[193], fully blocked peptide

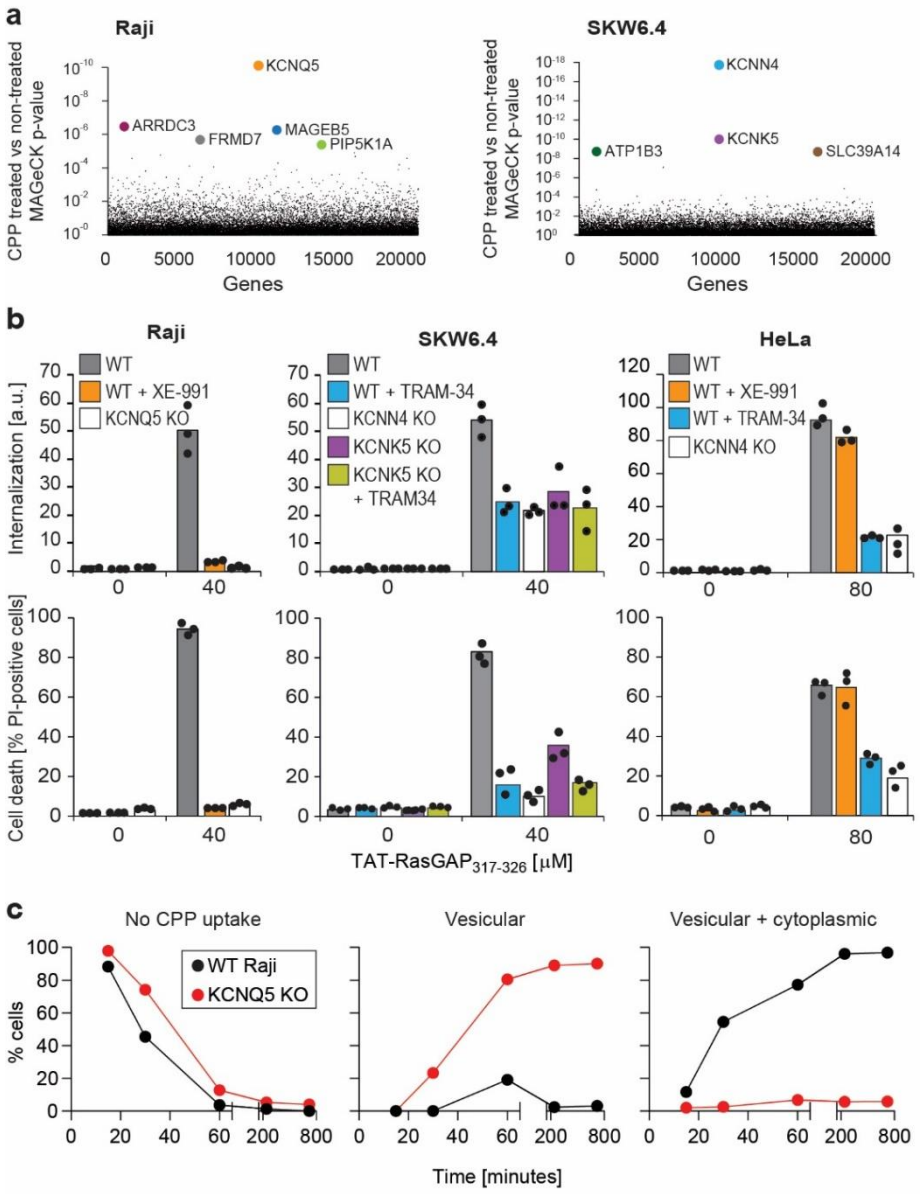

Fig. 1: Identification of potassium channels as mediators of CPP direct translocation into cells

a, Identification of genes implicated in TAT-RasGAP317-326 internalization in Raji and SKW6.4 cells. The graphs depict the p-value (calculated using the MAGeCK procedure; see Materials and Methods) for the difference in sgRNA expression between peptide-treated and control cells for the ~20'000 genes targeted by the CRISPR/Cas9 library. **b,** Quantitation of TAT-RasGAP317-326 entry (top) and induced death (bottom) in wild-type (WT) and knock-out (KO) cells. The WT and the corresponding potassium channel KO versions of the indicated cell lines were pretreated or not for 30 minutes with 10 μM XE-991 or with TRAM-34 and then incubated (still in the presence of the inhibitors when initially added) with, or without 40 μM (Raji and SKW6.4 cells) or 80 μM (HeLa cells) TAT-RasGAP317-326. Internalization was recorded after one hour and cell death after 16 hours (Raji and SKW6.4) or 24 hours (HeLa). Results correspond to the average of three independent experiments. TAT-RasGAP317-326 concentrations and time of incubation used were adjusted so that the CPP induced similar cell death (between 60% and 90%) in the wild-type versions of the different cell lines. **c,** Quantitation of the modalities of TAT-RasGAP317-326 entry in wild-type and KCNQ5 knock-out Raji cells. Cells were incubated with FITC-TAT-RasGAP317-326 for various periods of time and peptide staining was visually quantitated on confocal images (n>150 cells for each time-point). The high percentage of cells with vesicular staining in the knock-out (KO) cells results from the absence of strong diffuse staining masking endosomes. The results correspond to the average of three experiments.

internalization in Raji cells and protected them from the killing activity of the peptide (Fig. 1b). Knocking out KCNQ5 (Supplementary Fig. 4a) in these cells produced the same effect as XE-991 (Fig. 1b and Supplementary Fig. 4d). SKW6.4 cells individually lacking KCNN4 or KCNK5 (Supplementary Fig. 4b), or SKW6.4 cells treated with TRAM-34, a KCNN4 inhibitor[194,195] were impaired in their ability to take up the peptide and were partially protected against its cytotoxic activity (Fig. 1b and Supplementary Fig. 4d). Inhibition of KCNN4 activity with TRAM-34 in KCNK5 knock-out cells did not further protect the cells against TAT-RasGAP$_{317-326}$-induced death. In HeLa cells, TRAM-34, but not XE-991, inhibited TAT-RasGAP$_{317-326}$ internalization and subsequent death (Fig. 1b). Thus, in HeLa cells, KCNN4 channels participate in the cellular internalization of the peptide. This was confirmed by knocking out KCNN4 in these cells (Fig.

1b and Supplementary Fig. 4c). Resistance to TAT-RasGAP$_{317-326}$-induced death in KCNQ5 knock-out Raji cells and KCNN4 knock-out SKW6.4 or HeLa cells was restored through ectopic expression of the corresponding FLAG- or V5-tagged channels (Supplementary Fig. 4e-f and Supplementary Fig. 5), ruling out off-target effects.

To determine if the identified potassium channels affected the biological activity of TAT-RasGAP$_{317-326}$ once inside cells, incubation with the peptide was performed in the presence of pyrene butyrate, a counter anion that, through electrostatic interaction with arginine residues (Supplementary Fig. 6a), promotes quick and efficient translocation of arginine-bearing peptides into cells[196]. Pyrene butyrate, to promote peptide uptake, has to be used in the absence of serum[196]. But since serum removal sensitized cells to TAT-RasGAP$_{317-326}$-induced death (Supplementary Fig. 6b), we had to adapt the CPP concentrations to perform the experiments that employed pyrene butyrate (Supplementary Fig. 6c). Pyrene butyrate was not toxic at the concentrations used (Supplementary Fig. 6d). Potassium channel knock-out Raji and HeLa cells incubated with both pyrene butyrate and TAT-RasGAP$_{317-326}$ were no longer resistant against peptide-induced death (Supplementary Fig. 6e). These results demonstrate that specific potassium channels play crucial role in the cellular entry of TAT-RasGAP$_{317-326}$ but that they are not involved in the killing activity of the peptide if it is already in cells.

We next determined whether vesicular internalization or direct translocation were affected in cells with impaired potassium channel activities. Compared to their respective wild-type controls, the percentage of cells with diffuse cytosolic location of FITC-TAT-RasGAP$_{317-326}$ was drastically diminished in KCNQ5 knock-out Raji cells (Fig. 1c) and in KCNN4 and KCNK5 knock-out SKW6.4 cells (Supplementary Fig. 7a). The effect was similar in the case of KCNN4 knock-out HeLa cells, albeit to a lesser extent (Supplementary Fig. 7b). This was mirrored by an increase in the percentage of knock-out cells with vesicular staining (Fig. 1c and Supplementary Fig. 7a-b). To assess whether cytosolic peptide accumulation is due to direct translocation and not endosomal escape, FITC-TAT-RasGAP$_{317-326}$ internalization was quantitated over time in a condition where the peptide was allowed to enter cells by endocytosis but then removed from the medium. Supplementary Fig. 7c (left) shows that diffuse cytosolic internalization of the peptide occurred when the peptide was present in the medium (see also left panel of Supplementary Movie 4). However, no significant increase in the cytosolic signal was observed in washed out cells containing peptide-labelled endosomes (Supplementary Fig. 7c, middle and Supplementary Movie 4, right panel). We could nevertheless detect an increase in cytosolic fluorescence when endosomal escape was induced by LLOME[197]. This confirms our earlier observation (Supplementary Fig. 1 and Supplementary Movie 1-2) that in live cell conditions the diffuse cytosolic CPP signal originates from direct translocation and not endosomal escape. The invalidation of potassium channels did not affect transferrin internalization into cells (Supplementary Fig. 7d) or the infectivity of vesicular stomatitis virus[174], substantiating the non-involvement of these channels in

endocytosis pathways.

One possibility to explain the above-mentioned results is that the absence of potassium channels prevents the peptide binding to cells. At a 20 μM concentration, TAT-RasGAP$_{317-326}$ is readily taken up by wild-type Raji cells but not by KCNQ5 knock-out cells. At this concentration, peptide binding was slightly lower in knock-out than in wild-type cells (Supplementary Fig. 7e). However, augmenting the peptide concentrations in the extracellular medium of KCNQ5 knock-out cells to reach surface binding signals equivalent or higher than what was obtained in wild-type cells incubated with a 20 μM peptide concentration still did not result in peptide cellular internalization (Supplementary Fig. 7e). These data show that differences in peptide binding do not explain the inability of the knock-out cells to take up the peptide.

We assessed whether the role of potassium channels in cellular internalization also applied to TAT cargos other than RasGAP$_{317-326}$. TAT-PNA is an oligonucleotide covalently bound to TAT, which can correct a splicing mutation within the luciferase-coding sequence[198,199]. This can only occur if TAT-PNA reaches the cytosol. The luciferase activity triggered by TAT-PNA was diminished in the presence of potassium channel inhibitors and in potassium channel knock-out cell lines (Supplementary Fig. 8a). Cytosolic access of TAT-Cre, which can recombine a loxP-RFP-STOP-loxP-GFP[51,200] gene construct, was then assessed. Switch from red to green fluorescence occurs only when TAT-Cre reaches the nucleus. This took place in wild-type Raji cells but not in the KCNQ5 knock-out cells (Supplementary Fig. 8b). We finally tested a clinical phase III therapeutic D-JNKI1 compound[1,3] used in the context of hearing loss and intraocular inflammation. The internalization of this peptide was completely blocked in Raji cells lacking KCNQ5 (Supplementary Fig. 8c, left). D-JNKI1 internalization was also diminished in SKW6.4 cells lacking KCNN4 and KCNK5 channels, as well as in HeLa cells lacking KCNN4 potassium channel (Supplementary Fig. 8c, middle and right panels). These data demonstrate that the absence of specific potassium channels diminishes or even blocks the entry of various TAT-bound cargos.

Potassium channels maintain plasma membrane polarization that is required for CPP entry into cells

Potassium is the main ion involved in setting the plasma membrane potential (V_m). The potassium channels identified in the CRISPR/Cas9 screen may therefore participate in the establishment of the cell V_m. Figure 2a shows that genetic disruption or pharmacological inhibition of KCNQ5 in Raji cells led to an increase in their V_m (from -26 mV to -15 mV, validated with electrophysiological recordings;

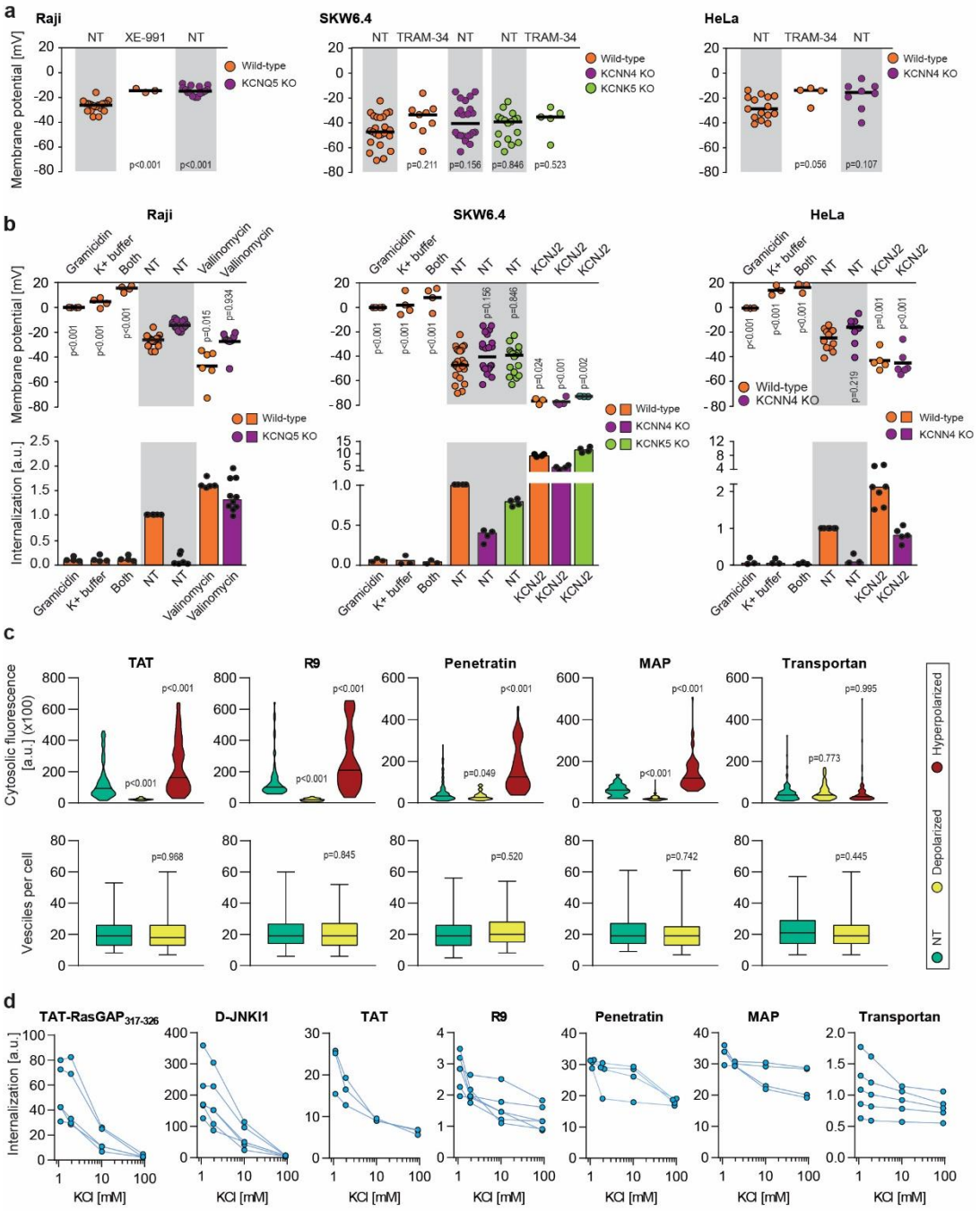

Fig. 2: Potassium channels maintain plasma membrane polarization that is required for CPP entry into cells

a, Assessment of the resting plasma membrane potential in the indicated wild-type cell lines and the corresponding potassium channel knock-out (KO) clones in the presence or in the absence 10 μM XE-991 or TRAM-34. The grey and white zones correspond to non-treated cells and inhibitor-treated cells, respectively. NT, not treated. The p-values correspond to the assessment of the significance of the differences with the control wild-type condition using ANOVA multiple comparison analysis with Dunnett's correction. Each dot in a given condition represents an independent experiment. **b,** Effect of cellular depolarization (left of the grey zone) and hyperpolarization (right of the grey zone) on peptide internalization in the absence of serum. The indicated cell lines and the corresponding channel knock-out (KO) clones were pretreated or not with depolarization agents (2 μg/ml gramicidin for 5 minutes or high extracellular potassium buffer for 30 minutes) or with hyperpolarization inducer (10 μM valinomycin), followed by the addition of TAT-RasGAP317-326 for one hour. Alternatively, hyperpolarization was achieved by ectopic expression of the KCNJ2 potassium channel. Membrane potential and peptide internalization were then determined. Membrane potential was measured in the presence of DiBac4(3) by flow cytometry. Peptide internalization was measured by flow cytometry in the presence of 0.2% trypan blue. The p-values correspond to the assessment of the significance of the differences with the control wild-type condition using ANOVA multiple comparison analysis with Dunnett's correction. Each dot in a given condition represents an independent experiment. **c,** Quantitation of cytosolic CPP signal (top) and the number of endocytic vesicles per cell (bottom) in wild-type HeLa cells (n>150 cells) incubated for one hour with 10 μM FITC-CPP in depolarizing (2 μg/ml gramicidin) or hyperpolarizing (10 μM valinomycin) conditions in the absence of serum based on confocal microscopy images (see Supplementary Fig. 9g). Comparison between different conditions to non-treated control was done using ANOVA test with Dunnett's correction for multiple comparison. The number of endocytic vesicles per cell was quantitated based on confocal images. Statistical comparison was done using t-tests. Quantitation of vesicles was not performed in hyperpolarizing conditions due to masking from strong cytosolic signal. The confocal images were acquired in the middle of the cells based on Hoechst fluorescence. d, Internalization of various CPPs in the presence of different concentrations of potassium chloride in the media. Data for a given experiment are linked with thin blue lines.

Supplementary Fig. 9a-b). Surprisingly, such minimal increase in V_m l between the wild-type and the respective knock-out cells practically abolished CPP internalization (Fig. 2b), indicating that above a certain threshold, the V_m l is no longer permissive for CPP direct translocation. In SKW6.4 and HeLa cells, V_m measurement was much more variable than in Raji cells. Nevertheless, a trend of increased V_m was observed when KCNN4 or KCNK5 were invalidated genetically or pharmacologically (Fig. 2a). As the CRISPR/Cas9 screens performed in various cell lines identified a variety of potassium channels required for efficient CPP internalization, we conclude that it is the V_m maintenance activity of these channels that is important for CPP direct translocation and not some specific features of the channels. If the reason why invalidation of the KCNQ5, KCNN4, and KCNK5 potassium channels inhibits TAT-$RasGAP_{317-326}$ cellular entry is cell depolarization, a similar response should be obtained by chemically inducing membrane depolarization. Figure 2b shows that depolarizing cells with gramicidin[201] (making non-specific 0.4 nm pores[202] within cell membranes) or by increasing the extracellular concentration of potassium (dissipating the potassium gradient) totally blocked peptide entry into the three studied cell lines. Hence, cellular depolarization in itself inhibits TAT-$RasGAP_{317-326}$ cellular internalization (Fig. 2b and Supplementary Fig. 9c). Next, we determined whether hyperpolarization could reverse the inability of potassium channel knock-out cells to take up TAT-$RasGAP_{317-326}$. Cells were either incubated in the presence of valinomycin[203], which leads to formation of potassium-like channels, or transfected with KCNJ2 channel that also provokes potassium efflux and membrane hyperpolarization[204]. Figure 2b shows that in Raji cells, treatment with valinomycin was able to hyperpolarize KCNQ5 knock-out cells to a V_m value similar to the one found in wild-type cells. This fully restored peptide translocation in the KCNQ5 knock-out cells. Hyperpolarization in SKW6.4 and HeLa cells was achieved through KCNJ2 ectopic expression. This reversed the poor capacity of the KCNN4 and KCNK5 knock-out SKW6.4 cells, as well as KCNN4 knock-out HeLa cells, to take up TAT-$RasGAP_{317-326}$ (Fig. 2b). Moreover, hyperpolarization increased peptide internalization in wild-type cells (Fig. 2b). Additionally, cells such as primary rat cortical neurons that naturally have a low V_m (-48 mV) take up the CPP in their cytosol more efficiently than cells with higher V_m such as HeLa cells (-25 mV) (Supplementary Fig. 9d). Altogether, these results demonstrate that the V_m modulates internalization of TAT-$RasGAP_{317-326}$ in various cell lines. This internalization can be manipulated through cellular depolarization to block it and through hyperpolarization to increase it, confirming earlier results obtained for the R8 CPP in Jurkat cells[67].

Next, we assessed whether the entry of different classes of CPPs was also regulated by the membrane potential. The most commonly used CPPs in biology and medicine, TAT, nanomeric arginine (R9), Penetratin, MAP, and Transportan were tested in depolarized and hyperpolarized conditions. The cytosolic signal of these CPPs in HeLa cells appeared to originate from both vesicular and diffuse cytosolic staining (Supplementary Fig. 9e-g). With the notable exception of Transportan, depolarization

led to decreased cytosolic fluorescence of all CPPs, while hyperpolarization favored CPP translocation in the cytosol (Fig. 2c, Supplementary Fig. 9g and 10a). Transportan, unlike the other tested CPPs, enters cells predominantly through endocytosis (Supplementary Fig. 9e), which could explain the difference in response to V_m modulation. The number of CPP-positive vesicles per cell was similar in normal and depolarized conditions, further confirming that CPP endocytosis is not affected by V_m (Fig. 2c, bottom panels). Next, we assessed if modulating V_m through changes in potassium concentrations in the extracellular medium (Supplementary Fig. 10b) impacted CPP internalization. Although the extent of the response varied from one CPP to another, the global observation was that the more depolarized the cells are, the less able they are to take up CPPs (Fig. 2d). CPP membrane binding was only minimally affected by depolarization (Supplementary Fig. 10c). The reason why depolarized cells do no take up CPPs is therefore not a consequence of reduced CPP binding to cells. The V_m also controlled peptide internalization in non-transformed rat primary cortical neurons (Supplementary Fig. 10d). Together these results show that CPP internalization can be modulated in vitro by varying the V_m of cells.

Extracellular pH might regulate CPP internalization[101]. However, in our experimental system, appearance of TAT-RasGAP$_{317-326}$ in the cytosol through direct translocation was unaffected by varying the extracellular pH, whether or not V_m modulators were used (Supplementary Fig. 10e-f).

CPP direct translocation modeling

To further study the mechanism of CPP cellular entry through direct translocation, we took advantage of coarse-grained molecular dynamics technique and MARTINI force field[92,205]. In our simulations we have used TAT-RasGAP$_{317-326}$, TAT, R9, Penetratin, MAP, and Transportan in presence of a natural cell membrane-like composition (for both inner and outer leaflets) while earlier studies have employed simpler membrane composition[87,112,116-119]. Membrane hyperpolarization was achieved by setting an ion imbalance[118,206-208] through a net charge difference of 30 positive ions (corresponding to a V_m of ~2V) between the intracellular and extracellular space. This protocol allowed us to observe CPP translocation across membranes within a few tens of nanoseconds (Fig. 3a-b, Supplementary Fig. 11a and Supplementary Movie 5).

In presence of the ~2V V_m, the CPPs approached the membrane on the extracellular side and this led to the formation of a water column within the membrane that the CPP then used to move to the intracellular space (Supplementary Movie 5). The movement of the positive charges carried by the CPPs, as well as extracellular cations, to the intracellular compartments via the water pore induced membrane depolarization. This depolarization provoked the collapse of the water pore and membrane resealing. Even though CPPs play an active role in their internalization, the mere presence of the CPP in the absence of a sufficiently low V_m was not sufficient to trigger water pore formation (Fig. 3b and

Supplementary Movie 6). These data confirm earlier work describing the role of the V_m in CPP penetration into or through bilipidic membranes[87,90,112,116-119]. Differences in the physico-chemical properties of CPPs not only influenced the tendency of each peptide to translocate into the intracellular compartment (Fig. 3b), but also modified the time needed for water pore formation at a given V_m (Supporting Figure 11b). The more positively charged a CPP (e.g. R9 peptide), the higher probability to translocate across cell membranes (Fig. 3c-d) and faster kinetics of water pore formation at a given V_m. As usually done in the computational field, we used very high V_m values in order to capture ns occurring events. To estimate the time needed for CPPs to translocate through membranes at -150 mV, we established the relationship between the time of CPP translocation and the V_m in the Volt range used during the simulation runs (Supplementary Fig. 11b) and extrapolated from this relationship the time needed for CPP translocation at a V_m of -150 mV (Supplementary Fig. 11b). Even though this extrapolation is likely to lack accuracy because of the well-known limitation of the MARTINI forcefield in describing the absolute kinetics of the molecular events, the values obtained are consistent with the kinetics of CPP direct translocation observed in living cells (Figure 1c and Supplementary Fig. 1b and 9e). With the exception of Transportan, the estimated CPP translocation occurred within minutes. This is consistent with our observation that Transportan enters cells predominantly through endocytosis and its internalization is therefore not affected by changes in V_m (Fig 2c-d and Supplemental Fig. 9e).

We also applied a metadynamics protocol to estimate the impact of the V_m on the free energy landscape of R9 translocation. The free energy barriers recorded in depolarized membranes (V_m = 0) and polarized membranes (V_m = -80 mV) were similar (Fig. 3c-d). The obtained value of about 200 kJ/mol is in in line with recent estimation of the free energy barrier associated with CPP tranlocation at a Vm=0[118]. Only at much lower V_m values (-150 mV) was a marked decreased in free energy barrier recorded. This indicates that hyperpolarization values found in resting cells (down to about -80 mV in neurons and higher in many other cells types[209]) are not more favorable than fully depolarized membranes to establish conditions favorable for the formation of water pores. It appears therefore that cells need to decrease their V_m to much lower values (e.g. -150 mV or lower) to reach conditions compatible with water pore formation.

This observation is in apparent contradiction with our results showing direct translocation in cells at –25 mV (Figure 2), as well as to the experiment demonstrating that CPP cytosolic internalization was more efficient in cortical neurons in comparison to less negatively charged HeLa cells (Supplementary Fig. 9d). We therefore postulate that the presence of CPPs on the cell surface induces locally a substantial voltage drop from the resting Vm. To test this assumption, we analyzed the electrostatic potential map in a molecular system composed of the R9 peptide in contact with the plasma

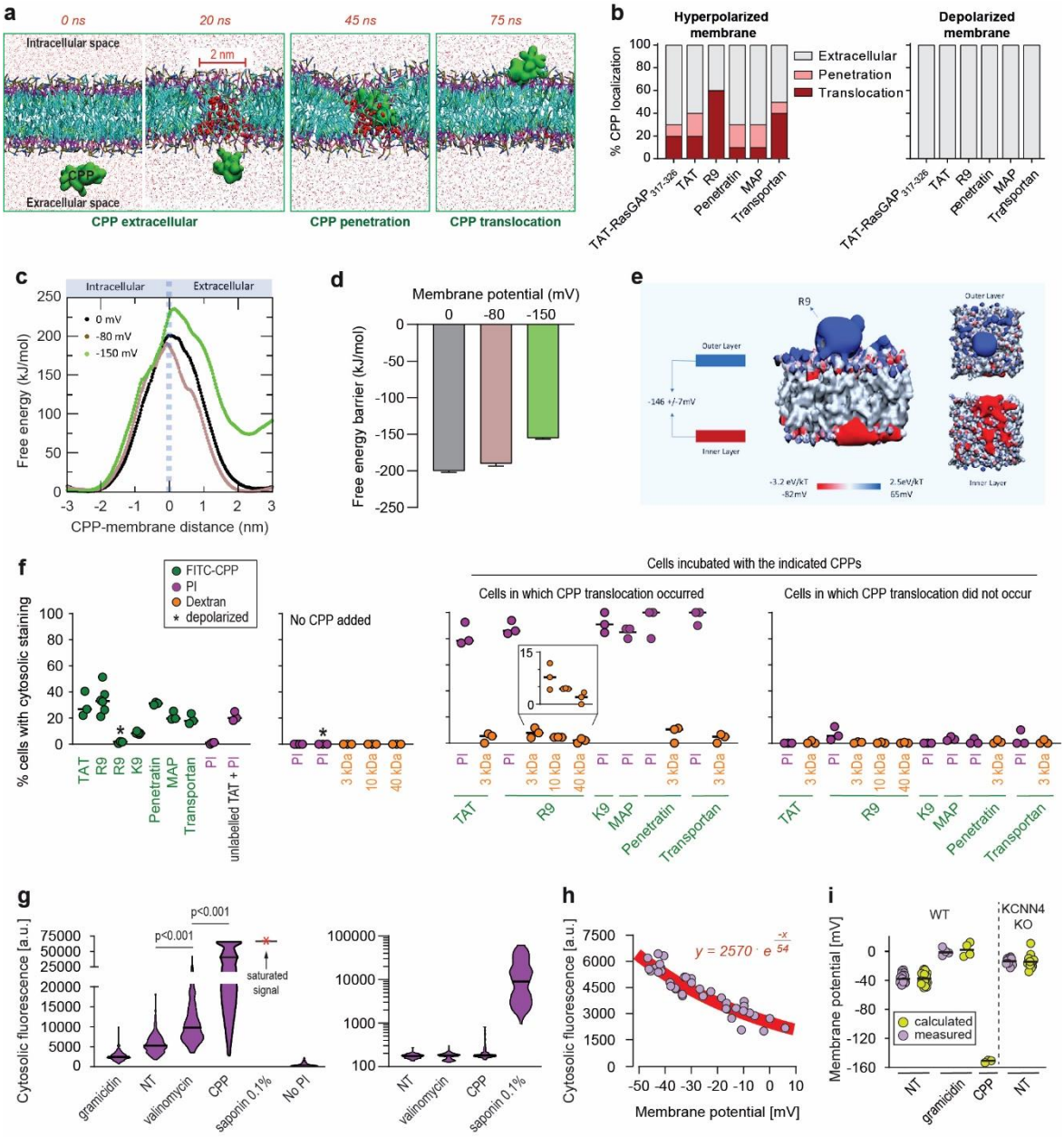

Fig. 3: Hyperpolarization favors the formation of ~2 nm-wide water pores used by CPPs to translocate into cells

a, Visualization of in silico modelled, time-dependent, TAT-RasGAP$_{317-326}$ penetration and subsequent translocation across cellular membrane through a water pore. Water molecules within membranes are depicted by red spheres (and by red dots outside the membrane). **b,** Quantitation of CPP localization in hyperpolarized or depolarized conditions based on coarse-grained molecular dynamics simulations. Membrane hyperpolarization was achieved through a net charge difference of 30 positive ions between intracellular and extracellular space in a double bilayer system obtaining a transmembrane potential of -2.2 V. Such low membrane potential was required to visualize translocation within the time frame of the simulations (100 nanoseconds). **c,** Free energy landscape of R9 translocation reported as a function of CPP-membrane distance. The metadynamics simulations have been performed at transmembrane potential values of 0 mV, -80 mV, and -150 mV (black, brown, and green curve). **d,** Free energy barrier for CPP translocation at different transmembrane potential values. **e,** Electrostatic potential maps of molecular systems that contain or not one R9 peptide in contact with the cell membrane, without any applied external electrostatic field. **f,** Quantitation of the percentage of cells with cytosolic staining after the indicated treatment. The indicated compounds (32 μg/ml PI, 200 μg/ml dextran, 40 μM CPP, except MAP, which was used at 20 μM) were incubated for 30 minutes on HeLa cells. Depolarization, indicated by an asterisk, was induced with 2 μg/ml gramicidin. The percentage of cells displaying cytosolic internalization of the indicated molecules was then determined on confocal images (n>200 cells; see Supplementary Fig. 12a-b). Inset corresponds to an enlargement of the percentage of cells positive for dextran in the presence of R9. The results correspond to at least three independent experiments. **g,** Left graph: quantitation of PI cytosolic internalization in wild type HeLa cells after 30 minutes of incubation in normal, depolarizing (2 μg/ml gramicidin) or hyperpolarizing (10 ⊠M valinomycin) conditions in the presence or in the absence of 40 μM FITC-R9. Cytosolic internalization was quantitated from confocal images using ImageJ (n>300 cells; see the methods and Supplementary Fig. 12b). Right graph: as in left graph, but using lower laser power to avoid saturation of the signal obtained in saponin-permeabilized cells. The p-values correspond to the assessment of the significance of the differences with the non-treated (NT) control condition using ANOVA multiple comparison analysis with Dunnett's correction. The results correspond to three independent experiments. h, Relation between cytosolic PI cytosolic internalization and membrane potential measured with the DiBac4(3) sensor in HeLa cells. Each dot represents an independent experiment. **i,** The relation between PI cytosolic internalization and membrane potential from panel e was used to calculate membrane potential based on PI fluorescence in HeLa cells and its corresponding KCNN4 KO. Measured membrane potential was acquired in the presence of DiBac4(3) based on its cytosolic fluorescence. Each dot in a given condition represents an independent experiment.

membrane in the absence of an external electrostatic field (Fig. 3e). The results indicate that the presence of CPPs at the cell surface is sufficient to decrease locally the transmembrane potential to about -150 mV (Fig. 3e). This was not observed in the absence of the CPP.

In conclusion, our data support a model where CPPs further decrease the Vm of resting cells to very low values (equal or less than -150 mV) that are compatible with spontaneous water pore formation and that we coin megapolarization.

Structural characterization of the pore allowing CPP entry in live cells

To evaluate the structural characteristics of the water pores triggered by CPPs in live cells, cells were co-incubated with molecules of different sizes and FITC-labelled CPPs at a peptide/lipid ratio of 0.012-0.018 (Supplementary Fig. 11c-d). These ratios correspond to the experimental conditions we are using when cells are exposed to 20-40 □M CPPs. Propidium iodide (PI), with a diameter of 0.8-1.5 nm[210] or 3 kDa, 10 kDa, and 40 kDa dextrans, 2.3 ±0.38 nm[211], 4.5 nm and 8.6 nm (size estimation provided by Thermofisher), respectively, were used to estimate the size of the water pores formed in the presence of CPP. While PI and CPPs efficiently co-entered cells, there was only marginal co-entry of the dextrans with the CPPs (Fig. 3f and Supplementary Fig. 12a-b). CPPs did not bind to PI (Supplementary Fig. 12c) and thus PI entry and accumulation within cells was not the result of CPP carry over. The marginal cytosolic co-internalization of dextrans was inversely correlated with their size (inset in the third panel of Fig. 3f). These data indicate that water pores triggered by CPPs allow molecules up to ~2 nm to efficiently enter cells. These results are in line with the *in silico* prediction of the water pore size obtained by analyzing the structure of the pore at the transition state (i.e. when the CPP is crossing the cell membrane; see Figure 3a). The average diameter of the water pore corresponding to the transition state is 1.6+/-0.26 nm.

Molecules in the 2-5 nm diameter range can still use this entry route to a limited extent (of note, the Cre recombinase with a diameter of 5 nm, estimated from crystal structure (NDB:PD0003), can translocate into cells when hooked to TAT; see Supplementary Fig. 8b) but molecules with larger diameters are mostly prevented to do so.

Despite identical net positive charges (Supplementary Fig. 9f), K9 was less capable of translocating into cells compared to R9 (Fig. 3f and Supplementary Fig. 9e)[65]. This may be due to the deprotonation of K9 once in the plasma membrane (see discussion). However, in the few cases when cells have taken up K9, PI co-internalized as well (Fig. 3f). This indicates that K9 has a reduced capacity compared to R9 to trigger water pore formation but when they do, PI can efficiently translocate through the pores created by K9.

PI staining is commonly used to assess cell membrane integrity, frequently associated with cell death (see for example Supplementary Fig. 2e). This dye poorly fluoresces in solution (Supplementary Fig.

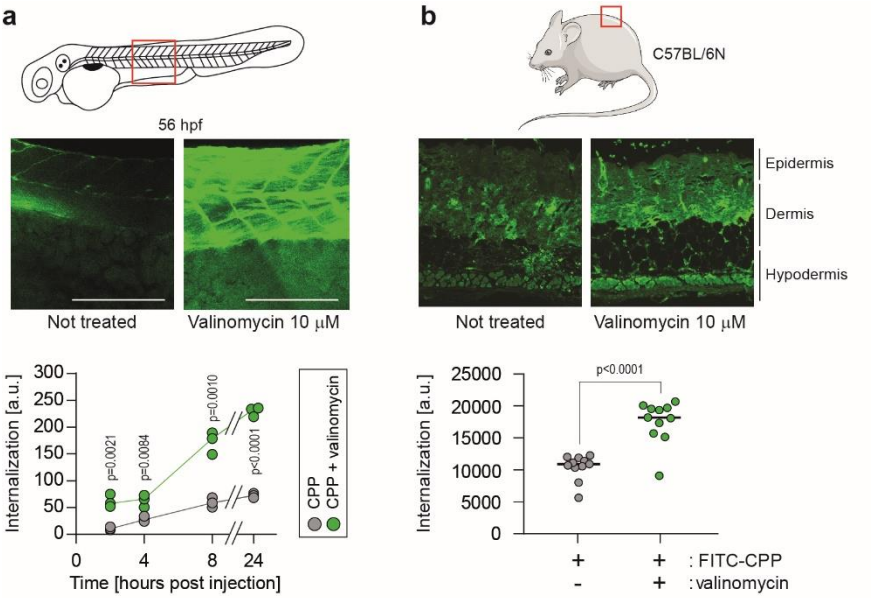

Fig. 4: Hyperpolarization improves CPP internalization in vivo.
a, CPP internalization in zebrafish embryos in normal and hyperpolarized conditions. Forty-eight-hour post fertilization, zebrafish embryos were injected with 3.12 μM FITC-TAT-Ras-GAP$_{317-326}$(W317A) with or without 10 μM valinomycin. Scale bar: 200 μm. The results correspond to three independent experiments. **b,** CPP internalization in C57BL/6N mice in normal and hyperpolarized conditions. Mice were injected with 5 μM FITC-TAT-RasGAP$_{317-326}$(W317A) with or without 10 μM valinomycin (n=11 injections per condition). In both panels, the p values associated with the comparisons of the "CPP" and "CPP + valinomycin" conditions were calculated using two-tailed paired t-tests.

12d). However, the PI cytosolic intensity values in dead permeabilized cells are several orders of magnitude higher than those recorded after cell hyperpolarization (compare the left and right panels of Fig. 3g). Cell viability was not affected by transient treatment with the indicated CPPs, V_m modulating agents and PI (Supplementary Fig. 12e). These results indicate that water pore formation does not compromise cell survival.

Modelling experiments indicate that water pores are created in membranes subjected to sufficiently high (absolute values) V_m. We therefore tested whether the mere hyperpolarization of cells (i.e. in the absence of CPPs) could trigger the translocation of PI into cells, indicative of water pore formation. Figure 3g (left) shows that the hyperpolarizing drug valinomycin significantly increased PI cell permeability. In contrast, depolarization, mediated by gramicidin, reduced PI internalization (Fig. 3g, left). Cells incubated with CPPs took up PI in their cytosol to an even greater extent than when cells were treated with valinomycin (Fig. 3g, left).

Figure 3h shows the correlation between cytosolic PI accumulation over time and V_m. Based on this correlation, we estimated the V_m of cells incubated with a CPP to be in the order of -150 mV (Fig. 3i). In accordance with the modelling experiments, these data further support the notion i) that water pore formation in cells is favored by cell hyperpolarization and inhibited by depolarization and ii) that CPPs themselves[100,212] further contribute to the establishment of local megapolarization in the plasma membrane.

Megapolarization improves CPP internalization *in vivo*

We investigated whether it was possible to experimentally manipulate the V_m to favor CPP internalization in *in vivo* situations. Systemic exposure of zebrafish embryos to valinomycin in eggwater led to cell hyperpolarization (Supplementary Fig. 13a) and improved internalization of a TAT-based CPP

(Supplementary Fig. 13b). This systemic treatment, while not acutely toxic, halted development (Supplementary Fig. 13c-e). However, local valinomycin injection did not affect long-term viability (Supplementary Fig. 13f) and efficiently increased CPP cellular internalization (Fig. 4a). Subcutaneous injections of valinomycin in mice induced tissue hyperpolarization (Supplementary Fig. 13g) and boosted the CPP delivery in skin cells (Fig. 4b). These results demonstrate that hyperpolarizing drugs can be used to ameliorate CPP internalization in animal tissues.

DISCUSSION

Multiple models, mostly inferred from artificial experimental paradigms, have been proposed to explain CPP direct translocation. These include the formation of pores made of the CPPs themselves that they use for their own entry, the formation of inverted micelles in the plasma membrane that translocate the CPPs, or diffusion of the CPPs across the plasma membrane[1,4,8,9,12]. Our simulation and cellular data, while providing no evidence for such models, demonstrate that CPP cellular internalization is potassium channel- and V_m -dependent *in vitro* and *in vivo*. Potassium channels are required to establish a basal low V_m, subsequently permissive for CPP direct translocation. Hyperpolarizing drugs, such as valinomycin, enhance permissiveness. When CPPs come into contact with the plasma membrane, they decrease even more the V_m, resulting in a locally megapolarized membrane. This increases the likelihood of water pore formation that the CPPs then use to penetrate cells according to their electrochemical gradient (Supplementary Fig. 14). Water pores are created by a combination of lipid head group reorientation coupled to intrusion of a column of water in the membrane bilayer. Water movement plays therefore an active role in the formation of the pore and is not merely occurring once the pores are formed. The movement of the positive charges carried by the CPPs into the cell, as well as the transport of extracellular cations (e.g. Na^+), dissipates the V_m, resulting in the collapse of the water pores and sealing of the plasma membrane. CPP-mediated formation of water pores is therefore transient and does not affect cell viability. Multiple rounds of CPP-driven water pore formation and CPP translocation into cells can lead to intracellular accumulation of the CPP to concentrations higher than found outside cells (Supplementary Fig. 1h).

It has not been possible to measure directly the precise values of the V_m that allow the formation of water pores used by CPPs to enter cells. Using an indirect calculation mode based on the uptake of PI alongside CPPs, we have estimated that a V_m in the order of -150 mV is required for water pores to be formed (Figure 3h). This might be an underestimation however as modeling data indicate that, at -150 mV, the free energy barrier, while being markedly diminished compared to those calculated at -80 mV or 0 mV, is not fully abrogated (Figure 3d). Possibly therefore, the local V_m where CPPs interact with the plasma membranes is much lower than -150 mV.

Our model posits that the number of positively charged amino acids influence the ability of CPPs to hyperpolarize cells and hence to form water pores that they take to translocate into cells. CPP hydropathy strongly correlates with penetration of water molecules in the lipid bilayer, thus supporting the hypothesis that the amount of water each CPP can route inside the membrane is modulated by the hydrophobic and hydrophilic character of the peptide[213]. The nature of cationic amino acids in peptides determines their translocation abilities. It is known for example that peptides made of 9 lysines (K9) poorly reaches the cytosol (Fig. 3f and Supplementary Fig. 9e) and that replacing arginine by lysine in Penetratin significantly diminishes its internalization[65,66]. According to our model, K9 should induce megapolarization and formation of water pores that should then allow their translocation into cells. However, it has been determined that, once embedded into membranes, lysine residues tend to lose protons[69,70]. This will thus dissipate the strong membrane potential required for the formation of water pores and leave the lysine-containing CPPs stuck within the phospholipids of the membrane. In contrast, arginine residues are not deprotonated in membranes and water pores can therefore be maintained allowing the arginine-rich CPPs to be taken up by cells. An additional potential explanation to the internalization differences observed between arginine- and lysine-rich peptides is that even though both arginine and lysine are basic amino acids, they differ in their ability to form hydrogen bonds, the guanidinium group of arginine being able to form two hydrogen bonds[68] while the lysyl group of lysine can only form one. Compared to lysine, arginine would therefore form more stable electrostic interactions with the plasma membrane.

Cationic residues are not the only determinant in CPP direct translocation. The presence of tryptophane residues also plays important roles in the ability of CPPs to cross cellular membranes. This can be inferred from the observation that Penetratin, despite only bearing 3 arginine residues penetrates cells with similar or even greater propensities compared to R9 or TAT that contain 9 and 8 arginine residues, respectively (Figure S9f). The aromatic characteristics of tryptophane is not sufficient to explain how it favors direct translocation as replacing tryptophane residue with the aromatic amino acid phenylalanine decreases the translocation potency of the RW9 (RRWWRRWRR) CPP[71]. Rather, differences in the direct translocation promoting activities of tryptophan and phenylalanine residues may come from the higher lipid bilayer insertion capability of tryptophane compared to phenylalanine[74-76]. There is a certain degree of interchangeability between arginine and tryptophan residues as demonstrated by the fact that replacing up to 4 arginine residues with tryptophan amino acids in the R9 CPP preserves its ability to enter cells (ref. 10). It appears that loss of positive charges that contribute to water pore formation can be compensated by acquisition of strengthened lipid interactions when arginine residues are replaced with tryptophan residues. This can explain why a limited number of arginine/tryptophane substitutions does not compromise CPP translocation through membranes.

This phenomenon however cannot be modeled by coarse-grained *in silico* simulations because the protonation state is fixed at the beginning of the simulation runs and is not allowed to evolve. Therefore, the uptake kinetics of lysine-rich peptide, such as MAP, appears artefactually similar as the uptake kinetics of arginine-rich peptides such as R9 (Supplementary Fig. 11b). CPPs can also enter cells through endocytosis, a mode of entry that is not inhibited by cell depolarization (Fig. 2c and Supplementary Fig. 7). The differences between CPPs in terms of how efficiently direct translocation is modulated by the V_m (Fig. 2c-d and Supplementary Fig. 10a) could be explained by their relative dependence on direct translocation or endocytosis to penetrate cells. The more positively charged a CPP is, the more it will enter cells through direct translocation and consequently the more sensitive it will be to cell depolarization (Fig. 2c). On the other hand, when endocytosis is the predominant type of entry, CPP cytosolic uptake will be less affected by both hyperpolarization and depolarization, which is what is observed for Transportan internalization in HeLa cells (Fig. 2c and Supplementary Fig. 10a).

We propose, based on the work described here, that hyperpolarization induced by drugs such as valinomycin represents a simple alternative or parallel approach to optimize CPP internalization. However hyperpolarizing drugs may be toxic when systemically applied. For example, valinomycin at the concentrations used to induce hyperpolarization (10 □M) would be lethal if systemically injected in mice (LD50 in the low micromolar[214]). On the other hand, local administration of valinomycin is far less toxic[215,216] as confirmed here in zebrafish and mice. Hyperpolarizing agents may therefore be preferentially used for local or topical applications, which is incidentally the case for the clinically approved CPPs[1,2].

Strategies to improve CPP delivery are becoming increasingly complex through the use of nanoparticles[217], double-coated nanoparticles[218], liposome-polycation-DNA complexes[219], branched peptides[220], etc. Our data provides a characterization at molecular level that can be taken advantage of to i) improve or optimize « old » CPPs, ii) design new CPPs, iii) help explain the behaviors of newly discovered CPPs[221-223], iv) discriminate between target cells and cells that should be left unaffected based on V_m and v) distinguish between direct translocation and endosomal escape. The present work indicates that the impact on megapolarization should be evaluated when chemical modifications are performed on cationic CPPs to augment their delivery capacities.

ACKNOWLEDGEMENTS

The lab of CW is supported by grants from the Swiss National Science Foundation (n° CRSII3_154420, IZCSZ0-174639 and 158116, awarded to CW and NC respectively). The zebrafish work performed in the lab of FA was supported the Swiss National Science Foundation (n° 320030_170062, to FA). We are thankful to Prof. Denise Nardelli Haefliger and her group, especially to Sonia Domingos Pereira and Laurent Derre for helpful discussions. We are thankful to the Cellular Imaging Facility, Mouse Pathology Facility and Genomic Technologies Facility at the University of Lausanne for the resources provided and their technical help. We would like to thank Giacomo Nanni, for his technical help in running the molecular simulations. We are also thankful to the Swiss National Supercomputing Centre (CSCS).

SUPPLEMENTARY INFORMATION

Effect of serum on cell sensitivity to TAT-RasGAP$_{317-326}$ and CPP internalization

Serum removal sensitized cells to TAT-RasGAP$_{317-326}$-induced death (Supplementary Fig. 6a); therefore, the peptide concentrations had to be adapted to perform the experiments in the absence of serum to reach a similar biological activity (Supplementary Fig. 6b) and CPP uptake in cells. Treatment with pyrene butyrate (Supplementary Fig. 6) and valinomycin (Fig. 2) was used in the absence of serum as the latter is expected to interfere with the drug[203]. Serum-removal did not affect the cell membrane potential (Supplementary Fig. 9b) and the cytosolic internalization results were very similar between the experiments performed in the presence or in the absence of serum, once the CPP concentrations were adjusted (Fig. 2c and Supplementary Fig. 10a). Our results are in line with the previous observations that cationic CPPs interact with proteins present in serum[56,163], which results in lower CPP availability in the media.

Evaluation of water pore formation free energy though MARTINI coarse-grained models

The metadynamics protocol applied in this study has been validated by estimating the water pore formation free energy in a well-studied[224,225] symmetric DOPC membrane. Each layer contained 100 lipids. The membrane was solvated with 3'000 water molecules, obtaining a molecular system of 11'500 particles The MARTINI force field[226,227] was used to define phospholipids' topology through a coarse-grained (CG) approach. The polarizable water model has been used to assess the water topology[228]. The molecular system has been minimized by a steepest descent protocol, and then equilibrated through five MD simulations of 1 ns each under the NPT ensemble. Position restraints were applied during the first three molecular dynamics (MD) simulations and gradually removed, from 200 kJ/mol*nm^2 to 10 kJ/mol*nm^2. Velocity rescaling[229] temperature coupling algorithm and time constant of 1.0 ps were applied to keep the temperature at 310.00 K. Berendsen[230] semi-isotropic pressure coupling algorithm with reference pressure equal to 1 bar and time constant 5.0 ps was employed. Electrostatic interactions were calculated by applying the particle-mesh Ewald (PME)[231] method and van der Waals interactions were defined within a cut-off of 1.2 nm. Periodic boundary conditions were applied in all directions. A metadynamics[232,233] protocol was applied to estimate the free energy of water pore formation. The lipid/water density index has been selected as collective variable (Supplementary Fig. 15). The well-tempered metadynamics simulations were computed using GROMACS 2019.4 package and the PLUMED 2.5. open-source plug-in. Gaussian deposition rate of 1.2 kJ/mol every 5 ps was initially applied and gradually decreased on the basis of an adaptive scheme, with a bias factor of 50. Gaussian widths of 0.5 was applied following a well-established scheme[232,234-237]. In particular, the Gaussian width value was of the same order of magnitude as the standard deviation of the distance CV, calculated during unbiased simulations. Each

system was simulated (with a 20 fs time step) until convergence was reached. The well-tempered metadynamics simulations were computed using GROMACS 2019.4 package[238] and the PLUMED 2.5 open-source plug-in[239] .The reconstruction of the free-energy surface was performed by the reweighting algorithm procedure[240], allowing the estimation of the free energy landscape. Further details about the convergence of the metadynamics simulation of a full DOPC membrane is reported in Supplementary Fig. 16. The comparison between the water pore formation free energy estimated by our MARTINI coarse-grained simulations and previous estimations available in literature is reported in Table S5.

In silico pore formation kinetics though Martini coarse-grained simulations

The water pore formation kinetics has been investigated in this study by applying a constant electrostatic potential to the molecular system[118,241-248]. An asymmetric multi-component membrane was constructed and solvated using CHARMM-GUI[249,250]. Each layer contained 100 lipids (Table S2), in a previously described composition[251]. The membrane was solvated with 3'000 water molecules, obtaining a molecular system of 11'500 particles. The MARTINI[226,227] force field was used to define phospholipids' topology through a coarse-grained (CG) approach. The polarizable water model has been used to model the water topology[228]. The elastic network ELNEDYN[252] has been applied to reproduce the structural and dynamic properties of the CPPs.

For each molecular system, one CPP was positioned 3 nm far from the membrane outer leaflet, in the water environment corresponding to the extracellular space. Then, the system was equilibrated through four MD simulations of 1 ns under the NPT ensemble. Position restraints were applied during the first three MD simulations ang gradually removed, from 200 kJ/mol*nm^2 to 10 kJ/mol*nm^2. Velocity rescaling[229] temperature coupling algorithm and time constant of 1.0 ps were applied to keep the temperature at 310.00 K. Berendsen[230] semi-isotropic pressure coupling algorithm with reference pressure equal to 1 bar and time constant 5.0 ps was employed. Then, all systems were simulated for the production run in the NPT ensemble with the time step of 20 fs. Electrostatic interactions were calculated by applying the particle-mesh Ewald (PME)[231] method and van der Waals interactions were defined within a cut-off of 1.2 nm. Periodic boundary conditions were applied in all directions. Trajectories were collected every 10 ps and the Visual Molecular Dynamics (VMD)[253] package was employed to visually inspect the simulated systems. GROMACS 2018 was used for simulations and data analysis[238]. The relatively small size of the molecular system and the application of Coarse-Grained Martini forcefield, allowed us to study the pore formation kinetics, requiring many simulations at varying field strengths. In detail, 25 simulations were performed for each molecular system at different external electric field strengths from 0.0055 V/nm to 0.090 V/nm. In the MD simulations, an external electric field E_{ext} was applied parallel to the membrane normal z, i.e., perpendicular to the bilayer

surface. This was achieved by including additional forces $F_i = q * E_{ext}$ acting on all charged particles *i.* All the MD simulations were performed until the water pore formation event was observed. In order to determine the effective electric field in simulations, we applied a computational procedure reported in literature[247]. The results are reported in Supplementary Figure 11.

Supplementary Tables

Table S1: Media composition

CAS Number	Components	Quantity in g/l
13477-34-4	Calcium Nitrate Tetrahydrate	0.10000000
7487-88-9	Magnesium Sulfate Anhydrous	0.04884000
50-99-7	D-Glucose Anhydrous	2.00000000
56-40-6	Glycine	0.01000000
39537-23-0	L-Alanyl-L-Glutamine	0.44600000
74-79-3	L-Arginine Free Base	0.20000000
70-47-3	L-Asparagine Anhydrous	0.05000000
56-84-8	L-Aspartic acid	0.02000000
30925-07-6	L-Cystine Dihydrochloride	0.06520000
56-86-0	L-Glutamic Acid	0.02000000
71-00-1	L-Histidine	0.01500000
51-35-4	L-Hydroxy-L-Proline	0.02000000
73-32-5	L-Isoleucine	0.05000000
61-90-5	L-Leucine	0.05000000
657-27-2	L-Lysine Monohydrochloride	0.04000000
63-68-3	L-Methionine	0.01500000
63-91-2	L-Phenylalanine	0.01500000
147-85-3	L-Proline	0.02000000
56-45-1	L-Serine	0.03000000
72-19-5	L-Threonine	0.02000000
73-22-3	L-Tryptophan	0.00500000
69847-45-6	L-Tyrosine Disodium Salt Dihydrate	0.02883000
72-18-4	L-Valine	0.02000000
67-48-1	Choline Chloride	0.00300000
58-85-5	D-Biotin	0.00020000
137-08-6	D-Ca Pantothenate	0.00025000

59-30-3	Folic Acid	0.00100000
87-89-8	Myo-Inositol	0.03500000
98-92-0	Nicotinamide (Nicotinic acid amide)	0.00100000
150-13-0	P-Aminobenzoic Acid (PABA)	0.00100000
58-56-0	Pyridoxine Hydrochloride	0.00100000
83-88-5	Riboflavin	0.00020000
67-03-8	Thiamine Hydrochloride	0.00100000
68-19-9	Vitamine B12	0.00000500
70-18-8	L-Glutathione Reduced	0.00100000
34487-61-1	Phenol Red Sodium Salt	0.00530000
WATER		996.66117500

Table S2. Phospholipid composition considered in the present study

	Inner membrane		Outer membrane	
type	Number of lipids	%	Number of lipids	%
POPC	18	18	39	39
POPE	27	27	6	6
PSM	10	10	21	21
POPS	11	11	-	-
POPI	5	5	-	-
CHOL	29	29	34	34
total	100	100	100	100

Table S3. Primer sequences for the second PCR

F2a	AATGATACGGCGACCACCGAGATCTACACTCTTTCCCTACACGACGCTCTTCCGATCTTCTTGTGGAAAGGACGAAACACCG
F2b	AATGATACGGCGACCACCGAGATCTACACTCTTTCCCTACACGACGCTCTTCCGATCTAGCTCTTGTGGAAAGGACGAAACACCG
F2c	AATGATACGGCGACCACCGAGATCTACACTCTTTCCCTACACGACGCTCTTCCGATCTCGAGCTCTTGTGGAAAGGACGAAACACCG
F2d	AATGATACGGCGACCACCGAGATCTACACTCTTTCCCTACACGACGCTCTTCCGATCTCATAACCTCTTGTGGAAAGGACGAAACACCG
F2e	AATGATACGGCGACCACCGAGATCTACACTCTTTCCCTACACGACGCTCTTCCGATCTGTGCTAACGTCTTGTGGAAAGGACGAAACACCG
R2_iC_26	CAAGCAGAAGACGGCATACGAGATGCTCATGTGACTGGAGTTCAGACGTGTGCTCTTCCGATCTTCTACTATTCTTTCCCCTGCACTGT
R2_iA_12	CAAGCAGAAGACGGCATACGAGATTACAAGGTGACTGGAGTTCAGACGTGTGCTCTTCCGATCTTCTACTATTCTTTCCCCTGCACTGT

Table S4. List of sgRNAs used to disrupt target genes

Target gene	sgRNA name	sgRNA sequence
KCNN4	sgKCNN4.1	CTGCCCGAGTGCTACAAGAA
KCNN4	sgKCNN4.2	CATGGTGCCCGGCACCACGT
KCNK5	sgKCNK5.1	ATGGTGGTAATGACGGTCGC
KCNK5	sgKCNK5.2	CTCTGCCTGACGTGGATCAG
KCNQ5	sgKCNQ5.1	TCTAGGAATTAATTCACAGC
KCNQ5	sgKCNQ5.2	ACAGATCCTCCGCATGGTCG

Table S5. Comparison of the nascent water pore free energy estimation

Force field	Free energy difference (kJ/mol)	References
All-atom (CHARMM36)	95.4	Ting, C.L. et al.[225]
All-atom (CHARMM36)	104.6 (by extrapolation)	Dixit, M. et al.[224]
CG-MARTINI	93+/-1.5	This study

Table S6. List of oligos used for sequencing after TA cloning

Target gene	Oligo name	Oligo sequence
KCNN4	KCNN4.1.TA.F	GCAGAGAAGCACGTGCA
KCNN4	KCNN4.1.TA.R	GGCAGCATGAGACTCCTTCC
KCNQ5	KCNQ5.1.TA.F	GGGACATGATGTACAATGGA
KCNQ5	KCNQ5.1.TA.F	CCAGAGAGCATCTGCATATG

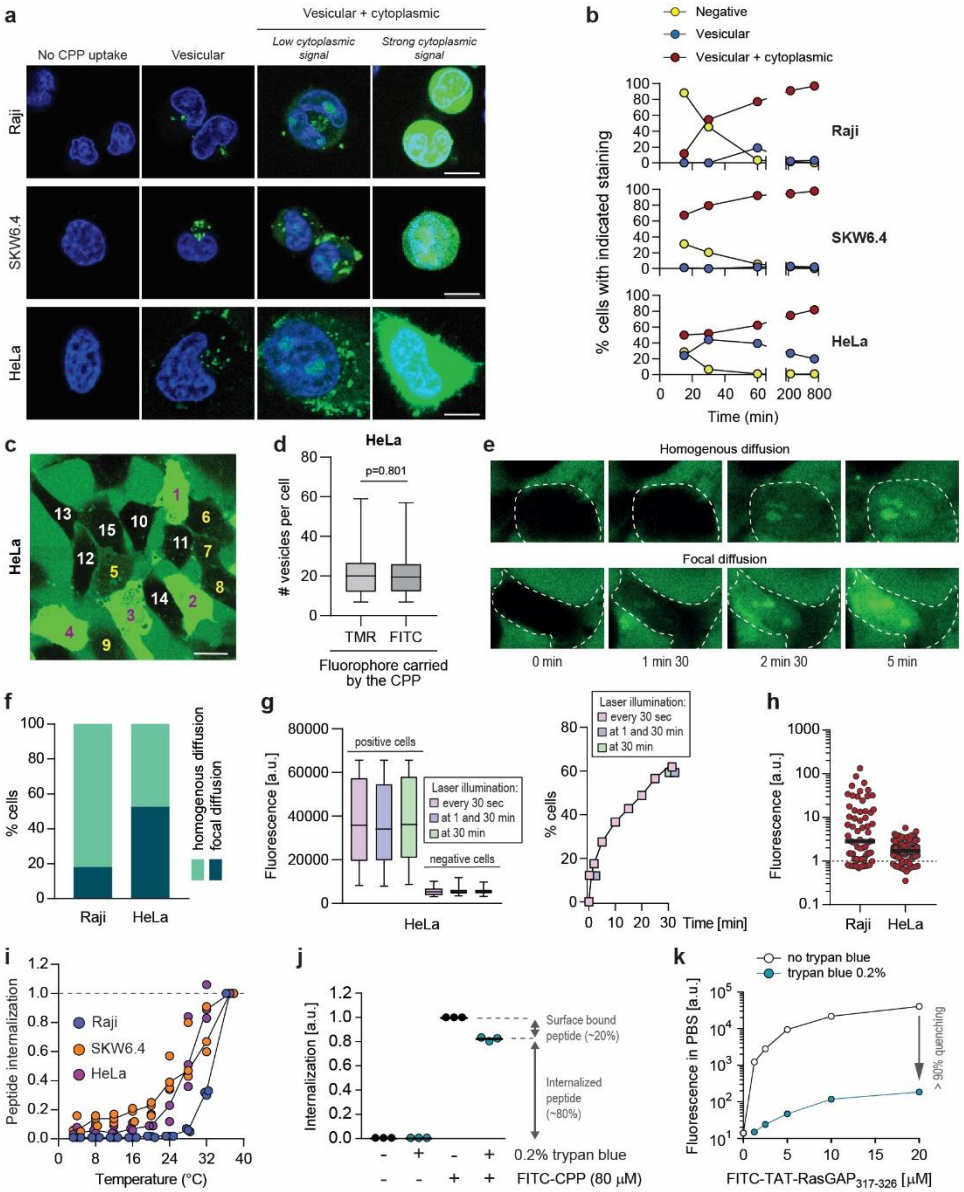

Supplementary Fig. 1: Characteristics of TAT-RasGAP317-326 internalization.

a, Depiction of the different modes of CPP entry into cells. Confocal microscopy was performed on the indicated cell lines incubated for one hour with 40 μM FITC-TAT-RasGAP$_{317-326}$ in RPMI, 10% FBS. Cells were washed with PBS prior to visualization. Vesicular staining is indicative of CPP endocytosis while diffuse cytosolic staining is a consequence of CPP direct translocation into cells. Scale bar: 10 μm. **b,** Quantitation of the different modes of CPP entry as a function of time (FITC-TAT-RasGAP$_{317-326}$ continually present in the media) using the experimental conditions presented in panel a. Types of staining were visually quantitated as indicated in panel c (n>150 cells per condition). There was no indication of fluorescence quenching due to endosomal acidification in at least the first hour of CPP exposure (see panel d). Results correspond to the average of three independent experiments. **c,** Visual attribution of the various types of staining associated with FITC-CPP internalization in wild-type Hela cells. Cells 1-9 took up the CPP through both direct translocation and endocytosis (cells 1-4 and cells 5-9 displaying strong and weak cytosolic signal, respectively); cells 10-15 acquired FITC-TAT-RasGAP$_{317-326}$ in vesicles only, no cytosolic staining being detected. The experimental conditions are those of panel a. Scale bar: 20 μm. **d,** Potential effect of fluorophore quenching in CPP-containing endosome detection. Wild-type HeLa cells were incubated for one hour at 37°C in the presence of 40 μM TAT-RasGAP317-326 labeled with either FITC (susceptible to quenching at low pH) or TMR (not quenched at low pH) fluorophores. The number of vesicles was visually determined based on confocal images. There were no fewer vesicles detected in cells when the peptide was labelled with FITC than when it was labelled with TMR. **e,** Representative confocal images of focal and homogenous cytosolic entry of 80 μM FITC-TAT-RasGAP$_{317-326}$ in HeLa cells over time. **f,** Quantitation in Raji and HeLa cells of the patterns described in panel e. An apparent homogenous type of entry could be focal if the entry point is outside of the confocal plane. Focal diffusion is likely therefore to be underestimated. The results correspond to three independent experiments. **g,** Cytosolic acquisition of fluorophore-labelled CPPs is not a consequence of laser-induced cellular damage. HeLa cells were incubated with 80 μM FITC-TAT-RasGAP$_{317-326}$ for 30 minutes with the indicated frequencies of laser exposures (n>130 cells per condition). Quantitation of the cytosolic fluorescence intensity (n<230 cells per condition) is shown on the left and the percentage of cells with cytosolic fluorescence is shown on the right. FITC-TAT-RasGAP$_{317-326}$ translocation into cells occurred similarly after 30 minutes whether the cells were illuminated once or 60 times over the 30 minutes period. Even if one argues that a single illumination is sufficient to cause the internalization seen after a 30 minute incubation period with the CPP, then the internalization should be the same whether the illumination is performed at 1 minute or at 30 minutes. This is not what is observed: the internalization of the FITC-labelled CPP increases overtime independently of the number of times the cells are illuminated. The results correspond to three independent experiments. **h,** Cells can concentrate CPPs in their cytosol. Wild-type Raji and HeLa cells were incubated with 40 μM FITC-TAT-RasGAP$_{317-326}$ for one hour at 37°C in RPMI, 10% FBS. Images were acquired with a confocal microscope. TAT-RasGAP$_{317-326}$ fluorescence quantitation was performed using ImageJ using region of interest within the cytosol of cells that had acquired the peptide through direct translocation. The dotted line represents the fluorescence in the cell culture media (i.e. outside of the cells). i, Quantitation of FITC-TAT-RasGAP$_{317-326}$ internalization at the indicated temperatures. Cells were incubated on a Thermoblock for one hour. Peptide internalization was measured by flow cytometry in the presence of 0.2% trypan blue to quench the surface-bound fluorescence. The results for each cell line correspond to three independent experiments. The data was normalized to the fluorescence at 37°C (dashed line). **j,** Assessment of the contribution of surface bound FITC-TAT-RasGAP$_{317-326}$ to overall cell-acquired fluorescence. HeLa cells were incubated with 80 μM FITC-TAT-RasGAP$_{317-326}$ for 60 minutes in 24 well plates in 0.5 ml RPMI, 10% FBS. Then, cells were washed once with PBS (1 ml), trypsinized, and resuspended in 0.5 ml PBS containing or not 0.2% trypan blue. Cell-associated fluorescence was recorded by flow cytometry. Data were normalized to the fluorescence values of cells incubated with FITC-TAT-RasGAP$_{317-326}$ in the absence of trypan blue. The results correspond to the average of three independent experiments. The efficiency of trypan blue-mediated FITC quenching is presented in the next panel. **k,** Quantitation, in the absence of cells, of the emitted FITC fluorescence at 525 nm (excitation at 488 nm) of FITC-TAT-RasGAP$_{317-326}$ at the indicated concentrations in PBS in the presence or in the absence of 0.2% trypan blue. Fluorescence was recorded in 96-well plates using a CYTATION3 apparatus.

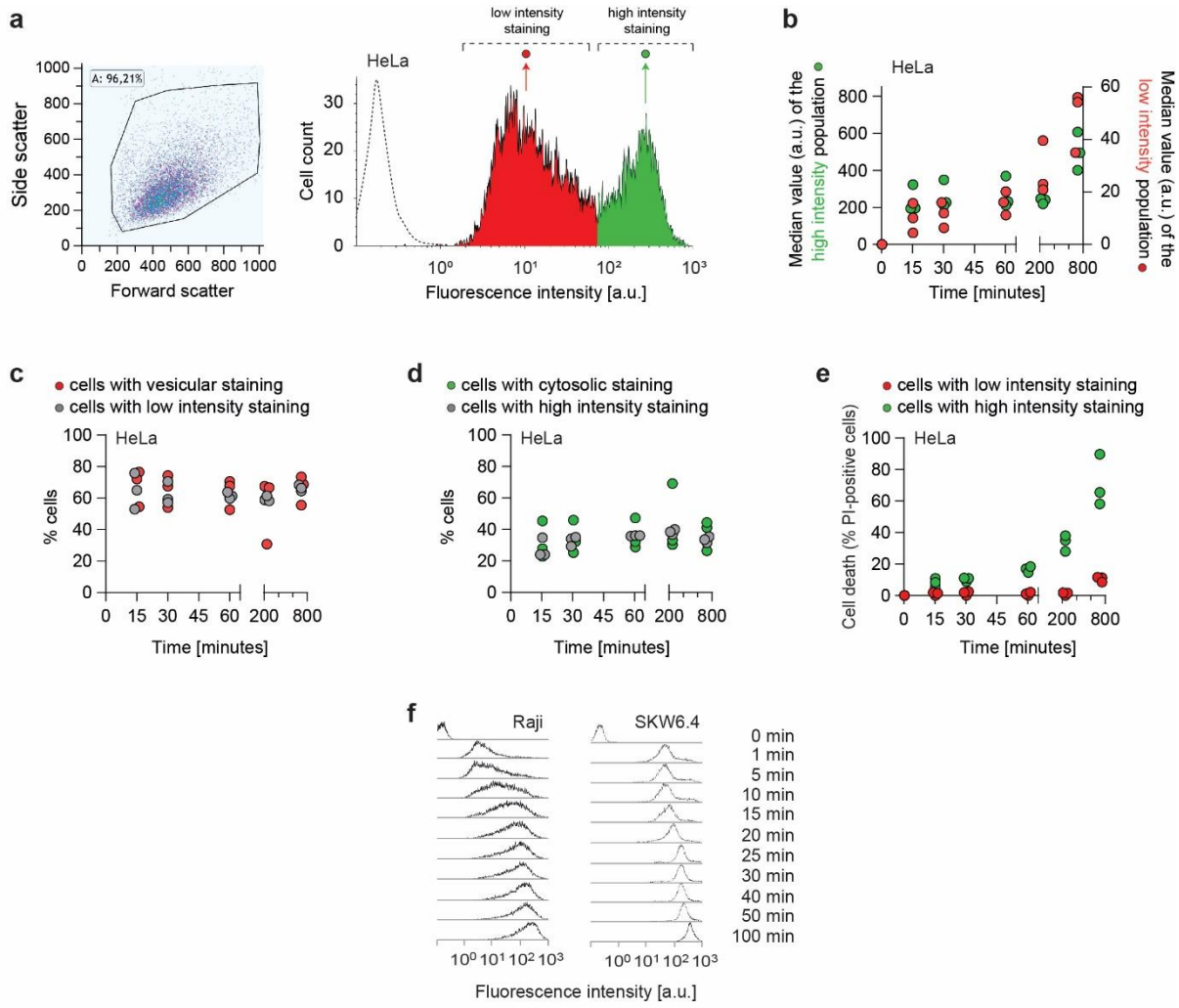

Supplementary Fig. 2: TAT-RasGAP317-326 enters cells via endocytosis and direct translocation, but only direct translocation mediates its biological activity

a-e, HeLa cells were incubated with 80 μM FITC-TAT-RasGAP$_{317-326}$ in RPMI, 10% FBS for the indicated periods of time. Peptide internalization and cell death was assessed by flow cytometry. a, Left: representative flow cytometry dot plot showing the gating strategy used in flow cytometry experiments. Right: representative flow cytometry histogram of HeLa cells incubated with FITC-TAT-RasGAP$_{317-326}$ in RPMI, 10% FBS for 60 minutes. The dotted line represents cellular auto-fluorescence. **b,** Variation over time of the low and high intensity peak values. Peptide internalization was assessed by flow cytometry. The results correspond to three independent experiments. Note the different scales used to plot the median values of the low and high intensity populations. **c,** Quantitation of cells with low intensity peptide fluorescence and vesicular staining. Total peptide internalization was assessed by flow cytometry. The percentage of cells with low CPP cytosolic fluorescence was visually quantitated on confocal images (n>150 cells per condition). The results correspond to three independent experiments. **d,** Quantitation of the pattern of appearance of cells with high intensity peptide fluorescence and strong diffuse cytosolic staining. Data assessment as in panel c. The results correspond to three independent experiments. **e,** Kinetics of FITC-TAT-RasGAP$_{317-326}$-induced death in the two populations described in panel (b). Cell death was assessed by propidium iodide (PI) staining. The results correspond to three independent experiments. **f,** Representative flow cytometry histograms of Raji (left) or SKW6.4 (right) cells incubated with 40 μM FITC-TAT-RasGAP$_{317-326}$ for different period of time. The results correspond to one of three independent experiments. Note: concentrations above 40 μM of TAT-RasGAP$_{317-326}$ led to too extensive Raji and SKW6.4 cell death, preventing analysis of peptide internalization at these concentrations.

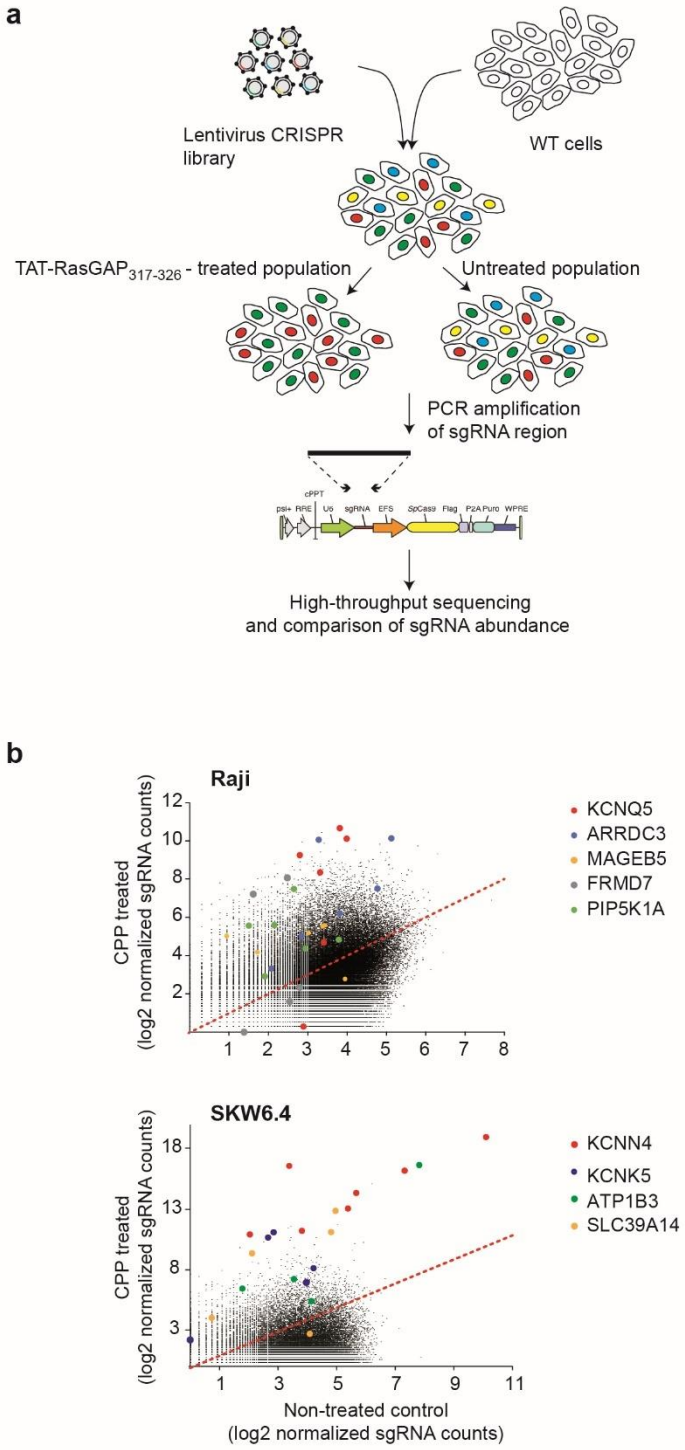

Supplementary Fig. 3: CRISPR/Cas9 screen and target gene identification.
a, Scheme of the CRISPR/Cas9 screening strategy to identify genes involved in TAT-RasGAP317-326 cellular entry. Raji and SKW6.4 cells were infected with a single guide RNA (sgRNA) CRISPR/Cas9 lentiviral library in conditions favoring the expression of only one specific sgRNA per cell (which is indicated by differentially colored cells). The infected cells were then incubated in the presence or in the absence of 40 μM TAT-RasGAP317-326 for 8 days (Raji) or 17 days (SKW6.4). The expression of sgRNAs in both populations was assessed by massive parallel sequencing to determine the enrichment or depletion in specific sgRNAs in the peptide-treated population. **b,** Scatter-plot depicting the changes in sgRNA expression between the control and treated cell populations. The most significantly modulated sgRNA sets are color-coded.

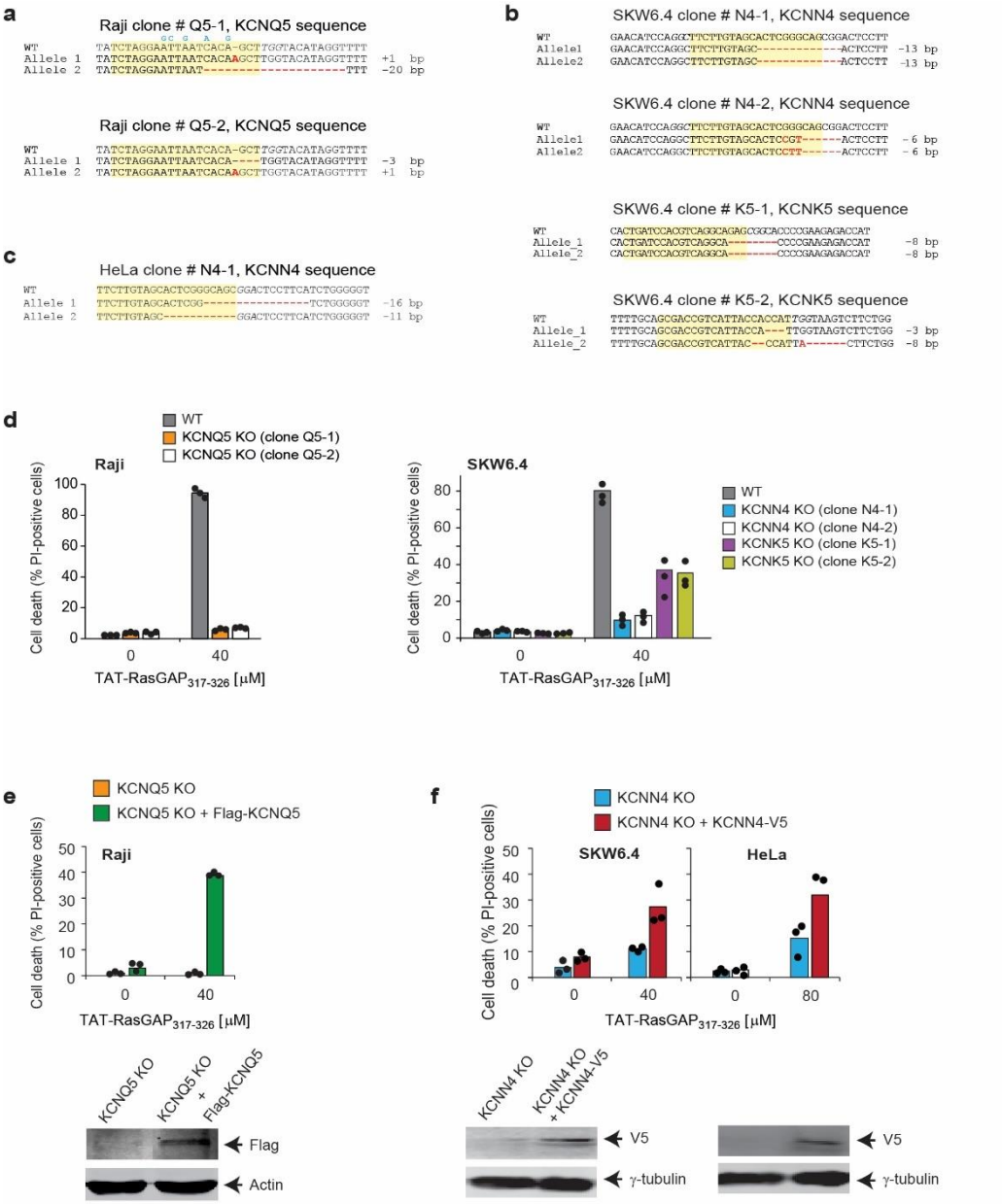

Supplementary Fig. 4: Validation of genes involved in the TAT-RasGAP317-326 internalization identified through CRISPR/Cas9 screening

a-c, Sequencing of the regions targeted by the sgRNAs disrupting KCNQ5, KCNK5 and KCNN4 potassium channels in Raji (panel a), SKW6.4 (panel b) or HeLa cells (panel c). Mutations, insertions and deletions induced by the CRISPR/Cas9 system are shown in red. Except the cases mentioned below, these mutations induce a frame shift and early termination of the open reading frame. The sequences targeted by the sgRNAs are highlighted in yellow. The sgRNA-induced mutations in the first allele of clone Q5-2, in the first allele of SKW6.4 cells clone N4-2, and in the first allele of clone K5-2 do not induce a frame-shift but are located in critical domains necessary for potassium channel activity, such as the pore-forming region of KCNK5 (uniprot accession number:O95279), region adjacent to the pore of KCNQ5 (uniprot accession number: Q9NR82) or calcium recognition domain of KCNN4 (uniprot accession number: O15554). Hence, these alleles presumably encode non-functional channels. Clones Q5-1 in Raji, N4-1 and K5-1 in SKW6.4, and N4-1 in HeLa cells were those that were used in subsequent experiments. The blue nucleotides correspond to silent changes, aimed at reducing sgRNA-targeting, introduced in the KCNQ5-encoding lentiviral vector used in panel e. PAM (protospacer adjacent motif) sequences are italicized. d, The indicated wild-type (WT) and knock-out (KO) cells were tested for their ability to be killed by TAT-RasGAP317-326. Cell death was assessed after 16 hours. e, Wild-type or KCNQ5 knock-out Raji cells were infected or not with a sgRNA-resistant FLAG-KCNQ5-encoding lentivirus and treated with TAT-RasGAP317-326 for 16 hours. Expression of FLAG-KCNQ5 construct was detected by western blot using an anti-FLAG antibody. f, KCNN4 knock-out (KO) SKW6.4 and HeLa cells were infected or not with a KCNN4-expressing lentivirus and then treated with TAT-RasGAP317-326 for 16 hours (SKW6.4) or 24 hours (HeLa). Cell death was assessed by flow cytometry of PI-stained cells. Expression of KCNN4-V5 construct was detected by western blot using an anti-V5 antibody. Note that the Raji, SKW6.4 and HeLa knock-out cell lines still express Cas9 and the sgRNAs targeting the potassium channels. Hence, the ectopically expressed wild-type channel-encoding cDNAs can be targeted by the CRISPR/Cas9 system but this nevertheless allows for a detectable expression of the FLAG- or V5-tagged constructs although to much lower levels than in similarly infected wild-type cells lacking Cas9 and sgRNAs (see Supplementary Fig. 5). In Raji cells, the re-expressed KCNQ5 channel contained 5 silent changes in the sgRNA recognition site (see panel a) but this proved insufficient to allow for a strong ectopic expression (see Supplementary Fig. 5a, last two lanes). In panels d to f, the results correspond to the average of three independent experiments.

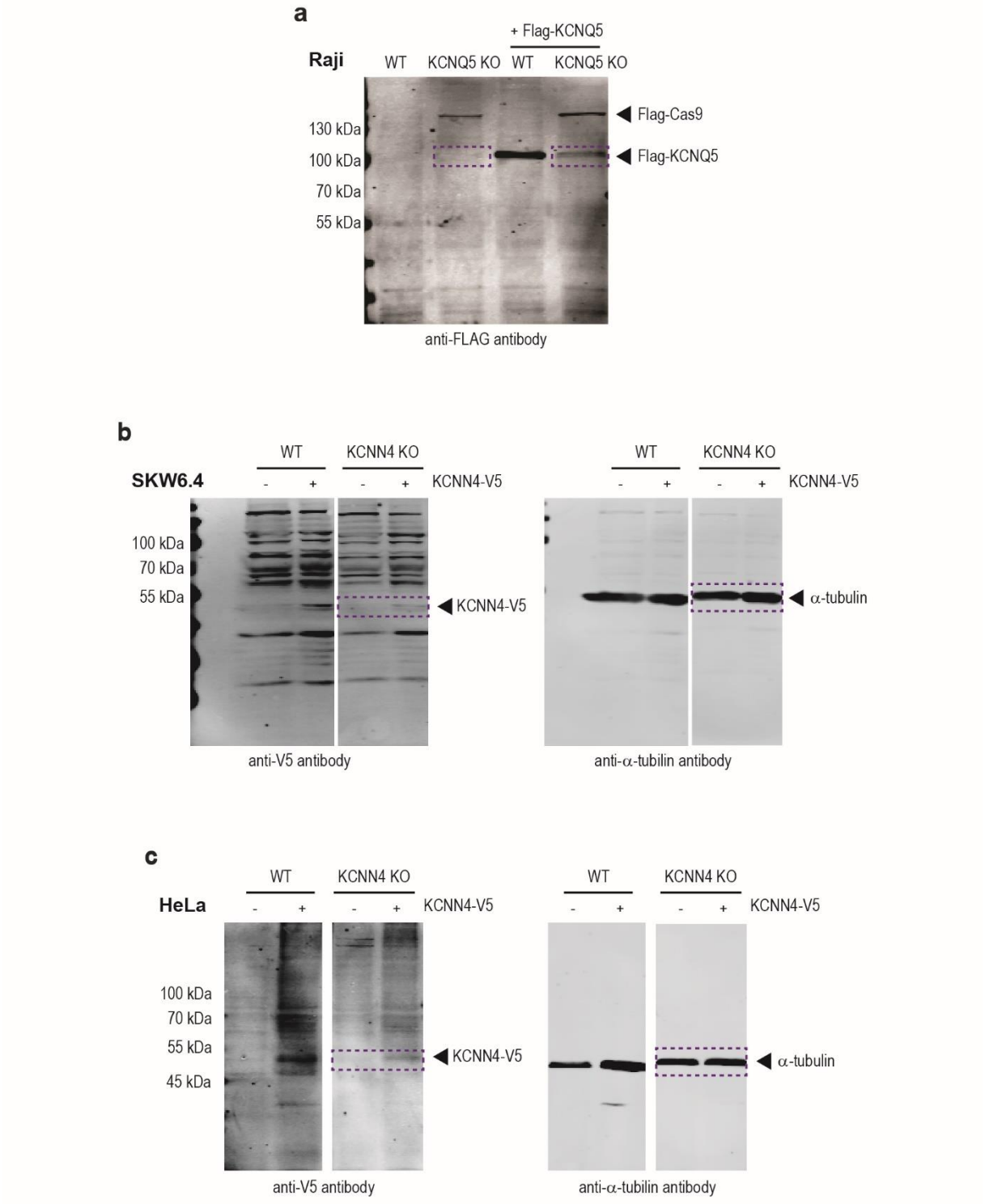

Supplementary Fig. 5: Uncropped western blots assessing the expression of tagged potassium channels through lentiviral expression

a, Wild-type and KCNQ5 knock-out Raji cells infected or not with FLAG-tagged KCNQ5. **b,** Wild-type and KCNN4 knock-out SKW6.4 cells infected or not with V5-tagged KCNN4. **c,** Wild-type and KCNN4 knock-out HeLa cells infected or not with V5-tagged KCNN4. The bands encompassed by dashed purple rectangles are those shown in Supplementary Fig. 4e-f.

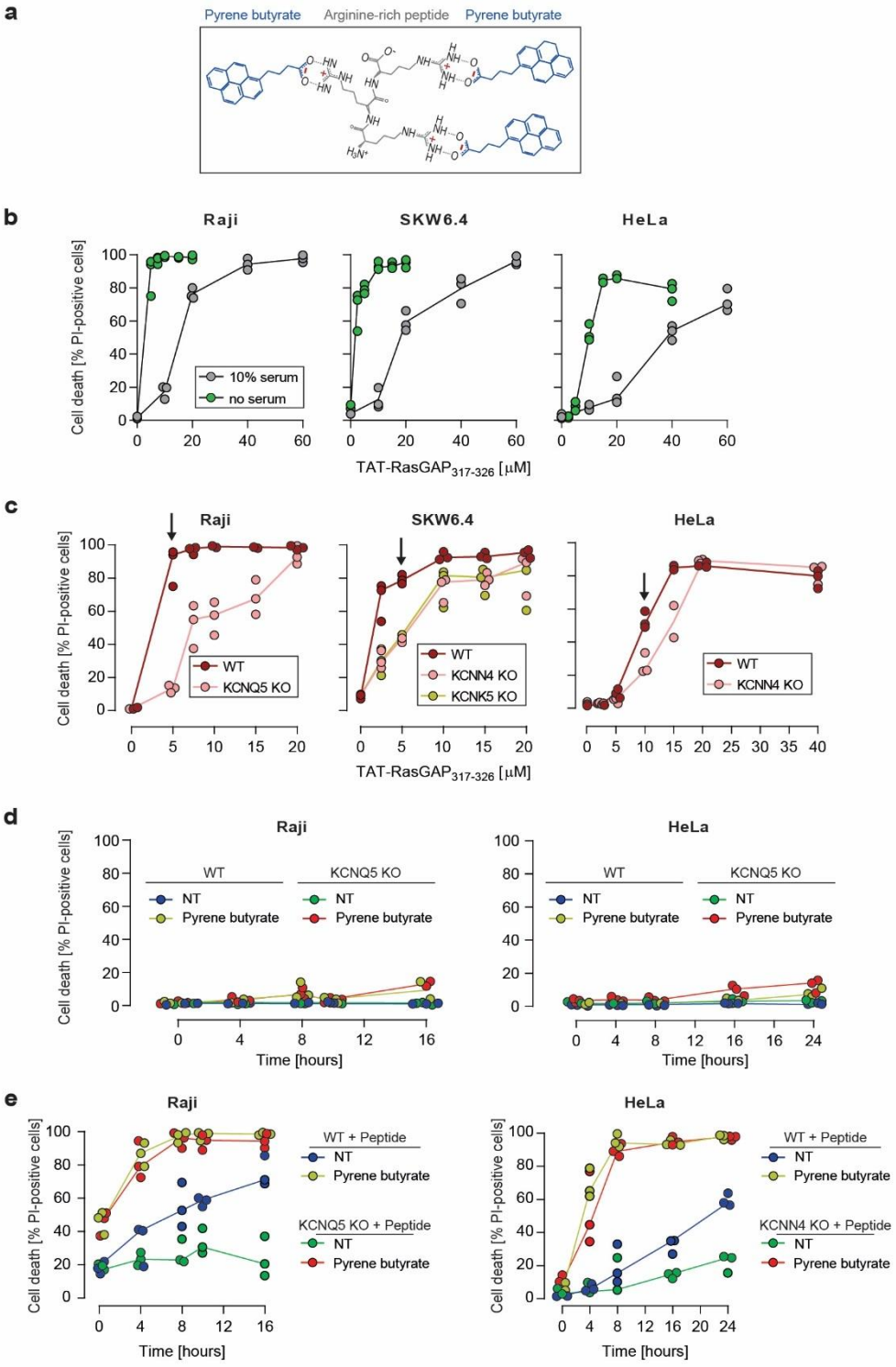

Supplementary Fig. 6: Potassium channels modulate TAT-RasGAP317-326 entry, but not how the peptide induces death. **a,** Structure of pyrene butyrate and its interaction with arginine residues found in CPPs. **b,** Quantitation of concentration-dependent TAT-RasGAP317-326 induced death in Raji, SKW6.4 and HeLa cells in the presence or in the absence of serum. The results correspond to the median of three independent experiments. **c,** Quantitation of wild-type (WT) and knock-out (KO) cell death after incubation for 16 hours (Raji and SKW6.4) or 24 hours (HeLa) in serum-free RPMI media in the presence of increasing concentrations of TAT-RasGAP317-326. Arrows indicate the chosen peptide concentrations for experiments performed in the absence of serum described in panels d and e. The results correspond to the median of three independent experiments. **d,** Cell death assessment in wild-type (WT) and knock-out (KO) Raji and HeLa cells incubated in RPMI without serum, treated (+ pyrene butyrate) or not (NT) with 50 μM pyrene butyrate for the indicated periods of time. DMSO (0.25% vol:vol) was used as a vehicle control for the condition in the absence of pyrene butyrate. The results correspond to the median of three independent experiments. The scheme on the right depicts the structure of pyrene butyrate and how the molecule interacts with arginine residues found in CPPs. **e,** Assessment of peptide-induced death at different time points in pyrene butyrate-treated cells lacking or not specific potassium channel. Cells were incubated with 5 μM (Raji) or 10 μM (HeLa) of TAT-RasGAP317-326, pre-incubated or not with 50 μM pyrene butyrate for 30 minutes (in RPMI without serum). The results correspond to the median of three independent experiments.

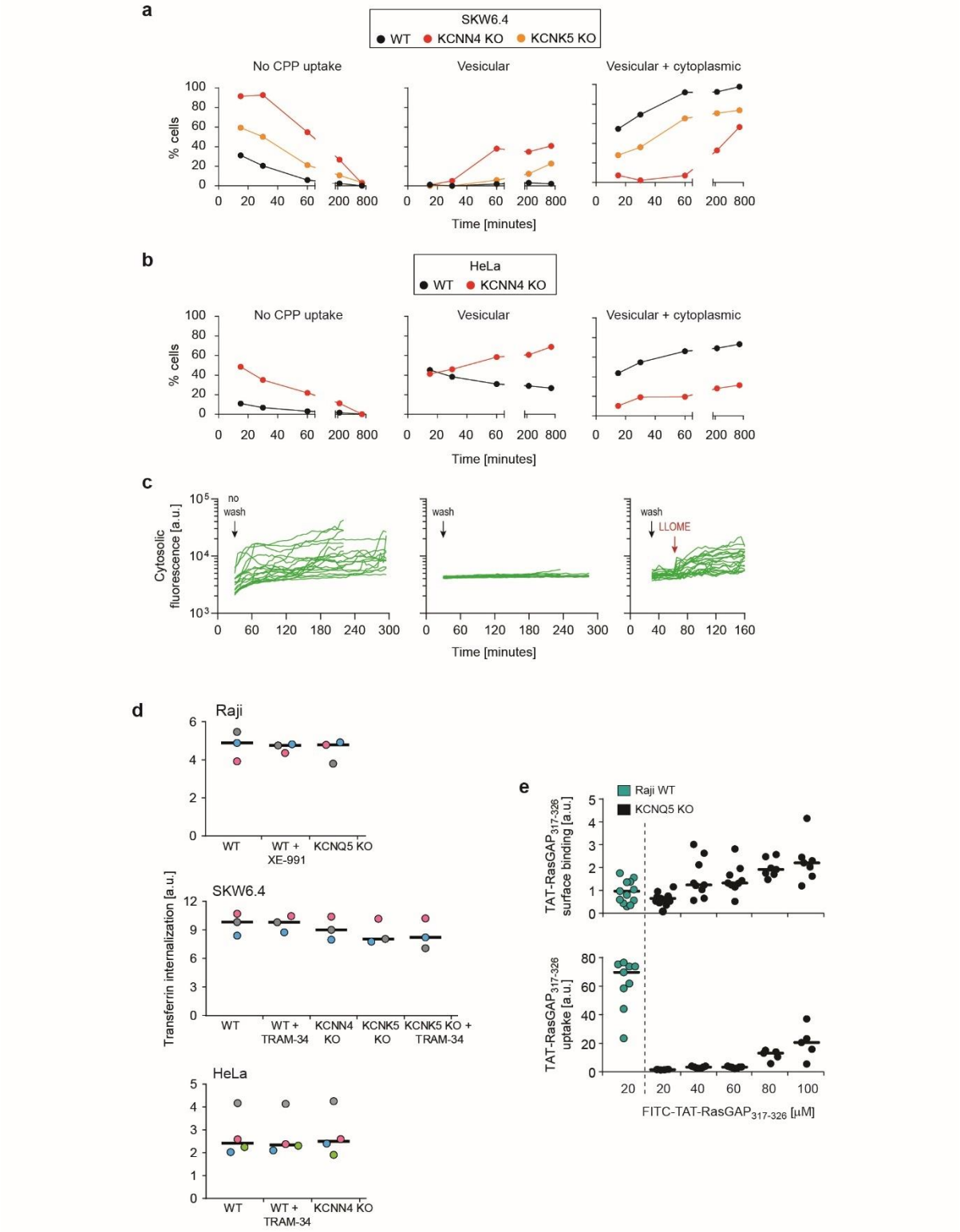

Supplementary Fig. 7: Potassium channels modulate direct CPP translocation, but not endocytosis.
a, Same as Fig. 1c, but for wild-type, KCNN4 and KCNK5 SKW6.4 knock-out cells. The results correspond to the average of three independent experiments. **b,** As panel a, but for wild-type and KCNN4 knock-out HeLa cells. The results correspond to the average of three independent experiments. **c,** Quantitation of TAT-RasGAP317-326 cytosolic access resulting from direct translocation (left, n=19) and endosomal escape (middle, n=16 and right. n=22) in the presence or in the absence of 1 mM LLOME, a endosome/lysosome disruptor35. In direct translocation condition, the peptide was continuously present in the media, while it was washed out after 30 minutes to assess endosomal escape. LLOME was used to show that our experimental setup allows for the detection of cytosolic CPPs if they are released from endocytic vesicles. The results correspond to three independent experiments. **d,** Quantitation by flow cytometry of 20 ⍰g/ml AlexaFluor488-transferrin internalization in the indicated wild-type (WT) cell lines and their corresponding knock-out (KO) versions, pretreated or not for 30 minutes with the XE-991 (10 ⍰ M) or TRAM-34 (10 ⍰M) potassium channel inhibitors. Transferrin internalization was allowed to proceed for 60 minutes (still in the presence of inhibitors when these were used in the 30 minute pre-incubation period). To quench membrane bound transferrin fluorescence, cells were incubated with 0.2% trypan blue prior to flow cytometry analysis. The independent experiment replicates are color-coded. **e,** Assessment of FITC-TAT-RasGAP317-326 cell surface binding on wild-type and KCNQ5 knock-out Raji cells after 60 seconds of incubation (top), as well as associated peptide internalization after one hour of treatment (bottom). The results correspond to at least five independent experiments.

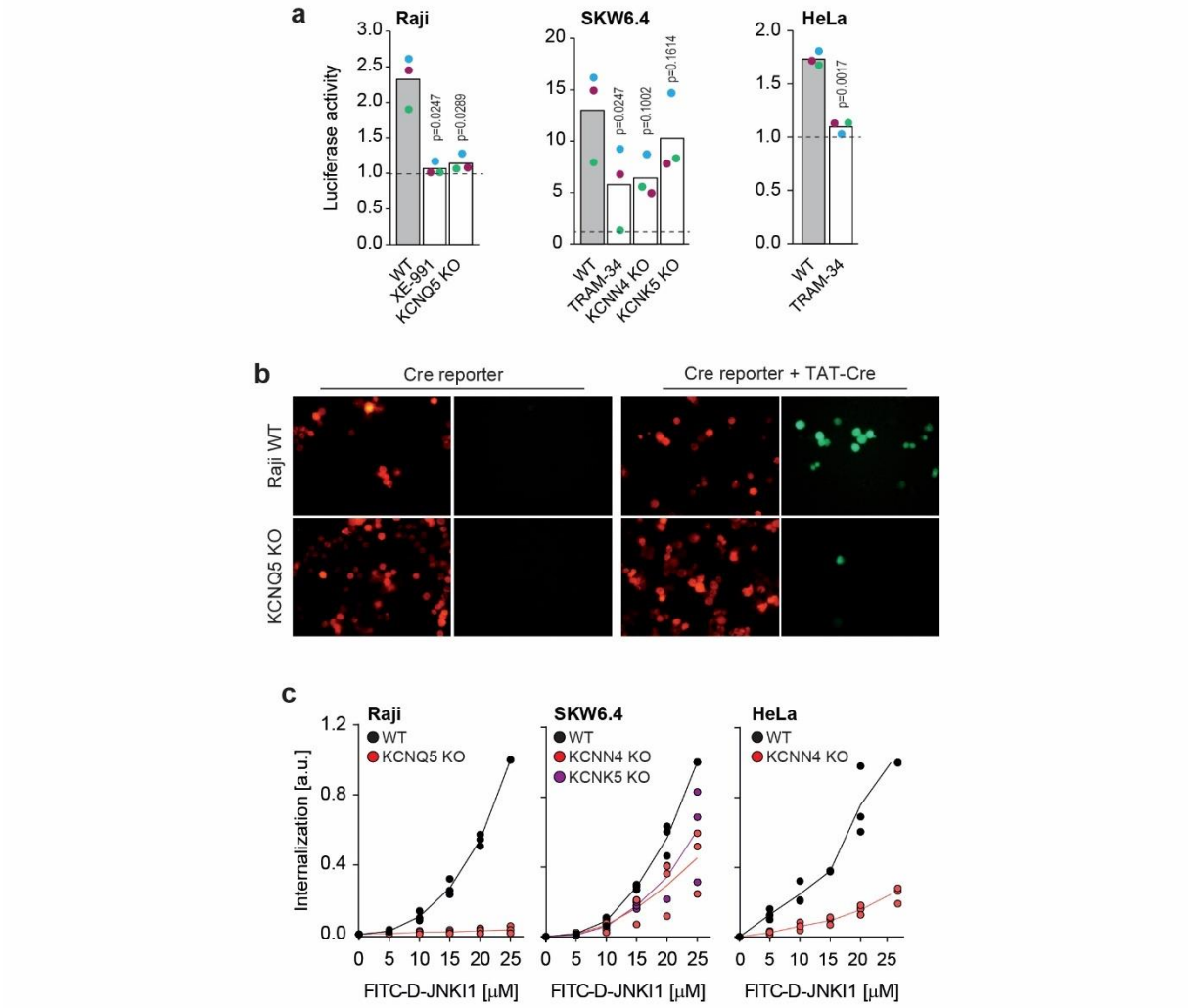

Supplementary Fig. 8: Potassium channels regulate the cellular internalization of various TAT-bound cargos.
a, TAT-PNA-induced luciferase activity in the indicated cell lines pretreated or not with potassium channel inhibitors (XE-991 or TRAM-34) or genetically invalidated for specific potassium channels. Results are normalized to non-stimulated cells (dashed lines). The independent experiment replicates are color-coded. The p-values correspond to the assessment of the significance of the differences with the control wild-type condition using ANOVA multiple comparison analysis with Dunnett's correction. **b,** Representative microscopy images of wild-type and KCNQ5 knock-out Raji cells expressing loxP-RFP-STOP-loxP-GFP and treated or not with 20 μM TAT-Cre for 48 hours. The results correspond to one of three independent experiments. **c,** Internalization of FITC-D-JNKI1 after one hour of incubation in the indicated cell lines genetically invalidated (KO) or not (WT) for specific potassium channels. The results correspond to the median of three independent experiments.

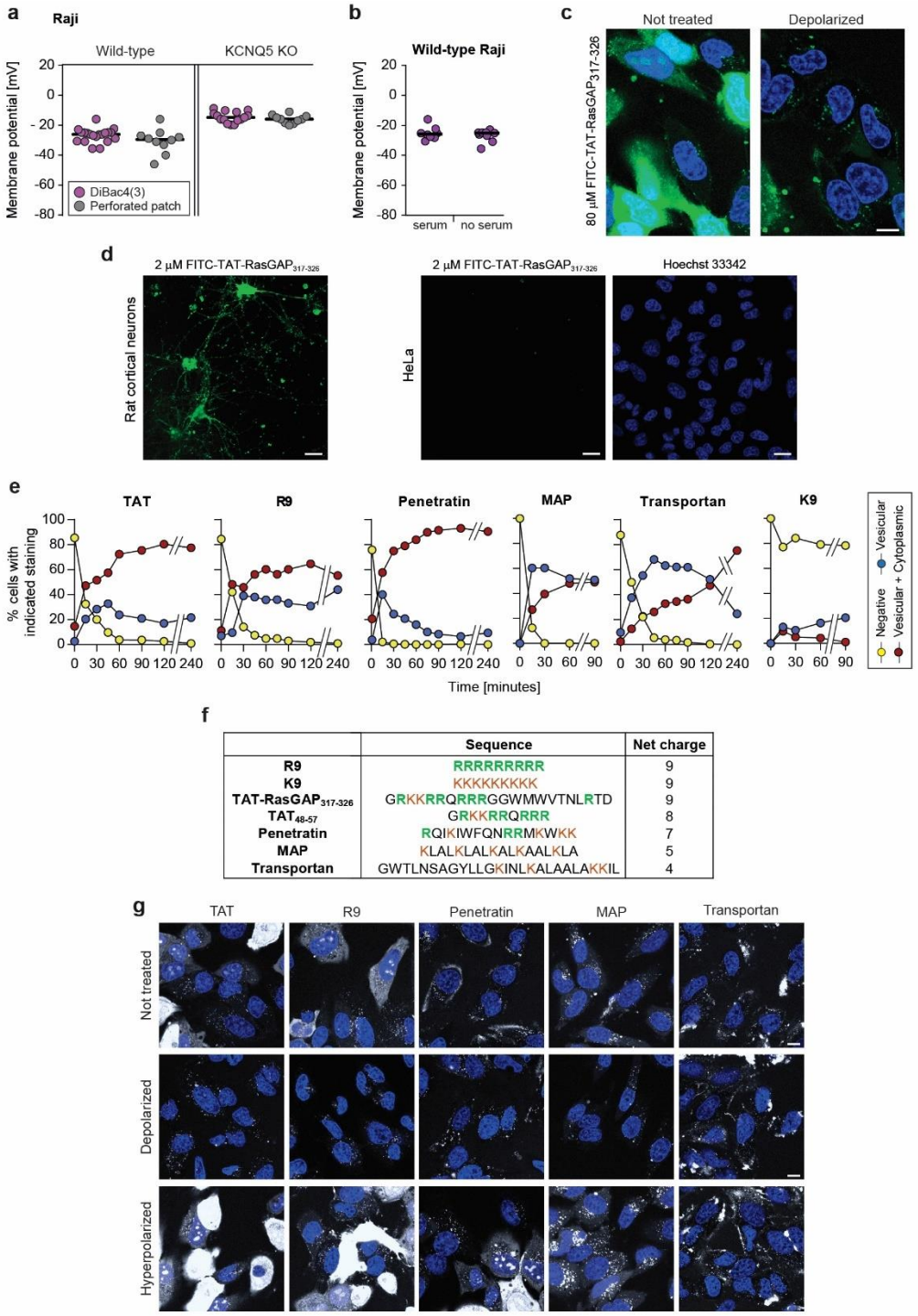

	Sequence	Net charge
R9	RRRRRRRRR	9
K9	KKKKKKKKK	9
TAT-RasGAP$_{317-326}$	GRKKRRQRRRGGWMWVTNLRTD	9
TAT$_{48-57}$	GRKKRRQRRR	8
Penetratin	RQIKIWFQNRRMKWKK	7
MAP	KLALKLALKALKAALKLA	5
Transportan	GWTLNSAGYLLGKINLKALAALAKKIL	4

Supplementary Fig. 9: Intracellular internalization of various CPPs.
a, Membrane potential measurement validation. Membrane potential of wild-type and KCNQ5 knockout (KO) Raji cells was measured using DiBac4(3), a fluorescent membrane potential sensor, or by performing perforated patch electrophysiology recordings. Each dot in the figures reporting DiBac4(3) measurements corresponds to the median of 10'000 cell recording. For perforated patch, each dot in the figures corresponds to the membrane potential of one cell. **b,** Membrane potential measurement in wild-type Raji cells performed in the presence or in the absence of 10% serum. Membrane potential was assessed using DiBac4(3). **c,** Representative confocal images of wild-type HeLa cells incubated with 80 µM FITC TAT RasGAP317 326 for one hour in the presence (depolarized) or in the absence (not treated) of 2 µg/ml gramicidin. Scale bar: 10 µm. **d,** Representative confocal images of primary rat cortical neurons (left) and wild-type HeLa cells (right) incubated for one hour at 37°C with FITC-TAT-RasGAP317-326 in the absence of serum. To highlight the differential capacity of these cells to take up the CPP in cytosol, a low concentration of TAT-RasGAP317-326 (2 µM) was used here. At higher concentrations, this CPP readily enters HeLa cells (see panel c). Post incubation cells were washed and imaged with a confocal microscope using the same laser settings for both cell types. Nuclei of HeLa cells were labelled with Hoechst (blue staining). Scale bar: 20 µm. **e,** Confocal microscopy quantitation of HeLa cells displaying the indicated types of CPP internalization. The CPPs (40 µM, except for MAP 20 µM) were continuously present in the media during the course of the experiment. The results correspond to the average of three independent experiments. **f,** Sequences of the indicated CPPs and their net charge. Positively charged amino acids (arginine and lysine) are color-coded. **g,** Representative confocal images of wild-type HeLa cells incubated with 10 µM of the indicated CPP in the absence of serum in physiological, depolarized (2 µg/ml gramicidin) or hyperpolarized (10 µM valinomycin) conditions. Refer to Fig. 2c for the corresponding quantitation of cytosolic fluorescence and number of CPP-positive endocytic vesicles per cell. Scale bar: 10 µm.

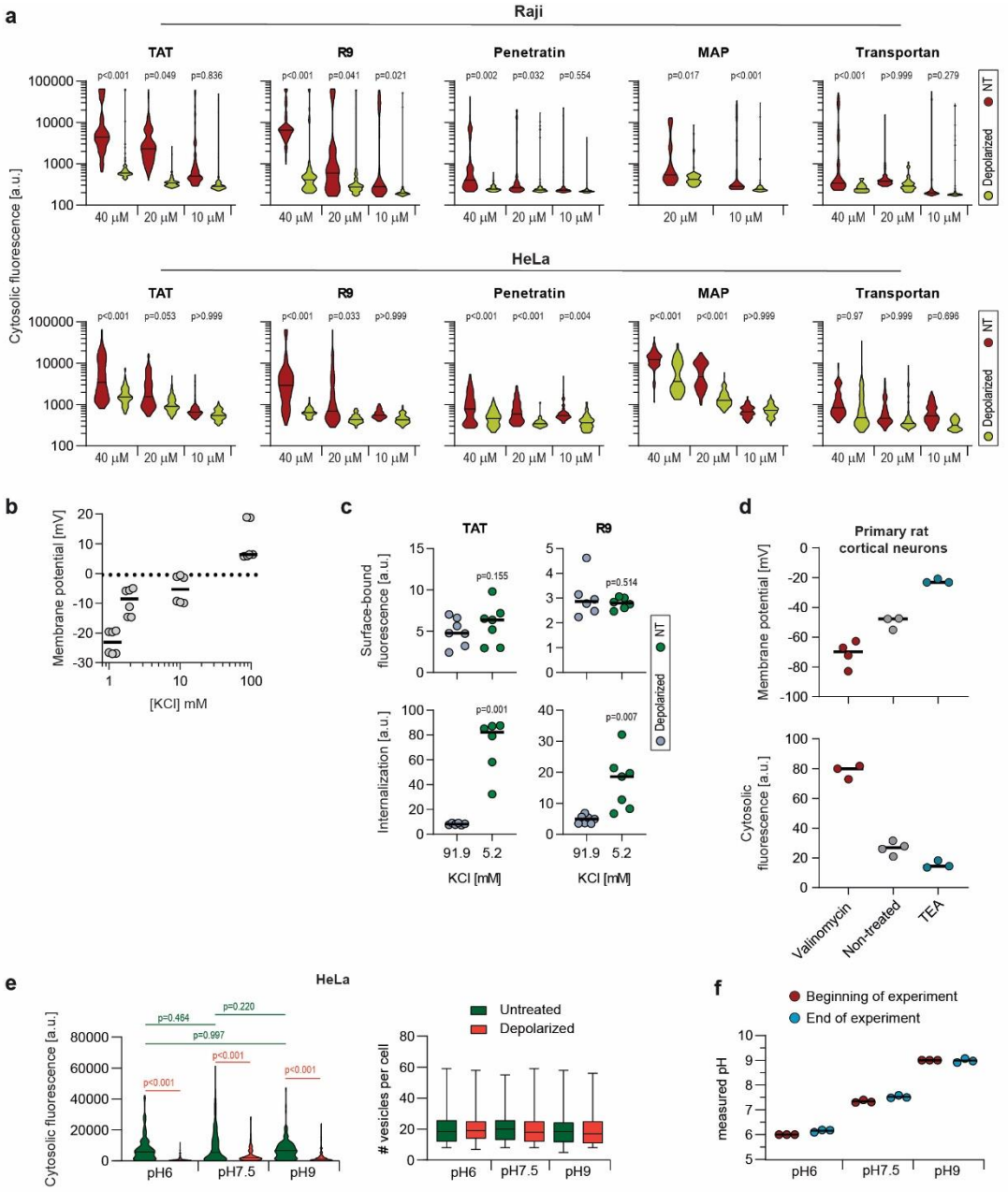

Supplementary Fig. 10: Effect of membrane potential modulation on CPP internalization.
a, Cytosolic CPP levels in normal or depolarized (2 µg/ml gramicidin) conditions in Raji (top) and HeLa (bottom) cells (n>150) incubated for one hour at 37°C with the indicated CPPs in RPMI with 10% FBS. Cytosolic fluorescence was quantitated using ImageJ based on confocal images by selecting a region within a cell devoid of CPP-containing endosomes. Statistical analysis to compare normal and depolarized conditions at given concentrations was performed using ANOVA test with Tuckey correction for multiple comparisons. **b,** Setting membrane potential by varying extracellular potassium concentrations. Assessment of membrane potential changes in Raji cells incubated in RPMI medium containing the indicated concentrations of potassium chloride (isotonicity was maintained by adapting the sodium chloride concentrations; see methods). Membrane potential was measured with DiBac4(3). The results correspond to the median of 4-6 independent experiments. **c,** Assessment of FITC-CPP binding to cellular membrane of wild-type Raji cells in normal or depolarized conditions after 60 seconds of incubation (top), as well as associated peptide internalization after one hour of treatment (bottom). Cells were preincubated for 30 minutes in the presence of RPMI-media containing 5.2 or 91.9 mM potassium chloride and then treated with 40 µM of the indicated CPPs. The results correspond to at least six independent experiments. Comparison between non-treated or depolarized conditions was done using two-tailed paired t-test. **d,** Assessment of membrane potential (top) and FITC-TAT-RasGAP317 326 cytosolic uptake (bottom) in control, depolarized (TEA-treated), and hyperpolarized (valinomycin-treated) primary rat cortical neurons. The results correspond to the median of at least three independent experiments based on confocal images (n>100 cells). **e,** Quantitation of cytosolic TMR-labelled TAT-RasGAP$_{317-326}$ internalization (left) and number of CPP-positive vesicles (right) in HeLa cells (n>150) at the indicated pH in depolarizing and control conditions. These experiments were performed in the presence of 10% FBS as acidification or alkalization were toxic for the cells in the absence of serum. Cells were preincubated in media at the indicated pH in presence or in the absence of 2 µg/ml gramicidin (depolarization), prior to addition of 40 µM TMR-TAT-RasGAP317-326 for one hour. The quantitation was performed based on confocal microscopy images using ImageJ. Statistical analysis was performed using ANOVA test with Tuckey correction for multiple comparisons. f. The pH values remained stable throughout the duration of the experiment in panel e.

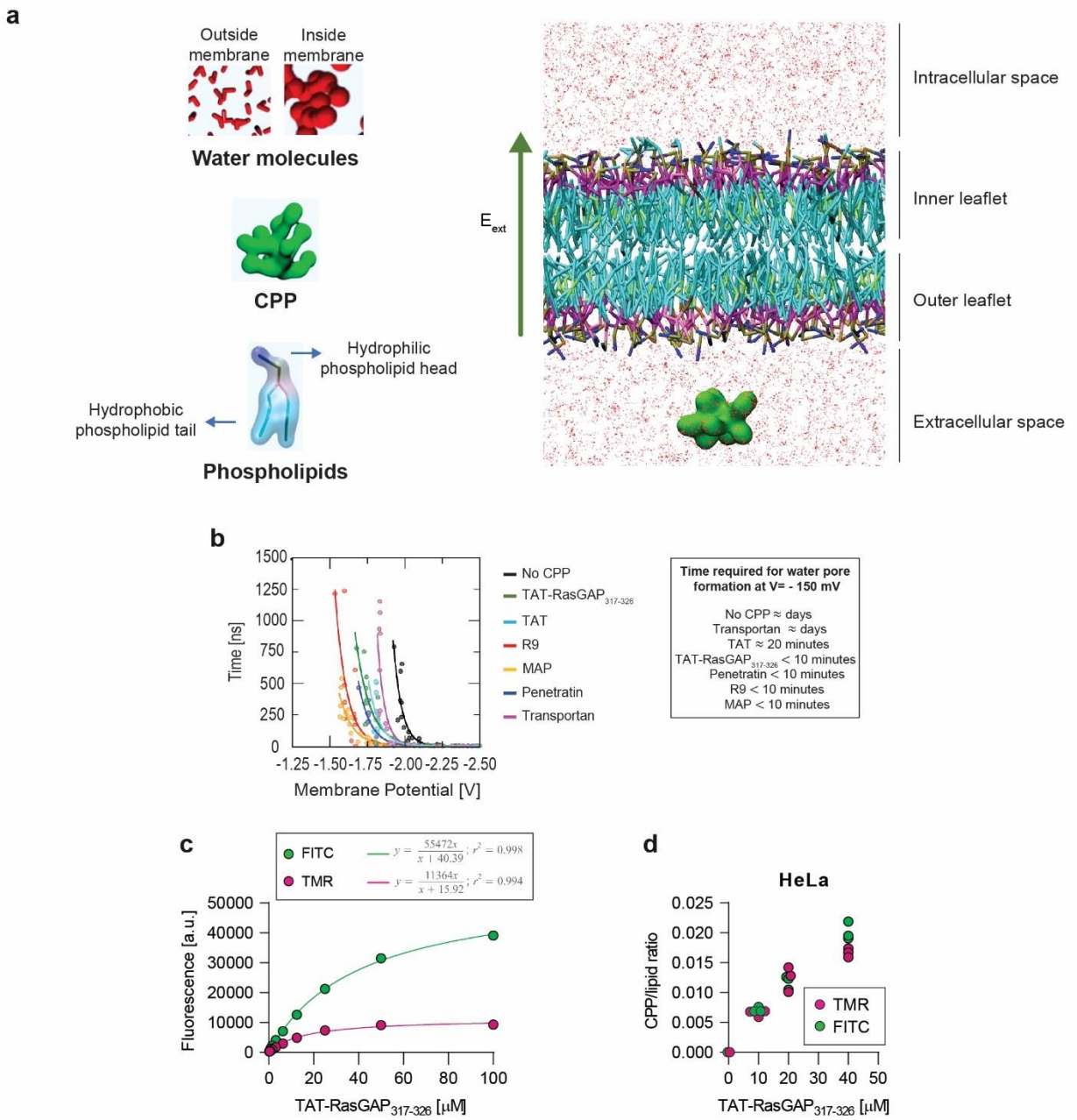

Supplementary Fig. 11: In silico modeling of CPP direct translocation.
a, Schematic depiction of the molecular system used estimate water pore formation kinetics. The static electric field (Eext) has been highlighted with a green arrow. Water molecules are shown as red structures (small when outside membranes and large when found within membranes). **b,** Assessment of the time necessary for water pore formation in the presence or in the absence of the indicated CPPs at 37°C based on in silico pore formation kinetics experiments. A fitting function [t=A0*e(A1*V)] was used, where t is the simulation time of water pore formation, V is the transmembrane potential, A0 and A1 the fitting coefficients. The Pearson correlation coefficients of the fitting curves are R_{R9}=0.85, $R_{Penetratin}$=0.95, R_{MAP}=0.92, $R_{TAT\text{-}RasGAP_{317\text{-}327}}$=0.91, $R_{Transportant}$=0.80, and R_{NoCPP}=0.87. **c,** Fluorescence of FITC- or TMR-labeled TAT-$RasGAP_{317\text{-}326}$ as a function of the peptide concentration in 200 μl PBS in 96-well plates using CYTATION3 apparatus. The curves were fitted with Michaelis-Menten-like equations). **d,** Fluorescence-based CPP/lipid ratio calculations in HeLa cells (the lipids considered here are those of the plasma membrane). Cells (75'000) were incubated with the indicated concentrations of FITC- or TMR-labeled TAT-$RasGAP_{317\text{-}326}$ for one minute at 37°C in 1 ml RPMI, 10% FBS (in this condition, no or only marginal CPP uptake into cells occurs; hence here the CPP signal associated with cells corresponds to cell surface-associated peptides). Cells were then washed on ice twice with ice-cold PBS, lysed in RIPA buffer and scraped. Fluorescence was measured using a CYTATION3 apparatus. This fluorescence was converted in moles of CPPs using the standard curve presented in panel c. Knowing the cell number, the cell surface area (≈ 1600 μm^2) and the number of lipid molecules per μm^2 of plasma membrane (≈$5*10^6$), the moles of lipids in the membrane of the 75'000 HeLa cells used in this experiment could be calculated. The graph reports the CPP to lipid ratio as a function of the CPP concentrations.

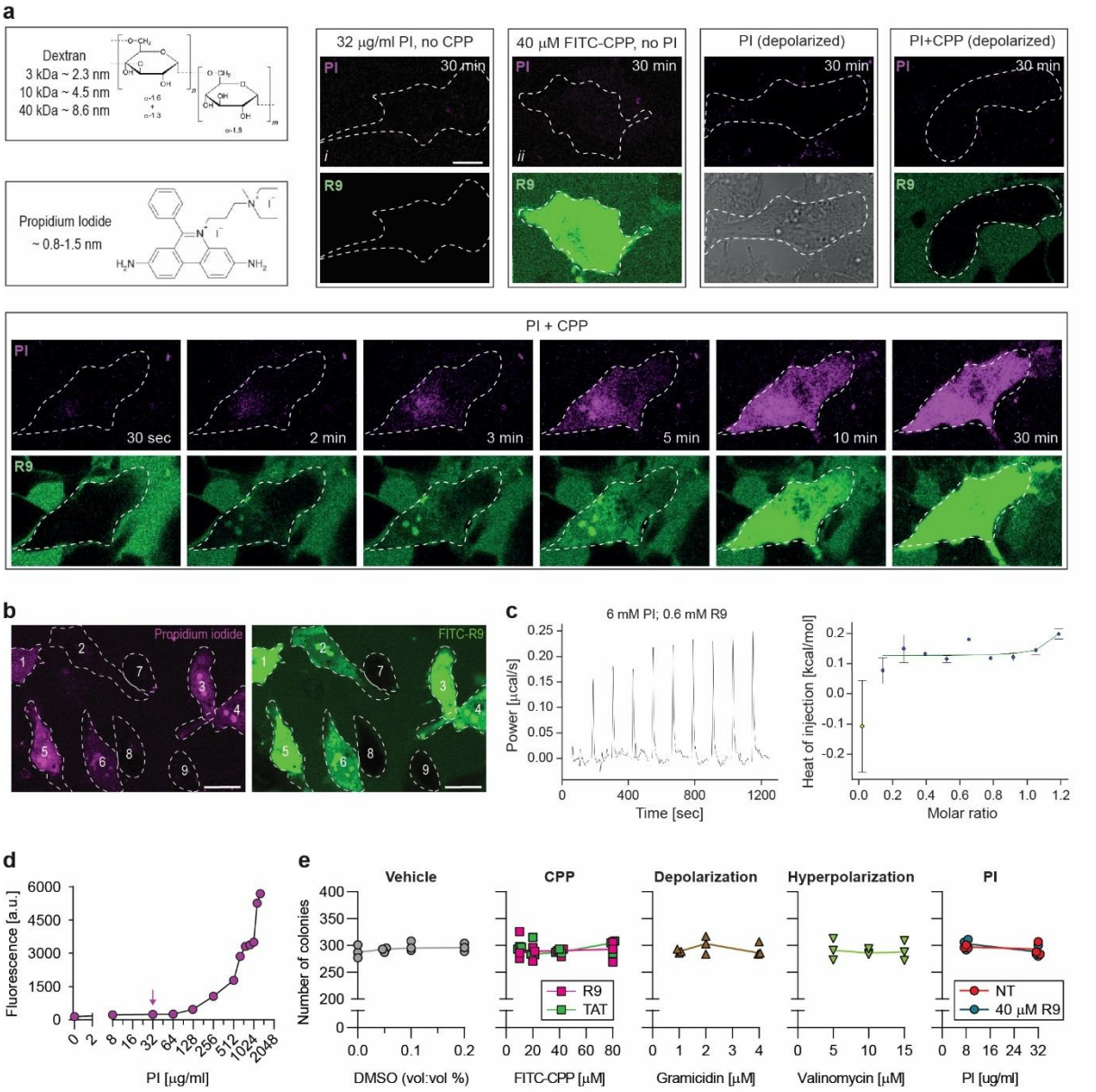

Supplementary Fig. 12: Evidence for low molecular weight pore formation in living cells during CPP direct translocation.
a, Representative images related to Fig. 3f. HeLa cells were incubated with 32 μg/ml propidium iodide (PI) in the presence or in the absence of 40 μM FITC-R9, or left untreated for 30 minutes at 37°C in RPMI, 10% FBS. Depolarization was induced with 2 μg/ml gramicidin. Images were obtained by confocal microscopy. As shown below in panel (d) the fluorescence produced by 32 μg/ml of PI is under the threshold of detection. The observed fluorescence dots and signal at this concentration correspond therefore to cell autofluorescence and not PI fluorescence (compare images i and ii). Hence, when PI fluorescence is detected in cells (see the example in panel a), the corresponding PI concentration is higher than 32 μg/ml (see panel d). In other words, cellular PI fluorescence is detected when cells are able to concentrate this cationic dye in their cytoplasm, as they are able to do with cationic CPP (see Supplementary Fig. 1h). **b,** Criteria used for the visual scoring performed for Fig. 3f, based on images in panel (a) of this figure in HeLa cells. The percentage of cells positive for PI and cells that have acquired FITC-R9 through direct translocation, have been assessed based on the following criteria. Cells 1, 3-6 are considered as positive for PI (left) and cells 1-6 are counted as those where direct translocation has occurred (right). The rest of the cells were considered as negative. Scale bar: 20 μm. **c,** PI does not interact with R9. The potential binding between PI (6 mM) and R9 (0.6 mM) at 37°C was assessed by isothermal titration calorimetry. Representative power and heat of injection are shown. This experiment was repeated three times with similar results. **d,** PI fluorescence detection in media in the absence of cells. Wells containing the indicated PI concentrations in RPMI were illuminated using the same settings as in Fig. 3f and 3g (left panel). Fluorescence intensity within the full region of the obtained images was quantitated using ImageJ. The arrow indicates the PI concentration used for water pore-related experiments (32 μg/ml). **e,** Assessment of colony formation potential after transient CPP and membrane potential treatments. DMSO was used as a vehicle for gramicidin and valinomycin. HeLa cells were incubated for one hour with the indicated treatment, washed and plated on 10 cm dishes. Number of colonies were counted after 14 days in culture after Giemsa staining.

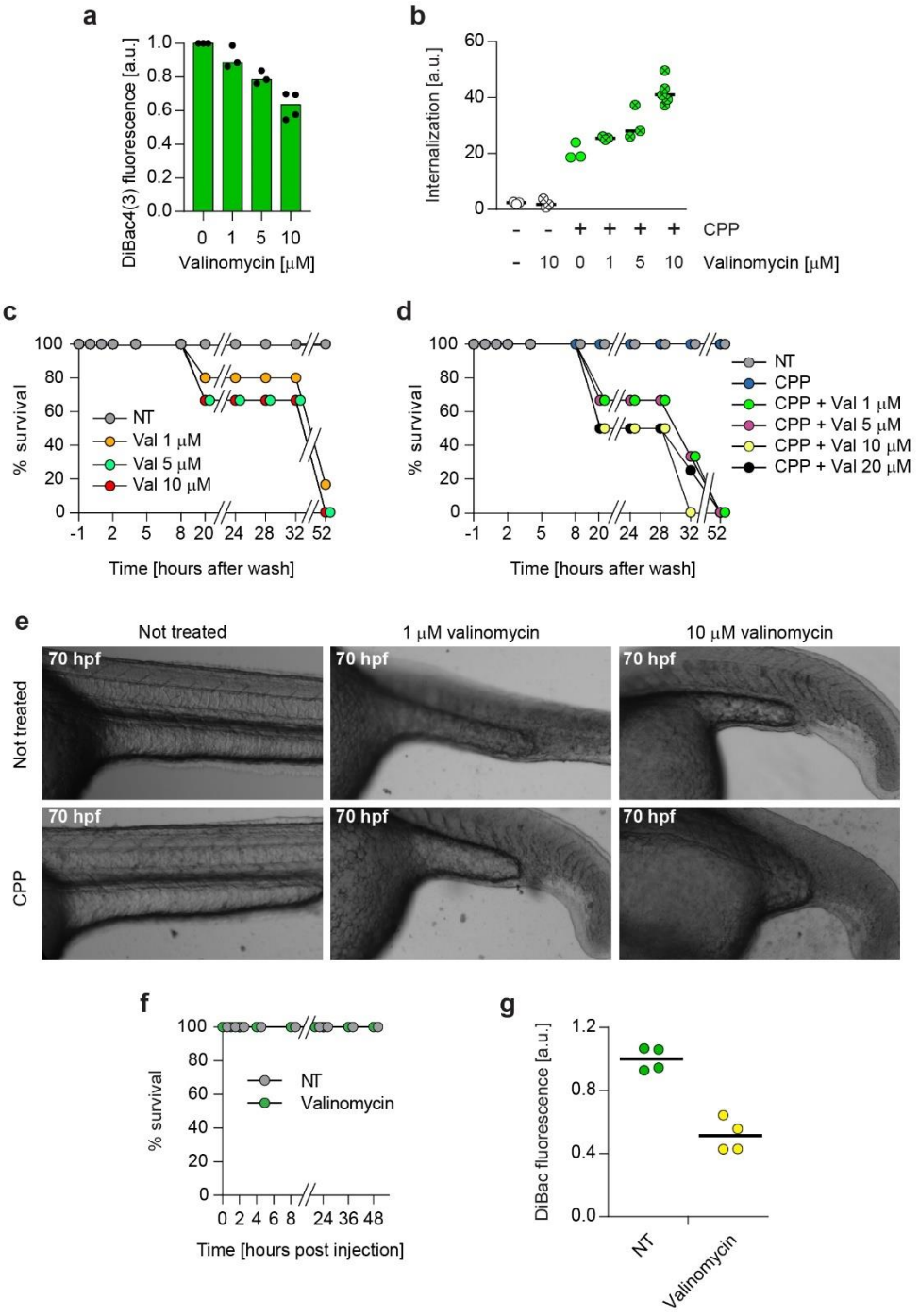

Supplementary Fig. 13: Zebrafish and mouse membrane potential modulation.
a, Eighteen hours post fertilization zebrafish embryos were incubated for 40 minutes with the indicated concentrations of valinomycin and 950 nM DiBac4(3). DiBac4(3) fluorescence was then recordedand normalized to the non-treated control. The decrease in DiBac4(3) fluorescence indicates membrane hyperpolarization. Membrane potential values could not be calculated, as a standard curve would have to be performed in zebrafish. DiBac4(3) internalization was assessed from confocal images of the fish tail region. **b,** Eighteen hours post fertilization zebrafish embryos were incubated with or without 3.12 μM TAT-$Ras_{317-326}$ (W317A), a mutant version that is not toxic to cells, in the presence of the indicated concentrations of valinomycin. Peptide internalization was assessed from confocal images of the fish tail region. **c-d,** Eighteen hours post fertilization zebrafish embryos were incubated 1 hour with the indicated concentrations of valinomycin, in the absence (panel c) or in the presence (panel d) of 3.12 μM TAT-$RasGAP_{317-326}$ (W317A), then washed, and incubated in Egg water. The viability of each fish was assessed over 52 hours at the indicated time points. **e,** Representative images of zebrafish treated as described in panel (c) and (d), washed, and further incubated in Egg water. Images were taken with a CYTATION3 apparatus at a 4x magnification at 70 hours post fertilization (hpf). **f,** Survival of 48 hours post fertilization zebrafish embryos following intramuscular injection of 3.12 μM TAT-$RasGAP_{317-326}$ (W317A) peptide in the presence or in the absence of 10 ⊠M valinomycin. Survival was visually assessed under a binocular microscope by taking into consideration the embryo transparency (as dead embryos appear opaque), development characteristics and motility. **g,** Mice were intradermally injected with DiBac4(3) in the presence or in the absence of 10 μM valinomycin. DiBac4(3) fluorescence was then recorded and normalized to the mean of non-treated (NT) control. DiBac4(3) fluorescence was assessed as in panel (a).

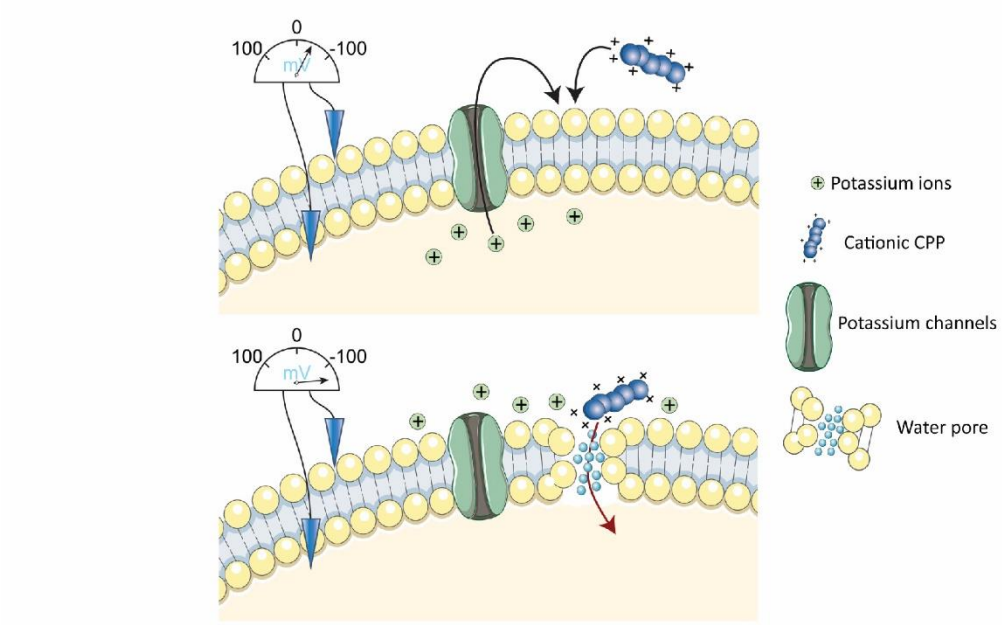

Supplementary Fig. 14: Model of CPP direct translocation through water pores.
Cationic CPP translocation across cellular membranes is favored by the opening of potassium channels or by hyperpolarizing drugs, such as valinomycin. This sets a sufficiently low membrane potential permissive for CPP direct translocation. When cationic CPPs bind to these already polarized membranes, they induce megapolarization (i.e. a membrane potential estimated to be -150 mV or lower). This leads to the formation of water pores that are then used by CPPs to enter cells.

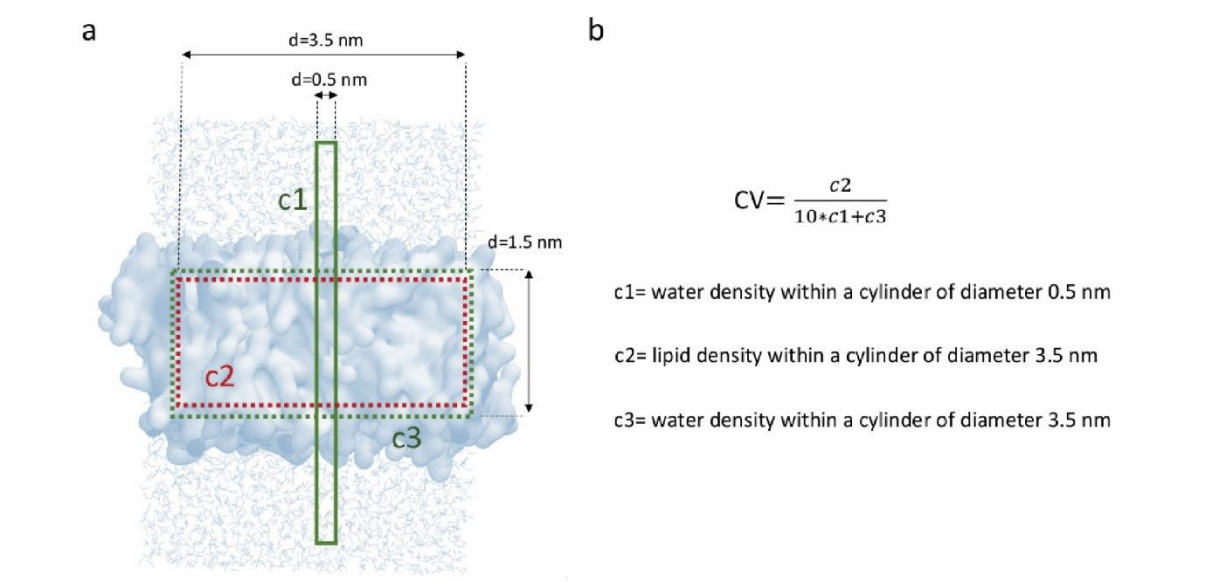

Supplementary Fig. 15: Design of the lipid/water density index collective variables.
a, Visual description of the collective variables (c1, c2, and c3) used to compute the lipid/water density index. **b,** Equation used to compute the lipid/water density index for each metadynamics simulation.

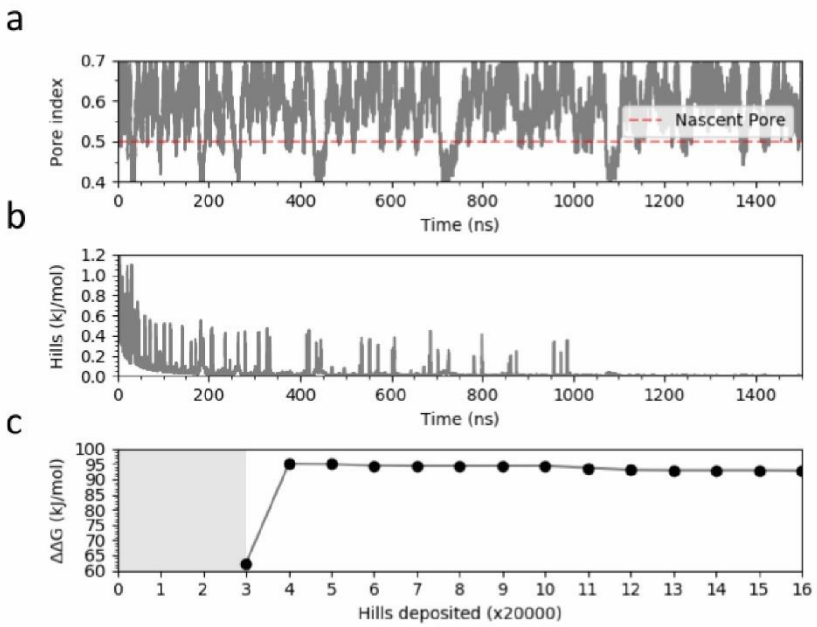

Supplementary Fig. 16: Convergence of the metadynamics simulation of water pore formation in a full DOPC membrane model.
The convergence of the metadynamics simulation was demonstrated by following a well-established computational procedure. **a,** Time evolution of the lipid/water density index. **b,** Gaussian height added to the system. **c,** The free energy difference between low energy states at different times along the simulation was calculated to assess the convergence. The estimated free energy profile is reasonably stable in the last 500 ns of the simulation. The uncertainty, calculated as the SD from the asymptotic value of the free energy obtained from the last part of the simulation, is 1.5 kJ/mol. It is worth mentioning, for this and the next supplementary figures, that the uncertainty does not consider the force-field inaccuracy. The diffusive behavior of the lipid/water density index CV is deduced by checking the ability of the system to overcome the free energy barriers when the gaussian height is closed to zero.

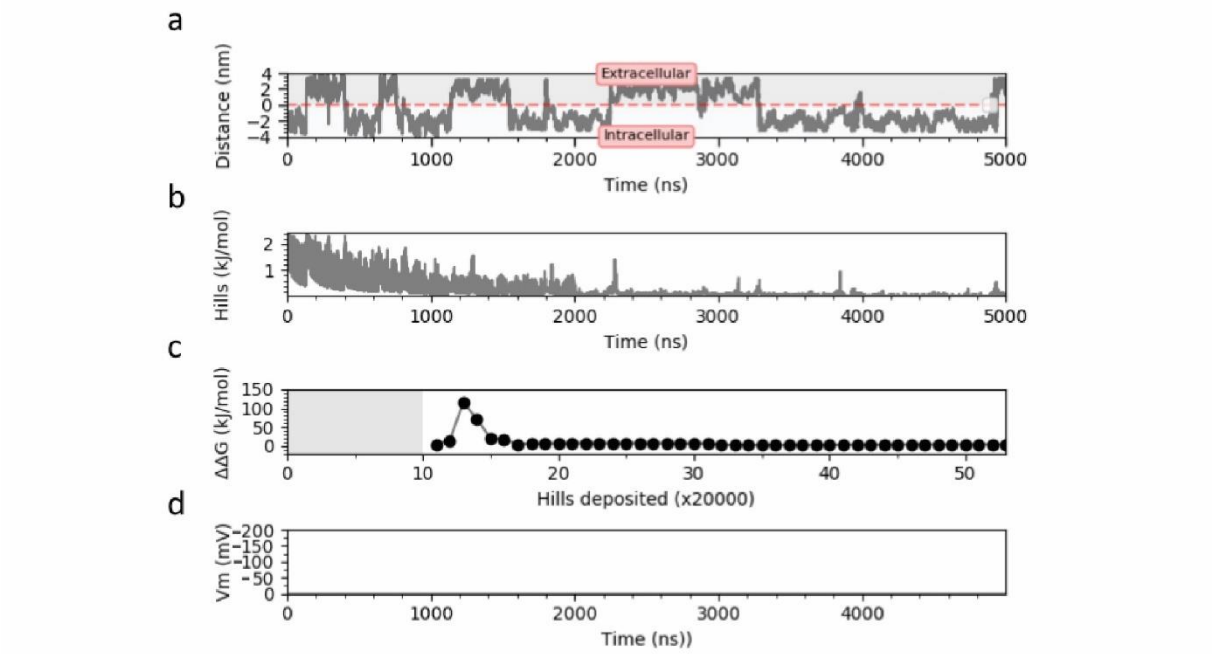

Supplementary Fig. 17: Convergence of the metadynamics simulation of CPP translocation with a Vm = 0 mV. The convergence of the metadynamics simulation was demonstrated by following a well-established computational procedure. **a,** Time evolution of the CPP-membrane distance. **b,** Gaussian height added to the system. **c,** The free energy difference between low energy states at different times along the simulation was calculated to assess the convergence. The estimated free energy profile is reasonably stable in the last 500 ns of the simulation. The uncertainty, calculated as the SD from the asymptotic value of the free energy obtained from the last part of the simulation is 1.9 kJ/mol. For this and the next supplementary figures, the diffusive behavior of the CPP-membrane distance CV was deduced by checking the ability of the system to overcome the free energy barriers when the gaussian height is close to zero. **d,** Transmembrane potential computed along the simulation every 10 ns and averaged over 10 windows.

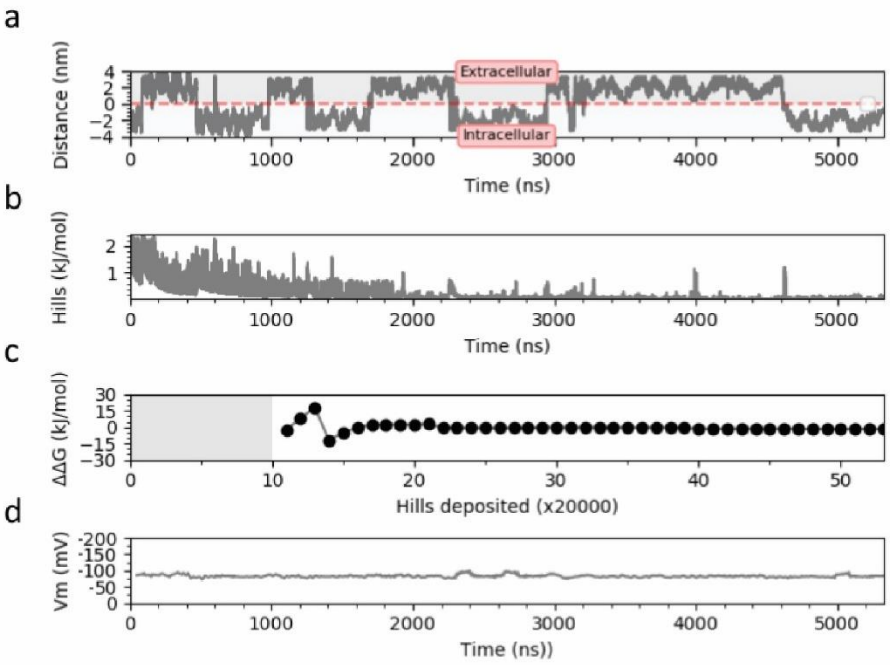

Supplementary Fig. 18: Convergence of the metadynamics simulation of CPP translocation with a Vm = -80 mV. The convergence of the metadynamics simulation was demonstrated by following a well-established computational procedure. **a,** Time evolution fo the CPP-membrane distance. **b,** Gaussian height added to the system. **c,** The free energy difference between low energy states at different times along the simulation was calculated to assess the convergence. The estimated free energy profile is reasonably stable in the last 500 ns of the simulation. The uncertainty, calculated as the SD from the asymptotic value of the free energy obtained from the last part of the simulation is 3.6 kJ/mol. d, Transmembrane potential computed along the simulation every 10 ns and averaged over 10 windows.

–

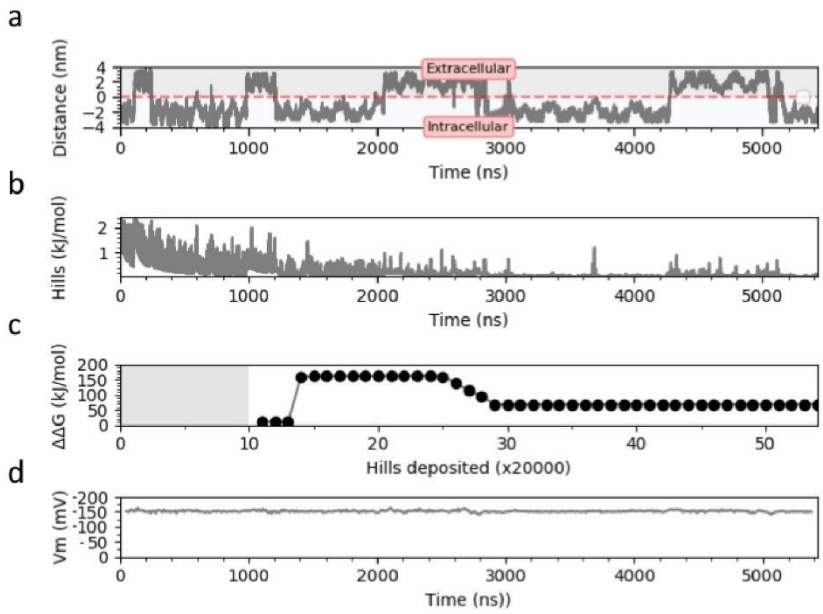

Supplementary Fig. 19: Convergence of the metadynamics simulation of CPP translocation with a Vm = -150 mV. The convergence of the metadynamics simulation was demonstrated by following a well-established computational procedure.

a, Time evolution of the CPP-membrane distance. **b,** Gaussian height added to the system. **c,** The free energy difference between low energy states at different times along the simulation was calculated to assess the convergence. The estimated free energy profile is reasonably stable in the last 500 ns of the simulation. The uncertainty, calculated as the SD from the asymptotic value of the free energy obtained from the last part of the simulation is 1.9 kJ/mol. **d,** Transmembrane potential computed along the simulation every 10 ns and averaged over 10 windows.

MATERIALS AND METHODS

Chemicals

Puromycin 10 mg/ml (Thermo Fisher, ref. no. A11138-02) was aliquoted and stored at -20 °C. Blasticidin (Applichem, ref. no. A3784) was dissolved at 1 mg/mL in water and stored at -20 °C. XE-991 and TRAM-34 (Alomone labs, ref. no. X-100 and T-105 respectively) was dissolved in DMSO at 100 mM and stored at -20 °C. Cells were preincubated with 10 □M of these inhibitors for 30 minutes and then kept throughout the experiments. Pyrene butyrate (Sigma, ref. no. 257354) was dissolved in DMSO at 20 mM and stored at -20 °C. Live Hoechst 33342 (Sigma, ref. no. CDS023389) was aliquoted and stored at -20°C. Trypan Blue 0.4% (Life technologies, ref. no. 15250061) was stored at room temperature. AlexaFluor488-labeled human transferrin was dissolved in PBS 5 at mg/ml and stored at 4°C (Thermo Fisher, ref. no. 13342). TexasRed-labelled neutral 3'000 and 40'000 Da dextran was dissolved in PBS at 10 mg/ml and stored at -20°C (Thermo Fisher, ref. no. D3329 and D1829, respectively). TMR-labelled 10'000 neutral dextran was dissolved in PBS at 10 mg/ml and stored at -20°C (Thermo Fisher, ref. no. D1816).

Antibodies

The rabbit polyclonal anti-V5 (Bethyl, ref. no. A190-A120), mouse monoclonal anti-FLAG antibody was from Sigma-Aldrich (ref. no. F1804), rabbit monoclonal anti-actin (Cell signaling, ref. no. 4970) and rat monoclonal anti-□-tubulin (Santa Cruz, ref. no. sc-51715) antibodies were used for Western blotting.

Cell lines

All cell lines were culture in 5 % CO2 at 37°C. Raji (kind gift from the laboratory of Aimable Nahimana, ATCC: CCL-86), SKW6.4 (kind gift from the laboratory of Pascal Schneider, ATCC: TIB-215) and HeLa (ATCC: CCL-2) cells were cultured in RPMI (Invitrogen, ref. no. 61870) supplemented with 10 % heat-inactivated fetal bovine serum (FBS; Invitrogen, ref. no. 10270-106). HEK293T (ATCC: CRL-3216) were cultured in DMEM supplemented with 10% FBS and were used only for lentiviral production. All cell lines were authenticated via Microsynth cell authentication service. Unless, otherwise indicated, experiments were performed in RPMI with 10% FBS.

Zebrafish

Zebrafish (Danio rerio) from AB line were bred and maintained in our animal facility under standard conditions93, more specifically at 28.5°C and on a 14:10 hours light:dark cycle at the Zebrafish facility of the School of Biology and Medicine (cantonal veterinary approval VD-H21). Zebrafish of 20 hours post fertilization were collected and treated with 0.2 mM phenylthiourea (PTU, Sigma, St. Louis, MO) to suppress pigmentation. Embryos were raised at 28.5°C in Eggwater (0.3 g sea salt/L reverse osmosis

water) up to 4 days post fertilization.

Mice

C57BL/6NCrl were acquired from Charles River laboratories, which were then housed and bred in our animal facility. All experiments were performed according to the principles of laboratory animal care and Swiss legislation under ethical approval (Swiss Animal Protection Ordinance; permit number VD3374.a).

Primary cortical neuronal culture

Sprague-Dawley rat pups (from Janvier, France) were euthanized in accordance with the Swiss Laws for the protection of animals, and the procedures were approved by the Vaud Cantonal Veterinary Office. Primary neuronal cultures from cortices of 2-day-old rats were prepared and maintained at 37 °C with a 5% CO2-containing atmosphere in neurobasal medium (Life Technologies, 21103-049) supplemented with 2% B27 (Invitrogen, 17504044), 0.5 mM glutamine (Sigma, G7513) and 100 µg/ml penicillin-streptomycin (Invitrogen, 15140122) as described previously[254]. Neurons were plated at a density of ~3×10^5 cells on 12-mm glass coverslips coated with 0.01% poly-L-lysine (Sigma, P4832). Half of the medium was changed every 3-4 days and experiments were performed at 12–13 days in vitro.

Confocal microscopy

Confocal microscopy experiments were done on live 300'000 cells. Cells were seeded for 16 hours onto glass bottom culture dishes (MatTek, corporation ref. no. P35G-1.5-14-C) in 2 mL RPMI, 10%FBS and treated as described in the Figures in 1 mL media, 10%FBS. For nuclear staining, 10 µg/ml live Hoechst 33342 (Molecular probes, ref. no. H21492) was added in the culture medium 5 minutes before washing cells twice with PBS. After washing, cells were examined with a plan Apochromat 63x oil immersion objective mounted on a Zeiss LSM 780 laser scanning fluorescence confocal microscope equipped with gallium arsenide phosphide detectors and three lasers (a 405 nm diode laser, a 458-476-488-514 nm argon laser, and a 561 nm diode-pumped solid-state laser). Time-lapse experiments were done using an incubation chamber set at 37°C, 5% CO2 and visualized with a Zeiss LSM710 Quasar laser scanning fluorescence confocal microscope equipped with either Neofluar 63x, 1.2 numerical aperture (NA) or plan Neofluar 100x, 1.3 NA plan oil immersion objective (and the same lasers as above). Visual segregation of cells based on type of CPP entry, associated either with vesicular or diffuse cytosolic staining, was performed as shown in Supplementary Fig. 1c. Cell images were acquired at a focal plane near the middle of the cell making sure that nuclei were visible. Note: image acquisition was performed using the same settings for the data presented in the same panel or in the related supplementary panels, unless otherwise indicated.

Flow cytometry

Flow cytometry experiments were performed using a Beckman Coulter FC500 instrument. Cells were centrifuged and resuspended in PBS prior to flow cytometry. Data analysis was done with Kaluza Version 1.3 software (Beckman Coulter).

Cell death and CPP internalization measurements

With the exception of neurons, cell death was quantitated with 8 g/ml propidium iodide (Sigma, ref. no. 81845). Unless otherwise indicated, cell death was assessed after 16 hours of continuous incubation in Raji and SKW6.4 cells and 24 hours in HeLa cells. Prior to treatment, 300'000 cells were seeded in 6-well plates for 16 hours in 2 mL media, 10% FBS. Treatment was done in 1 mL media with 10%FBS. Cell death and peptide internalization were analyzed by flow cytometry. Internalization measurements were done after one hour of incubation. Peptide internalization in primary cortical neurons was assessed by confocal microscopy with LSM780. Cell-associated fluorescence was quantitated with ImageJ.

Lentivirus production

Recombinant lentiviruses were produced as described[92,93] with the following modification: the envelope plasmid pMD.G and the packaging vector pCMV R8.91 were replaced by pMD2.G and psPAX2, respectively.

In vitro membrane potential measurements

Two methods were used to assess cellular membrane potential in vitro. With the first method, the membrane potential was determined by incubating 300'000 cells for 40 minutes with 100 nM of the fluorescent probe DiBAC4(3) (Thermofisher, ref. no. B438) in 6-well plates in 1 mL media, 10% FBS. and the median fluorescence intensity was then assessed by flow cytometry. Calculation of the actual membrane potential in mV based on the DiBAC4(3) signals was performed as described earlier[255,256]. The second method relied on electrophysiology recordings. To perform these, the bath solution composition was (in mM): 103.9 NaCl, 23.9 NaHCO3, 2 CaCl2, 1.2 MgCl2, 5.2 KCl, 1.2 NaH2PO4, 2 glucose and 1.7 ascorbic acid. The pipet solution was composed of (in mM): 140 KMeSO4, 10 HEPES, 10 KCl, 0.1 EGTA, 10 phosphocreatine and 4 MgATP. The patch pipets had a resistance of 2.4-3.6 MΩ. Perforated patch recordings were performed as previously described[257]. Briefly, freshly prepared gramicidin D (Sigma, ref. no. G5002), at 2.8 M final concentration, was added to prefiltered patch pipet solution and then sonicated for three consecutive times during 10 seconds. Cell-attached configuration was achieved by applying negative pressure on patch pipet until seal resistance of over

one Giga Ohm was reached. After gaining cell access through gramicidin created pores, membrane potential measurements were done in current clamp at 0 pA for at least three minutes. Since primary rat neurons are killed following full depolarization induced by gramicidin, the standard curve from membrane potential calculations[105,106] were performed using gramicidin-treated Raji cells incubated with increasing concentrations of DiBac4(3) for 40 minutes. Images of the cells were then taken using a LSM780 confocal microscope and the cell-associated fluorescence quantitated with ImageJ.

Relative membrane potential assessment in vivo

Zebrafish embryos in Egg water (see Zebrafish section) were incubated for 40 minutes in the presence or in the absence of various concentrations of valinomycin together with 950 nM DiBac4(3). The embryos were then fixed and visualized under a confocal LSM710 microscope[258]. DiBac4(3)-associated fluorescence of a region of interest of about 0.0125 mm2 in the tail region was quantitated with ImageJ. The values were normalized to the control condition (i.e. in the absence of valinomycin). Mice were intradermally injected with 10 □l of a 950 nM DiBac4(3) PBS solution containing or not 10 □M valinomycin and sacrificed one hour later. The skin was excised, fixed in 4% formalin, paraffin-embedded and used to prepare serial histological slices. Pictures of the slices were taken with a CYTATION3 apparatus. The DiBac4(3)-associated fluorescence in the whole slice was quantitated with ImageJ. The slice in the series of slices prepared from a given skin sample displaying the highest fluorescence signal was considered as the one nearest to the injection site. The signals from such slices are those reported in the Figures.

Experimental modulation of the plasma membrane potential

Flow cytometry assessment of CPP internalization

Raji, SKW6.4 or HeLa cells: three hundred thousand cells were plated on non-coated plates to avoid cell adherence in 500 □l RPMI, 10% FBS. Cellular depolarization was induced by preincubating the cells at 37°C with 2 □g/ml gramicidin for 5 minutes and/or by placing them in potassium-rich buffer[33] for 30 minutes (40 mM KCl, 100 mM potassium glutamate, 1 mM MgCl2, 1 mM CaCl2, 5 mM glucose, 20 mM HEPES, pH7.4). Cells were then treated with the selected CPPs at the indicated concentrations for one hour when peptide internalization was recorded or with 100 nM DiBac4(3) for 40 minutes when membrane potential needed to be measured. Hyperpolarization in Raji cells in the presence of TAT-RasGAP317-326 was performed by treating the cells with 10 □M valinomycin for 20 minutes in RPMI without serum. Cells were then treated with 5 µM TAT-RasGAP317-326 for one hour or 100 nM DiBac4(3) for 40 minutes. In the case of SKW6.4 and HeLa cells, hyperpolarization was induced by infection with a viral construct expressing KCNJ2 (see “virus production” section). Cells were then treated with 40 µM of indicated CPP for one hour or 100 nM DiBac4(3) for 40 minutes.

CPP cytosolic internalization quantitation based on confocal microscopy

Three hundred thousand wild-type HeLa cells were plated overnight on glass-bottom dishes in 2 mL RPMI with 10% FBS. The next day, serum was removed and cells were preincubated at 37°C with 2 □g/ml gramicidin for 5 minutes, 10 □M valinomycin for 20 minutes or were left untreated in 1 mL media with 10%FBS. The indicated CPPs were then added and cells were incubated for one hour at 37°C. Cells were then washed and visualized in RPMI without serum under a confocal microscope. CPP cytosolic internalization was quantitated within a cytosolic region devoid of endosomes using ImageJ. The number of CPP-positive vesicles was visually determined per cell in a given focal plane.

Neurons (12 days post-isolation) were preincubated 30 minutes with 5 mM TEA (tetraethylammonium, Sigma Aldrich, ref. no.T2265; gramicidin is toxic in these neurons; see section "Membrane potential measurements in vitro") to induce depolarization or 10 □M valinomycin to induce hyperpolarization in bicarbonate-buffered saline solution (116 mM NaCl, 5.4 mM KCl, 0.8 mM MgSO4, 1 mM NaH2PO4, 26.2 mM NaHCO3, 0.01 mM glycine, 1.8 mM CaCl2, 4.5 mg/mL glucose) in a 37°C, 5% CO2 incubator. The cells were then incubated one hour with 2 □M of FITC-labeled TAT-RasGAP$_{317-326}$. The cells were finally washed thrice with PBS and images were acquired using a LSM780 confocal microscope. Cell-associated peptide fluorescence was quantitated using ImageJ.

Setting membrane potential by changing potassium concentrations in the media

RPMI-like media made without potassium chloride and without sodium chloride was from Biowest (Table S1). Varying concentrations of potassium chloride were added to this medium containing 10% FBS. Sodium chloride was also added so that the sum of potassium and sodium chloride equaled 119 mM (considering the concentrations of sodium and potassium in FBS). Three hundred thousand cells were preincubated in 1 mL media, 10% FBS containing different concentrations of potassium for 20 minutes, then different CPPs at a 40 □M concentration were added and cells were incubated for one hour at 37°C in 5% CO2. Cells were washed once in PBS and CPP internalization was measured by flow cytometry. The corresponding membrane potential was measured with DiBac4(3).

In silico CPP translocation free energy though MARTINI coarse-grained simulations

An asymmetric multi-component membrane was constructed and solvated using CHARMM-GUI[97,98]. Each layer contained 100 lipids (Table S2), in a previously described composition[99]. The membrane was solvated with 2700 water molecules, obtaining a molecular system of 10200 particles. The MARTINI force field[205] was used to define phospholipids' topology through a coarse-grained (CG) approach. The polarizable water model has been used to assess the water topology[228]. The R9 peptide model has been obtained by PEPFOLD-3 server[259], as done in previous studies in the field[212,260]. For each molecular system, R9 peptide was positioned 3 nm far from the membrane outer leaflet, in the water

environment corresponding to the extracellular space. The elastic network ELNEDYN[252] has been applied to reproduce the structural and dynamic properties of the CPPs. The molecular system has been minimized by a steepest descent protocol, and then equilibrated through five MD simulations of 1ns each under the NPT ensemble. Position restraints were applied during the first three molecular dynamics (MD) simulations and gradually removed, from 200 kJ/mol*nm2 to 10 kJ/mol*nm2. Velocity rescaling[102] temperature coupling algorithm and time constant of 1.0 ps were applied to keep the temperature at 310.00 K. Berendsen[230] semi-isotropic pressure coupling algorithm with reference pressure equal to 1 bar and time constant 5.0 ps was employed. Electrostatic interactions were calculated by applying the particle-mesh Ewald (PME)[231] method and van der Waals interactions were defined within a cut-off of 1.2 nm. Periodic boundary conditions were applied in all directions. Trajectories were collected every 10 ps and the Visual Molecular Dynamics (VMD)[253] package was employed to visually inspect the simulated systems. Three different transmembrane potential values have been considered: 0 mV, 80 mV, and 150 mV. In the MD simulations, an external electric field Eext was applied parallel to the membrane normal z, i.e., perpendicular to the bilayer surface. This was achieved by including additional forces Fi =q*Eext acting on all charged particles i. In order to determine the effective electric field in simulations, we applied a computational procedure reported in literature[247]. A well-tempered metadynamics protocol[261] was applied to estimate the free energy landscape of CPP translocation. Two collective variables have been considered: the lipid/water density index, and the CPP-membrane distance. Further details about the lipid/water density index definition are reported in Supplementary Fig. 15. The metadynamics protocol has been carefully validated, as reported in Supplementary Table S5. Gaussian deposition rate of 2.4 kJ/mol every 5 ps was initially applied and gradually decreased on the basis of an adaptive scheme. Gaussian widths of 0.5, and 0.2 nm were applied following a well-established scheme[232,234,236,237]. In particular, the Gaussian width value was of the same order of magnitude as the standard deviation of the distance CV, calculated during unbiased simulations. The well-tempered metadynamics simulations were computed using GROMACS 2019.4 package[238] and the PLUMED 2.5 open-source plug-in[239]. The reconstruction of the free-energy surface was performed by the reweighting algorithm procedure[262], allowing the estimation of the free energy landscape. Each system was simulated (with a 20 fs time step) until convergence was reached. Further details about the convergence of each metadynamics simulation are reported in Supplementary Fig. 17-19. The electrostatic potential maps were computed by the APBS package[263] on the molecular system composed of R9 peptide in contact with the cell membrane, without any applied external electrostatic field. In detail, the non-linear Poisson-Boltzmann equation was applied using single Debye-Huckel sphere boundary conditions on a 97x97x127 grid with a spacing of 1Å centered at the COM of the molecular system. The relative dielectric constants of the solute and the solvent were set to 2.5 and 78.4, respectively. The ionic strength was set to 150 mM and the temperature was fixed

at 310K[263], [236]. The average and standard deviation values of the local transmembrane potential have been computed considering ten different trajectory snapshots taken from the molecular trajectory.

In silico cell membrane hyperpolarization modeling through ion-imbalance in Martini coarse-grained simulations

The translocation mechanism of each CPP has been studied by ion-imbalance in a double bilayer system[118,206-208]. The same asymmetric membrane considered to perform the single-bilayer simulations was used to build up the double-bilayer system. The double-membrane system was solvated with 4300 water molecules, obtaining a molecular system of 20000 particles. The MARTINI force field was used to define phospholipids' topology through a coarse-grained (CG) approach. The polarizable water model has been used to model the water topology[228]. The elastic network ELNEDYN[264] has been applied to reproduce the structural and dynamic properties of the CPPs.

For each molecular system, one CPP was positioned in the middle of the double bilayer system, 2nm far from the membrane outer leaflets, in the water environment corresponding to the extracellular space. Then, the system was equilibrated through four MD simulations of 100ps, 200ps, 500 ps, and 100 ns under the NPT ensemble. Position restraints were applied during the first three MD simulations ang gradually removed, from 200 kJ/mol*nm2 to 10 kJ/mol*nm2. Velocity rescaling[229] temperature coupling algorithm and time constant of 1.0 ps were applied to keep the temperature at 310.00 K. Berendsen[230] semi-isotropic pressure coupling algorithm with reference pressure equal to 1 bar and time constant 5.0 ps was employed. Then, all systems were simulated for the production run in the NPT ensemble with the time step of 20 fs with Parrinello-Rahman pressure coupling[265].

Membrane hyperpolarization was achieved through a net charge difference of 30 positive ions between intracellular and extracellular space, considering all charged ions of the system and fulfilling the full system electroneutrality. Ten different replicas of each molecular simulation have been performed until the water pore formation and closure events have been observed. The visual inspection of the simulated molecular systems is reported in Supplementary Figure 11a. To analyze whether the CPPs were able to cross the membrane and reach the intracellular compartment, their trajectories were studied in the last five nanoseconds of each simulation replica. Considering the CPP position with respect the membrane bilayers and the CPP's solvent accessible surface area (SASA), three different compartments were defined: intracellular space, lipid bilayer (cell membrane) and extracellular space. The radius of the water pores within the membrane was calculated as previously done in literature[66,121]. We assumed that the central part of the cylindrical water pore contains N water molecules at the same density as outside of the water flux.

In vitro assessment of water pores

Three hundred thousand wild-type HeLa cells were incubated with 32 ug/ml PI (0.8-1.5 nm diameter 75) or 200 µg/ml dextran of different size in the presence or in the absence of indicated CPP in normal, depolarizing (2 µg/ml gramicidin) or hyperpolarizing (10 µM valinomycin) conditions in 1 mL media, 10% FBS. Time-lapse images were acquired by confocal microscopy every 10 seconds. The percentage of cells where direct CPP translocation has occurred, as well as the percentage of cells positively stained for PI, were manually quantitated using ImageJ based on snap shot images taken after 30 minutes of incubation, as shown in Supplementary Fig. 12b. Quantitation of cell percentage was not selective in terms of fluorescence intensity. Cytosolic PI fluorescence was assessed with ImageJ, by selecting a region within the cell cytoplasm devoid of endosomes. Saponin 0.1% (Sigma, ref. no. 4706, diluted in PBS weight:volume) was used as a permeabilizing agent (30 minutes incubation at 37°C in a 5% CO2 incubator) that leads to cell death to differentiate signal intensity between live cells with water pores and dead cells. As, the signal of PI internalization in saponin treated cells was saturated, lower laser settings were used to look at dead cells than at cells with water pores. Three fitting models were obtained:

- exponential decline: $y = 2570 \cdot e^{(-x/54)}$
- exponential: $y = 2570 \cdot e^{-0.02\,x}$
- modified power: $y = 2570 \cdot 0.98^{x}$

These equations fitted equally well the PI uptake/Vm curve in Fig. 3h. For the calculations used in Fig. 3i, the exponential decline equation was used.

Zebrafish viability

FITC-TAT-RasGAP$_{317\text{-}326}$(W317A) internalization in zebrafish was assessed either by adding the peptide directly in Egg water or by injection. Experiments in which the peptide was added in the water were performed on fish between four and 24 hours post fertilization. Viability assays were done on embryos of four, six and 24 hours post fertilization to determine a maximal nonlethal dose of the peptide that can be used. Different concentrations of the peptide were added to 500 µl water per well in 24-well plate, with between eight and eleven embryo per well. Fish viability was visually assessed at 20 hours post incubation with the peptide. Hyperpolarization associated viability was visually assessed at different time points in presence or in the absence of the peptide and in presence or in the absence of different concentration of valinomycin. Zebrafish were visualized with binocular microscope and CYTATION3 apparatus. Survival was visually assessed under a binocular microscope by taking into consideration the embryo transparency (as dead embryos appear opaque), general development characteristics and motility.

CPP internalization in vivo

To assess peptide internalization in zebrafish, two methods were used: 1) addition of the peptide directly in 500 µl of Egg water in 24-well plates containing between eight and twelve embryos per well or 2) intramuscular injections. In the case of the first method, after the indicated treatments, zebrafish were washed, fixed in 4% PFA/PBS for one hour at room temperature. Whole embryos were mounted on slides with Fluoromount-G (cBioscience, ref. no. 00-4958-02). Zebrafish were then visualized under a LSM710 confocal microscope. Experiments where the peptide was added directly to the water were performed on zebrafish at 18 hours post fertilization to limit cuticle development that would hinder peptide access to the cells. In the case of the second method, 8 nl injections (containing the various combinations of peptide and valinomycin and 0.05 % (vol:vol) phenol red as an injection site labelling agent) were done on 48 hours post fertilization embryos into the tail muscle around the extremity of yolk extension, after chorion removal and anesthesia with 0.02% (w:vol) tricaine [122] buffered in sodium bicarbonate to pH7.3. At this age, zebrafish already have well developed tissues that can be easily visually distinguished. Injections were done with an Eppendorf Microinjections FemtoJet 4i apparatus. After the indicated treatments, embryos were fixed in 4% PFA/PBS and visualized under a confocal microscope. Some embryos were kept alive for viability evaluation post injection until the age of 4 days.

Experiments with mice were performed in 10-14 weeks old C57BL/6NCrl mice anaesthetized with ketasol/xylasol (9.09 mg/ml ketasol and 1.82 mg/ml xylasol in water; injection: 10 µl per g of body weight). The back of the mice was shaved and intradermic injections were performed (a total of 10 µl was injected). Mice were kept under anesthesia for one hour and Artificial tears (Lacryvisc) were used to avoid eye dryness. Mice were then sacrificed by CO2 inhalation, skin was cut at injection sites, fixed in 4% formalin and paraffin embedded for histology analysis. For each sample, 10 to 15 slides were prepared and peptide internalization was visualized with a CYTATION3 apparatus. Fluorescence intensity was quantitated with ImageJ. The slices displaying the highest fluorescence signal were considered as those nearest to the injection site and the fluorescent values from these slides were used in Fig. 4b.

Temperature dependent internalization

Two hundred thousand cells were incubated with 40 µM (Raji and SKW6.4) or 80 µM (HeLa) of FITC-labelled TAT-RasGAP$_{317-326}$ for one hour in Eppendorf tubes in RPMI media supplemented with 10% serum and 10 mM Hepes on a thermoblock at different temperatures. Peptide internalization was measured by flow cytometry after PBS wash and addition of 0.2% trypan blue (in PBS) to quench extracellular fluorescence.

Pyrene butyrate treatment

Three hundred thousand cells were seeded in 6-well plates in 2 mL RPMI, 10% FBS for 16 hours. Cells were then washed twice with serum-free medium and treated for 10 minutes with 50 µM pyrene butyrate or 0.25% (vol:vol) DMSO as vehicle control at 37°C in 5% CO2 in 1 mL media. Then cells were treated with TAT-RasGAP$_{317-326}$ for the indicated period of time.

Assessment of endosomal escape and direct translocation

Three hundred thousand cells were seeded onto glass-bottom dishes in 2 mL RPMI, 10% FBS for 16 hours. Quantitation of cytosolic fluorescence was performed within live HeLa cells pre-incubated with 80 µM TAT-RasGAP$_{317-326}$ for 30 minutes at 37°C in 1 mL media, with 10% FBS and then incubated for the indicated periods of time in the presence (i.e. no wash after the pre-incubation) or in the absence (i.e. following three consecutive washes with RPMI supplemented with 10% FBS) of extracellular labelled peptide. Endosomal escape from lysosomes was induced in presence of 1 mM LLOME (L-Leucyl-L-Leucine methyl ester)[197], added in the 1 mL media, 10% FBS 30 minutes after CPP was washed out and persisted throughout the experiment). Confocal images were taken every five minutes after the 30-minute pre-incubation. For each cell, the fluorescence intensity of one region of interest (ROI) devoid of labelled endosomes throughout the experiment was quantitated over time using ImageJ Time Series Analyzer V3. The surface of the ROI was identical for all cells. Only cells displaying labelled endosomes after the 30-minute pre-incubation were analyzed. Note that the washing steps, for reasons unclear at this time, induced a slightly higher initial ROI intensity signal.

Transferrin internalization quantitation

Wild-type HeLa cells were plated in 12-well plates (200'000 cells per well) for 16 hours in 1 ml RPMI (Invitrogen, ref. no. 61870), supplemented with 10 % heat-inactivated fetal bovine serum (FBS; Invitrogen, ref. no. 10270-106). Cells were then incubated in presence of 20 µg/ml AlexaFluor-488 conjugated transferrin for 20 minutes at 37°C in 5% CO2. Cells were washed with PBS and pelleted after trypsinization. To quench membrane bound transferrin fluorescence, cells were resuspended in 0.2% trypan blue diluted in PBS. Transferrin internalization was quantified by flow cytometry using Beckman Coulter FC500 instrument. Data analysis was done with Kaluza Version 1.3 software (Beckman Coulter).

TAT-PNA-induced luciferase activity

The LeGOiG2-LUC705 lentiviral construct encodes a luciferase gene interrupted by a mutated human beta globin intron 2. This mutation creates a new aberrant splicing site at position 705 that when used produced an mRNA that encodes a truncated non-functional luciferase[50]. In the presence of the TAT-

peptide nucleic acid (TAT-PNA) CPP described below, the aberrant splice site is masked allowing the production of a functional luciferase enzyme. Lentiviruses produced using this construct were employed to infect cells. The doses used resulted in >90% cells infected (based on GFP expression from the lentiviral vector). The infected cells (200'000 cells in 12-well plates containing 1 ml of RPMI, 10% FBS) were treated or not with 5 µM TAT-PNA (GRKKRRQRRR-CCTCCTACCTCAGTTACA). TAT-PNA is made of TAT_{48-57} and an an oligonucleotide complimentary to a sequence containing the aberrant splice site. After 16 hours incubation, cells were washed twice in HKR buffer (119 mM NaCl, 2.5 mM KCl, 1 mM NaH2PO4, 2.5 mM CaCl2, 1.3 mM MgCl2, 20 mM HEPES, 11 mM dextrose, pH 7.4) and lysed in 40 µl HKR containing 0.1 % Triton X-100 for 15 minutes at room temperature. Luciferase activity was measured with a GLOMAXTM 96 Microplate Luminometer (Promega) using a Dual-Luciferase Reporter Assay (Promega) and normalized to the protein content. Results are displayed as the ratio between the protein-normalized luciferase signal obtained in TAT-PNA-treated cells and the signal obtained in control untreated cells.

TAT-Cre recombinase production, purification and recombination assay

Raji cells were infected with a lentivirus encoding a Cre-reporter gene construct[200]. TAT-Cre recombinase was produced as described[51]. Briefly, E. coli BL21 transformed with the pTAT-Cre plasmid (#917, Addgene plasmid #35619) were grown for 16 hours in LB containing 100 µg/mL kanamycin. Protein production was induced at OD600 of 0.6 with 500 µM IPTG (isopropyl β-D-1-thiogalactopyranoside) for three hours. Bacteria were collected by centrifugation at 5000 x g and kept at -20°C. Purification was performed on Äkta prime (GE, Healthcare, USA) equipped with a 1 ml HisTrap FF column equilibrated with binding buffer (20 mM sodium phosphate, 500 mM NaCl, 5 mM imidazole pH 7.4). The day of the purification, bacterial pellet was resuspended in lysis buffer (binding buffer with protease inhibitors (Roche, ref. no. 4693132001; one tablet per 50 ml), 0.025 mg/ml DNase I (Roche, ref. no. 04716728001), and 2 mg/ml lysozyme (Roche, ref. no. 10 837 059 001) and sonicated six times for 30 seconds. After 20 minutes centrifugation at 5'000 x g, the supernatant was filtered through Steriflip 0.45µm and loaded on the column. Elution buffer (20 mM sodium phosphate, 500 mM NaCl, 500 mM imidazole pH 7.4) was used to detach His-tagged proteins from the column. Imidazole was removed from collected fractions by overnight dialysis using 10K MWCO cassette (Thermo Scientific, ref. no. 66807) in PBS. Raji cells encoding the Cre-reporter were treated for 48 hours with 20 µM TAT-Cre-recombinase. Fluorescence was imaged using a Nikon Eclipse TS100 microscope.

Extracellular pH manipulation

Three hundred thousand HeLa cells were incubated in 1 mL RPMI media, supplemented with 10% FBS

in 6-well plates, set at the indicated pH for 20 minutes at 37°C in 5% CO2, with or without 2 µg/ml gramicidin to induce depolarization. Changes to the extracellular pH were done by adding NaOH or HCl to the RMPI media. The pH was measured with a pH meter (Metrohm, 744 pH Meter) at the start and at the end of the experiment. TMR-TAT-RasGAP$_{317-326}$ 40 µM was then added to cells for one hour. Cytosolic peptide internalization as well as TMR-TAT-RasGAP$_{317-326}$-positive vesicles were quantitated based on confocal images. Cytosolic CPP fluorescence was assessed with ImageJ, by selecting a region within the cell cytoplasm devoid of endosomes. These experiments were performed in the presence of FBS because in its absence, cells are too sensitive to acidification or alkalization. In addition, TMR-labelled peptide was used to avoid FITC-quenching at acidic pH.

Assessment of CPP binding to plasma membranes

Three hundred thousand cells were incubated for 60 seconds in 1 mL RPMI supplemented with 10% FBS and 10 mM HEPES in Eppendorf tubes at 37°C in the presence of increasing concentrations of FITC-TAT-RasGAP$_{317-326}$. Half of the cells were then immediately placed on ice, pelleted at 4°C, and resuspended in one ml of ice-cold PBS and then split into two tubes, one of which receiving a final concentration of 0.2% (w:w) trypan blue to quench surface-associated FITC signals. The cells (still kept at 4°C) were then analyzed by flow cytometry. The surface associated peptide signal was calculated by subtracting total fluorescence measured in PBS and fluorescence measured after trypan blue quenching. The other half of the cells after the 60 second peptide incubation was incubated at 37°C for one hour at which time the cellular internalization of the labelled peptide was assessed by flow cytometry.

Transient calcium phosphate transfection in HeLa cells

Calcium phosphate-based transfection of HeLa cells was performed as previously described[266]. Briefly, cells were plated overnight in DMEM (Invitrogen, ref. no. 61965) medium supplemented with 10 % heat-inactivated FBS (Invitrogen, ref. no. 10270-106), 2.5 ug of total plasmid DNA of interest was diluted in water, CaCl2 was added and the mixture was incubated in presence of HEPES 2x for 60 seconds before adding the total mixture drop by drop to the cells. Media was changed 10 hours after.

Isothermal titration calorimetry (ITC)

ITC was performed using MicroCal ITC200 (Malvern Panalytical) at 37°C with 600 M FITC-R9 in the cell (total volume 300 µl) and consecutive injections (2.5 µl/injection, except for the first injection of 0.4 µl) of 6 mM PI from the syringe (total volume 40 µl) with 2 minutes delay between injections and 800 rotations/minute rotation speed. Differential power was set to 7, as we had no prior knowledge of the expected reaction thermodynamics. The results in Supplementary Fig. 12c are represented as a:

thermogram (measurement of thermal power need to ensure that there is no temperature difference between reference and sample cells in the calorimeter as a function of time) and a binding isotherm (normalized heat per peak as a function of molar ratio).

Colony formation assay

Three hundred thousand wild-type HeLa cells were plated overnight in RPMI with 10% FBS in 6-well plates. Cells were then treated for one hour in the presence of indicated concentrations of CPP, PI and membrane potential modulating agents (gramicidin or valinomycin) in 1 mL RPMI. As control, cells were either left untreated or incubated in presence of DMSO used as vehicle for gramicidin and valinomycin. Cells were then washed, trypsinized and plated on 10 cm dishes at a density of 300 cells per condition. Colonies were counted at day 14 after 100% ethanol fixation for 10 minutes and Giemsa staining. Washes were done with PBS.

Genome-scale CRISPR/Cas9 Knockout screening

The human GeCKO v2 library (2 plasmid system) (Addgene plasmid #1000000049) was amplified by electroporation using a Bio-Rad Gene Pulser II electroporation apparatus (Bio-Rad #165-2105) and the Lucigen Endura bacteria (Lucigen ref. no. 60242). Cells were plated on LB Agar plates containing 100 µg/mL ampicillin. After 14 hours at 32°C, colonies were scrapped and plasmids recovered with the Plasmid Maxi kit (Qiagen, ref. no. 12162). To produced lentivirus library, 12 T-225 flasks were seeded with 12x106 HEK293T cells per flask in 40 ml DMEM, 10% FBS. The day after, 10 µg pMD2.G, 30 µg psPAX2 and 25 µg GeCKO plasmid library in 1.8 ml H2O were mixed with 0.2 ml 2.5 M CaCl2 (final calcium concentration: 250 mM). This solution was mixed (v/v) with 2x HEPES buffer (280 mM NaCl, 10 mM KCl, 1.5 mM Na_2HPO_4, 12 mM D-glucose, 50 mM HEPES), incubated for one minute at room temperature, added to the culture medium, and the cells placed back in a 37°C, 5% CO_2 incubator for seven hours. The culture medium was then removed and replaced by DMEM supplemented with 10 % FBS containing 100 U/ml penicillin and 100 µg/ml streptomycin. Forty-eight hours later, the medium was collected and centrifuged 5 min at 2'000 g to pellet the cells. The remaining cell-free medium (12 x 40 ml) was then filtered through a 0.45 µm HV/PVDF (Millipore, ref. no. SE1M003M00) and concentrated ~100 times by resuspending the viral pellet obtained by ultracentrifugation at 70'000 g for two hours at 4°C in ~5 ml ice-cold PBS. The concentrated viruses were aliquoted in 500 µl samples and stored at -80°C.

To express the Cas9 endonuclease, cells (e.g. Raji or SKW6.4) were infected with Cas9 expressing viruses that were produced in HEK293T cells transfected with the lentiCas9-Blast (#849, Addgene plasmid #52962), pMD2.G, and psPAX2 plasmids as described in the main method under "Lentivirus production". The infected cells were selected with 10 µg/mL blasticidin for a week. The multiplicity of

infection (MOI) of the GeCKO virus library was determined as follow. Different volumes of the virus library were added to $3x10^6$ Cas9-expressing cells plated in 12-well plates. Twenty-four hours later, the cells were split in two wells of 12-well plates. One well per pair was treated with 10 µg/mL puromycin for 3 days (the other cultured in normal medium). Cell viability was determined by trypan blue exclusion and MOI was calculated as the number of cells in the well treated with puromycin divided by the number of cells in the control well. The virus volume yielding to a MOI ~0.4 was chosen to perform large-scale infection of 12x107 cells that was carried out in 12-well plates with 3x106 cells per well. After 24 hours, the infected cells were collected and pooled in a T-225 flask and selected with 10 µg/mL puromycin for a week. Thirty million of these were frozen (control untreated cells) and 60 million others were treated with 40 µM TAT-$RasGAP_{317-326}$ for 8 days (Raji) or for 17 days (SKW6.4) with a medium and peptide renewal every 2-3 days. Thirty million of the peptide-treated cells were then also frozen. Genomic DNA was extracted from the control and the peptide-treated frozen cells using the Blood & Cell Culture DNA Midi Kit according to manufacturer's instructions (Qiagen, ref. no. 13343). A first PCR was performed to amplify the lentiCRISPR sgRNA region using the following primers:

F1: 5'-AATGGACTATCATATGCTTACCGTAACTTGAAAGTATTTCG-3'

R1: 5'-CTTTAGTTTGTATGTCTGTTGCTATTATGTCTACTATTCTTTCC-3

A second PCR (see Table S3 for the primers used) was performed on 5 µl of the first PCR reaction to attach Illumina adaptors with barcodes (nucleotides highlighted in green) and to increase library complexity (using the sequences highlighted in red) to prevent signal saturation when the sequencing is performed. The blue sequences are complementary to the extremities of the first PCR fragments.

Both PCRs were performed in 100 µl with the 2 µl of the Herculase II Fusion DNA Polymerase from Agilent (ref. no. 600675) according the manufacturer's instructions. Amplicons were gel extracted, quantitated, mixed and sequenced with a MiSeq (Illumina). Raw FASTQ files were demultiplexed and processed to contain only unique sgRNA sequences. The number of reads of each sgRNA was normalized as described[125]. The MAGeCK algorithm[126] was used to rank screening hits by the consistent enrichment among multiple sgRNAs targeting the same gene.

CRISPR/Cas9-based genome editing

Single guide RNAs targeting the early exon of the protein of interest were chosen in the sgRNA library133 and are listed in table I below (Table S4). LentiCRISPR plasmids specific for a gene were created according to the provided instructions[127]. Briefly, oligos were designed as follow: Forward 5'-CACCGnnnnnnnnnnnnnnnnnnn-3'; Reverse-3'-CnnnnnnnnnnnnnnnnnnnCAA-5', where nnnnnnnnnnnnnnnnnnn in the forward oligo corresponds to the 20 bp sgRNA. Oligos were synthetized, then phosphorylated and annealed to form oligo complex. LentiCRISPR vector was BsmBI digested and dephosphorylated. Linearized vector was purified and gel extracted and ligated to oligo

complex. The lentiCRISPR vector containing the sgRNA was then used for virus production. Recombinant lentiviruses were produced as described[93] with the following modification: pMD.G and pCMVDR8.91 were replaced by pMD2.G and psPAX2 respectively. Cells were infected and selected with the appropriate dose of puromycin (2 µg/ml for HeLa). Clone isolation was performed by limiting dilution in 96 well-plate.

TA cloning

TA cloning is a subcloning technique that allows integration of a PCR-amplified product of choice into a PCR2.1 vector based on complementarity of deoxyadenosine added onto the PCR fragment by Taq polymerase. This approach is useful to distinguish between several alleles and to determine whether the cells are heterozygous or homozygous at a given locus. TA cloning kit (Life technologies, ref. no. K202020) was used according to manufacturer's instructions to sequence DNA fragment containing the region targeted by a given sgRNA. Briefly, DNA was isolated and the fragment of interest was PCR-amplified using primers in Table S6, then ligated into PCR2.1 vector. *E. coli* competent cells were then transformed and at least 15 colonies were selected per condition for DNA isolation and sequencing.

Plasmid constructs

The hKCNN4-V5.lti (#953) lentiviral plasmid encoding a V5-labeled version of the KCNN4 potassium channel was from DNASU (ref. n° HsCD00441560). The hKCNK5-FLAG.dn3 (#979) plasmid encoding the human KCNK5 potassium channel (NCBI reference sequence NM_003740.3), Flag-tagged at the C-terminus, was purchased from GenScript (ref. n° OHu13506). The Myc-mKCNJ2-T2A-IRES-tdTomato.lti (#978) lentiviral vector encoding the mouse Kir2.1 (KCNJ2) potassium channel and tdTomato (separated by an IRES) was generated by subcloning myc-mKCNJ2-T2A-Tomato.pCAG plasmid (#974, Addgene plasmid #60598) into a lentiviral backbone LeGo-iT2 (#809), a gift from Boris Fehse (Addgene plasmid #27343), through ligation of both plasmids after digestion with BamHI (NEB, reg. no. R313614). The pMD2.G plasmid (#554, Addgene plasmid #12259) encodes the envelope of lentivirus. The psPAX2 plasmid (#842, Addgene plasmid #12260) encodes the packaging system. Both pMD2.G and psPAX2 plasmids were used for lentiviral production. The Flag-hKCNQ5(G278S)-IRES-NeoR plasmid (#938) codes for the N-terminal Flag-tagged G278S human KCNQ5 inactive mutant and a neomycin resistant gene separated by an IRES sequence. It was generated by subcloning a BamHI/XmaI digested PCR fragment obtained by amplification of pShuttle-Flag-hKCNQ5(G278S)-IRES-hrGFP2 (#937, kind gift from Dr. Kenneth L. Byron) using forward primer #1397 (CAT CGG GAT CCG CTA TAC CGG CCA CCA TGG ATT ACA AGG A) and reverse primer #1398 (CAT CGC CCG GGG CTA TAC CGT ACC GTC GAC TGC AGA ATT C) into the lentiviral vector TRIP-PGK-IRES-Neo (#350) opened with the same enzyme. The Flag-hKCNQ5(SM,G278S)-IRES-Neo (#939) plasmid is identical to Flag-hKCNQ5(G278S)-IRES-NeoR except

that the sequence targeted by the sgKCNQ5.1 sgRNA (Table S4) was mutated with the aim to decrease Cas9-mediated degradation. Silent mutations (SM), at the protein level, were introduced using the QuikChange II XL Site-Directed Mutagenesis Kit (ref. no. 200522) according to manufacturer's instructions using forward primer #1460 (AAA TAA GAA CCA AAA ATC CTA TGT ACC ATG CCG TTA TCA GCT CCT TGC TGT GAG CAT AAA CCA CTG AAC CCA G) and reverse primer #1461 (CTG GGT TCA GTG GTT TAT GCT CAC AGC AAG GAG CTG ATA ACG GCA TGG TAC ATA GGA TTT TTG GTT CTT ATT T).

The Flag-hKCNQ5(SM)-IRES-NeoR (#940) lentiviral construct codes for a Flag-tagged wild-type version of human KCNQ5. It was made by reverting the G278S mutation in Flag-hKCNQ5(SM,G278S)-IRES-Neo (#939) using the QuikChange II XL Site-Directed Mutagenesis Kit with the #1462 forward primer (TTT TGT CTC CAT AGC CAA TAG TTG TCA ATG TAA TTG TGC CCC) and the #1463 reverse primer (GGG GCA CAA TTA CAT TGA CAA CTA TTG GCT ATG GAG ACA AAA). The pLUC705[50] (#876, gift from Dr. Bing Yang) plasmid encodes a luciferase gene interrupted by a mutated human beta globin intron 2. This mutation creates a new aberrant splicing site at position 705 that when used produced an mRNA that encodes a truncated non-functional luciferase[50]. To introduce this construct into a lentiviral vector, the pLUC705 plasmid was digested with HindIII/XhoI, blunted with T4 DNA polymerase, and ligated into StuI-digested and dephosphorylated LeGO-iG2 (#807, Addgene plasmid #27341), resulting in plasmid pLUC705.LeGO-iG2 (#875). The pTAT-Cre (#917, Addgene plasmid #35619) bacterial plasmid encodes a histidine-tagged TAT-Cre recombinase. The Cre reporter lentiviral vector (#918, Addgene plasmid #62732) encodes a LOXP-RFP-STOP-LOXP-GFP gene construct. Cells expressing this plasmid appear red but once recombination has occurred when TAT-Cre is translocated into cells the RFP-STOP fragment will be excised, GFP but not RFP will now be produced, and cells will appear green.

Peptides

TAT-RasGAP$_{317-326}$ is a retro-inverso peptide (i.e. synthesized with D-amino-acids in the opposite direction compared to the natural sequence) labeled or not with FITC or TMR. The TAT moiety corresponds to amino-acids 48–57 of the HIV TAT protein (RRRQRRKKRG) and the RasGAP$_{317–326}$ moiety corresponds to amino-acids from 317 to 326 of the human RasGAP protein (DTRLNTVWMW). These two moieties are separated by two glycine linker residues in the TAT-Ras-GAP317–326 peptide. FITC-bound peptides without cargo: TAT, MAP (KLALKLALKALKAALKLA), Penetratin (RQIKWFQNRRMKWKK), Transportan (GWTLNSAGYLLGKINLKALAALAKKIL), R9 (RRRRRRRRR), K9 (KKKKKKKKK) and (RE)9 (RERERERERERERERERE) were synthesized in D-amino-acid conformation. All peptides were synthesized in retro-inverso conformation (over the years different suppliers were used with routine checks for activity of TAT-RasGAP$_{317-326}$ derived peptides, Biochemestry Department of University of Lausanne, SBS Genetech, China and Creative Peptides, USA) and resuspended to 1 mM in water.

Statistical analysis

Statistical analysis was performed on non-normalized data, using GraphPad Prism 7. ANOVA multiple comparison analysis to wild-type condition was done using Dunnett's correction (Fig. 2a, 2b and 2c (top panel) and PI internalization in Fig. 3f, as well as TAT-PNA internalization in Supplementary Fig. 8a. ANOVA multiple comparison analysis between several conditions was done using Tuckey's correction (Supplementary Fig. 10a and 10e). Comparison between two conditions was done using two-tailed paired t-test for the CPP internalization experiments described in Fig. 2c (bottom panel), 4a-b and Supplementary Fig. 1d, 10c. All measurements were from biological replicates. Unless otherwise stated, the horizontal bars in the graph represent the median, the height of columns correspond to averages, and the dots in the Figures correspond to values derived from independent experiments.

Data availability

DNA sequencing data from the CRISPR/Cas9-based screens are available through the following link: https://www.ncbi.nlm.nih.gov/sra/SRP161445. Note: this link is currently blocked for public access, but will be released upon publication.

RESULTS PART II:

Identification of a new, Rab14-dependent, endolysosomal pathway

CONTRIBUTIONS

All experiments were performed by me, under the supervision of Prof. Christian Widmann. Dr. Yuta Homma created the Rab knockout library in MDCK-II cells in the laboratory of Prof. Mitsunori Fukuda, Tohuku University, Japan.

ABSTRACT

Cells can endocytose material from the surrounding environment. Endocytosis and endosome dynamics are controlled by proteins of the small GTPase Rab family. Several endocytosis pathways have been described (e.g. clathrin-mediated endocytosis, macropinocytosis, CLIC/GEEC pathway). Besides possible recycling routes to the plasma membrane and various organelles, these pathways all appear to funnel the endocytosed material to Rab5-positive early endosomes that then mature into Rab7-positive late endosomes/lysosomes. By studying the uptake of a series of cell-penetrating peptides (CPPs) used in research and clinic, we have discovered a second endocytic pathway that moves material to late endosomes/lysosomes and that is fully independent of Rab5 and Rab7 but requires the Rab14 protein. This newly identified pathway differs from the conventional Rab5-dependent endocytosis at the stage of vesicle formation already and is not affected by a series of compounds that inhibit the Rab5-dependent pathway. The Rab14-dependent pathway is also used by physiological cationic molecules such as polyamines and homeodomains found in homeoproteins. Rab14 is expressed by the last eukaryotic common ancestor. The Rab14-dependent pathway may therefore correspond to a primordial endosomal pathway taken by cationic cargos.

INTRODUCTION

Endocytosis is a major entry route used by cells to take up a variety of extracellular substances ranging from nutrients, fluid phase material, growth factors, hormones, receptors, cellular penetrating peptides (CPPs), viruses or bacteria. Various forms of endocytosis have been described, the main routes being clathrin-mediated endocytosis, macropinocytosis, and the clathrin-independent carrier/glycosylphosphotidylinositol-anchored protein enriched endocytic compartment (CLIC/GEEC) pathway [reviewed in[153-155,267,268]]. Which form of endocytosis is used and the ultimate fate of the endocytosed material depend on the nature of the substances being taken up by cells.

Endocytic vesicles (endosomes) are formed by membrane invaginations, actin-driven membrane protrusions (in the case of macropinocytosis for example), or ruffling. In the case of clathrin-mediated endocytosis, vesicle formation is triggered through the detection of the endosomal cargo by AP2 adaptor domains and subsequent recruitment of clathrin triskelions[269,270]. Several AP2 adaptors bound to the plasma membrane through PI(4,5)P_2 are necessary for efficient clathrin binding[270]. Accumulation of AP2/clathrin complexes (within seconds) at the membrane leads to membrane bending and endocytic vesicle formation[269-271].

Endosomes are dynamic structures that undergo fusion and fission events[272]. Early endosomes mature into multivesicular bodies (MVBs), late endosomes and finally lysosomes, where degradation of the endocytosed material occurs[157,158]. The endocytosed material can also be recycled back to the plasma membrane or trafficked towards other cellular compartments[157-159].

Each stage of endosomal maturation is meticulously controlled by the sequential recruitment of various endosomal protein and lipids. For example, on the early endosomes, Rab5, activated by its guanine exchange factor (GEF) Rabex-5, controls local generation of PI(3)P by recruiting the Vps34 PI3 kinase. This in turn leads to recruitment of EEA1 via its capacity to bind PI(3)P through its FYVE domain. EEA1 can also directly interact with the active GTP-bound form of Rab5. The ability of EEA1 to bind simultaneously Rab5 and PI(3)P on separate vesicles makes it a tethering protein that contributes to endosomal fusion[273]. Vps34 knock-out in mammalian cells leads to enlarged early endosomes and interruption of the progression of endocytosed cargo to lysosomes[274]. Vesicle maturation proceeds through the recruitment of the Mon1-Ccz1 complex that interacts with Rab5 and PI(3)P. The Mon1-Ccz1 complex has a GEF activity towards Rab7 that leads to the activation of this small GTPase on endosomes [reviewed in[158,275]]. Concomitantly, Rab5 GTPase-activating protein (GAP) turns off Rab5 and promotes release of the latter from early endosomes. Hence, Rab5 and Rab7 regulate essential steps in the endocytic pathway that moves endocytosed material to lysosome. The Rab5/Rab7-controlled endocytic pathway is currently the only molecularly characterized route taken by endocytosed material that end up in lysosomes[154,268,275].

In this study we show that endocytosed CPPs, homeoproteins, and polyamines, follow a newly discovered endosomal pathway towards lysosomes that requires Rab14 but not Rab5 or Rab7. Endocytosis of CPPs is also unaffected by phosphoinositide 3-kinase (PI3K) inhibitors or various pharmacological agents known to inhibit the uptake of classical cargos such as transferrin and dextran. This work therefore defines a second independent endocytic maturation pathway that moves endocytosed material to lysosomes.

RESULTS

CPPs employ unconventional endocytosis

CPPs can be used for intracellular transport of bioactive cargo into cells[1,3,4,8-16,98]. Various non-exclusive mechanisms of CPP endocytosis have been proposed[1,3,4,8-12,16,97,276,277]. However, there is no consensus and clarity regarding the precise nature of the endosomal pathway used by CPPs and its underlying mechanisms. CPPs additionally enter cells through direct translocation via water pores that are formed as a consequence of membrane megapolarization induced by the CPP themselves and the activity of potassium channels[167]. Direct translocation can be inhibited through plasma membrane depolarization or invalidation of specific potassium channels (e.g. KCNN4 in HeLa cells), without affecting endocytosis of CPPs[167], transferrin[278] or vesicular stomatitis virus (VSV)[278]. Here, we took advantage of KCNN4 knockout HeLa cells to study specifically endocytosis in the absence of possible confounding effects mediated by CPP direct translocation. To investigate the endocytic pathway employed by CPPs, we phenotypically characterized CPP containing vesicles (Supplementary Fig. 1a-b) for the presence of early (Rab5 and EEA1) and late (Rab7 and Lamp1) endosomal markers. We selected five most commonly used CPPs in research and in clinic (TAT, R9, Penetratin, MAP and Transportan) as well as TAT-RasGAP$_{317-326,}$ a prototypical TAT-cargo complex[167,178-186,279,280]. Pulse-chase experiments (Fig. 1a-b and Supplementary Fig. 1b) demonstrated colocalization of transferrin, EGF and dextran with EEA1, Rab5A and Rab5B at early time points, and Rab7 and Lamp1 at later time points. These results are consistent with previous knowledge that these molecules enter cells through clathrin-mediated endocytosis (transferrin and EGF) and macropinocytosis (dextran). To ensure that ectopic expression of endosomal markers does not interfere with normal endocytosis, we compared the pattern of EEA1-positive and Lamp1-positive vesicle, which we found to be qualitatively similar in control cells and in cells expressing ectopic GFP-tagged versions of these markers (Supplementary Fig. 1c). Moreover, ectopic expression of the tagged EEA1 and Lamp1 constructs did not alter the kinetics of transferrin colocalization with EEA1- or Lamp1-positive vesicles (Supplementary Fig. 1d). These results indicate that ectopic expression of fluorescent endosomal markers, in live cells in particular, does not appear to affect endocytic processes. CPPs were found in EEA1- and Lamp1-positive vesicles at early and late

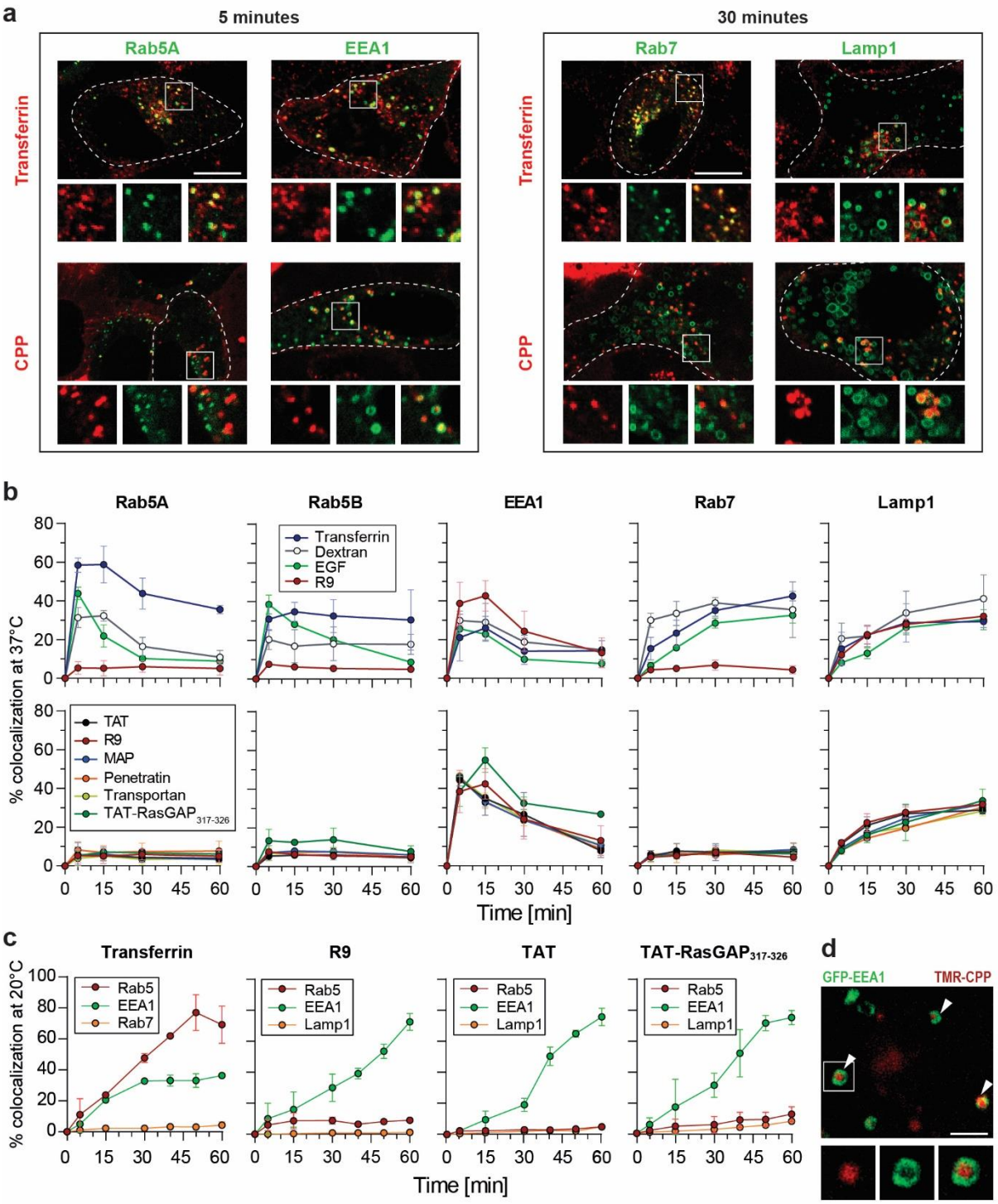

Figure 1: CPPs follow a Rab5-independent endocytic pathway.
a-d, HeLa KCNN4 knock-out cells ectopically expressing the fluorescently-tagged early (Rab5A, Rab5B and EEA1) or late (Rab7 and Lamp1) endosomal markers were incubated with 20 μg/ml transferrin, 0.2 mg/ml dextran 10 kDa, 2 μg/ml EGF or with 40 μM of CPPs linked or not to a cargo for 5 minutes, then washed and imaged at the indicated time points by confocal microscopy (see Supplementary Fig. 1b for experimental setup). All experiments were performed on live cells at 37°C unless indicated otherwise. **a,** Representative confocal images of HeLa KCNN4 knock-out cells, expressing GFP-tagged endosomal markers, incubated with AlexaFluor568-transferrin or TMR-TAT. Images were acquired at 5 or 30 minutes after the addition of endosomal material. Scale bar: 10 μm. **b-c,** Quantitation of colocalization between the indicated fluorescent material and fluorescently-tagged early and late endosomal markers. Colocalization analysis was performed as described in Methods and Supplementary Fig. 1a. The data correspond to mean ± SD of three independent experiments. In panel b, the data obtained with R9 are shown, for comparison, both on the top graphs and the bottom graphs. In panel c, cells were incubated at 20°C to delay endosomal maturation. d, Representative confocal, Airyscan acquired, high-resolution images of cells ectopically expressing GFP-EEA1 incubated with 40 μM TMR-TAT for 5 minutes. Scale bar: 2 μm.

time points, respectively (Fig. 1a-b and Supplementary Fig. 1a) but surprisingly only a minority of CPP-containing vesicles were positive for Rab5 and Rab7 (Fig. 1a-b). Even though the selected CPPs have different physico-chemical properties they all carry positive charges within their sequence and appear to be found in the same endocytic vesicles (Supplementary Fig. 1e).

To rule out that association of Rab5 with CPP-containing vesicles could be transient, we performed experiments at 20°C such that endosomal maturation is considerably slowed down, as can be observed for transferrin (Fig. 1c, left). However, CPP-positive endosomes remained mostly Rab5-negative (Fig. 1c). Additionally, Rab5- and Rab7-positive CPP-containing vesicles were only marginally detected in the continuous presence of the CPPs despite extensive colocalization with EEA1 (Supplementary Fig. 1f). High resolution confocal images showed that TAT was found inside EEA1-positive vesicles already a few minutes after being added to cells (Fig. 1d) confirming that CPPs are indeed located in EEA1-positive endosomes. In addition, TAT-RasGAP$_{317-326}$ did not interfere with the progression of transferrin through early and late endosomes (Supplementary Fig. 1g) and did not lead to generation of aberrant endosomes bearing EEA1 and Lamp1 at the same time (Supplementary Fig. 1h). This indicates that CPPs do not reprogram the manner by which cells take up material through classical endocytosis. Lack of colocalization with Rab5A and Rab7 was observed previously for tryptophane/arigine-rich peptide WRAP linked to siRNA[137]. Additionally, based on visual inspection of representative images in literature, R8 and TAT also colocalize only partially with Rab5A[141].

We then used pharmacological agents such as EIPA[135], IPA3[143,144], ML7[281,282], Jasplakinolide[283] and Cytochalasin D[138,139] that block distinct steps of endocytic vesicle formation and maturation, such as actin filament polymerization, Na^+/H^+ exchange inhibition, as well as macropinosome formation and closure, to determine whether these steps are parts of the CPP endocytic pathway. We observed no effect of these inhibitors on the internalization of TAT-RasGAP$_{317-326}$ in contrast to what was seen for dextran uptake (Supplementary Fig. 2a-b). Additionally, as opposed to transferrin internalization, the early stages of CPP endocytosis were dynamin-independent (Supplementary Fig. 2c).

Lipids such as phosphoinositides (PIs) that can be phosphorylated at positions 3, 4, or 5 of the inositol ring, represent another type of markers of endocytosis. For example, PI(4,5)P_2 is enriched in the plasma membrane, whereas PI(3)P and PI(3,5)P_2 are enriched in early and late endosomes, respectively, and participate in their formation [reviewed in [284-288]]. In conventional endocytosis, EEA1 is recruited to early endosomes through interactions with Rab5 and PI(3)P[289-291]. The latter is produced by Vps34, a PI3-kinase that is also recruited by Rab5. We therefore, used pan-PI3K inhibitors (wortmannin and LY294002) and assessed the colocalization between selected endosomal material and EEA1 or Lamp1. Our data show that, in the presence of LY294002, transferrin and dextran endosomal maturation and progression was halted, consistent with observations reported in the literature[274,292] (Fig. 2a and Supplementary Fig. 2d). However, colocalization between CPPs and EEA1 or Lamp1 was not affected

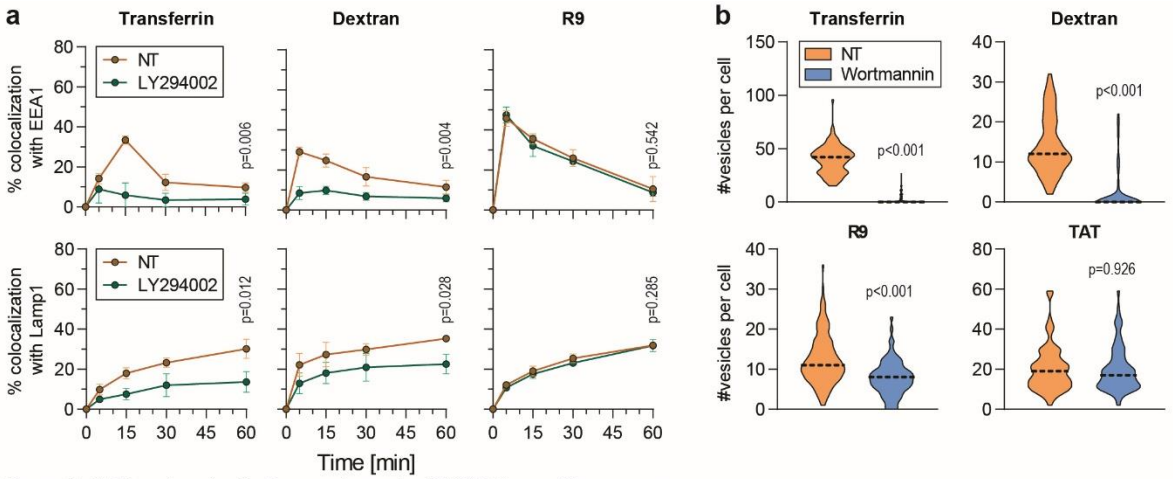

Figure 2: CPP endocytosis does not require PI(3)P-kinase-like enzymes.
a, Colocalization quantitation between the indicated endosomal material and endosomal markers in the presence or in the absence of LY294002, a pan-PI3-kinase inhibitor. HeLa KCNN4 knock-out cells, ectopically expressing GFP-tagged EEA1 or Lamp1, were incubated with 20 μg/ml AlexaFluor568-Transferrin, 0.2 mg/ml TMR-Dextran 10 kDa or 40 ⊠M TMR-R9 for a pulse of 5 minutes. Cells were preincubated or not for 30 minutes with 25 μM LY294002, which was still present during the full duration of the experiment. The data correspond to mean ± SD of three independent experiments. The p-values were calculated based on area under the curve (AUC) analysis followed by a t-test. **b,** Quantitation of the number of endosomal vesicles per cell in the presence or in the absence of wortmannin, a pan-PI3-kinase inhibitor. HeLa KCNN4 knock-out cells were incubated with 20 μg/ml AlexaFluor568-Transferrin, 0.2 mg/ml TMR-Dextran 10 kDa or 40 μM TMR-CPP for a pulse of 5 minutes. Cells were preincubated or not for 30 minutes with 10 μM wortmannin, which was still present during the full duration of the experiment. The number of vesicles positive for the indicated endosomal material were visually calculated based on confocal images, acquired in the middle of the cell. A minimum of 150 cells were quantitated per condition. The results correspond to three independent experiments. The p-values were calculated using paired t-test.

(Fig. 2a). Furthermore, depletion of $PI(3,4)P_2$, enriched on the plasma membrane[288], blocks the maturation of clathrin-coated vesicles prior to their fission from the plasma membrane[293], and prevents macropinosome closure[294,295]. As these events precede Rab5 recruitment, we next determined whether the presence of wortmannin, which at high micromolar concentrations, besides PI(3)P depletion, additionally inhibits PI4-kinases [296,297] and leads to depletion of $PI(3,4,5)P_3$[298] and $PI(3,4)P_2$[299,300], would have an effect on CPP endocytosis. Indeed, wortmannin treatment almost fully inhibited the endocytosis of transferrin and dextran, as opposed to the tested CPPs, where the number of vesicles was either only marginally reduced (R9) or remained unchanged (TAT) (Fig. 2b).

Even though previous studies have shown some contradictory results of CPP internalization in the presence of the endocytic inhibitors used in this study [decreased uptake[51,55,130,141], no effect[123,127,130,137], increased uptake [124]], our data clearly indicate that CPPs enter cells through an uncharacterized endocytic pathway, which differs from classical endocytosis already at the stage of endocytic vesicle formation.

Rab14 is required for the maturation of CPP-containing endosomes

All previously characterized endocytic pathways appear to converge to Rab5-positive vesicles[153,154,301-310]. In the absence of Rab5, the number of maturing endocytic vesicles is decreased and endocytosis is halted[291]. To determine whether EEA1 recruitment to CPP-positive vesicles occurs in the absence of Rab5, we took advantage of a knockout Rab library in MDCK cells, which consists of single and multiple

knockouts (>50 cell lines) targeting either different protein isoforms or multiple Rab proteins simultaneously[311]. This library includes a Rab5 conditional knockout cell line, where Rab5A, B and C isoforms have been knocked out and replaced by a Rab5A version that can be degraded through auxin-induced ubiquitination upon addition of indole-3-acetic acid (IAA)[312] (Y. Homma et al., manuscript in preparation) (Supplementary Fig. 3a). The recruitment of EEA1 (15 minutes post incubation), as well as Lamp1 (30 minutes post incubation) to TAT-containing vesicles was not affected by the absence of Rab5 (Fig. 3 and Supplementary Fig. 3b). Furthermore, inhibiting Rab5 with dominant-negative constructs (Rab5A S34N, Rab5B S34N or Rab5C S35N) in HeLa cells, while reducing the percentage of EEA1-positive transferrin- and dextran-containing vesicles, as expected, had no significant effect on the percentage of EEA1-positive (Supplementary Fig. 3c-d) or Lamp1-positive (Supplementary Fig. 3e) CPP-containing endosomes. This set of data argues against a role of Rab5 isoforms in the maturation of CPP-containing endosomes and for EEA1 recruitment on these endosomes.

Using a candidate-based approach and the Blastp database, we identified a subset of candidate proteins with amino acid sequence similarity to Rab5. Using GPS Protein (http://gpsprot.org/navigator.php?q=8411), a database of protein-protein interactions, we restricted the pool of these Rab5-like proteins to those that have the potential to interact with EEA1. We identified three top candidates using this approach: Rab14, Rab22 and Rab31 (also known as Rab22B). Additionally, Rab21 bears sequence similarity to Rab5 and colocalizes with early endosomal markers (Rab5 and EEA1[313-315]). Rab14 colocalizes with early endosomal markers[316-318], but not late endosomal markers[316,318,319] (Supplementary Fig. 4) and has so far been shown to be involved in endosomal recycling[320], endosome-endosome fusion, and MHC class I cross presentation[319]. Rab14 and Rab22 are

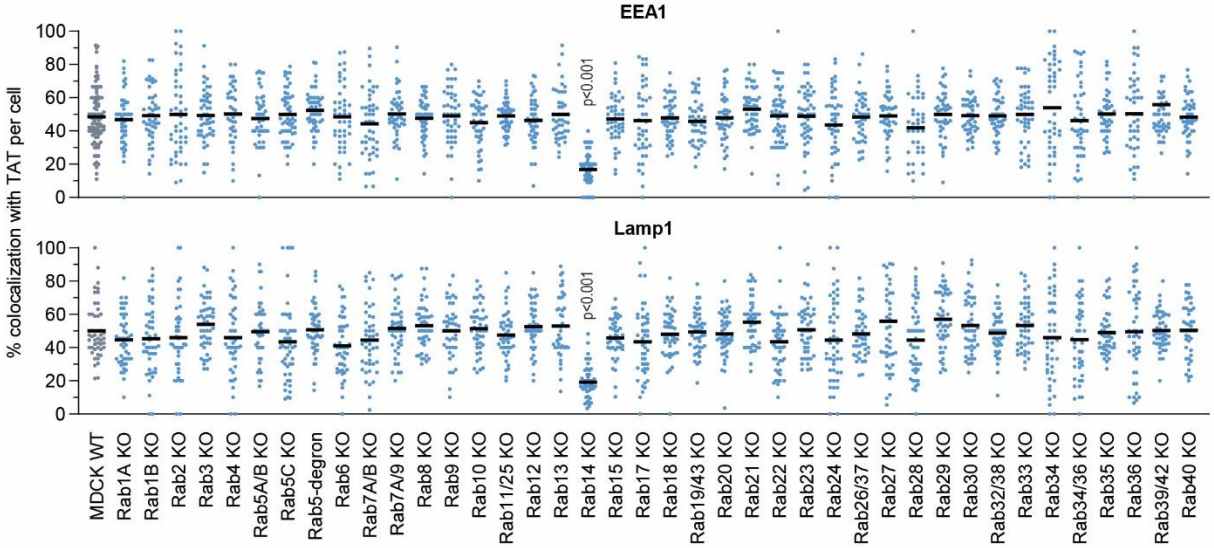

Figure 3: CPP endosomal maturation is Rab14-dependent.
Quantitation of colocalization between TMR-TAT and GFP-EEA1 (15 minutes, top) or Lamp1-GFP (30 minutes, bottom) in a pulse chase experiment in MDCK-II wild-type cells and the indicated Rab knock-outs. A minimum of 50 cells were quantitated per condition. Statistical analysis was performed with ANOVA multiple comparison to wild-type condition with Dunett's correction. Only significant p-values are shown on the Figure. Rab5-degron cells were treated with 1 ⍰g/ml doxycycline and 500 ⍰M IAA for 48 hours to induce degradation of degron-tagged Rab5A in the Rab5B/C knockout cell line.

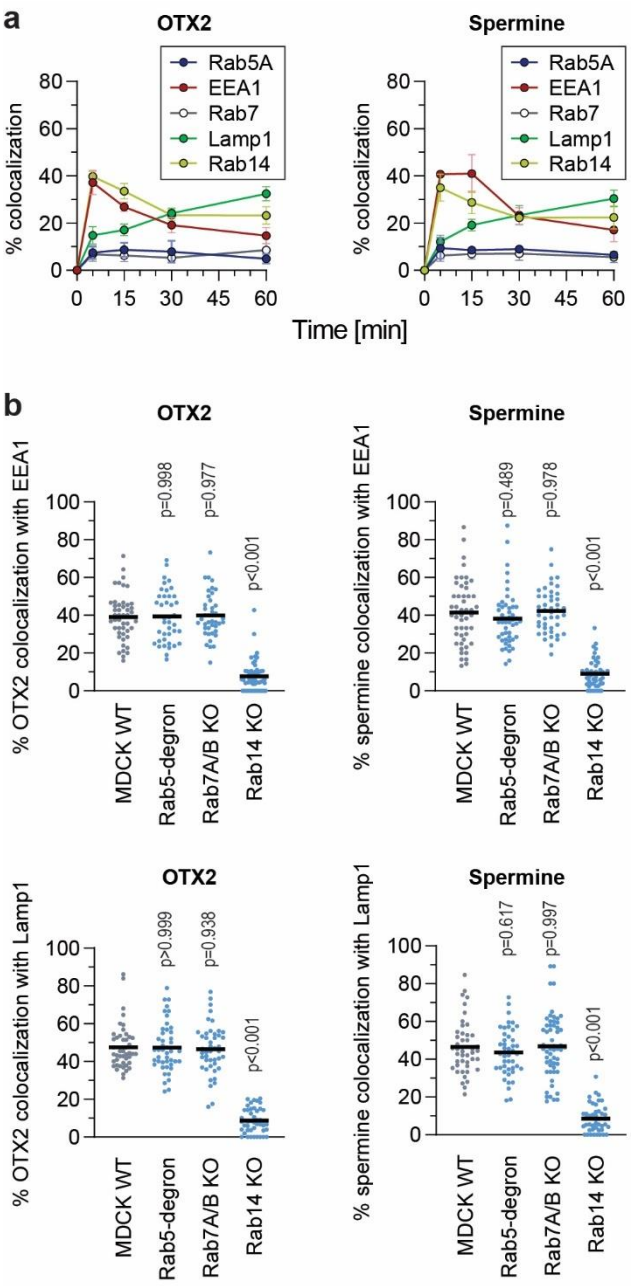

Figure 4: HDs and polyamines are following a Rab5-independent, Rab14-dependent endocytic route.
a, Colocalization quantitation between endosomal markers and HD or polyamine. HeLa KCNN4 knock-out cells, ectopically expressing the indicated endosomal markers, were subjected to a 5-minute pulse incubation with fluorescently labelled OTX2 HD (10 μM) or spermine (5 μM). Quantitation assessment was based on confocal images. The results correspond to mean ± SD of three independent experiments. **b,** Colocalization quantitation between fluorescent versions of OTX2-HD (10 μM) or spermine (5 μM) with EEA1 (top) or Lamp1 (bottom) in MDCK-II wild-type and the indicated Rab knockouts. Cells were incubated for 5 minutes, then washed and confocal images were acquired at 15- and 30-minutes post incubation for early and late endosomal markers, respectively. A minimum of 50 cells were quantitated per condition. Statistical analysis was performed with ANOVA multiple comparison to wild-type condition with Dunett's correction.

both involved in endosome to Golgi trafficking[316,318,321], and Rab31 plays a role in Golgi-endosome directional transport[322]. Rab22 can directly interact with EEA1[321,323], supporting the hypothesis that it could function in a manner similar to Rab5. Our data showed that Rab14, Rab21 and Rab22 colocalize relatively frequently (as opposed to Rab31) with transferrin[316,317], and CPPs, as well as to a lesser extent with dextran (Supplementary Fig. 5a). Furthermore, dominant-negative versions of these proteins (Rab14 S25N, Rab14 N124I, Rab21 T31N, Rab22 S19N) were used to assess the role of the respective Rab proteins in CPP-containing vesicle maturation. Supplementary Fig. 5 shows diminished colocalization between CPPs and EEA1 in cells expressing Rab14 S25N and Rab14 N124I, but not in cells expressing the other dominant negative mutants. Rab14 is therefore a strong candidate that can substitute for Rab5 function in the recruitment of EEA1 to maturing CPP-containing endosomes. The colocalization between transferrin, as well as dextran and EEA1 appears not to be affected in the Rab14 dominant negative background (Supplementary Fig.5b). Similarly, earlier work has reported that EEA1 colocalization with mannose receptors [319] or with EGF [318] is not affected when Rab14 is depleted in cells.

We then used a MDCK-II comprehensive Rab knock-out library to test whether colocalization between CPPs and EEA1 or Lamp1 is affected by the depletion of various

Rab protein isoforms at 15- and 30-minutes post incubation. The obtained data further support the involvement of Rab14 in the maturation of CPP-containing vesicles (Fig. 3). Surprisingly, none of the other tested single or multiple Rab knockouts had an effect on EEA1 or Lamp1 recruitment to CPP-positive endosomes (Fig. 3). Taken together our data demonstrates that ensuing their uptake by cells, CPPs follow a Rab5-independent, Rab14-dependent endocytic route.

Homeoproteins and polyamines use the same endocytic pathway as CPPs

Homeoproteins (HPs) are a family of transcription factors involved in multiple biological processes[324-327]. Additionally, HPs, such as Engrailed 2 and OTX2, exhibit therapeutic properties[328-333]. The vast majority of HPs contain a conserved 60 amino-acids domain called the homeodomain (HD) that carries HP internalization and secretion motifs. Interestingly, the HP internalization motifs bear CPP sequences[324,326]. We therefore hypothesized that HDs could be endocytosed similarly as CPPs. Through colocalization experiments we determined that there is indeed colocalization between HD-containing endosomes and the EEA1 or Lamp1 markers, and that their colocalization with Rab5A or Rab7A is only marginal (Fig. 4a, left). As for CPPs, EEA1 and Lamp1 recruitment to HD-positive endosomes was significantly reduced in cells lacking Rab14 (Fig. 4b, left). This indicates that HDs follow a Rab5-independent, Rab14-dependent endosomal pathway. Polyamines are small signaling molecules involved in numerous cellular processes (gene regulation, cell proliferation, cell survival and cell death)[334-338]. In mammalian cells polyamines enter cells through endocytosis[339-342], and possibly also through a polyamine specific transporter[340]. Polyamine-containing vesicles mature to Lamp1-containing acidic endosomes and are then exported into the cytosol[342]. The mechanism of polyamines endocytosis has not been described at the molecular level. Similarly, to CPPs and HDs, polyamine-containing vesicles colocalized only marginally with Rab5A and Rab7A markers and their maturation down to Lamp1-containing endosomes was Rab14-dependent (Fig. 4a-b, right and Supplementary Fig. 6). These data indicate that physiological molecules such as polyamines, and by extension homeoproteins if they behave like their homeodomains, do not enter cells through the classical Rab5-dependent endocytic route but via a Rab14-dependent pathway.

DISCUSSION

We have characterized a previously undescribed Rab5-independent, Rab14-dependent endosomal pathway. In this pathway, EEA1 is recruited to early endosomes in the absence of Rab5 (Fig. 1, 3 and Supplementary Fig. 3) and endosomal maturation requires Rab14 (Fig. 3 and Supplementary Fig. 5). This pathway appears to differ from previously described endocytosis already at the early stages of vesicle formation (Fig. 2). We showed that synthetic molecules as CPP, as well as physiological

molecules such as polyamines take advantage of the Rab5-independent, Rab14-dependent pathway to enter cells and reach lysosomes.

The molecules that we have found to be endocytosed via the Rab14-dependent pathway are characterized by their strong cationic nature. As Rab14 is expressed in most tissues (according to Protein Atlas and CCLE database) and seems to be present in the last eukaryote common ancestor[320,343], it is possible that Rab14 is involved in a primordial endosomal pathway taken by cationic cargos. Whether this pathway is used by other types of cargos can now be assessed functionally in cells in which Rab14 is inactivated or invalidated.

Besides Rab14, no other Rab proteins could be evidenced to play a role in maturation of the endocytic pathway taken by CPPs, HDs, or polyamines. In particular, we did not find a Rab7 homolog that would be required for the acquisition of the Lamp1 marker in this pathway. Either Rab14 is the sole Rab necessary for cargo progression along the endocytic pathway used by CPPs, HDs, or polyamines or there is an as yet unknown Rab isoform that is redundant with Rab7 in this pathway. Because there is only marginal colocalization between Rab14 and Lamp1[316,319] (Supplementary Fig. 4), the possibility that Rab14 plays a dual role in the recruitment of EEA1 and Lamp1 is unlikely. Based on phylogeny and clustering analysis[318,320,343], Rab7 is most closely related to Rab9. However, cells lacking both Rab7 and Rab9 were not compromised in their ability to move cationic cargos along the Rab14-dependent pathway all the way down to Lamp1-containing vesicles (Fig. 3). The Rab isoform that is redundant with Rab7, if it exists, remains therefore to be discovered.

There was minimal colocalization between CPP-, HP- or polyamine-containing endosomes and the Rab5 and Rab7 endosomal markers. This marginal entry could correspond to non-selective bulk liquid uptake, as it occurs during macropinocytosis [344]. Alternatively, a small fraction of these cargos may enter the Rab5-dependent endosomal pathway as previously reported for CPPs[1,4,8-12].

There have been earlier circumstantial indications of the existence of a Rab5-independent pathway specifically in the context of viral infections, as well as trafficking to yeast vacuole[345,346]. It has been shown that some viruses use unconventional endocytosis, such as Herpes Simplex Virus 1[347], SARS[348], Lassa virus, the Amr53b and We54 strains of LCMV (lymphocytic choriomeningitis virus)[349-352], Lujo virus[353,354] and some influenza A strains[355] that appear to skip the early Rab5-positive endosomes. Rab14 also appears to be involved in viral trafficking, more specifically in the endocytosis of Ebola virus matrix protein VP40[356]. Additionally, Rab14 depletion delayed *Candida albicans*- containing phagosome maturation to Lamp1, even though Rab5 and Rab7 markers were still present during the maturation process[357]. Possibly, the Rab5-independent, Rab14-dependent endosomal pathway is used by some pathogens to infect cells. Therefore, our findings may not only concern the physiological delivery of cationic cargo into cells, but could also be relevant for the search of anti-viral or antimicrobial drugs.

ACKNOWLEDGEMENTS

The laboratory of YH is supported by Grant-in-Aid for Young Scientists from the Ministry of Education, Culture, Sports, Science and Technology (MEXT) of Japan (grant number 20K15739). The laboratory of MF is supported by Grant-in-Aid for Scientific Research(B) from the MEXT (grant number 19H03220) and Japan Science and Technology Agency (JST) CREST (grant number JPMJCR17H4). We are thankful to the Cellular Imaging Facility and Bioinformatics Competence Centre at the University of Lausanne for the resources provided and their technical help.

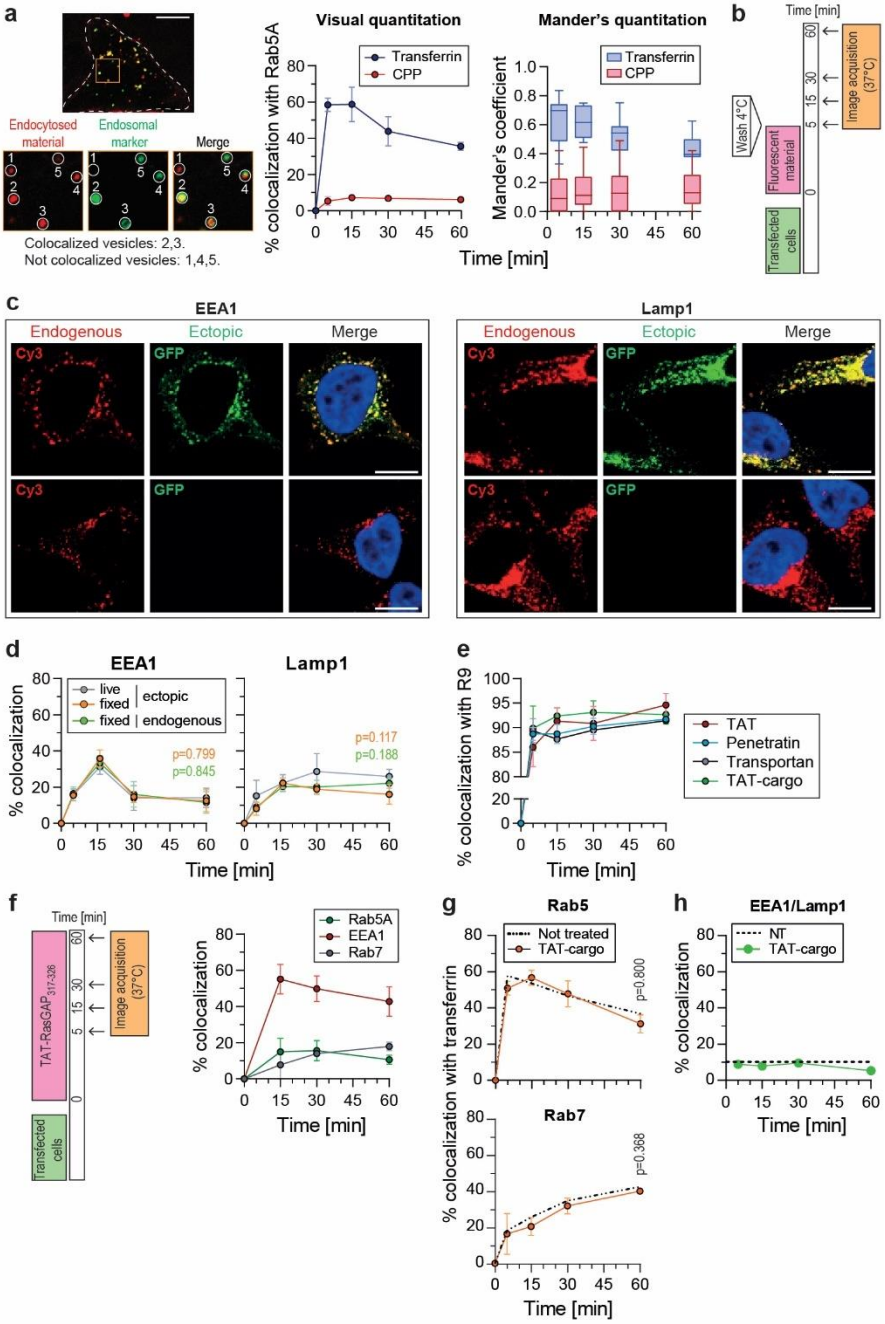

Supplementary Fig. 1: Colocalization quantitation and experimental setup.
a, Colocalization quantitation between fluorescently labeled endosomal material and endocytic markers. Left: representative confocal images of HeLa KCNN4 knock-out cells expressing GFP-Rab5A, in the presence of 20 μg/ml AlexaFluor568-Transferrin for 5 minutes. Colocalization assessment between endocytosed material and a given endosomal marker was performed on confocal images by visual assessment, switching back and forth between the color channels. The samples were randomized to blind the experimentators from the nature of the samples they were analyzing. The images shown on the left are cropped regions of cell transfected with GFP-Rab5 and incubated with AlexaFluor568-transferrin. The circles numbered 1 to 5 depict examples of colocalization versus non-colocalization between Rab5 and transferrin. Scale bar: 10 μm. Graphs on the right-hand side: our visual quantitation (mean ± SD of three independent experiments performed on 165 cells per condition) was validated by Mander's coefficient calculation performed on the same samples using the JaCoP plugin in ImageJ (shown as box plots). **b,** Scheme of the pulse chase experiments used in the experiments depicted in the figures. Cells were incubated five minutes with various fluorescent material, washed, and the endosomal maturation followed overtime. **c,** Ectopic expression does not alter the subcellular location of endosomal markers. Ectopic (top row) and endogenous (bottom row) location of EEA1 and Lamp1. Scale bar: 10 μm. **d,** Quantitation of the colocalization between ectopic or endogenous EEA1 or Lamp1 with Alexa568-transferrin in live or fixed KCNN4 knock-out HeLa cells. The data correspond to mean ± SD of three independent experiments. The p-values were calculated using ANOVA analysis with Dunett's correction based on AUC values from fixed samples compared to live samples. **e,** Colocalization quantitation of the indicated FITC-CPPs with TMR-R9. The data correspond to the mean ± SD of three independent experiments. **f,** Colocalization between TAT-RasGAP$_{317-326}$ (40 μM) and GFP-tagged Rab5, EEA1 or Rab7 in HeLa KCNN4 knock-out cell line. Cells were incubated in the continuous presence of TAT-RasGAP$_{317-326}$. The data correspond to mean ± SD of three independent experiments. **g,** Colocalization between transferrin and Rab5 (top) or Rab7 (bottom) in the presence or in the absence of 40 μM TAT-RasGAP$_{317-326}$. The data correspond to mean ± SD of three independent experiments. The p-values were calculated based on AUC analysis. h, Colocalization quantitation between ectopically expressed BFP-EEA1 and Lamp1-GFP in the presence or in the absence of 40 μM TAT-RasGAP$_{317-326}$. The data correspond to mean ± SD of three independent experiments.

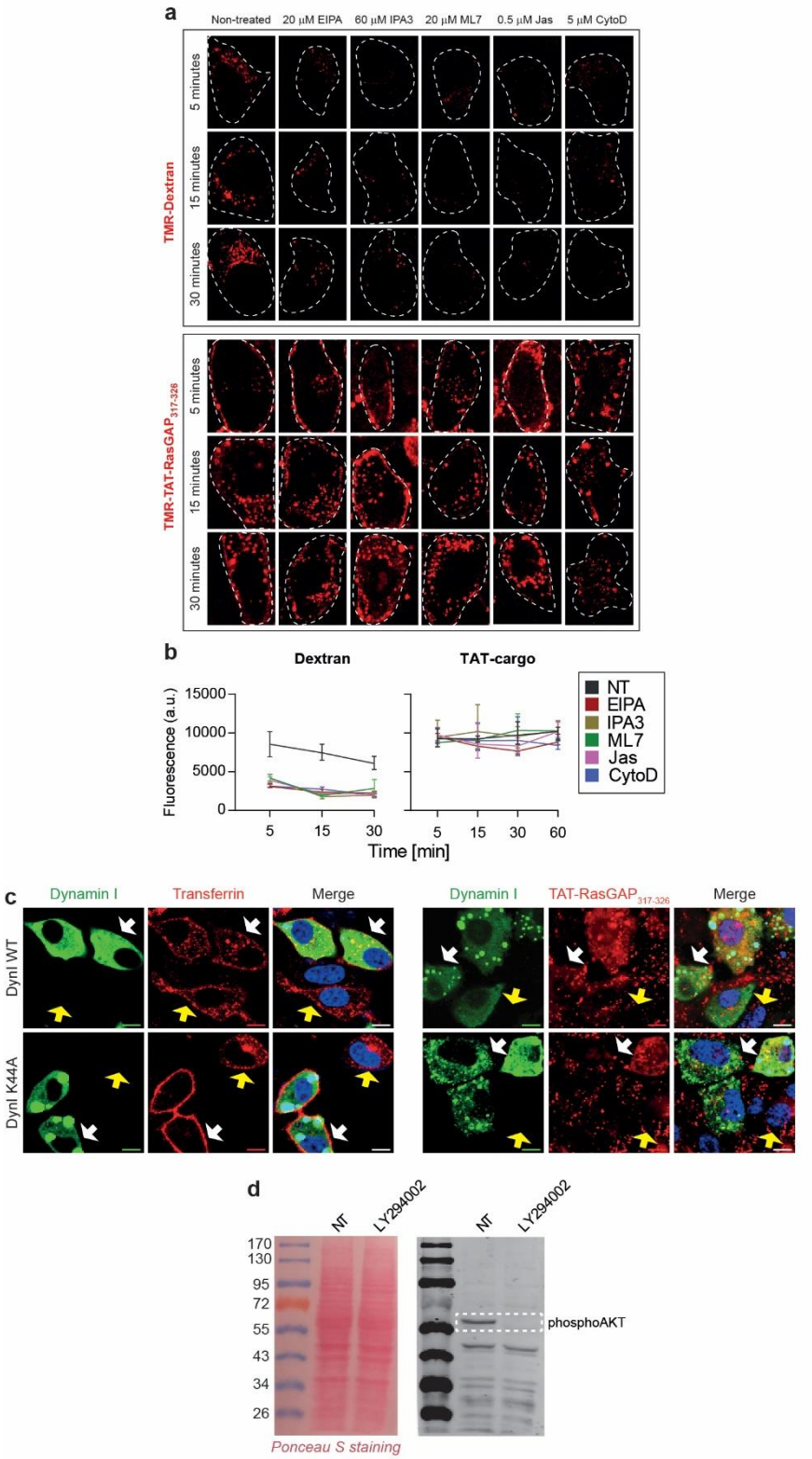

Supplementary Fig. 2: Endosomal vesicle formation inhibitors do not affect CPP uptake.
a, Representative confocal images of HeLa KCNN4 knock-out cells preincubated or not with the indicated inhibitors for 30 minutes prior to the addition of 0.2 mg/ml TMR-Dextran 10 kDa or 40 μM TMR-TAT-RasGAP317-326 for a 5-minute pulse. Confocal images were acquired at 5, 30 and 60 minutes after the addition of endosomal material. The inhibitors were present throughout the full duration of the experiment. **b,** Total cell fluorescence quantitation based on images acquired in panel a. Results correspond to mean ± SD of three independent experiments (n>150 cells per condition). **c,** Representative confocal images of HeLa KCNN4 knock-out cells ectopically expressing wild-type (Dynl WT) or dominant negative (Dynl K44A) version of dynamin I. Cells were incubated with 20 μg/ml AlexaFluor568-transferrin or 40 μM TAT-RasGAP317-326. Cell nuclei were labeled with live Hoechst. White arrows point to cells positively transfected with GFP-dynamin constructs and yellow arrows indicate non-transfected cells. Images were acquired at 15 minutes post incubation with the cargos. **d,** Left panel: red Ponceau S stained membrane, right panel: phospho-AKT antibody signal detection. HeLa KCNN4 knock-out cells incubated in the presence or in the absence of 25 μM pan-PI3-kinase inhibitor, LY294002. To stimulate AKT phosphorylation cells were preincubated in a serum-free media for one hour. Phosphorylated AKT was used as a proxy for PI3-kinase activity.

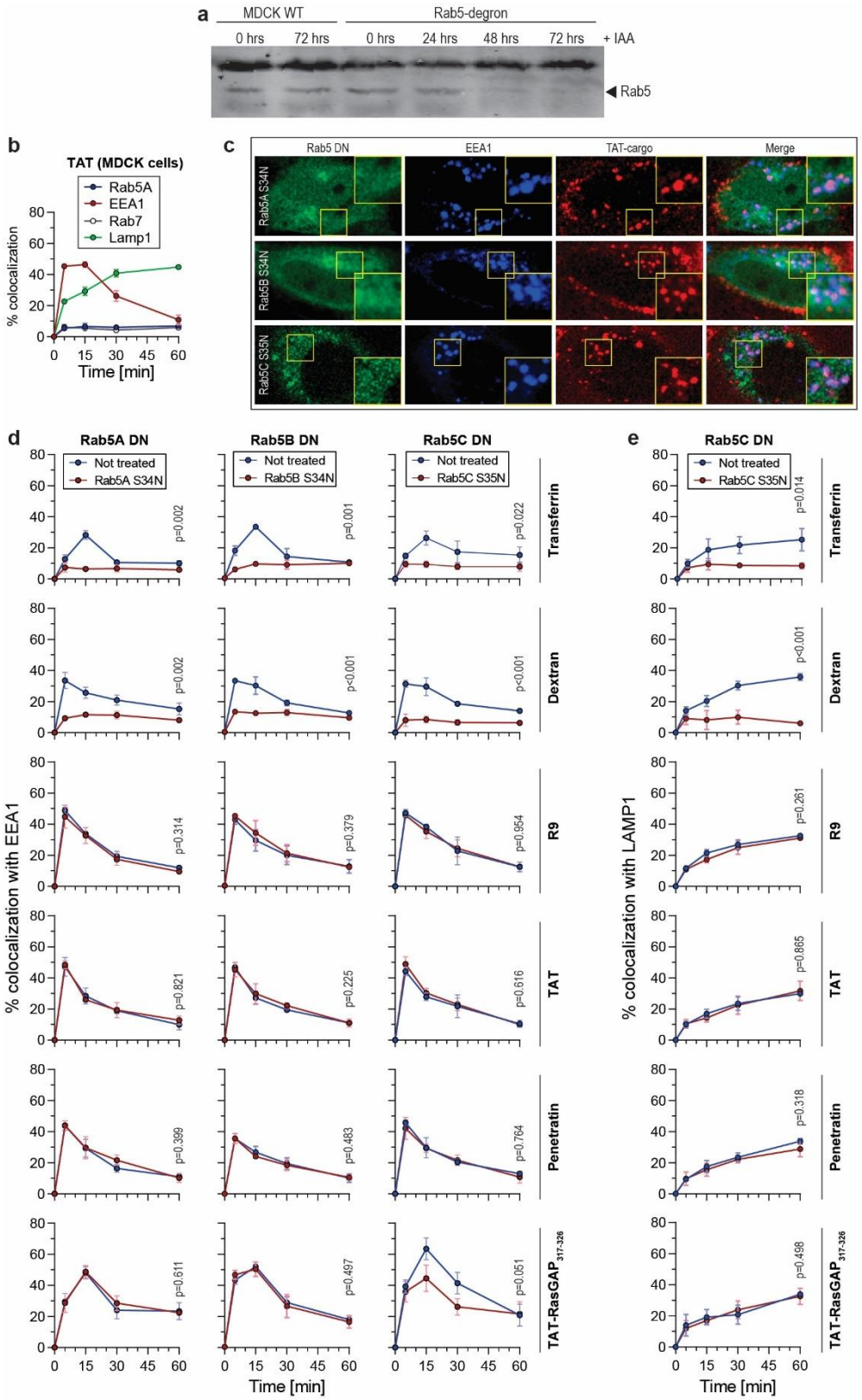

Supplementary Fig. 3: CPP endocytosis is Rab5-independent.
a, Western blot-mediated Rab5 detection in MDCK-II wild-type or Rab5-degron cell lysates incubated in the presence of 1 μg/ml doxycycline and 500 ⊠M IAA for the indicated periods of time to induce degradation of Rab5A. **b,** Colocalization of TAT-containing vesicles with the indicated endosomal markers. MDCK-II wild-type cells were incubated with 40 μM TMR-TAT for 5-minute pulse. **c,** Representative confocal images of cells analyzed in panel d-e in HeLa KCNN4 knockout cells. **d-e,** Colocalization quantitation of transferrin, dextran, and the indicated CPP with EEA1 (panel d) or Lamp1 (panel e) in cells transfected with the indicated Rab5 dominant negative constructs in HeLa KCNN4 knockout cells in a pulse experiment setting (see Supplementary Fig. 1b). The data correspond to mean ± SD of three independent experiments. Statistical analysis was performed using two-tailed t-test based on AUC values. The p-values correspond to the comparison between the cells within the same population transfected or not with the dominant negative constructs.

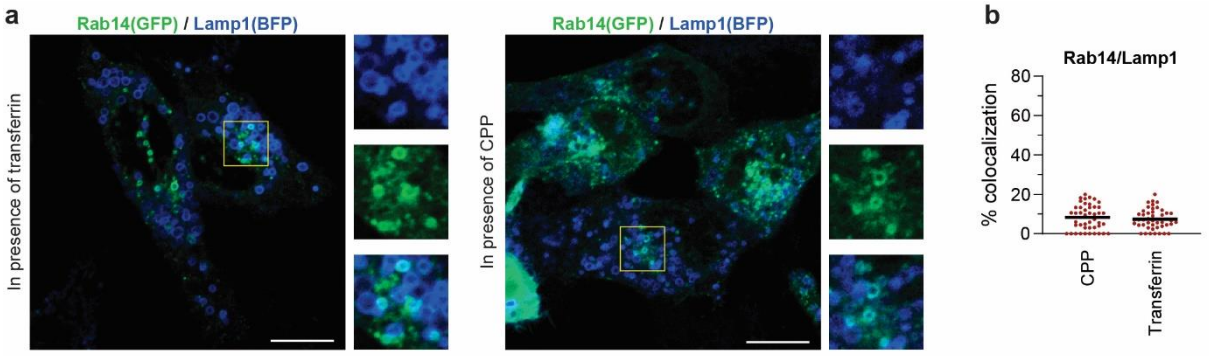

Supplementary Fig. 4: Limited colocalization between Rab14 and Lamp1.
a, Representative confocal images of HeLa KCNN4 knockout cells ectopically expressing GFP-Rab14 and Lamp1-BFP that were incubated for 5 minutes with 20 μg/ml AlexaFluor647-Transferrin or 40 μM TMR-TAT. Images were acquired at 30 minutes post-incubation with endosomal cargo. Scale bar: 10 μm. **b,** Colocalization quantitation of Rab14 with Lamp1 from the experiment in panel a. A minimum of 50 cells were quantitated per condition.

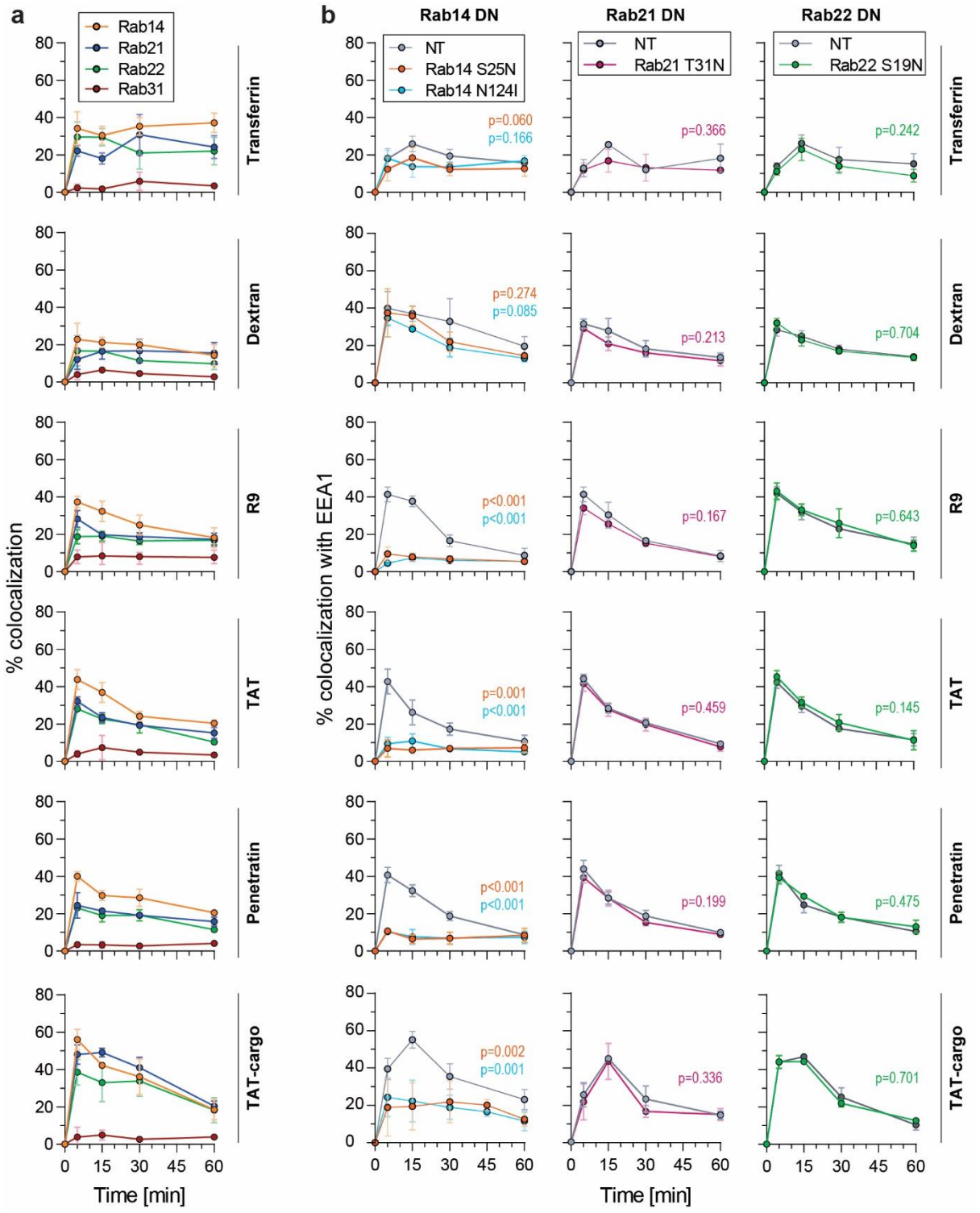

Supplementary Fig. 5: Rab14 dominant negative mutants block the maturation of CPP-containing endosomes.

a, Colocalization quantitation between the indicated endocytosed material and the indicated GFP-labeled Rab proteins ectopically expressed in HeLa KCNN4 knockout cells. The results correspond to mean ± SD of three independent experiments. **b,** Colocalization quantitation between the indicated endocytosed material and EEA1 in cells transfected with Rab14, Rab21 or Rab22 dominant negative constructs. The data correspond to the mean ± SD of three independent experiments. Statistical analysis was performed using ANOVA test with Dunett's correction, based on AUC values. The p-values correspond to the comparison between the cells within the same population transfected or not with the dominant negative constructs.

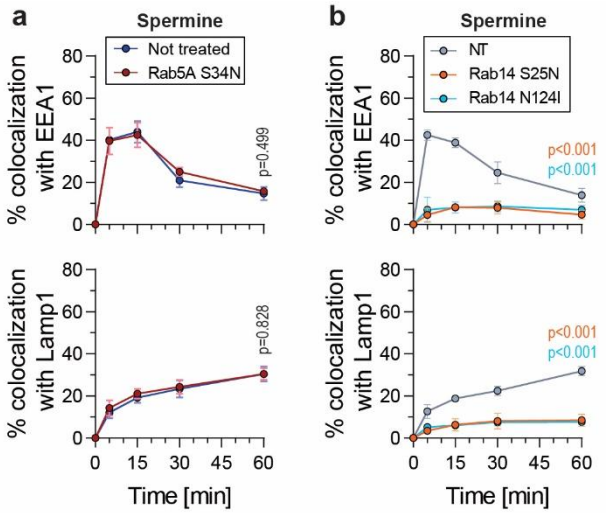

Supplementary Fig. 6: Spermine follows a Rab5-independent, Rab14-dependent endosomal maturation. **a,** Colocalization between 5 μM spermine with EEA1 (top) or Lamp1 (bottom) in the Rab5A dominant negative background. HeLa KCNN4 knockout cells were incubated for 5-minute pulse with endosomal cargo. The results correspond to mean ± SD of three independent experiments. Statistical analysis was performed using two-tailed t-test based on AUC values. The p-values correspond to the comparison between the cells within the same population transfected or not with the dominant negative constructs. **b,** Colocalization between 5 μM spermine with EEA1 (top) or Lamp1 (bottom) in HeLa KCNN4 knockout cells expressing Rab14 dominant negative mutants. The cells were exposed to the cargos during a 5-minute pulse. The results correspond to mean ± SD of three independent experiments. Statistical analysis was performed using ANOVA test with Dunett's correction, based on AUC values. The p-values correspond to the comparison between the cells within the same population transfected or not with the dominant negative constructs.

MATERIALS AND METHODS

Reagents

Live Hoechst 33342 (Sigma, CDS023389) was aliquoted and stored at -20°C. AlexaFluor488-, AlexaFluor568-, AlexaFluor647-labeled human transferrin was dissolved in PBS at 5 mg/ml and stored at 4°C (Thermo Fisher, T13342, T23365 and T23366). TMR-labelled 10,000 neutral dextran was dissolved in PBS at 10 mg/ml and stored at -20°C (Thermo Fisher, D1816). AlexaFluor647-labeled and biotinylated epidermal growth factor (EGF) was dissolved in water at 1 mg/ml, aliquoted and stored at -20°C (Thermo Fisher, E35351). EIPA (stock concentration 10 mM), IPA3 (stock concentration 5 mM), ML7 (stock concentration 10 mM), CytoD (stock concentration 1 mM), Jas (stock concentration 1 mM) a kind gift from Stefan Kunz laboratory, were dissolved in DMSO, aliquoted and stored at -20°C. LY294002 was dissolved in DMSO at 20 mg/ml, aliquoted and stored at -20°C (Sigma Aldrich, 440202). Wortmannin was aliquoted and stored at -20°C (Sigma Aldrich, W1344). Indole-3-acetic acid (IAA) (Sigma-Aldrich, I2886) was dissolved in ethanol, aliquoted and stored at -20°C. Doxycycline (Sigma-Aldrich, D3447) was dissolved in DMSO, aliquoted and stored at -20°C.

Antibodies

The mouse monoclonal anti-EEA1, stored at -20°C (BD Transduction Laboratories, 610457) and anti-Lamp1, stored at 4°C (BD Pharmingen, 555798) antibodies were used in immunofluorescence experiments. Donkey polyclonal anti-mouse Cy3 secondary antibody was aliquoted and stored at -20°C in glycerol (Jackson ImmunoResearch, 715-165-150). Phospho-AKT (Ser473) rabbit polyclonal antibody was stored at -20°C (Cell signaling, 92715) and was used for western blotting. Anti-Rab5C antiserum, which can recognize all three Rab5 isoforms[358], was stored at -20°C.

Cell lines

All cell lines were cultured in 5% CO_2 at 37°C. HeLa (ATCC: CCL-2) cells were cultured in RPMI media (Thermo Fisher, 61870044) supplemented with 10% heat-inactivated fetal bovine serum (FBS; Thermo Fisher, 10270-106). MDCK-II parental and knock-out cell lines[99] (available from RIKEN BioResource Research Center Cell Bank (https://cell.brc.riken.jp/en); RCB5099–RCB5148) were cultured in DMEM (Thermo Fisher, 10566016). MDCK-II Rab5 knock-out and degron-Rab5A-expressing cell line will be described elsewhere (Homma et al., manuscript in preparation).

Confocal microscopy

Confocal microscopy experiments were done on live cells. Cells were seeded onto glass bottom culture dishes (MatTek, corporation P35G-1.5-14-C) and treated as described in the Figures. For nuclear staining, 10 µg/ml live Hoechst 33342 (Molecular probes, H21492) was added in the culture medium

5 minutes before washing cells twice with media. After washing, cells were examined at the indicated time point with a plan Apochromat 63x oil immersion objective mounted on a Zeiss LSM 780 laser scanning fluorescence confocal microscope equipped with gallium arsenide phosphide detectors and three lasers (a 405 nm diode laser, a 458-476-488-514 nm argon laser, and a 561 nm diode-pumped solid-state laser). Cell images were acquired at a focal plane near the middle of the cell making sure that nuclei were visible. Experiments at 20°C were done using an incubation chamber set at 20°C, 5% CO_2 and visualized with a Zeiss LSM710 Quasar laser scanning fluorescence confocal microscope equipped with either Neofluar 63x, 1.2 numerical aperture (NA) or plan Neofluar 100x, 1.3 NA plan oil immersion objective (and the same lasers as above).

Colocalization

Colocalization assessment between endocytosed material and a given endosomal marker was performed on confocal images by visual assessment, switching back and forth between the color channels. The samples were randomized to blind the experimentators from the nature of the samples they were analyzing. The randomization script is available at https://github.com/BICC-UNIL-EPFL/randomizer. The visual quantitation was validated by Mander's coefficient calculation performed on the same samples using the JaCoP plugin in ImageJ. Examples of colocalization quantitation analysis is shown in Supplementary Fig. 1a.

Immunofluorescence

Immunofluorescence experiments for the localization of endogenous and ectopically expressed EEA1 and Lamp1 endosomal markers was performed as described[286]. Briefly, cells were plated on poly L-lysine-coated coverslips and fixed with 4% paraformaldehyde for 20 minutes at room temperature at the indicated time points after treatment. Following a 5-minute permeabilization at room temperature in PBS, 0.25% triton X100, the samples were blocked for 20 minutes at room temperature in PBS, 3% BSA. Incubation with primary antibodies was done for two hours at room temperature in PBS, 1% BSA. The cells were then incubated for 45 minutes at room temperature with Cy3-labelled secondary antibodies in the same buffers as above. Coverslips were finally incubated 5 minutes with PBS, 10 □g/ml Hoechst. Three PBS washes were done between each incubation steps. Coverslips were mounted in Fluoromount-G (cBiosience, 00-4958-02). Samples were visualized with a Zeiss LSM780 confocal microscope.

Transient transfection

Calcium phosphate based transfection of HeLa cells was performed as previously described [266]. Briefly, cells were plated overnight in DMEM (Invitrogen, 61965) medium supplemented with 10% heat-

inactivated FBS (Invitrogen, 10270-106), 2.5 µg of total plasmid DNA of interest was diluted in water, $CaCl_2$ was added and the mixture was incubated in presence of HEPES 2x for 60 seconds before adding the total mixture drop by drop to the cells. Media was changed 10 hours after.
Transient transfection in MDCK cells was done with Lipofectamin 2000 reagent according to supplier's instructions (Thermo Fisher, 11668030).

PI3-kinase inhibitors

For the colocalization experiments, cells ectopically expressing GFP-EEA1, were preincubated in the presence or in the absence of PI3K inhibitors 25 µM LY294002 or 10 µM wortmannin for 30 minutes, then Alexa548-transferrin or TMR-CPP were added to the cells for 5 minutes. Cells were washed on ice with RPMI, 10% FBS and incubated in same media in the presence of the inhibitors. Cells were visualized with LSM780 confocal microscope at the indicated time points. Colocalization between fluorescent cargo and EEA1 was visually quantitated. For western blotting experiments phosphorylated AKT was used as a proxy of PI3K activity. To stimulate phosphorylation, cells were incubated in serum-free medium for one hour. Medium was then changed to RPMI, 10% serum and cells were incubated for 20 minutes with 25 µM LY294002. Phosphorylated AKT was detected using rabbit anti-phosphoAKT antibody (Cell signaling, 92715).

Macropinocytosis inhibition

Cells ectopically expressing GFP-EEA1 were starved overnight to stimulate macropinocytosis. Media was then changed to RMPI containing 10% FBS and cells were preincubated for 30 minutes with the indicated macropinocytosis inhibitors (kind gift from Dr. Stephan Kunz lab). Cells were pulsed for 5 minutes with TexasRed-dextran or TMR-TAT-$RasGAP_{317-326}$, washed and visualized under confocal microscope in RPMI, 10% FBS in the presence of macropinocytosis inhibitors.

Plasmid constructs

The RFP-hRab5A.dn3 (#921) plasmid encoding RFP-labeled version of human Rab5A protein was from Addgene (14437). The mCh-hRab7A (#922) plasmid encoding mCherry-labeled version of human Rab7A protein was from Addgene (61804). GFP-hRab5A.dn3 (#966), GFP-hRab7A.dn3 (#968), GFP-DynI.dn3 (#963) plasmid encoding GFP-labeled versions of the indicated human proteins, as well as dominant negative isoforms of the following proteins GFP-hRab5A(S34N).dn3 (#961), GFP-Rab7A(T22N).dn3 (#969), GFP-DynI(K44A).dn3 (#964) were a kind gift from Stefan Kunz laboratory. mCh-hRab5(S34N) (#933), plasmid encoding a mCherry-labeled dominant negative mutant version of human Rab5A was from Addgene (35139). GFP-hRab5B.dn3 (#1008) plasmid encoding GFP-labeled wild-type version of human Rab5B isoform was from Addgene (61802). GFP-hRab5B(S34N) (#1067)

plasmid encoding GFP-labeled dominant negative mutant version of human Rab5B isoform was introduced to plasmid #1008 using Q5 Site-Directed Mutagenisis kit (NEB, E0554S) according to manufacturer's instructions using forward primer #1554 (AGTGGGAAAGaacAGCCTGGTATTAC) and reverse primer #1555 (GCAGATTCTCCCAGCAGG). GFP-Rab5C.dn3 (#1074) plasmid encoding GFP-labeled version of human Rab5C isoform was from Genescript (OHu09753C). CFP-hRab5C(S35N).dn3 (#1006) encoding Cerulean-labeled dominant negative mutant version of human Rab5C isoform was from Addgene (11504). GFP-hEEA1 (#970) and hLamp1-GFP.dn3 (#971) encoding GFP-labeled version of human EEA1 and Lamp1, respectively were from Addgene (42307 and 34831). BFP-EEA1 (#1009) plasmid was generated by subcloning GFP-hEEA1 (#970) into a BFP-hRab7A-Myc backbone (#1005, Addgene, 79803) through ligation of both plasmids after digestion with BamHI (NEB, R313614) and BspEI (NEB, R0540S). hLamp1-BFP (#1016) plasmid encoding BFP-labeled version of human Lamp1 protein was from Addgene (98828). GFP-hRab14.dn3 (#1017), GFP-hRab21.dn3 (#1023), GFP-hRab22.dn3 (#1018) and GFP-hRab31.dn3 (#1019) plasmids encoding GFP-labeled versions of the indicated human wild-type proteins were from Addgene (49549, 83421, 49600 and 49610, respectively). GFP-hRab14(S25N).dn3 (#1037) and GFP-hRab14(N124I).dn3 (#1038) plasmids encoding GFP-labeled versions of dominant negative Rab14 mutant were from Addgene (49594 and 49593). GFP-hRab21(T31N) (#1039) plasmid encoding GFP-labeled version of dominant negative Rab21 mutant was from Addgene (83423). GFP-hRab22(S19N) (#1068) was generated using Q5 Site-Directed Mutagenisis kit (NEB, E0554S) according to manufacturer's instructions with forward primer #1556 (TGTAGGTAAAaacAGTATTGTGTGGCGG) and reverse primer #1557 (CCTGTATCCCCGAGCAGA) on plasmid #1018 that encodes the wild-type isoform of human Rab22 protein.

Peptides

TAT-RasGAP$_{317-326}$ is a retro-inverso peptide (i.e. synthesized with D-amino-acids in the opposite direction compared to the natural sequence) labeled or not with FITC or TMR. The TAT moiety corresponds to amino-acids 48–57 of the HIV TAT protein (RRRQRRKKRG) and the RasGAP$_{317–326}$ moiety corresponds to amino-acids from 317 to 326 of the human RasGAP protein (DTRLNTVWMW). These two moieties are separated by two glycine linker residues in the TAT-Ras-GAP$_{317–326}$ peptide. FITC- or TMR-bound peptides without cargo: TAT, MAP (KLALKLALKALKAALKLA), Penetratin (RQIKWFQNRRMKWKK), Transportan (GWTLNSAGYLLGKINLKALAALAKKIL), R9 (RRRRRRRRR), were synthesized in retro-inverso conformation. FITC-labeled homeodomain: OTX2-HD (QRRERTTFTRAQLDVLEALFAKTRYPDIFMREEVALKINLPESRVQVWFKNRRAKCRQQQ). All peptides were synthesized by SBS Genetech, China and resuspended to 1 mM in water.

Polyamine labeling

Spermine fluorescent labeling with CF405M or CF594 dyes was performed using a Mix-n-Stain Small Ligand Labeling Kit (Biotium, 92362 and 92352, respectively) according to manufacturer's instructions. The labeling efficiency was assessed by reverse-phase HPLC at Protein and Peptide Chemistry Facility at University of Lausanne.

Statistical analysis

Statistical analysis was performed on non-normalized data, using GraphPad Prism 7. All measurements were from biological replicates. Unless otherwise stated, the vertical bars in the graph represent the standard deviation of mean from at least three independent experiments.

Code availability

Image randomization script can be found at: https://github.com/BICC-UNIL-EPFL/randomizer.

DISCUSSION AND PERSPECTIVES

In drug/therapeutic development, the most often asked questions are related to drug associated efficacy, toxicity and potential secondary effects. However, the main challenges start already at the stage of drug delivery. Efficient delivery of a drug is difficult to achieve as the cells are surrounded by a protective barrier, a plasma membrane. CPPs represent one of the solutions to promote intracellular delivery of a therapeutic compound.

CPPs can be hooked to a variety of bioactive cargos and are readily taken up by cells[1-16]. For this reason, CPPs and CPP-derived therapeutics are of interest in biological and medical studies. CPPs enter cell through two mutually non-exclusive mechanisms direct translocation and endocytosis, which were both addressed in this study.

1. Direct translocation

1.1 Cell-penetrating peptides

Our research through *in silico* and intracellular approaches showed that successful CPP direct translocation occurs through a combination of potassium ion movement outside of the cell, combined with a cationic CPP interaction at the cell membrane. This joint effect of the accumulation of positive charges on outer leaflet of the cell membrane leads to an important local decrease in the membrane potential that we refer to as megapolarization (-150 mV). These conditions are favorable to the formation of 2-nm wide water pores, which CPPs can then use to cross the cell membrane and access the cytosol.

Various other direct translocation mechanisms have been described (see Introduction section 3). The majority of existing models have been derived from studies using acellular approaches or analysis that was not or could not be done in live cells. For some proposed models, alternative interpretations have been proposed. For example, visualization of inverted micelle-, fusion pore-like structures with electron microscopy can potentially be interpreted as endocytic vesicles, associated to membrane ruffling[33,77,79,104]. Here, we have characterized the water pore formation conditions and their size through a combination of *in silico* and for the first time, intracellular approaches. Due to current technical limitations we cannot visualize such small, transient structures as water pores and some of the already available data could be compatible with several proposed models. This remains to be determined, however factors as the importance of initial electrostatic interactions between CPPs and cell membrane, as well as cellular membrane potential create a solid base for further research.

1.2 Homeoprotein internalization

One of the first characterized CPPs, Penetratin[359], is a sequence found in the homeodomain of the Antennapedia homeoprotein. Homeoproteins (HPs) are a class of transcription factors involved in

multiple biological processes, such as tissue patterning, axon guidance, cell migration during development, and neuroplasticity[324-327]. Additionally, HPs, such as Engrailed 2 and OTX2, exhibit therapeutic properties[328-333]. For example, OTX2, which regulates neuronal plasticity within the mouse visual cortex[332], provides neuronal protection against nerve crush and to NMDA (N-methyl-D-aspartic acid)-induced retinal ganglion cell death[333]. Another HP, Engrailed, has aging therapeutic potential in the context of Parkinson disease, where it protects mesencephalic dopaminergic neurons against stresses[328-331]. Early studies in the field revealed that the vast majority of HPs contain a conserved 60 amino-acids domain called the homeodomain (HD), originally described for its ability to regulate transcription[360] is in fact, responsible for the membrane translocation properties of HPs and by extension CPPs[19,324,326,361]. As HPs are also secreted from cells, they act as paracrine factors making their translocation properties necessary for their physiological activity[326]. A common feature of CPPs[1,4,10,11], HPs and HDs, is the presence of cationic residues, which facilitate the interaction of the protein with the negatively charged plasma membrane. HP cellular internalization may be modulated by the membrane lipid composition[362,363], interaction with GAGs[364], as well as temperature[327,365]. Additionally, the primary and secondary structures of the HDs[327,365,366] may play a role in HP cellular internalization. HPs with the estimated diameter of 5-nm (calculated with PepCalc) represent one of the largest molecules able to cross the cell membrane. Even though a number of studies have reported the ability of HPs to enter cells[19,326,327,362,363,365,367], how they do this mechanistically remains ill-defined. As, CPPs[1,3,4,8-12], HPs appear to enter cells through direct translocation and endocytosis[368], we therefore hypothesize that HP and CPP internalization may occur in a similar manner.

We propose that initial interactions between HPs (as seen previously for CPPs) and the plasma membrane are a critical step in their internalization process. This suggests that several parameters play an important role in this process: i) cell membrane composition, including the presence of cell surface negatively charged polysaccharides, as GAGs, ii) HP sequence composition more specifically the presence of arginine and tryptophane, as well as iii) ratio of HPs to membrane lipids. These can ensure initial HP binding to cell membrane, their positioning with regards to the cell membrane, as well as HP initial insertion into the cell membrane. Furthermore, based on our CPP research we hypothesize that the cell membrane potential is of crucial importance for water pore formation, therefore direct translocation of HPs into cells. The HP/lipid interactions may also facilitate the water pore formation, as it is dependent on lipid head group reorientation coupled to intrusion of a water column in the membrane bilayer. In our opinion efficient CPP/HP direct translocation can only occur in optimal combination of polysaccharides and lipids with the CPP/HP in addition to permissive membrane potential. However, the water pores that we have characterized in the presence of CPPs allow successful translocation of 2-nm molecules in diameter, the molecules of larger dimensions of up to 5-nm also enter cells through such water pores though with decreased efficiency. Would this HP-cell

membrane interaction lead to water pore formation even though HPs are larger in size than CPPs? Would polysaccharides stabilize the interaction between the HP and cell membrane to facilitate/trigger translocation? Can HP uptake be regulated through membrane potential? Are there tangible electrophysiological changes associated with single HP molecule translocation? What other factors are involved in CPP direct translocation that are not charge related? These are the open questions that remain to be addressed in future research.

2. Endocytosis

2.1 Cell-penetrating peptides

CPP endocytosis has been extensively studied over the years and CPPs were shown to enter cells through clathrin-mediated endocytosis, macropinocytosis, and CLIC/GEEC[153-155]. Many of the CPP endocytosis-related studies rely on the use of endocytic inhibitors, which at least in the case of CPPs do not yield reliable results (see Introduction section 4.1). In this study, by taking advantage of dominant negative versions of various Rab proteins, as well as knock out library of single and multiple Rab proteins, we demonstrated that cationic CPPs, including TAT, R9 and Penetratin enter cells through an unconventional endocytic route. In this newly described endocytic pathway, endosomal maturation occurs in Rab14-dependent and Rab5-, Rab7-independent manner. There are however, several indications in the literature alluding to the existence of Rab5-independent viral internalization[347-355] in mammalian cells and vacuole trafficking in yeast[345,346]. Furthermore, we determined that this mode of entry is not only used by synthetic peptides, but is also relevant for physiological molecules as HPs (regulators of transcription and development that possess a CPP-like fragment within their sequence responsible for their cellular internalization) and polyamines (small signaling molecules involved in a multitude of cellular processes).

There are however several outstanding questions that should be answered in future studies. How is Rab14 recruited to CPP-positive endosomes? What are the interacting partners of Rab14? How is EEA1 recruited to Rab14-positive endosomes? Which proteins in the Rab14-dependent endocytosis could replace the function/activity of Rab7? Does Rab14 play a primordial role in endocytosis? Is this pathway used by pathogens? Toxins? Other cargo?

2.2 Pathogens

The stereotypical steps of endosomal progression have been highjacked by viruses[154,301] and bacteria[369,370] to infect host cells and gain cytosolic access. Viral internalization occurs following interactions of viral attachment proteins displayed on virion particles with plasma membrane molecules, triggering viral particle endocytosis and vesicular transport of the pathogens via the endosomal route. Many viruses use the endosomal pH gradient as guidance cue to trigger membrane

penetration, which releases the viral genetic material into the cytosol by uncoating. Once viruses have escaped the endosomes, they can proceed with their replication within the cytosol for most RNA-viruses or by translocating to the nucleus for most DNA viruses and retroviruses (reviewed in[154,301]). Most viruses appear to be using either the classical clathrin-mediated pathway or macropinocytosis to overcome the barrier of the plasma membrane (reviewed in[154,301]). Regardless of the endocytic pathway used and early vesicle interactions, all known pathways appear to converge to Rab5-positive vesicles[153,154,301]. In the absence of Rab5, the number of maturing endocytic vesicles is decreased and endocytosis is halted[291]. Nevertheless, there are some viruses that use unconventional endocytosis, such as Herpes Simplex Virus 1[347], SARS[348], Lassa virus, the Amr53b and We54 strains of LCMV (lymphocytic choriomeningitis virus)[349-352], Lujo virus[353,354] and some influenza A strains[355] that use ill-defined shortcuts that possibly could skip the early Rab5-positive endosomes. The internalization of such viruses should be studied further at molecular level, as their endocytic uptake may be Rab14-dependent.

Two main mechanisms of bacteria endocytosis have been described: the zipper mechanism, which is clathrin- and actin-mediated, and the trigger mechanism that is related to macropinocytosis[370]. There are however bacterial endocytic entry routes that have not been characterized yet such as the one taken by *Bartonella*[370]. To replicate, many intracellular bacteria need to change the nature and the maturation potential of their endosomes, which are then called vacuoles rather than endosomes. Indeed, endosomal maturation, by progressively generating a highly acidic and proteolytic environment, might lead to bacteria destruction (although there are species that are remarkably resilient in such environment). Some intracellular bacteria also eventually need to escape the vacuoles to replicate. Different strategies are employed to reach these goals[371]. For example, *Legionella* block endosomal maturation by inhibiting the recruitment of the Rab5 effectors Rabaptin5 and EEA1 on early endosomes. *Legionella*, *Brucella* and *Waddlia* replicate in vacuoles that acquire endoplasmic reticulum markers such as protein disulfide isomerase, calnexin and calreticulin[372-374]. *Chlamydia trachomatis* colocalizes at time of replication in vacuoles containing Golgi-associated markers such as GM130 and golgin[375]. Other bacterial strains, such as *Listeria* and *Rickettsia*, use phospoholipase activities and take advantage of actin tails to gain cytosolic access (actin recruitment occurs through ActA and RickA protein in the case of *Listeria* and *Rickettsia* infection, respectively)[376,377]. Moreover, some intracellular bacteria such as *Mycobacteria* and *Parachlamydia* are able to resist lysosomal hydrolases and low pH[378,379]. There are however many aspects in the endosomal dynamics and modulation associated with bacterial infection that are still very poorly characterized at the molecular level and may be of interest in the context of Rab14-dependent, Rab5-independent endocytosis.

2.3 Toxins

Homeoproteins are just one example of natural CPPs, other molecules as toxins may carry CPP-like characteristics. Toxins are widely studied for their pharmacological potential as well as in the context of receptor manipulation. Unlike many toxins that require a receptor to exert their biological activity[380], scorpion toxin WaTx[381], spider toxin Latarcin 1[382] and rattlesnake venom protein crotamine[383] have been shown be able to rapidly penetrate into cell cytoplasm in a receptor-independent manner. Furthermore, there is a number of toxins of bacterial and plant origin have also been shown to take advantage of endocytosis to enter cells[384-393]. Toxins are able to modify the endocytic route to their advantage (for example anthrax) and can use several pathways in parallel (for example cholera toxin B). Even though originating from different species, these molecules carry a number of positive charges within their sequence, however they come predominantly from lysine residues, not arginine. It has been shown that peptides made of 9 lysines (K9) poorly enter cells and replacing arginine by lysine in Penetratin significantly diminishes its uptake[65,66]. Therefore, studying the mode of entry of these toxin molecules may reveal an additional factor that would allow their cellular penetration.

Table 1: List of toxins that possess cell-penetrating characteristics.

Molecule	Origin	Sequence	Positive charges
Crotamine	Rattlesnake venom	YKQCHKKGGHCFPKEKICLPPSSDFGKMDCRWRWKCCKKGS	11
WaTx	Scorpion toxin	ASPQQAKYCYEQCNVNKVPFDQCYQMCSPLERS	3
Latarcin 1 (ltc 1)	Spider venom	MKYFVVALALAVALVCIAESTAYDVNEELENELDDLSDAAWLAK AAEDLQALDDFEESEESRSMWSGMWRRKLKKLRNALKKKLKGEK	14
LDP (ltc 1 derived)	Spider venom	WRRKLKKLR	6

3. Biodistribution

Besides the efficiency of CPP cellular internalization in the context of fundamental and clinical research, CPP-derived therapeutic biodistribution to the targeted site of bioactivity plays a crucial role. Even though in preclinical studies many CPP-derived therapeutics had a desirable effect, post i.v. or i.p. injections they all appear to accumulate predominantly in liver, kidneys and spleen[179,184,394-398], then eliminated with urine. However, modified CPP-cargo complexes coupled with liposomes and in some cases with transferrin, display an increased uptake and more homogenous biodistribution[399,400]. Such liposome complexes, as well as cationic lipoplexes used for bioactive cargo delivery[217-219,401-403], may therefore enter cells in a manner other than CPP direct translocation or endocytosis. A more efficient biodistribution that reach more organs and not only liver and kidneys, would allow to decreases CPP-derived therapeutic dosage at injection. However, as many CPPs lack specificity and enter all cells

types, having an increased internalization in many tissues may lead to undesirable effects. Therefore, along with biodistribution, CPP target specificity would have to be improved when CPP-cargo complex is systemically injected.

On the other hand, this would not be an issue for local, topical CPP-derived therapeutic applications. This has been demonstrated with XG102 and AM111 compounds that are currently in phase III clinical trials, which are injected directly at the site of action eye and ear, respectively[1-3,15]. Similarly, local HP, OTX2, injections into the eye vitreous space promotes survival of retinal ganglion cells[333]. Therefore, perhaps local CPP-cargo complex applications may prove to be more efficient, specifically in situations where the application site is easily accessible and is limited by the organ itself.

Concluding remarks

Alongside with novel insights into direct translocation and endocytosis of CPP internalization, this study provides a solid base for further research in the context of other positively charged cargos, as HPs and polyamines, as well as pathogens.

LIST OF PUBLICATIONS

Trofimenko, E., Homma, Y., Fukuda, M., Widman, C. Identification of a new, Rab14-dependent, endo-lysosomal pathway. *Submitted to Nature Cell Biology* (**2021**).

Trofimenko, E., Grasso, G., Heulot, M., Chevalier, N., Deriu, M. A., Dubuis, G., Arribat, Y., Serulla, M., Michel, S., Vantomme, G., Ory, F., Puyal, J., Amati, F., Lüthi, A., Danani, A. & Widmann, C. Genetic, cellular and structural characterization of the membrane potential-dependent cell-penetrating peptide translocation pore. S*ubmitted to eLife* (**2021**).
Available at: https://doi.org/10.1101/2020.02.25.963017

Taylor, A., Barros, D., Gobet, N., Schuepback, T., Aeschbach, L., Rabdall, E. L., **Trofimenko, E.**, McAllister, B., Heuchan, E., Barszcz, P., Ciosi, M., Massey, T., Monckton, D., Jones, L., Xenarios, I. & Dion, V. Microhomology-mediated mechanisms generate frequent structural rearrangements and interruptions at expanded CAG/CTG disease loci. *Submitted* (**2021**).

Torriani, G., **Trofimenko, E.**, Mayor, J., Fedeli, C., Moreno, H., Michel, S., Heulot, M., Chevalier, N., Zimmer, G., Shrestha, N., Plattet, P., Engler, O., Rothenberger, S., Widmann, C. & Kunz, S. Identification of Clotrimazole Derivatives as Specific Inhibitors of Arenavirus Fusion. *J Virol* **93**, doi:10.1128/JVI.01744-18 (**2019**).
Available at: https://jvi.asm.org/content/93/6/e01744-18

Malbec, R., Chami, B., Aeschbach, L., Ruiz Buendia, G. A., Socol, M., Joseph, P., Leichle, T., **Trofimenko, E.**, Bancaud, A. & Dion, V. microLAS: Sizing of expanded trinucleotide repeats with femtomolar sensitivity in less than 5 minutes. *Sci Rep* **9**, 23, doi:10.1038/s41598-018-36632-5 (**2019**).
Available at: https://www.nature.com/articles/s41598-018-36632-5

Heulot, M., Jacquier, N., Aeby, S., Le Roy, D., Roger, T., **Trofimenko, E.**, Barras, D., Greub, G. & Widmann, C. The Anticancer Peptide TAT-RasGAP317-326 Exerts Broad Antimicrobial Activity. *Front Microbiol* **8**, 994, doi:10.3389/fmicb.2017.00994 (**2017**).
Available at: https://www.frontiersin.org/articles/10.3389/fmicb.2017.00994/full

Morales, M., Sentchilo, V., Bertelli, C., Komljenovic, A., Kryuchkova-Mostacci, N., Bourdilloud, A., Linke, B., Goesmann, A., Harshman, K., Segers, F., Delapierre, F., Fiorucci, D., Seppey, M., **Trofimenko, E.**, Berra, P., El Taher, A., Loiseau, C., Roggero, D., Sulfiotti, M., Etienne, A., Ruiz Buendia, G., Pillard, L., Escoriza, A., Moritz, R., Schneider, C., Alfonso, E., Ben Jeddou, F., Selmoni, O., Resch, G., Greub, G., Emery, O., Dubey, M., Pillonel, T., Robinson-Rechavi, M. & van der Meer, J. R. The Genome of the Toluene-Degrading Pseudomonas veronii Strain 1YdBTEX2 and Its Differential Gene Expression in Contaminated Sand. *PLoS One* 11, e0165850, doi:10.1371/journal.pone.0165850 (**2016**).
Available at: https://journals.plos.org/plosone/article?id=10.1371/journal.pone.0165850

REFERENCES

1 Guidotti, G., Brambilla, L. & Rossi, D. Cell-Penetrating Peptides: From Basic Research to Clinics. *Trends Pharmacol Sci* **38**, 406-424, doi:10.1016/j.tips.2017.01.003 (2017).

2 Guo, Z., Peng, H., Kang, J. & Sun, D. Cell-penetrating peptides: Possible transduction mechanisms and therapeutic applications. *Biomed Rep* **4**, 528-534, doi:10.3892/br.2016.639 (2016).

3 Vasconcelos, L., Parn, K. & Langel, U. Therapeutic potential of cell-penetrating peptides. *Ther Deliv* **4**, 573-591, doi:10.4155/tde.13.22 (2013).

4 Bechara, C. & Sagan, S. Cell-penetrating peptides: 20 years later, where do we stand? *FEBS Lett* **587**, 1693-1702, doi:10.1016/j.febslet.2013.04.031 (2013).

5 Ye, J., Liu, E., Yu, Z., Pei, X., Chen, S., Zhang, P., Shin, M. C., Gong, J., He, H. & Yang, V. C. CPP-Assisted Intracellular Drug Delivery, What Is Next? *Int J Mol Sci* **17**, doi:10.3390/ijms17111892 (2016).

6 Kauffman, W. B., Fuselier, T., He, J. & Wimley, W. C. Mechanism Matters: A Taxonomy of Cell Penetrating Peptides. *Trends Biochem Sci* **40**, 749-764, doi:10.1016/j.tibs.2015.10.004 (2015).

7 Maiolo, J. R., Ferrer, M. & Ottinger, E. A. Effects of cargo molecules on the cellular uptake of arginine-rich cell-penetrating peptides. *Biochim Biophys Acta* **1712**, 161-172, doi:10.1016/j.bbamem.2005.04.010 (2005).

8 Trabulo, S., Cardoso, A. L., Mano, M. & De Lima, M. C. Cell-Penetrating Peptides-Mechanisms of Cellular Uptake and Generation of Delivery Systems. *Pharmaceuticals (Basel)* **3**, 961-993, doi:10.3390/ph3040961 (2010).

9 Futaki, S., Hirose, H. & Nakase, I. Arginine-rich peptides: methods of translocation through biological membranes. *Curr Pharm Des* **19**, 2863-2868 (2013).

10 Jones, A. T. & Sayers, E. J. Cell entry of cell penetrating peptides: tales of tails wagging dogs. *J Control Release* **161**, 582-591, doi:10.1016/j.jconrel.2012.04.003 (2012).

11 Madani, F., Lindberg, S., Langel, U., Futaki, S. & Graslund, A. Mechanisms of cellular uptake of cell-penetrating peptides. *J Biophys* **2011**, 414729, doi:10.1155/2011/414729 (2011).

12 Koren, E. & Torchilin, V. P. Cell-penetrating peptides: breaking through to the other side. *Trends Mol Med* **18**, 385-393, doi:10.1016/j.molmed.2012.04.012 (2012).

13 Illien, F., Rodriguez, N., Amoura, M., Joliot, A., Pallerla, M., Cribier, S., Burlina, F. & Sagan, S. Quantitative fluorescence spectroscopy and flow cytometry analyses of cell-penetrating peptides internalization pathways: optimization, pitfalls, comparison with mass spectrometry quantification. *Sci Rep* **6**, 36938, doi:10.1038/srep36938 (2016).

14 Mueller, J., Kretzschmar, I., Volkmer, R. & Boisguerin, P. Comparison of cellular uptake using 22 CPPs in 4 different cell lines. *Bioconjug Chem* **19**, 2363-2374, doi:10.1021/bc800194e (2008).

15 Xie, J., Bi, Y., Zhang, H., Dong, S., Teng, L., Lee, R. J. & Yang, Z. Cell-Penetrating Peptides in Diagnosis and Treatment of Human Diseases: From Preclinical Research to Clinical Application. *Front Pharmacol* **11**, 697, doi:10.3389/fphar.2020.00697 (2020).

16 Ruseska, I. & Zimmer, A. Internalization mechanisms of cell-penetrating peptides. *Beilstein J Nanotechnol* **11**, 101-123, doi:10.3762/bjnano.11.10 (2020).

17 Frankel, A. D. & Pabo, C. O. Cellular uptake of the tat protein from human immunodeficiency virus. *Cell* **55**, 1189-1193 (1988).
18 Green, M. & Loewenstein, P. M. Autonomous functional domains of chemically synthesized human immunodeficiency virus tat trans-activator protein. *Cell* **55**, 1179-1188 (1988).
19 Joliot, A., Pernelle, C., Deagostini-Bazin, H. & Prochiantz, A. Antennapedia homeobox peptide regulates neural morphogenesis. *Proc Natl Acad Sci U S A* **88**, 1864-1868 (1991).
20 Oehlke, J., Scheller, A., Wiesner, B., Krause, E., Beyermann, M., Klauschenz, E., Melzig, M. & Bienert, M. Cellular uptake of an alpha-helical amphipathic model peptide with the potential to deliver polar compounds into the cell interior non-endocytically. *Biochim Biophys Acta* **1414**, 127-139 (1998).
21 Milletti, F. Cell-penetrating peptides: classes, origin, and current landscape. *Drug Discov Today* **17**, 850-860, doi:10.1016/j.drudis.2012.03.002 (2012).
22 Gao, C., Mao, S., Ditzel, H. J., Farnaes, L., Wirsching, P., Lerner, R. A. & Janda, K. D. A cell-penetrating peptide from a novel pVII-pIX phage-displayed random peptide library. *Bioorg Med Chem* **10**, 4057-4065 (2002).
23 Staecker, H., Jokovic, G., Karpishchenko, S., Kienle-Gogolok, A., Krzyzaniak, A., Lin, C. D., Navratil, P., Tzvetkov, V., Wright, N. & Meyer, T. Efficacy and Safety of AM-111 in the Treatment of Acute Unilateral Sudden Deafness-A Double-blind, Randomized, Placebo-controlled Phase 3 Study. *Otol Neurotol* **40**, 584-594, doi:10.1097/MAO.0000000000002229 (2019).
24 Chiquet, C., Aptel, F., Creuzot-Garcher, C., Berrod, J. P., Kodjikian, L., Massin, P., Deloche, C., Perino, J., Kirwan, B. A., de Brouwer, S., Combette, J. M. & Behar-Cohen, F. Postoperative Ocular Inflammation: A Single Subconjunctival Injection of XG-102 Compared to Dexamethasone Drops in a Randomized Trial. *Am J Ophthalmol* **174**, 76-84, doi:10.1016/j.ajo.2016.10.012 (2017).
25 Harayama, T. & Riezman, H. Understanding the diversity of membrane lipid composition. *Nature Reviews Molecular Cell Biology* **19**, 281-296, doi:10.1038/nrm.2017.138 (2018).
26 Sezgin, E., Levental, I., Mayor, S. & Eggeling, C. The mystery of membrane organization: composition, regulation and roles of lipid rafts. *Nature Reviews Molecular Cell Biology* **18**, 361-374, doi:10.1038/nrm.2017.16 (2017).
27 Ajit Varki, R. L. S., and Roland Schauer. *Essentials of Glycobiology*. Vol. Cold Spring Harbor Laboratory Press (2017).
28 Gandhi, N. S. & Mancera, R. L. The Structure of Glycosaminoglycans and their Interactions with Proteins. *Chemical Biology & Drug Design* **72**, 455-482, doi:10.1111/j.1747-0285.2008.00741.x (2008).
29 Iozzo, R. V. & Schaefer, L. Proteoglycan form and function: A comprehensive nomenclature of proteoglycans. *Matrix Biology* **42**, 11-55, doi:https://doi.org/10.1016/j.matbio.2015.02.003 (2015).
30 Poon, G. M. K. & Gariépy, J. Cell-surface proteoglycans as molecular portals for cationic peptide and polymer entry into cells. *Biochemical Society Transactions* **35**, 788-793, doi:10.1042/bst0350788 (2007).
31 Rostand, K. S. & Esko, J. D. Microbial adherence to and invasion through proteoglycans. *Infect Immun* **65**, 1-8 (1997).

32 Verdurmen, W. P., Thanos, M., Ruttekolk, I. R., Gulbins, E. & Brock, R. Cationic cell-penetrating peptides induce ceramide formation via acid sphingomyelinase: implications for uptake. *J Control Release* **147**, 171-179, doi:10.1016/j.jconrel.2010.06.030 (2010).

33 Hirose, H., Takeuchi, T., Osakada, H., Pujals, S., Katayama, S., Nakase, I., Kobayashi, S., Haraguchi, T. & Futaki, S. Transient focal membrane deformation induced by arginine-rich peptides leads to their direct penetration into cells. *Mol Ther* **20**, 984-993, doi:10.1038/mt.2011.313 (2012).

34 Melikov, K., Hara, A., Yamoah, K., Zaitseva, E., Zaitsev, E. & Chernomordik, L. V. Efficient entry of cell-penetrating peptide nona-arginine into adherent cells involves a transient increase in intracellular calcium. *Biochem J* **471**, 221-230, doi:10.1042/BJ20150272 (2015).

35 Bechara, C., Pallerla, M., Zaltsman, Y., Burlina, F., Alves, I. D., Lequin, O. & Sagan, S. Tryptophan within basic peptide sequences triggers glycosaminoglycan-dependent endocytosis. *The FASEB Journal* **27**, 738-749, doi:10.1096/fj.12-216176 (2013).

36 Illien, F., Rodriguez, N., Amoura, M., Joliot, A., Pallerla, M., Cribier, S., Burlina, F. & Sagan, S. Quantitative fluorescence spectroscopy and flow cytometry analyses of cell-penetrating peptides internalization pathways: optimization, pitfalls, comparison with mass spectrometry quantification. *Scientific Reports* **6**, 36938, doi:10.1038/srep36938 (2016).

37 Alves, I. D., Bechara, C., Walrant, A., Zaltsman, Y., Jiao, C.-Y. & Sagan, S. Relationships between Membrane Binding, Affinity and Cell Internalization Efficacy of a Cell-Penetrating Peptide: Penetratin as a Case Study. *PLOS ONE* **6**, e24096, doi:10.1371/journal.pone.0024096 (2011).

38 Gump, J. M., June, R. K. & Dowdy, S. F. Revised role of glycosaminoglycans in TAT protein transduction domain-mediated cellular transduction. *The Journal of biological chemistry* **285**, 1500-1507, doi:10.1074/jbc.M109.021964 (2010).

39 Ziegler, A. Thermodynamic studies and binding mechanisms of cell-penetrating peptides with lipids and glycosaminoglycans. *Advanced Drug Delivery Reviews* **60**, 580-597, doi:https://doi.org/10.1016/j.addr.2007.10.005 (2008).

40 Rullo, A., Qian, J. & Nitz, M. Peptide–glycosaminoglycan cluster formation involving cell penetrating peptides. *Biopolymers* **95**, 722-731, doi:10.1002/bip.21641 (2011).

41 Gonçalves, E., Kitas, E. & Seelig, J. Binding of Oligoarginine to Membrane Lipids and Heparan Sulfate: Structural and Thermodynamic Characterization of a Cell-Penetrating Peptide. *Biochemistry* **44**, 2692-2702, doi:10.1021/bi048046i (2005).

42 Rusnati, M., Tulipano, G., Spillmann, D., Tanghetti, E., Oreste, P., Zoppetti, G., Giacca, M. & Presta, M. Multiple Interactions of HIV-I Tat Protein with Size-defined Heparin Oligosaccharides. *Journal of Biological Chemistry* **274**, 28198-28205, doi:10.1074/jbc.274.40.28198 (1999).

43 Butterfield, K. C., Caplan, M. & Panitch, A. Identification and Sequence Composition Characterization of Chondroitin Sulfate-Binding Peptides through Peptide Array Screening. *Biochemistry* **49**, 1549-1555, doi:10.1021/bi9021044 (2010).

44 Åmand, H. L., Rydberg, H. A., Fornander, L. H., Lincoln, P., Nordén, B. & Esbjörner, E. K. Cell surface binding and uptake of arginine- and lysine-rich penetratin peptides in absence and presence of proteoglycans. *Biochimica et Biophysica Acta (BBA) - Biomembranes* **1818**, 2669-2678, doi:https://doi.org/10.1016/j.bbamem.2012.06.006 (2012).

45 Ghibaudi, E., Boscolo, B., Inserra, G., Laurenti, E., Traversa, S., Barbero, L. & Ferrari, R. P. The interaction of the cell-penetrating peptide penetratin with heparin, heparansulfates and phospholipid vesicles investigated by ESR spectroscopy. *Journal of Peptide Science* **11**, 401-409, doi:10.1002/psc.633 (2005).
46 Fuchs, S. M. & Raines, R. T. Pathway for polyarginine entry into mammalian cells. *Biochemistry* **43**, 2438-2444, doi:10.1021/bi035933x (2004).
47 Ziegler, A. & Seelig, J. Contributions of Glycosaminoglycan Binding and Clustering to the Biological Uptake of the Nonamphipathic Cell-Penetrating Peptide WR9. *Biochemistry* **50**, 4650-4664, doi:10.1021/bi1019429 (2011).
48 Ziegler, A. & Seelig, J. Interaction of the Protein Transduction Domain of HIV-1 TAT with Heparan Sulfate: Binding Mechanism and Thermodynamic Parameters. *Biophysical Journal* **86**, 254-263, doi:https://doi.org/10.1016/S0006-3495(04)74101-6 (2004).
49 Hakansson, S. & Caffrey, M. Structural and Dynamic Properties of the HIV-1 Tat Transduction Domain in the Free and Heparin-Bound States. *Biochemistry* **42**, 8999-9006, doi:10.1021/bi020715+ (2003).
50 Yang, S.-T., Zaitseva, E., Chernomordik, L. V. & Melikov, K. Cell-penetrating peptide induces leaky fusion of liposomes containing late endosome-specific anionic lipid. *Biophysical journal* **99**, 2525-2533, doi:10.1016/j.bpj.2010.08.029 (2010).
51 Wadia, J. S., Stan, R. V. & Dowdy, S. F. Transducible TAT-HA fusogenic peptide enhances escape of TAT-fusion proteins after lipid raft macropinocytosis. *Nat Med* **10**, 310-315, doi:10.1038/nm996 (2004).
52 Suzuki, T., Futaki, S., Niwa, M., Tanaka, S., Ueda, K. & Sugiura, Y. Possible Existence of Common Internalization Mechanisms among Arginine-rich Peptides. *Journal of Biological Chemistry* **277**, 2437-2443, doi:10.1074/jbc.M110017200 (2002).
53 Yang, H., Liu, S., Cai, H., Wan, L., Li, S., Li, Y., Cheng, J. & Lu, X. Chondroitin sulfate as a molecular portal that preferentially mediates the apoptotic killing of tumor cells by penetratin-directed mitochondria-disrupting peptides. *The Journal of biological chemistry* **285**, 25666-25676, doi:10.1074/jbc.M109.089417 (2010).
54 Tyagi, M., Rusnati, M., Presta, M. & Giacca, M. Internalization of HIV-1 Tat Requires Cell Surface Heparan Sulfate Proteoglycans. *Journal of Biological Chemistry* **276**, 3254-3261, doi:10.1074/jbc.M006701200 (2001).
55 Kaplan, I. M., Wadia, J. S. & Dowdy, S. F. Cationic TAT peptide transduction domain enters cells by macropinocytosis. *J Control Release* **102**, 247-253, doi:10.1016/j.jconrel.2004.10.018 (2005).
56 Ziegler, A., Nervi, P., Dürrenberger, M. & Seelig, J. The Cationic Cell-Penetrating Peptide CPPTAT Derived from the HIV-1 Protein TAT Is Rapidly Transported into Living Fibroblasts: Optical, Biophysical, and Metabolic Evidence. *Biochemistry* **44**, 138-148, doi:10.1021/bi0491604 (2005).
57 Marty, C., Meylan, C., Schott, H., Ballmer-Hofer, K. & Schwendener, R. A. Enhanced heparan sulfate proteoglycan-mediated uptake of cell-penetrating peptide-modified liposomes. *Cellular and Molecular Life Sciences CMLS* **61**, 1785-1794, doi:10.1007/s00018-004-4166-0 (2004).
58 Walrant, A., Correia, I., Jiao, C.-Y., Lequin, O., Bent, E. H., Goasdoué, N., Lacombe, C., Chassaing, G., Sagan, S. & Alves, I. D. Different membrane behaviour and cellular uptake of three basic arginine-rich peptides. *Biochimica et Biophysica Acta (BBA) -*

Biomembranes **1808**, 382-393, doi:https://doi.org/10.1016/j.bbamem.2010.09.009 (2011).

59 Kawamura, K. S., Sung, M., Bolewska-Pedyczak, E. & Gariépy, J. Probing the Impact of Valency on the Routing of Arginine-Rich Peptides into Eukaryotic Cells. *Biochemistry* **45**, 1116-1127, doi:10.1021/bi051338e (2006).

60 Jiao, C.-Y., Delaroche, D., Burlina, F., Alves, I. D., Chassaing, G. & Sagan, S. Translocation and endocytosis for cell-penetrating peptide internalization. *The Journal of biological chemistry* **284**, 33957-33965, doi:10.1074/jbc.M109.056309 (2009).

61 Nakase, I., Tadokoro, A., Kawabata, N., Takeuchi, T., Katoh, H., Hiramoto, K., Negishi, M., Nomizu, M., Sugiura, Y. & Futaki, S. Interaction of Arginine-Rich Peptides with Membrane-Associated Proteoglycans Is Crucial for Induction of Actin Organization and Macropinocytosis. *Biochemistry* **46**, 492-501, doi:10.1021/bi0612824 (2007).

62 Letoha, T., Keller-Pintér, A., Kusz, E., Kolozsi, C., Bozsó, Z., Tóth, G., Vizler, C., Oláh, Z. & Szilák, L. Cell-penetrating peptide exploited syndecans. *Biochimica et Biophysica Acta (BBA) - Biomembranes* **1798**, 2258-2265, doi:https://doi.org/10.1016/j.bbamem.2010.01.022 (2010).

63 Nakase, I., Niwa, M., Takeuchi, T., Sonomura, K., Kawabata, N., Koike, Y., Takehashi, M., Tanaka, S., Ueda, K., Simpson, J. C., Jones, A. T., Sugiura, Y. & Futaki, S. Cellular Uptake of Arginine-Rich Peptides: Roles for Macropinocytosis and Actin Rearrangement. *Molecular Therapy* **10**, 1011-1022, doi:https://doi.org/10.1016/j.ymthe.2004.08.010 (2004).

64 Imamura, J., Suzuki, Y., Gonda, K., Roy, C. N., Gatanaga, H., Ohuchi, N. & Higuchi, H. Single Particle Tracking Confirms That Multivalent Tat Protein Transduction Domain-induced Heparan Sulfate Proteoglycan Cross-linkage Activates Rac1 for Internalization. *Journal of Biological Chemistry* **286**, 10581-10592, doi:10.1074/jbc.M110.187450 (2011).

65 Mitchell, D. J., Kim, D. T., Steinman, L., Fathman, C. G. & Rothbard, J. B. Polyarginine enters cells more efficiently than other polycationic homopolymers. *J Pept Res* **56**, 318-325 (2000).

66 Amand, H. L., Rydberg, H. A., Fornander, L. H., Lincoln, P., Norden, B. & Esbjorner, E. K. Cell surface binding and uptake of arginine- and lysine-rich penetratin peptides in absence and presence of proteoglycans. *Biochim Biophys Acta* **1818**, 2669-2678, doi:10.1016/j.bbamem.2012.06.006 (2012).

67 Rothbard, J. B., Jessop, T. C., Lewis, R. S., Murray, B. A. & Wender, P. A. Role of Membrane Potential and Hydrogen Bonding in the Mechanism of Translocation of Guanidinium-Rich Peptides into Cells. *Journal of the American Chemical Society* **126**, 9506-9507, doi:10.1021/ja0482536 (2004).

68 Fromm, J. R., Hileman, R. E., Caldwell, E. E. O., Weiler, J. M. & Linhardt, R. J. Differences in the Interaction of Heparin with Arginine and Lysine and the Importance of these Basic Amino Acids in the Binding of Heparin to Acidic Fibroblast Growth Factor. *Archives of Biochemistry and Biophysics* **323**, 279-287, doi:https://doi.org/10.1006/abbi.1995.9963 (1995).

69 Armstrong, C. T., Mason, P. E., Anderson, J. L. & Dempsey, C. E. Arginine side chain interactions and the role of arginine as a gating charge carrier in voltage sensitive ion channels. *Sci Rep* **6**, 21759, doi:10.1038/srep21759 (2016).

70 Li, L., Vorobyov, I. & Allen, T. W. The different interactions of lysine and arginine side chains with lipid membranes. *J Phys Chem B* **117**, 11906-11920, doi:10.1021/jp405418y (2013).
71 Derossi, D., Joliot, A. H., Chassaing, G. & Prochiantz, A. The third helix of the Antennapedia homeodomain translocates through biological membranes. *The Journal of biological chemistry* **269**, 10444-10450 (1994).
72 Delaroche, D., Aussedat, B., Aubry, S., Chassaing, G., Burlina, F., Clodic, G., Bolbach, G., Lavielle, S. & Sagan, S. Tracking a New Cell-Penetrating (W/R) Nonapeptide, through an Enzyme-Stable Mass Spectrometry Reporter Tag. *Analytical Chemistry* **79**, 1932-1938, doi:10.1021/ac061108l (2007).
73 Walrant, A., Bauza, A., Girardet, C., Alves, I. D., Lecomte, S., Illien, F., Cardon, S., Chaianantakul, N., Pallerla, M., Burlina, F., Frontera, A. & Sagan, S. Ionpair-pi interactions favor cell penetration of arginine/tryptophan-rich cell-penetrating peptides. *Biochim Biophys Acta Biomembr* **1862**, 183098, doi:10.1016/j.bbamem.2019.183098 (2020).
74 Jobin, M. L., Blanchet, M., Henry, S., Chaignepain, S., Manigand, C., Castano, S., Lecomte, S., Burlina, F., Sagan, S. & Alves, I. D. The role of tryptophans on the cellular uptake and membrane interaction of arginine-rich cell penetrating peptides. *Biochim Biophys Acta* **1848**, 593-602, doi:10.1016/j.bbamem.2014.11.013 (2015).
75 MacCallum, J. L., Bennett, W. F. D. & Tieleman, D. P. Distribution of amino acids in a lipid bilayer from computer simulations. *Biophysical journal* **94**, 3393-3404, doi:10.1529/biophysj.107.112805 (2008).
76 Christiaens, B., Symoens, S., Vanderheyden, S., Engelborghs, Y., Joliot, A., Prochiantz, A., Vandekerckhove, J., Rosseneu, M. & Vanloo, B. Tryptophan fluorescence study of the interaction of penetratin peptides with model membranes. *European Journal of Biochemistry* **269**, 2918-2926, doi:10.1046/j.1432-1033.2002.02963.x (2002).
77 Derossi, D., Calvet, S., Trembleau, A., Brunissen, A., Chassaing, G. & Prochiantz, A. Cell internalization of the third helix of the Antennapedia homeodomain is receptor-independent. *J Biol Chem* **271**, 18188-18193, doi:10.1074/jbc.271.30.18188 (1996).
78 Berlose, J. P., Convert, O., Derossi, D., Brunissen, A. & Chassaing, G. Conformational and associative behaviours of the third helix of antennapedia homeodomain in membrane-mimetic environments. *Eur J Biochem* **242**, 372-386, doi:10.1111/j.1432-1033.1996.0372r.x (1996).
79 Afonin, S., Frey, A., Bayerl, S., Fischer, D., Wadhwani, P., Weinkauf, S. & Ulrich, A. S. The cell-penetrating peptide TAT(48-60) induces a non-lamellar phase in DMPC membranes. *Chemphyschem* **7**, 2134-2142, doi:10.1002/cphc.200600306 (2006).
80 Kawamoto, S., Takasu, M., Miyakawa, T., Morikawa, R., Oda, T., Futaki, S. & Nagao, H. Inverted micelle formation of cell-penetrating peptide studied by coarse-grained simulation: importance of attractive force between cell-penetrating peptides and lipid head group. *J Chem Phys* **134**, 095103, doi:10.1063/1.3555531 (2011).
81 Pouny, Y., Rapaport, D., Mor, A., Nicolas, P. & Shai, Y. Interaction of antimicrobial dermaseptin and its fluorescently labeled analogues with phospholipid membranes. *Biochemistry* **31**, 12416-12423, doi:10.1021/bi00164a017 (1992).
82 Thennarasu, S., Tan, A., Penumatchu, R., Shelburne, C. E., Heyl, D. L. & Ramamoorthy, A. Antimicrobial and membrane disrupting activities of a peptide derived from the human cathelicidin antimicrobial peptide LL37. *Biophys J* **98**, 248-257, doi:10.1016/j.bpj.2009.09.060 (2010).

83 Yang, L., Harroun, T. A., Weiss, T. M., Ding, L. & Huang, H. W. Barrel-stave model or toroidal model? A case study on melittin pores. *Biophys J* **81**, 1475-1485, doi:10.1016/S0006-3495(01)75802-X (2001).
84 Matsuzaki, K., Murase, O., Fujii, N. & Miyajima, K. An antimicrobial peptide, magainin 2, induced rapid flip-flop of phospholipids coupled with pore formation and peptide translocation. *Biochemistry* **35**, 11361-11368, doi:10.1021/bi960016v (1996).
85 Matsuzaki, K., Yoneyama, S., Murase, O. & Miyajima, K. Transbilayer transport of ions and lipids coupled with mastoparan X translocation. *Biochemistry* **35**, 8450-8456, doi:10.1021/bi960342a (1996).
86 Ludtke, S. J., He, K., Heller, W. T., Harroun, T. A., Yang, L. & Huang, H. W. Membrane pores induced by magainin. *Biochemistry* **35**, 13723-13728, doi:10.1021/bi9620621 (1996).
87 Herce, H. D., Garcia, A. E., Litt, J., Kane, R. S., Martin, P., Enrique, N., Rebolledo, A. & Milesi, V. Arginine-rich peptides destabilize the plasma membrane, consistent with a pore formation translocation mechanism of cell-penetrating peptides. *Biophys J* **97**, 1917-1925, doi:10.1016/j.bpj.2009.05.066 (2009).
88 Illya, G. & Deserno, M. Coarse-grained simulation studies of peptide-induced pore formation. *Biophys J* **95**, 4163-4173, doi:10.1529/biophysj.108.131300 (2008).
89 Alves, I. D., Goasdoue, N., Correia, I., Aubry, S., Galanth, C., Sagan, S., Lavielle, S. & Chassaing, G. Membrane interaction and perturbation mechanisms induced by two cationic cell penetrating peptides with distinct charge distribution. *Biochim Biophys Acta* **1780**, 948-959, doi:10.1016/j.bbagen.2008.04.004 (2008).
90 Herce, H. D. & Garcia, A. E. Molecular dynamics simulations suggest a mechanism for translocation of the HIV-1 TAT peptide across lipid membranes. *Proc Natl Acad Sci U S A* **104**, 20805-20810, doi:10.1073/pnas.0706574105 (2007).
91 Marrink, S. J., Corradi, V., Souza, P. C. T., Ingolfsson, H. I., Tieleman, D. P. & Sansom, M. S. P. Computational Modeling of Realistic Cell Membranes. *Chem Rev* **119**, 6184-6226, doi:10.1021/acs.chemrev.8b00460 (2019).
92 Marrink, S. J. & Tieleman, D. P. Perspective on the Martini model. *Chem Soc Rev* **42**, 6801-6822, doi:10.1039/c3cs60093a (2013).
93 Belitsky, J. M., Leslie, S. J., Arora, P. S., Beerman, T. A. & Dervan, P. B. Cellular uptake of N-methylpyrrole/N-methylimidazole polyamide-dye conjugates. *Bioorg Med Chem* **10**, 3313-3318, doi:10.1016/s0968-0896(02)00204-3 (2002).
94 Richard, J. P., Melikov, K., Vives, E., Ramos, C., Verbeure, B., Gait, M. J., Chernomordik, L. V. & Lebleu, B. Cell-penetrating peptides. A reevaluation of the mechanism of cellular uptake. *J Biol Chem* **278**, 585-590, doi:10.1074/jbc.M209548200 (2003).
95 Lundberg, M. & Johansson, M. Positively Charged DNA-Binding Proteins Cause Apparent Cell Membrane Translocation. *Biochemical and Biophysical Research Communications* **291**, 367-371, doi:https://doi.org/10.1006/bbrc.2002.6450 (2002).
96 Leifert, J. A., Harkins, S. & Whitton, J. L. Full-length proteins attached to the HIV tat protein transduction domain are neither transduced between cells, nor exhibit enhanced immunogenicity. *Gene Therapy* **9**, 1422-1428, doi:10.1038/sj.gt.3301819 (2002).
97 Futaki, S. & Nakase, I. Cell-Surface Interactions on Arginine-Rich Cell-Penetrating Peptides Allow for Multiplex Modes of Internalization. *Acc Chem Res* **50**, 2449-2456, doi:10.1021/acs.accounts.7b00221 (2017).

98 Kristensen, M., Birch, D. & Morck Nielsen, H. Applications and Challenges for Use of Cell-Penetrating Peptides as Delivery Vectors for Peptide and Protein Cargos. *Int J Mol Sci* **17**, doi:10.3390/ijms17020185 (2016).

99 Trofimenko, E., Grasso, G., Heulot, M., Chevalier, N., Deriu, M. A., Dubuis, G., Arribat, Y., Serulla, M., Michel, S., Vantomme, G., Ory, F., Dam, L. C., Puyal, J., Amati, F., Lüthi, A., Danani, A. & Widmann, C. Genetic, cellular and structural characterization of the membrane potential-dependent cell-penetrating peptide translocation pore *bioRxiv*, 2020.2002.2025.963017, doi:10.1101/2020.02.25.963017 (2021).

100 Wallbrecher, R., Ackels, T., Olea, R. A., Klein, M. J., Caillon, L., Schiller, J., Bovee-Geurts, P. H., van Kuppevelt, T. H., Ulrich, A. S., Spehr, M., Adjobo-Hermans, M. J. W. & Brock, R. Membrane permeation of arginine-rich cell-penetrating peptides independent of transmembrane potential as a function of lipid composition and membrane fluidity. *J Control Release* **256**, 68-78, doi:10.1016/j.jconrel.2017.04.013 (2017).

101 Herce, H. D., Garcia, A. E. & Cardoso, M. C. Fundamental molecular mechanism for the cellular uptake of guanidinium-rich molecules. *J Am Chem Soc* **136**, 17459-17467, doi:10.1021/ja507790z (2014).

102 Ziegler, A., Blatter, X. L., Seelig, A. & Seelig, J. Protein transduction domains of HIV-1 and SIV TAT interact with charged lipid vesicles. Binding mechanism and thermodynamic analysis. *Biochemistry* **42**, 9185-9194, doi:10.1021/bi0346805 (2003).

103 Thoren, P. E., Persson, D., Karlsson, M. & Norden, B. The antennapedia peptide penetratin translocates across lipid bilayers - the first direct observation. *FEBS Lett* **482**, 265-268, doi:10.1016/s0014-5793(00)02072-x (2000).

104 Allolio, C., Magarkar, A., Jurkiewicz, P., Baxova, K., Javanainen, M., Mason, P. E., Sachl, R., Cebecauer, M., Hof, M., Horinek, D., Heinz, V., Rachel, R., Ziegler, C. M., Schrofel, A. & Jungwirth, P. Arginine-rich cell-penetrating peptides induce membrane multilamellarity and subsequently enter via formation of a fusion pore. *Proc Natl Acad Sci U S A* **115**, 11923-11928, doi:10.1073/pnas.1811520115 (2018).

105 Ciobanasu, C., Siebrasse, J. P. & Kubitscheck, U. Cell-penetrating HIV1 TAT peptides can generate pores in model membranes. *Biophys J* **99**, 153-162, doi:10.1016/j.bpj.2010.03.065 (2010).

106 Potocky, T. B., Menon, A. K. & Gellman, S. H. Cytoplasmic and nuclear delivery of a TAT-derived peptide and a beta-peptide after endocytic uptake into HeLa cells. *J Biol Chem* **278**, 50188-50194, doi:10.1074/jbc.M308719200 (2003).

107 Drin, G., Cottin, S., Blanc, E., Rees, A. R. & Temsamani, J. Studies on the internalization mechanism of cationic cell-penetrating peptides. *J Biol Chem* **278**, 31192-31201, doi:10.1074/jbc.M303938200 (2003).

108 Melikov, K., Hara, A., Yamoah, K., Zaitseva, E., Zaitsev, E. & Chernomordik, L. V. Efficient entry of cell-penetrating peptide nona-arginine into adherent cells involves a transient increase in intracellular calcium. *The Biochemical journal* **471**, 221-230, doi:10.1042/BJ20150272 (2015).

109 Cheng, X., Zhang, X., Yu, L. & Xu, H. Calcium signaling in membrane repair. *Semin Cell Dev Biol* **45**, 24-31, doi:10.1016/j.semcdb.2015.10.031 (2015).

110 Almeida, P. F. & Pokorny, A. Mechanisms of antimicrobial, cytolytic, and cell-penetrating peptides: from kinetics to thermodynamics. *Biochemistry* **48**, 8083-8093, doi:10.1021/bi900914g (2009).

111 Duchardt, F., Fotin-Mleczek, M., Schwarz, H., Fischer, R. & Brock, R. A Comprehensive Model for the Cellular Uptake of Cationic Cell-penetrating Peptides. *Traffic* **8**, 848-866, doi:10.1111/j.1600-0854.2007.00572.x (2007).
112 Zhang, X., Jin, Y., Plummer, M. R., Pooyan, S., Gunaseelan, S. & Sinko, P. J. Endocytosis and membrane potential are required for HeLa cell uptake of R.I.-CKTat9, a retro-inverso Tat cell penetrating peptide. *Mol Pharm* **6**, 836-848, doi:10.1021/mp800121f (2009).
113 O'Connor, L. J., Nicholas, T. & Levin, R. M. Subcellular distribution of free fatty acids, phospholipids, and endogenous lipase activity of rabbit urinary bladder smooth muscle and mucosa. *Adv Exp Med Biol* **462**, 265-273, doi:10.1007/978-1-4615-4737-2_20 (1999).
114 Saitta, F., Motta, P., Barbiroli, A., Signorelli, M., La Rosa, C., Janaszewska, A., Klajnert-Maculewicz, B. & Fessas, D. Influence of Free Fatty Acids on Lipid Membrane-Nisin Interaction. *Langmuir* **36**, 13535-13544, doi:10.1021/acs.langmuir.0c02266 (2020).
115 Damaghi, M., Wojtkowiak, J. W. & Gillies, R. J. pH sensing and regulation in cancer. *Front Physiol* **4**, 370, doi:10.3389/fphys.2013.00370 (2013).
116 Via, M. A., Klug, J., Wilke, N., Mayorga, L. S. & Del Popolo, M. G. The interfacial electrostatic potential modulates the insertion of cell-penetrating peptides into lipid bilayers. *Phys Chem Chem Phys* **20**, 5180-5189, doi:10.1039/c7cp07243k (2018).
117 Lin, J. & Alexander-Katz, A. Cell membranes open "doors" for cationic nanoparticles/biomolecules: insights into uptake kinetics. *ACS Nano* **7**, 10799-10808, doi:10.1021/nn4040553 (2013).
118 Gao, X., Hong, S., Liu, Z., Yue, T., Dobnikar, J. & Zhang, X. Membrane potential drives direct translocation of cell-penetrating peptides. *Nanoscale* **11**, 1949-1958, doi:10.1039/c8nr10447f (2019).
119 Moghal, M. M. R., Islam, M. Z., Hossain, F., Saha, S. K. & Yamazaki, M. Role of Membrane Potential on Entry of Cell-Penetrating Peptide Transportan 10 into Single Vesicles. *Biophys J* **118**, 57-69, doi:10.1016/j.bpj.2019.11.012 (2020).
120 Futaki, S., Suzuki, T., Ohashi, W., Yagami, T., Tanaka, S., Ueda, K. & Sugiura, Y. Arginine-rich peptides. An abundant source of membrane-permeable peptides having potential as carriers for intracellular protein delivery. *J Biol Chem* **276**, 5836-5840, doi:10.1074/jbc.M007540200 (2001).
121 Deshayes, S., Plenat, T., Charnet, P., Divita, G., Molle, G. & Heitz, F. Formation of transmembrane ionic channels of primary amphipathic cell-penetrating peptides. Consequences on the mechanism of cell penetration. *Biochim Biophys Acta* **1758**, 1846-1851, doi:10.1016/j.bbamem.2006.08.010 (2006).
122 Bodor, N. & Buchwald, P. Recent advances in the brain targeting of neuropharmaceuticals by chemical delivery systems. *Adv Drug Deliv Rev* **36**, 229-254, doi:10.1016/s0169-409x(98)00090-8 (1999).
123 Polyakov, V., Sharma, V., Dahlheimer, J. L., Pica, C. M., Luker, G. D. & Piwnica-Worms, D. Novel Tat-peptide chelates for direct transduction of technetium-99m and rhenium into human cells for imaging and radiotherapy. *Bioconjug Chem* **11**, 762-771, doi:10.1021/bc000008y (2000).
124 Duchardt, F., Fotin-Mleczek, M., Schwarz, H., Fischer, R. & Brock, R. A comprehensive model for the cellular uptake of cationic cell-penetrating peptides. *Traffic* **8**, 848-866, doi:10.1111/j.1600-0854.2007.00572.x (2007).

125 He, L., Sayers, E. J., Watson, P. & Jones, A. T. Contrasting roles for actin in the cellular uptake of cell penetrating peptide conjugates. *Sci Rep* **8**, 7318, doi:10.1038/s41598-018-25600-8 (2018).
126 Al Soraj, M., He, L., Peynshaert, K., Cousaert, J., Vercauteren, D., Braeckmans, K., De Smedt, S. C. & Jones, A. T. siRNA and pharmacological inhibition of endocytic pathways to characterize the differential role of macropinocytosis and the actin cytoskeleton on cellular uptake of dextran and cationic cell penetrating peptides octaarginine (R8) and HIV-Tat. *J Control Release* **161**, 132-141, doi:10.1016/j.jconrel.2012.03.015 (2012).
127 Kawaguchi, Y., Takeuchi, T., Kuwata, K., Chiba, J., Hatanaka, Y., Nakase, I. & Futaki, S. Syndecan-4 Is a Receptor for Clathrin-Mediated Endocytosis of Arginine-Rich Cell-Penetrating Peptides. *Bioconjug Chem* **27**, 1119-1130, doi:10.1021/acs.bioconjchem.6b00082 (2016).
128 Mueller, J., Kretzschmar, I., Volkmer, R. & Boisguerin, P. Comparison of Cellular Uptake Using 22 CPPs in 4 Different Cell Lines. *Bioconjugate Chemistry* **19**, 2363-2374, doi:10.1021/bc800194e (2008).
129 Tanaka, G., Nakase, I., Fukuda, Y., Masuda, R., Oishi, S., Shimura, K., Kawaguchi, Y., Takatani-Nakase, T., Langel, U., Graslund, A., Okawa, K., Matsuoka, M., Fujii, N., Hatanaka, Y. & Futaki, S. CXCR4 stimulates macropinocytosis: implications for cellular uptake of arginine-rich cell-penetrating peptides and HIV. *Chem Biol* **19**, 1437-1446, doi:10.1016/j.chembiol.2012.09.011 (2012).
130 Nakase, I., Niwa, M., Takeuchi, T., Sonomura, K., Kawabata, N., Koike, Y., Takehashi, M., Tanaka, S., Ueda, K., Simpson, J. C., Jones, A. T., Sugiura, Y. & Futaki, S. Cellular uptake of arginine-rich peptides: roles for macropinocytosis and actin rearrangement. *Mol Ther* **10**, 1011-1022, doi:10.1016/j.ymthe.2004.08.010 (2004).
131 Richard, J. P., Melikov, K., Brooks, H., Prevot, P., Lebleu, B. & Chernomordik, L. V. Cellular uptake of unconjugated TAT peptide involves clathrin-dependent endocytosis and heparan sulfate receptors. *J Biol Chem* **280**, 15300-15306, doi:10.1074/jbc.M401604200 (2005).
132 Vives, E., Brodin, P. & Lebleu, B. A truncated HIV-1 Tat protein basic domain rapidly translocates through the plasma membrane and accumulates in the cell nucleus. *J Biol Chem* **272**, 16010-16017, doi:10.1074/jbc.272.25.16010 (1997).
133 Suzuki, T., Futaki, S., Niwa, M., Tanaka, S., Ueda, K. & Sugiura, Y. Possible existence of common internalization mechanisms among arginine-rich peptides. *J Biol Chem* **277**, 2437-2443, doi:10.1074/jbc.M110017200 (2002).
134 Ferrari, A., Pellegrini, V., Arcangeli, C., Fittipaldi, A., Giacca, M. & Beltram, F. Caveolae-mediated internalization of extracellular HIV-1 tat fusion proteins visualized in real time. *Mol Ther* **8**, 284-294, doi:10.1016/s1525-0016(03)00122-9 (2003).
135 Koivusalo, M., Welch, C., Hayashi, H., Scott, C. C., Kim, M., Alexander, T., Touret, N., Hahn, K. M. & Grinstein, S. Amiloride inhibits macropinocytosis by lowering submembranous pH and preventing Rac1 and Cdc42 signaling. *J Cell Biol* **188**, 547-563, doi:10.1083/jcb.200908086 (2010).
136 Wang, L. H., Rothberg, K. G. & Anderson, R. G. Mis-assembly of clathrin lattices on endosomes reveals a regulatory switch for coated pit formation. *J Cell Biol* **123**, 1107-1117, doi:10.1083/jcb.123.5.1107 (1993).
137 Deshayes, S., Konate, K., Dussot, M., Chavey, B., Vaissiere, A., Van, T. N. N., Aldrian, G., Padari, K., Pooga, M., Vives, E. & Boisguerin, P. Deciphering the internalization

mechanism of WRAP:siRNA nanoparticles. *Biochim Biophys Acta Biomembr* **1862**, 183252, doi:10.1016/j.bbamem.2020.183252 (2020).
138 Sampath, P. & Pollard, T. D. Effects of cytochalasin, phalloidin, and pH on the elongation of actin filaments. *Biochemistry* **30**, 1973-1980 (1991).
139 Fujimoto, L. M., Roth, R., Heuser, J. E. & Schmid, S. L. Actin Assembly Plays a Variable, but not Obligatory Role in Receptor-Mediated Endocytosis. *Traffic* **1**, 161-171, doi:10.1034/j.1600-0854.2000.010208.x (2000).
140 Hill, T. A., Gordon, C. P., McGeachie, A. B., Venn-Brown, B., Odell, L. R., Chau, N., Quan, A., Mariana, A., Sakoff, J. A., Chircop, M., Robinson, P. J. & McCluskey, A. Inhibition of dynamin mediated endocytosis by the dynoles--synthesis and functional activity of a family of indoles. *J Med Chem* **52**, 3762-3773, doi:10.1021/jm900036m (2009).
141 Appelbaum, J. S., LaRochelle, J. R., Smith, B. A., Balkin, D. M., Holub, J. M. & Schepartz, A. Arginine topology controls escape of minimally cationic proteins from early endosomes to the cytoplasm. *Chem Biol* **19**, 819-830, doi:10.1016/j.chembiol.2012.05.022 (2012).
142 Wei, H., Malcor, J. M. & Harper, M. T. Lipid rafts are essential for release of phosphatidylserine-exposing extracellular vesicles from platelets. *Sci Rep* **8**, 9987, doi:10.1038/s41598-018-28363-4 (2018).
143 Viaud, J. & Peterson, J. R. An allosteric kinase inhibitor binds the p21-activated kinase autoregulatory domain covalently. *Mol Cancer Ther* **8**, 2559-2565, doi:10.1158/1535-7163.MCT-09-0102 (2009).
144 Dharmawardhane, S., Schurmann, A., Sells, M. A., Chernoff, J., Schmid, S. L. & Bokoch, G. M. Regulation of macropinocytosis by p21-activated kinase-1. *Mol Biol Cell* **11**, 3341-3352, doi:10.1091/mbc.11.10.3341 (2000).
145 Mayor, S. & Pagano, R. E. Pathways of clathrin-independent endocytosis. *Nat Rev Mol Cell Biol* **8**, 603-612, doi:10.1038/nrm2216 (2007).
146 Liu, N. Q., Lossinsky, A. S., Popik, W., Li, X., Gujuluva, C., Kriederman, B., Roberts, J., Pushkarsky, T., Bukrinsky, M., Witte, M., Weinand, M. & Fiala, M. Human immunodeficiency virus type 1 enters brain microvascular endothelia by macropinocytosis dependent on lipid rafts and the mitogen-activated protein kinase signaling pathway. *J Virol* **76**, 6689-6700 (2002).
147 Rodal, S. K., Skretting, G., Garred, O., Vilhardt, F., van Deurs, B. & Sandvig, K. Extraction of cholesterol with methyl-beta-cyclodextrin perturbs formation of clathrin-coated endocytic vesicles. *Mol Biol Cell* **10**, 961-974, doi:10.1091/mbc.10.4.961 (1999).
148 Jones, S. W., Christison, R., Bundell, K., Voyce, C. J., Brockbank, S. M., Newham, P. & Lindsay, M. A. Characterisation of cell-penetrating peptide-mediated peptide delivery. *Br J Pharmacol* **145**, 1093-1102, doi:10.1038/sj.bjp.0706279 (2005).
149 Jin, M. & Snider, M. D. Role of microtubules in transferrin receptor transport from the cell surface to endosomes and the Golgi complex. *J Biol Chem* **268**, 18390-18397 (1993).
150 Bolard, J. How do the polyene macrolide antibiotics affect the cellular membrane properties? *Biochim Biophys Acta* **864**, 257-304, doi:10.1016/0304-4157(86)90002-x (1986).

151 Dutta, D., Williamson, C. D., Cole, N. B. & Donaldson, J. G. Pitstop 2 is a potent inhibitor of clathrin-independent endocytosis. *PLoS One* **7**, e45799, doi:10.1371/journal.pone.0045799 (2012).
152 Wymann, M. P., Bulgarelli-Leva, G., Zvelebil, M. J., Pirola, L., Vanhaesebroeck, B., Waterfield, M. D. & Panayotou, G. Wortmannin inactivates phosphoinositide 3-kinase by covalent modification of Lys-802, a residue involved in the phosphate transfer reaction. *Mol Cell Biol* **16**, 1722-1733, doi:10.1128/mcb.16.4.1722 (1996).
153 Johannes, L., Parton, R. G., Bassereau, P. & Mayor, S. Building endocytic pits without clathrin. *Nat Rev Mol Cell Biol* **16**, 311-321, doi:10.1038/nrm3968 (2015).
154 Mercer, J., Schelhaas, M. & Helenius, A. Virus entry by endocytosis. *Annu Rev Biochem* **79**, 803-833, doi:10.1146/annurev-biochem-060208-104626 (2010).
155 Kaksonen, M. & Roux, A. Mechanisms of clathrin-mediated endocytosis. *Nat Rev Mol Cell Biol* **19**, 313-326, doi:10.1038/nrm.2017.132 (2018).
156 Ter-Avetisyan, G., Tunnemann, G., Nowak, D., Nitschke, M., Herrmann, A., Drab, M. & Cardoso, M. C. Cell entry of arginine-rich peptides is independent of endocytosis. *J Biol Chem* **284**, 3370-3378, doi:10.1074/jbc.M805550200 (2009).
157 Scott, C. C., Vacca, F. & Gruenberg, J. Endosome maturation, transport and functions. *Semin Cell Dev Biol* **31**, 2-10, doi:10.1016/j.semcdb.2014.03.034 (2014).
158 Huotari, J. & Helenius, A. Endosome maturation. *EMBO J* **30**, 3481-3500, doi:10.1038/emboj.2011.286 (2011).
159 Naslavsky, N. & Caplan, S. The enigmatic endosome - sorting the ins and outs of endocytic trafficking. *J Cell Sci* **131**, doi:10.1242/jcs.216499 (2018).
160 Dunn, K. W., Kamocka, M. M. & McDonald, J. H. A practical guide to evaluating colocalization in biological microscopy. *Am J Physiol Cell Physiol* **300**, C723-742, doi:10.1152/ajpcell.00462.2010 (2011).
161 Walrant, A., Cardon, S., Burlina, F. & Sagan, S. Membrane Crossing and Membranotropic Activity of Cell-Penetrating Peptides: Dangerous Liaisons? *Accounts of Chemical Research* **50**, 2968-2975, doi:10.1021/acs.accounts.7b00455 (2017).
162 Fretz, M. M., Penning, N. A., Al-Taei, S., Futaki, S., Takeuchi, T., Nakase, I., Storm, G. & Jones, A. T. Temperature-, concentration- and cholesterol-dependent translocation of L- and D-octa-arginine across the plasma and nuclear membrane of CD34+ leukaemia cells. *The Biochemical journal* **403**, 335-342, doi:10.1042/BJ20061808 (2007).
163 Kosuge, M., Takeuchi, T., Nakase, I., Jones, A. T. & Futaki, S. Cellular Internalization and Distribution of Arginine-Rich Peptides as a Function of Extracellular Peptide Concentration, Serum, and Plasma Membrane Associated Proteoglycans. *Bioconjugate Chemistry* **19**, 656-664, doi:10.1021/bc700289w (2008).
164 Allolio, C., Magarkar, A., Jurkiewicz, P., Baxová, K., Javanainen, M., Mason, P. E., Šachl, R., Cebecauer, M., Hof, M., Horinek, D., Heinz, V., Rachel, R., Ziegler, C. M., Schröfel, A. & Jungwirth, P. Arginine-rich cell-penetrating peptides induce membrane multilamellarity and subsequently enter via formation of a fusion pore. *Proceedings of the National Academy of Sciences* **115**, 11923-11928, doi:10.1073/pnas.1811520115 (2018).
165 Hirose, H., Takeuchi, T., Osakada, H., Pujals, S., Katayama, S., Nakase, I., Kobayashi, S., Haraguchi, T. & Futaki, S. Transient Focal Membrane Deformation Induced by Arginine-rich Peptides Leads to Their Direct Penetration into Cells. *Molecular Therapy* **20**, 984-993, doi:https://doi.org/10.1038/mt.2011.313 (2012).

166 Trofimenko, E., Grasso, G., Heulot, M., Chevalier, N., Deriu, M. A., Dubuis, G., Arribat, Y., Serulla, M., Michel, S., Vantomme, G., Ory, F., Puyal, J., Amati, F., Lüthi, A., Danani, A. & Widmann, C. Potassium channels, megapolarization, and water pore formation are key determinants for cationic cell-penetrating peptide translocation into cells. *bioRxiv*, 2020.2002.2025.963017, doi:10.1101/2020.02.25.963017 (2020).
167 Trofimenko, E., Grasso, G., Heulot, M., Chevalier, N., Deriu, M. A., Dubuis, G., Arribat, Y., Serulla, M., Michel, S., Vantomme, G., Ory, F., Dam, L. C., Puyal, J., Amati, F., Lüthi, A., Danani, A. & Widmann, C. Genetic, cellular and structural characterization of the membrane potential-dependent cell-penetrating peptide translocation pore. *bioRxiv*, 2020.2002.2025.963017, doi:10.1101/2020.02.25.963017v2 (2021).
168 Loison, F., Nizard, P., Sourisseau, T., Le Goff, P., Debure, L., Le Drean, Y. & Michel, D. A ubiquitin-based assay for the cytosolic uptake of protein transduction domains. *Molecular Therapy* **11**, 205-214, doi:https://doi.org/10.1016/j.ymthe.2004.10.010 (2005).
169 Lee, Y.-J., Datta, S. & Pellois, J.-P. Real-Time Fluorescence Detection of Protein Transduction into Live Cells. *Journal of the American Chemical Society* **130**, 2398-2399, doi:10.1021/ja7102026 (2008).
170 Lee, Y.-J., Johnson, G., Peltier, G. C. & Pellois, J.-P. A HA2-Fusion tag limits the endosomal release of its protein cargo despite causing endosomal lysis. *Biochimica et Biophysica Acta (BBA) - General Subjects* **1810**, 752-758, doi:https://doi.org/10.1016/j.bbagen.2011.05.013 (2011).
171 Pan, C., Lu, B., Chen, H. & Bishop, C. E. Reprogramming human fibroblasts using HIV-1 TAT recombinant proteins OCT4, SOX2, KLF4 and c-MYC. *Molecular Biology Reports* **37**, 2117-2124, doi:10.1007/s11033-009-9680-6 (2010).
172 Henriques, S. T., Costa, J. & Castanho, M. A. Translocation of beta-galactosidase mediated by the cell-penetrating peptide pep-1 into lipid vesicles and human HeLa cells is driven by membrane electrostatic potential. *Biochemistry* **44**, 10189-10198, doi:10.1021/bi0502644 (2005).
173 Chaloin, L., De, E., Charnet, P., Molle, G. & Heitz, F. Ionic channels formed by a primary amphipathic peptide containing a signal peptide and a nuclear localization sequence. *Biochim Biophys Acta* **1375**, 52-60, doi:10.1016/s0005-2736(98)00139-4 (1998).
174 Torriani, G., Trofimenko, E., Mayor, J., Fedeli, C., Moreno, H., Michel, S., Heulot, M., Chevalier, N., Zimmer, G., Shrestha, N., Plattet, P., Engler, O., Rothenberger, S., Widmann, C. & Kunz, S. Identification of Clotrimazole Derivatives as Specific Inhibitors of Arenavirus Fusion. *J Virol* **93**, doi:10.1128/JVI.01744-18 (2019).
175 LeCher, J. C., Nowak, S. J. & McMurry, J. L. Breaking in and busting out: cell-penetrating peptides and the endosomal escape problem. *Biomol Concepts* **8**, 131-141, doi:10.1515/bmc-2017-0023 (2017).
176 Erazo-Oliveras, A., Muthukrishnan, N., Baker, R., Wang, T.-Y. & Pellois, J.-P. Improving the endosomal escape of cell-penetrating peptides and their cargos: strategies and challenges. *Pharmaceuticals (Basel)* **5**, 1177-1209, doi:10.3390/ph5111177 (2012).
177 Erazo-Oliveras, A., Najjar, K., Dayani, L., Wang, T.-Y., Johnson, G. A. & Pellois, J.-P. Protein delivery into live cells by incubation with an endosomolytic agent. *Nature Methods* **11**, 861, doi:10.1038/nmeth.2998
https://www.nature.com/articles/nmeth.2998#supplementary-information (2014).

178 Michod, D., Yang, J. Y., Chen, J., Bonny, C. & Widmann, C. A RasGAP-derived cell permeable peptide potently enhances genotoxin-induced cytotoxicity in tumor cells. *Oncogene* **23**, 8971-8978, doi:10.1038/sj.onc.1207999 (2004).
179 Michod, D., Annibaldi, A., Schaefer, S., Dapples, C., Rochat, B. & Widmann, C. Effect of RasGAP N2 fragment-derived peptide on tumor growth in mice. *J Natl Cancer Inst* **101**, 828-832, doi:10.1093/jnci/djp100 (2009).
180 Pittet, O., Petermann, D., Michod, D., Krueger, T., Cheng, C., Ris, H. B. & Widmann, C. Effect of the TAT-RasGAP(317-326) peptide on apoptosis of human malignant mesothelioma cells and fibroblasts exposed to meso-tetra-hydroxyphenyl-chlorin and light. *J Photochem Photobiol B* **88**, 29-35, doi:10.1016/j.jphotobiol.2007.04.009 (2007).
181 Tsoutsou, P., Annibaldi, A., Viertl, D., Ollivier, J., Buchegger, F., Vozenin, M. C., Bourhis, J., Widmann, C. & Matzinger, O. TAT-RasGAP317-326 Enhances Radiosensitivity of Human Carcinoma Cell Lines In Vitro and In Vivo through Promotion of Delayed Mitotic Cell Death. *Radiat Res* **187**, 562-569, doi:10.1667/RR14509.1 (2017).
182 Chevalier, N., Gross, N. & Widmann, C. Assessment of the chemosensitizing activity of TAT-RasGAP317-326 in childhood cancers. *PLoS One* **10**, e0120487, doi:10.1371/journal.pone.0120487 (2015).
183 Barras, D., Lorusso, G., Lhermitte, B., Viertl, D., Ruegg, C. & Widmann, C. Fragment N2, a caspase-3-generated RasGAP fragment, inhibits breast cancer metastatic progression. *Int J Cancer* **135**, 242-247, doi:10.1002/ijc.28674 (2014).
184 Heulot, M., Jacquier, N., Aeby, S., Le Roy, D., Roger, T., Trofimenko, E., Barras, D., Greub, G. & Widmann, C. The Anticancer Peptide TAT-RasGAP317-326 Exerts Broad Antimicrobial Activity. *Front Microbiol* **8**, 994, doi:10.3389/fmicb.2017.00994 (2017).
185 Heulot, M., Chevalier, N., Puyal, J., Margue, C., Michel, S., Kreis, S., Kulms, D., Barras, D., Nahimana, A. & Widmann, C. The TAT-RasGAP317-326 anti-cancer peptide can kill in a caspase-, apoptosis-, and necroptosis-independent manner. *Oncotarget* **7**, 64342-64359, doi:10.18632/oncotarget.11841 (2016).
186 Serulla, M., Ichim, G., Stojceski, F., Grasso, G., Afonin, S., Heulot, M., Schober, T., Roth, R., Godefroy, C., Milhiet, P. E., Das, K., Garcia-Saez, A. J., Danani, A. & Widmann, C. TAT-RasGAP317-326 kills cells by targeting inner-leaflet-enriched phospholipids. *Proc Natl Acad Sci U S A*, doi:10.1073/pnas.2014108117 (2020).
187 Zheng, Q., Jockusch, S., Zhou, Z. & Blanchard, S. C. The contribution of reactive oxygen species to the photobleaching of organic fluorophores. *Photochem Photobiol* **90**, 448-454, doi:10.1111/php.12204 (2014).
188 Ha, T. & Tinnefeld, P. Photophysics of fluorescent probes for single-molecule biophysics and super-resolution imaging. *Annu Rev Phys Chem* **63**, 595-617, doi:10.1146/annurev-physchem-032210-103340 (2012).
189 Dixit, R. & Cyr, R. Cell damage and reactive oxygen species production induced by fluorescence microscopy: effect on mitosis and guidelines for non-invasive fluorescence microscopy. *Plant J* **36**, 280-290 (2003).
190 Levitus, M. & Ranjit, S. Cyanine dyes in biophysical research: the photophysics of polymethine fluorescent dyes in biomolecular environments. *Q Rev Biophys* **44**, 123-151, doi:10.1017/S0033583510000247 (2011).

191 Suh, B. C. & Hille, B. PIP2 is a necessary cofactor for ion channel function: how and why? *Annu Rev Biophys* **37**, 175-195, doi:10.1146/annurev.biophys.37.032807.125859 (2008).
192 Shieh, C. C., Coghlan, M., Sullivan, J. P. & Gopalakrishnan, M. Potassium channels: molecular defects, diseases, and therapeutic opportunities. *Pharmacol Rev* **52**, 557-594 (2000).
193 Schroeder, B. C., Hechenberger, M., Weinreich, F., Kubisch, C. & Jentsch, T. J. KCNQ5, a novel potassium channel broadly expressed in brain, mediates M-type currents. *J Biol Chem* **275**, 24089-24095, doi:10.1074/jbc.M003245200 (2000).
194 Wulff, H., Miller, M. J., Hansel, W., Grissmer, S., Cahalan, M. D. & Chandy, K. G. Design of a potent and selective inhibitor of the intermediate-conductance Ca2+-activated K+ channel, IKCa1: a potential immunosuppressant. *Proc Natl Acad Sci U S A* **97**, 8151-8156 (2000).
195 Wulff, H., Gutman, G. A., Cahalan, M. D. & Chandy, K. G. Delineation of the clotrimazole/TRAM-34 binding site on the intermediate conductance calcium-activated potassium channel, IKCa1. *J Biol Chem* **276**, 32040-32045, doi:10.1074/jbc.M105231200 (2001).
196 Katayama, S., Nakase, I., Yano, Y., Murayama, T., Nakata, Y., Matsuzaki, K. & Futaki, S. Effects of pyrenebutyrate on the translocation of arginine-rich cell-penetrating peptides through artificial membranes: recruiting peptides to the membranes, dissipating liquid-ordered phases, and inducing curvature. *Biochim Biophys Acta* **1828**, 2134-2142, doi:10.1016/j.bbamem.2013.05.016 (2013).
197 Repnik, U., Borg Distefano, M., Speth, M. T., Ng, M. Y. W., Progida, C., Hoflack, B., Gruenberg, J. & Griffiths, G. L-leucyl-L-leucine methyl ester does not release cysteine cathepsins to the cytosol but inactivates them in transiently permeabilized lysosomes. *J Cell Sci* **130**, 3124-3140, doi:10.1242/jcs.204529 (2017).
198 Kang, S. H., Cho, M. J. & Kole, R. Up-regulation of luciferase gene expression with antisense oligonucleotides: implications and applications in functional assay development. *Biochemistry* **37**, 6235-6239, doi:10.1021/bi980300h (1998).
199 Abes, S., Turner, J. J., Ivanova, G. D., Owen, D., Williams, D., Arzumanov, A., Clair, P., Gait, M. J. & Lebleu, B. Efficient splicing correction by PNA conjugation to an R6-Penetratin delivery peptide. *Nucleic Acids Res* **35**, 4495-4502, doi:10.1093/nar/gkm418 (2007).
200 D'Astolfo, D. S., Pagliero, R. J., Pras, A., Karthaus, W. R., Clevers, H., Prasad, V., Lebbink, R. J., Rehmann, H. & Geijsen, N. Efficient intracellular delivery of native proteins. *Cell* **161**, 674-690, doi:10.1016/j.cell.2015.03.028 (2015).
201 Eisenman, G., Sandblom, J. & Neher, E. Interactions in cation permeation through the gramicidin channel. Cs, Rb, K, Na, Li, Tl, H, and effects of anion binding. *Biophys J* **22**, 307-340, doi:10.1016/S0006-3495(78)85491-5 (1978).
202 Kelkar, D. A. & Chattopadhyay, A. The gramicidin ion channel: a model membrane protein. *Biochim Biophys Acta* **1768**, 2011-2025, doi:10.1016/j.bbamem.2007.05.011 (2007).
203 Rimmele, T. S. & Chatton, J. Y. A novel optical intracellular imaging approach for potassium dynamics in astrocytes. *PLoS One* **9**, e109243, doi:10.1371/journal.pone.0109243 (2014).
204 Xue, M., Atallah, B. V. & Scanziani, M. Equalizing excitation-inhibition ratios across visual cortical neurons. *Nature* **511**, 596-600, doi:10.1038/nature13321 (2014).

205 Marrink, S. J., Risselada, H. J., Yefimov, S., Tieleman, D. P. & de Vries, A. H. The MARTINI force field: coarse grained model for biomolecular simulations. *J Phys Chem B* **111**, 7812-7824, doi:10.1021/jp071097f (2007).
206 Gurtovenko, A. A. & Vattulainen, I. Ion leakage through transient water pores in protein-free lipid membranes driven by transmembrane ionic charge imbalance. *Biophys J* **92**, 1878-1890, doi:10.1529/biophysj.106.094797 (2007).
207 Delemotte, L., Dehez, F., Treptow, W. & Tarek, M. Modeling membranes under a transmembrane potential. *J Phys Chem B* **112**, 5547-5550, doi:10.1021/jp710846y (2008).
208 Herrera, F. E. & Pantano, S. Salt induced asymmetry in membrane simulations by partial restriction of ionic motion. *J Chem Phys* **130**, 195105, doi:10.1063/1.3132705 (2009).
209 Yang, M. & Brackenbury, W. J. Membrane potential and cancer progression. *Front Physiol* **4**, 185, doi:10.3389/fphys.2013.00185 (2013).
210 Bowman, A. M., Nesin, O. M., Pakhomova, O. N. & Pakhomov, A. G. Analysis of plasma membrane integrity by fluorescent detection of Tl(+) uptake. *J Membr Biol* **236**, 15-26, doi:10.1007/s00232-010-9269-y (2010).
211 Thorne, R. G. & Nicholson, C. In vivo diffusion analysis with quantum dots and dextrans predicts the width of brain extracellular space. *Proc Natl Acad Sci U S A* **103**, 5567-5572, doi:10.1073/pnas.0509425103 (2006).
212 Rao, Y., Kwok, S. J., Lombardi, J., Turro, N. J. & Eisenthal, K. B. Label-free probe of HIV-1 TAT peptide binding to mimetic membranes. *Proc Natl Acad Sci U S A* **111**, 12684-12688, doi:10.1073/pnas.1411817111 (2014).
213 Grasso, G., Muscat, S., Rebella, M., Morbiducci, U., Audenino, A., Danani, A. & Deriu, M. A. Cell penetrating peptide modulation of membrane biomechanics by Molecular dynamics. *J Biomech* **73**, 137-144, doi:10.1016/j.jbiomech.2018.03.036 (2018).
214 Daoud, S. S. & Juliano, R. L. Reduced toxicity and enhanced antitumor effects in mice of the ionophoric drug valinomycin when incorporated in liposomes. *Cancer Res* **46**, 5518-5523 (1986).
215 Gad, S. C., Reilly, C., Siino, K., Gavigan, F. A. & Witz, G. Thirteen cationic ionophores: their acute toxicity, neurobehavioral and membrane effects. *Drug Chem Toxicol* **8**, 451-468, doi:10.3109/01480548509041069 (1985).
216 Waksman, S. A. Antibiotics and chemotherapy. *Calif Med* **78**, 417-423 (1953).
217 Bansal, K., Aqdas, M., Kumar, M., Bala, R., Singh, S., Agrewala, J. N., Katare, O. P., Sharma, R. K. & Wangoo, N. A Facile Approach for Synthesis and Intracellular Delivery of Size Tunable Cationic Peptide Functionalized Gold Nanohybrids in Cancer Cells. *Bioconjug Chem* **29**, 1102-1110, doi:10.1021/acs.bioconjchem.7b00772 (2018).
218 Khalil, I. A., Kimura, S., Sato, Y. & Harashima, H. Synergism between a cell penetrating peptide and a pH-sensitive cationic lipid in efficient gene delivery based on double-coated nanoparticles. *J Control Release* **275**, 107-116, doi:10.1016/j.jconrel.2018.02.016 (2018).
219 Wu, Y., Sun, J., Li, A. & Chen, D. The promoted delivery of RRM2 siRNA to vascular smooth muscle cells through liposome-polycation-DNA complex conjugated with cell penetrating peptides. *Biomed Pharmacother* **103**, 982-988, doi:10.1016/j.biopha.2018.03.068 (2018).

220 Jeong, C., Yoo, J., Lee, D. & Kim, Y. C. A branched TAT cell-penetrating peptide as a novel delivery carrier for the efficient gene transfection. *Biomater Res* **20**, 28, doi:10.1186/s40824-016-0076-0 (2016).
221 Kauffman, K. M., Hussain, F. A., Yang, J., Arevalo, P., Brown, J. M., Chang, W. K., VanInsberghe, D., Elsherbini, J., Sharma, R. S., Cutler, M. B., Kelly, L. & Polz, M. F. A major lineage of non-tailed dsDNA viruses as unrecognized killers of marine bacteria. *Nature* **554**, 118-122, doi:10.1038/nature25474 (2018).
222 Yin, H., Moulton, H. M., Betts, C., Seow, Y., Boutilier, J., Iverson, P. L. & Wood, M. J. A fusion peptide directs enhanced systemic dystrophin exon skipping and functional restoration in dystrophin-deficient mdx mice. *Hum Mol Genet* **18**, 4405-4414, doi:10.1093/hmg/ddp395 (2009).
223 Du, L., Kayali, R., Bertoni, C., Fike, F., Hu, H., Iversen, P. L. & Gatti, R. A. Arginine-rich cell-penetrating peptide dramatically enhances AMO-mediated ATM aberrant splicing correction and enables delivery to brain and cerebellum. *Hum Mol Genet* **20**, 3151-3160, doi:10.1093/hmg/ddr217 (2011).
224 Dixit, M. & Lazaridis, T. Free energy of hydrophilic and hydrophobic pores in lipid bilayers by free energy perturbation of a restraint. *J Chem Phys* **153**, 054101, doi:10.1063/5.0016682 (2020).
225 Ting, C. L., Awasthi, N., Muller, M. & Hub, J. S. Metastable Prepores in Tension-Free Lipid Bilayers. *Phys Rev Lett* **120**, 128103, doi:10.1103/PhysRevLett.120.128103 (2018).
226 Wassenaar, T. A., Ingolfsson, H. I., Bockmann, R. A., Tieleman, D. P. & Marrink, S. J. Computational Lipidomics with insane: A Versatile Tool for Generating Custom Membranes for Molecular Simulations. *J Chem Theory Comput* **11**, 2144-2155, doi:10.1021/acs.jctc.5b00209 (2015).
227 Marrink, S. J., de Vries, A. H. & Mark, A. E. Coarse Grained Model for Semiquantitative Lipid Simulations. *The Journal of Physical Chemistry B* **108**, 750-760, doi:10.1021/jp036508g (2004).
228 Yesylevskyy, S. O., Schafer, L. V., Sengupta, D. & Marrink, S. J. Polarizable water model for the coarse-grained MARTINI force field. *PLoS Comput Biol* **6**, e1000810, doi:10.1371/journal.pcbi.1000810 (2010).
229 Bussi, G., Donadio, D. & Parrinello, M. Canonical sampling through velocity rescaling. *J Chem Phys* **126**, 014101, doi:10.1063/1.2408420 (2007).
230 Berendsen, H. J. C., Postma, J.P.M, van Gunsteren, W.F., DiNola, A. and Haak, J.R.. Molecular dynamics with coupling to an external bath. *The Journal of Chemical Physics* **81**, 3684-3690 (1984).
231 Darden, T., York, D. & Pedersen, L. Particle mesh Ewald: An N ·log(N) method for Ewald sums in large systems. *J. Chem. Phys.* **98**, 10089-10092 (1993).
232 Laio, A. & Gervasio, F. L. Metadynamics: a method to simulate rare events and reconstruct the free energy in biophysics, chemistry and material science. *Reports on Progress in Physics* **71**, 126601, doi:10.1088/0034-4885/71/12/126601 (2008).
233 Barducci, A., Bonomi, M. & Parrinello, M. Metadynamics. *WIREs Computational Molecular Science* **1**, 826-843, doi:https://doi.org/10.1002/wcms.31 (2011).
234 Granata, D., Camilloni, C., Vendruscolo, M. & Laio, A. Characterization of the free-energy landscapes of proteins by NMR-guided metadynamics. *Proc Natl Acad Sci U S A* **110**, 6817-6822, doi:10.1073/pnas.1218350110 (2013).

235 Grasso, G., Morbiducci, U., Massai, D., Tuszynski, J. A., Danani, A. & Deriu, M. A. Destabilizing the AXH Tetramer by Mutations: Mechanisms and Potential Antiaggregation Strategies. *Biophys J* **114**, 323-330, doi:10.1016/j.bpj.2017.11.025 (2018).
236 Grasso, G., Deriu, M. A., Patrulea, V., Borchard, G., Moller, M. & Danani, A. Free energy landscape of siRNA-polycation complexation: Elucidating the effect of molecular geometry, polymer flexibility, and charge neutralization. *PLoS One* **12**, e0186816, doi:10.1371/journal.pone.0186816 (2017).
237 Deriu, M. A., Grasso, G., Tuszynski, J. A., Gallo, D., Morbiducci, U. & Danani, A. Josephin Domain Structural Conformations Explored by Metadynamics in Essential Coordinates. *PLoS Comput Biol* **12**, e1004699, doi:10.1371/journal.pcbi.1004699 (2016).
238 Abraham, M. J., Murtola, T., Schulz, R., Páll, S., Smith, J. C., Hess, B. & Lindahl, E. GROMACS: High performance molecular simulations through multi-level parallelism from laptops to supercomputers. *SoftwareX* **1-2**, 19-25, doi:https://doi.org/10.1016/j.softx.2015.06.001 (2015).
239 Tribello, G. A., Bonomi, M., Branduardi, D., Camilloni, C. & Bussi, G. PLUMED 2: New feathers for an old bird. *Computer Physics Communications* **185**, 604-613, doi:https://doi.org/10.1016/j.cpc.2013.09.018 (2014).
240 Bonomi, M., Barducci, A. & Parrinello, M. Reconstructing the equilibrium Boltzmann distribution from well-tempered metadynamics. *Journal of computational chemistry* **30**, 1615-1621, doi:10.1002/jcc.21305 (2009).
241 Tieleman, D. P. The molecular basis of electroporation. *BMC Biochem* **5**, 10, doi:10.1186/1471-2091-5-10 (2004).
242 Gurtovenko, A. A. & Lyulina, A. S. Electroporation of asymmetric phospholipid membranes. *J Phys Chem B* **118**, 9909-9918, doi:10.1021/jp5028355 (2014).
243 Böckmann, R. A., de Groot, B. L., Kakorin, S., Neumann, E. & Grubmüller, H. Kinetics, Statistics, and Energetics of Lipid Membrane Electroporation Studied by Molecular Dynamics Simulations. *Biophysical Journal* **95**, 1837-1850, doi:https://doi.org/10.1529/biophysj.108.129437 (2008).
244 Fernandez, M. L., Marshall, G., Sagues, F. & Reigada, R. Structural and kinetic molecular dynamics study of electroporation in cholesterol-containing bilayers. *J Phys Chem B* **114**, 6855-6865, doi:10.1021/jp911605b (2010).
245 Ziegler, M. J. & Vernier, P. T. Interface water dynamics and porating electric fields for phospholipid bilayers. *J Phys Chem B* **112**, 13588-13596, doi:10.1021/jp8027726 (2008).
246 Kotnik, T., Rems, L., Tarek, M. & Miklavcic, D. Membrane Electroporation and Electropermeabilization: Mechanisms and Models. *Annu Rev Biophys* **48**, 63-91, doi:10.1146/annurev-biophys-052118-115451 (2019).
247 Gumbart, J., Khalili-Araghi, F., Sotomayor, M. & Roux, B. Constant electric field simulations of the membrane potential illustrated with simple systems. *Biochim Biophys Acta* **1818**, 294-302, doi:10.1016/j.bbamem.2011.09.030 (2012).
248 Kirsch, S. A. & Bockmann, R. A. Membrane pore formation in atomistic and coarse-grained simulations. *Biochim Biophys Acta* **1858**, 2266-2277, doi:10.1016/j.bbamem.2015.12.031 (2016).

249 Qi, Y., Ingolfsson, H. I., Cheng, X., Lee, J., Marrink, S. J. & Im, W. CHARMM-GUI Martini Maker for Coarse-Grained Simulations with the Martini Force Field. *J Chem Theory Comput* **11**, 4486-4494, doi:10.1021/acs.jctc.5b00513 (2015).
250 Jo, S., Kim, T., Iyer, V. G. & Im, W. CHARMM-GUI: a web-based graphical user interface for CHARMM. *Journal of computational chemistry* **29**, 1859-1865, doi:10.1002/jcc.20945 (2008).
251 Ingolfsson, H. I., Melo, M. N., van Eerden, F. J., Arnarez, C., Lopez, C. A., Wassenaar, T. A., Periole, X., de Vries, A. H., Tieleman, D. P. & Marrink, S. J. Lipid organization of the plasma membrane. *J Am Chem Soc* **136**, 14554-14559, doi:10.1021/ja507832e (2014).
252 Periole, X., Cavalli, M., Marrink, S. J. & Ceruso, M. A. Combining an Elastic Network With a Coarse-Grained Molecular Force Field: Structure, Dynamics, and Intermolecular Recognition. *J Chem Theory Comput* **5**, 2531-2543, doi:10.1021/ct9002114 (2009).
253 Humphrey, W., Dalke, A. & Schulten, K. VMD: visual molecular dynamics. *J Mol Graph* **14**, 33-38, 27-38 (1996).
254 Vaslin, A., Puyal, J., Borsello, T. & Clarke, P. G. Excitotoxicity-related endocytosis in cortical neurons. *J Neurochem* **102**, 789-800, doi:10.1111/j.1471-4159.2007.04564.x (2007).
255 Krasznai, Z., Marian, T., Balkay, L., Emri, M. & Tron, L. Flow cytometric determination of absolute membrane potential of cells. *J Photochem Photobiol B* **28**, 93-99 (1995).
256 Klapperstuck, T., Glanz, D., Klapperstuck, M. & Wohlrab, J. Methodological aspects of measuring absolute values of membrane potential in human cells by flow cytometry. *Cytometry A* **75**, 593-608, doi:10.1002/cyto.a.20735 (2009).
257 Cueni, L., Canepari, M., Lujan, R., Emmenegger, Y., Watanabe, M., Bond, C. T., Franken, P., Adelman, J. P. & Luthi, A. T-type Ca2+ channels, SK2 channels and SERCAs gate sleep-related oscillations in thalamic dendrites. *Nat Neurosci* **11**, 683-692, doi:10.1038/nn.2124 (2008).
258 Adams, D. S. & Levin, M. Measuring resting membrane potential using the fluorescent voltage reporters DiBAC4(3) and CC2-DMPE. *Cold Spring Harb Protoc* **2012**, 459-464, doi:10.1101/pdb.prot067702 (2012).
259 Lamiable, A., Thevenet, P., Rey, J., Vavrusa, M., Derreumaux, P. & Tuffery, P. PEP-FOLD3: faster de novo structure prediction for linear peptides in solution and in complex. *Nucleic Acids Res* **44**, W449-454, doi:10.1093/nar/gkw329 (2016).
260 Grasso, G., Deriu, M. A., Prat, M., Rimondini, L., Verne, E., Follenzi, A. & Danani, A. Cell Penetrating Peptide Adsorption on Magnetite and Silica Surfaces: A Computational Investigation. *J Phys Chem B* **119**, 8239-8246, doi:10.1021/jp512782e (2015).
261 Barducci, A., Bussi, G. & Parrinello, M. Well-tempered metadynamics: a smoothly converging and tunable free-energy method. *Phys Rev Lett* **100**, 020603, doi:10.1103/PhysRevLett.100.020603 (2008).
262 Tiwary, P. & Parrinello, M. A time-independent free energy estimator for metadynamics. *J Phys Chem B* **119**, 736-742, doi:10.1021/jp504920s (2015).
263 Baker, N. A. Poisson-Boltzmann methods for biomolecular electrostatics. *Methods Enzymol* **383**, 94-118, doi:10.1016/s0076-6879(04)83005-2 (2004).

264 Monticelli, L., Kandasamy, S. K., Periole, X., Larson, R. G., Tieleman, D. P. & Marrink, S. J. The MARTINI Coarse-Grained Force Field: Extension to Proteins. *J Chem Theory Comput* **4**, 819-834, doi:10.1021/ct700324x (2008).
265 Parrinello, M. a. R., A. Polymorphic Transitions in Single Crystals: A New Molecular Dynamics Method. *Journal of Applied Physics* **52**, 7182-7190, doi:https://doi.org/10.1063/1.328693 (1981).
266 Jordan, M., Schallhorn, A. & Wurm, F. M. Transfecting mammalian cells: optimization of critical parameters affecting calcium-phosphate precipitate formation. *Nucleic Acids Res* **24**, 596-601 (1996).
267 Schmid, S. L., Sorkin, A. & Zerial, M. Endocytosis: Past, present, and future. *Cold Spring Harb Perspect Biol* **6**, a022509, doi:10.1101/cshperspect.a022509 (2014).
268 Thottacherry, J. J., Sathe, M., Prabhakara, C. & Mayor, S. Spoiled for Choice: Diverse Endocytic Pathways Function at the Cell Surface. *Annu Rev Cell Dev Biol* **35**, 55-84, doi:10.1146/annurev-cellbio-100617-062710 (2019).
269 Takei, K. & Haucke, V. Clathrin-mediated endocytosis: membrane factors pull the trigger. *Trends Cell Biol* **11**, 385-391, doi:10.1016/s0962-8924(01)02082-7 (2001).
270 Cocucci, E., Aguet, F., Boulant, S. & Kirchhausen, T. The first five seconds in the life of a clathrin-coated pit. *Cell* **150**, 495-507, doi:10.1016/j.cell.2012.05.047 (2012).
271 Chen, Z. & Schmid, S. L. Evolving models for assembling and shaping clathrin-coated pits. *J Cell Biol* **219**, doi:10.1083/jcb.202005126 (2020).
272 Gautreau, A., Oguievetskaia, K. & Ungermann, C. Function and regulation of the endosomal fusion and fission machineries. *Cold Spring Harb Perspect Biol* **6**, doi:10.1101/cshperspect.a016832 (2014).
273 Murray, D. H., Jahnel, M., Lauer, J., Avellaneda, M. J., Brouilly, N., Cezanne, A., Morales-Navarrete, H., Perini, E. D., Ferguson, C., Lupas, A. N., Kalaidzidis, Y., Parton, R. G., Grill, S. W. & Zerial, M. An endosomal tether undergoes an entropic collapse to bring vesicles together. *Nature* **537**, 107-111, doi:10.1038/nature19326 (2016).
274 Jaber, N., Mohd-Naim, N., Wang, Z., DeLeon, J. L., Kim, S., Zhong, H., Sheshadri, N., Dou, Z., Edinger, A. L., Du, G., Braga, V. M. & Zong, W. X. Vps34 regulates Rab7 and late endocytic trafficking through recruitment of the GTPase-activating protein Armus. *J Cell Sci* **129**, 4424-4435, doi:10.1242/jcs.192260 (2016).
275 Langemeyer, L., Frohlich, F. & Ungermann, C. Rab GTPase Function in Endosome and Lysosome Biogenesis. *Trends Cell Biol* **28**, 957-970, doi:10.1016/j.tcb.2018.06.007 (2018).
276 Raagel, H., Saalik, P. & Pooga, M. Peptide-mediated protein delivery-which pathways are penetrable? *Biochim Biophys Acta* **1798**, 2240-2248, doi:10.1016/j.bbamem.2010.02.013 (2010).
277 Cleal, K., He, L., Watson, P. D. & Jones, A. T. Endocytosis, intracellular traffic and fate of cell penetrating peptide based conjugates and nanoparticles. *Curr Pharm Des* **19**, 2878-2894, doi:10.2174/13816128113199990297 (2013).
278 Torriani, G., Trofimenko, E., Mayor, J., Fedeli, C., Moreno, H., Michel, S., Heulot, M., Chevalier, N., Zimmer, G., Shrestha, N., Plattet, P., Engler, O., Rothenberger, S., Widmann, C. & Kunz, S. Identification of clotrimazole-derivatives as specific inhibitors of Arenavirus fusion. *J Virol*, doi:10.1128/JVI.01744-18 (2019).
279 Annibaldi, A., Dousse, A., Martin, S., Tazi, J. & Widmann, C. Revisiting G3BP1 as a RasGAP Binding Protein: Sensitization of Tumor Cells to Chemotherapy by the RasGAP 317-326 Sequence Does Not Involve G3BP1. *PLoS One* **6**, doi:ARTN e29024

DOI 10.1371/journal.pone.0029024 (2011).
280 Barras, D., Lorusso, G., Ruegg, C. & Widmann, C. Inhibition of cell migration and invasion mediated by the TAT-RasGAP317-326 peptide requires the DLC1 tumor suppressor. *Oncogene* **33**, 5163-5172, doi:10.1038/onc.2013.465 (2014).
281 McLAUCHLAN, H., ELLIOTT, M. & COHEN, P. The specificities of protein kinase inhibitors: an update. *Biochemical Journal* **371**, 199-204, doi:10.1042/bj20021535 (2003).
282 Araki, N., Hatae, T., Furukawa, A. & Swanson, J. A. Phosphoinositide-3-kinase-independent contractile activities associated with Fcγ-receptor-mediated phagocytosis and macropinocytosis in macrophages. *Journal of Cell Science* **116**, 247-257, doi:10.1242/jcs.00235 (2003).
283 Bubb, M. R., Senderowicz, A. M., Sausville, E. A., Duncan, K. L. & Korn, E. D. Jasplakinolide, a cytotoxic natural product, induces actin polymerization and competitively inhibits the binding of phalloidin to F-actin. *J Biol Chem* **269**, 14869-14871 (1994).
284 Wenk, M. R. & De Camilli, P. Protein-lipid interactions and phosphoinositide metabolism in membrane traffic: insights from vesicle recycling in nerve terminals. *Proc Natl Acad Sci U S A* **101**, 8262-8269, doi:10.1073/pnas.0401874101 (2004).
285 Campa, C. C., Franco, I. & Hirsch, E. PI3K-C2alpha: One enzyme for two products coupling vesicle trafficking and signal transduction. *FEBS Lett* **589**, 1552-1558, doi:10.1016/j.febslet.2015.05.001 (2015).
286 Bissig, C., Johnson, S. & Gruenberg, J. Studying lipids involved in the endosomal pathway. *Methods Cell Biol* **108**, 19-46, doi:10.1016/B978-0-12-386487-1.00002-X (2012).
287 Miaczynska, M. & Zerial, M. Mosaic organization of the endocytic pathway. *Exp Cell Res* **272**, 8-14, doi:10.1006/excr.2001.5401 (2002).
288 Ramadani, F., Bolland, D. J., Garcon, F., Emery, J. L., Vanhaesebroeck, B., Corcoran, A. E. & Okkenhaug, K. The PI3K isoforms p110alpha and p110delta are essential for pre-B cell receptor signaling and B cell development. *Sci Signal* **3**, ra60, doi:10.1126/scisignal.2001104 (2010).
289 Simonsen, A., Lippe, R., Christoforidis, S., Gaullier, J. M., Brech, A., Callaghan, J., Toh, B. H., Murphy, C., Zerial, M. & Stenmark, H. EEA1 links PI(3)K function to Rab5 regulation of endosome fusion. *Nature* **394**, 494-498, doi:10.1038/28879 (1998).
290 McBride, H. M., Rybin, V., Murphy, C., Giner, A., Teasdale, R. & Zerial, M. Oligomeric complexes link Rab5 effectors with NSF and drive membrane fusion via interactions between EEA1 and syntaxin 13. *Cell* **98**, 377-386 (1999).
291 Zeigerer, A., Gilleron, J., Bogorad, R. L., Marsico, G., Nonaka, H., Seifert, S., Epstein-Barash, H., Kuchimanchi, S., Peng, C. G., Ruda, V. M., Del Conte-Zerial, P., Hengstler, J. G., Kalaidzidis, Y., Koteliansky, V. & Zerial, M. Rab5 is necessary for the biogenesis of the endolysosomal system in vivo. *Nature* **485**, 465-470, doi:10.1038/nature11133 (2012).
292 Fili, N., Calleja, V., Woscholski, R., Parker, P. J. & Larijani, B. Compartmental signal modulation: Endosomal phosphatidylinositol 3-phosphate controls endosome morphology and selective cargo sorting. *Proc Natl Acad Sci U S A* **103**, 15473-15478, doi:10.1073/pnas.0607040103 (2006).
293 Posor, Y., Eichhorn-Gruenig, M., Puchkov, D., Schoneberg, J., Ullrich, A., Lampe, A., Muller, R., Zarbakhsh, S., Gulluni, F., Hirsch, E., Krauss, M., Schultz, C., Schmoranzer,

J., Noe, F. & Haucke, V. Spatiotemporal control of endocytosis by phosphatidylinositol-3,4-bisphosphate. *Nature* **499**, 233-237, doi:10.1038/nature12360 (2013).
294 Hasegawa, J., Tokuda, E., Tenno, T., Tsujita, K., Sawai, H., Hiroaki, H., Takenawa, T. & Itoh, T. SH3YL1 regulates dorsal ruffle formation by a novel phosphoinositide-binding domain. *J Cell Biol* **193**, 901-916, doi:10.1083/jcb.201012161 (2011).
295 Maekawa, M., Terasaka, S., Mochizuki, Y., Kawai, K., Ikeda, Y., Araki, N., Skolnik, E. Y., Taguchi, T. & Arai, H. Sequential breakdown of 3-phosphorylated phosphoinositides is essential for the completion of macropinocytosis. *Proc Natl Acad Sci U S A* **111**, E978-987, doi:10.1073/pnas.1311029111 (2014).
296 Balla, A. & Balla, T. Phosphatidylinositol 4-kinases: old enzymes with emerging functions. *Trends Cell Biol* **16**, 351-361, doi:10.1016/j.tcb.2006.05.003 (2006).
297 Santos Mde, S., Naal, R. M., Baird, B. & Holowka, D. Inhibitors of PI(4,5)P2 synthesis reveal dynamic regulation of IgE receptor signaling by phosphoinositides in RBL mast cells. *Mol Pharmacol* **83**, 793-804, doi:10.1124/mol.112.082834 (2013).
298 Naguib, A. Following the trail of lipids: Signals initiated by PI3K function at multiple cellular membranes. *Sci Signal* **9**, re4, doi:10.1126/scisignal.aad7885 (2016).
299 Zhang, S. X., Duan, L. H., He, S. J., Zhuang, G. F. & Yu, X. Phosphatidylinositol 3,4-bisphosphate regulates neurite initiation and dendrite morphogenesis via actin aggregation. *Cell Res* **27**, 253-273, doi:10.1038/cr.2017.13 (2017).
300 Gozzelino, L., De Santis, M. C., Gulluni, F., Hirsch, E. & Martini, M. PI(3,4)P2 Signaling in Cancer and Metabolism. *Front Oncol* **10**, 360, doi:10.3389/fonc.2020.00360 (2020).
301 Yamauchi, Y. & Helenius, A. Virus entry at a glance. *J Cell Sci* **126**, 1289-1295, doi:10.1242/jcs.119685 (2013).
302 Barbieri, M. A., Roberts, R. L., Gumusboga, A., Highfield, H., Alvarez-Dominguez, C., Wells, A. & Stahl, P. D. Epidermal growth factor and membrane trafficking. EGF receptor activation of endocytosis requires Rab5a. *J Cell Biol* **151**, 539-550 (2000).
303 Bucci, C., Lutcke, A., Steele-Mortimer, O., Olkkonen, V. M., Dupree, P., Chiariello, M., Bruni, C. B., Simons, K. & Zerial, M. Co-operative regulation of endocytosis by three Rab5 isoforms. *FEBS Lett* **366**, 65-71 (1995).
304 Roberts, R. L., Barbieri, M. A., Ullrich, J. & Stahl, P. D. Dynamics of rab5 activation in endocytosis and phagocytosis. *J Leukoc Biol* **68**, 627-632 (2000).
305 Schnatwinkel, C., Christoforidis, S., Lindsay, M. R., Uttenweiler-Joseph, S., Wilm, M., Parton, R. G. & Zerial, M. The Rab5 effector Rabankyrin-5 regulates and coordinates different endocytic mechanisms. *PLoS biology* **2**, E261-E261, doi:10.1371/journal.pbio.0020261 (2004).
306 Kalia, M., Kumari, S., Chadda, R., Hill, M. M., Parton, R. G. & Mayor, S. Arf6-independent GPI-anchored Protein-enriched Early Endosomal Compartments Fuse with Sorting Endosomes via a Rab5/Phosphatidylinositol-3′-Kinase-dependent Machinery. *Molecular Biology of the Cell* **17**, 3689-3704, doi:10.1091/mbc.e05-10-0980 (2006).
307 Duclos, S., Diez, R., Garin, J., Papadopoulou, B., Descoteaux, A., Stenmark, H. & Desjardins, M. Rab5 regulates the kiss and run fusion between phagosomes and endosomes and the acquisition of phagosome leishmanicidal properties in RAW 264.7 macrophages. *Journal of Cell Science* **113**, 3531-3541 (2000).

308 Pelkmans, L., Burli, T., Zerial, M. & Helenius, A. Caveolin-stabilized membrane domains as multifunctional transport and sorting devices in endocytic membrane traffic. *Cell* **118**, 767-780, doi:10.1016/j.cell.2004.09.003 (2004).
309 Smith, J. L., Campos, S. K., Wandinger-Ness, A. & Ozbun, M. A. Caveolin-1-Dependent Infectious Entry of Human Papillomavirus Type 31 in Human Keratinocytes Proceeds to the Endosomal Pathway for pH-Dependent Uncoating. *Journal of Virology* **82**, 9505-9512, doi:10.1128/jvi.01014-08 (2008).
310 Frittoli, E., Palamidessi, A., Pizzigoni, A., Lanzetti, L., Garrè, M., Troglio, F., Troilo, A., Fukuda, M., Di Fiore, P. P., Scita, G. & Confalonieri, S. *The Primate-specific Protein TBC1D3 Is Required for Optimal Macropinocytosis in a Novel ARF6-dependent Pathway*. Vol. 19 (2008).
311 Homma, Y., Kinoshita, R., Kuchitsu, Y., Wawro, P. S., Marubashi, S., Oguchi, M. E., Ishida, M., Fujita, N. & Fukuda, M. Comprehensive knockout analysis of the Rab family GTPases in epithelial cells. *J Cell Biol* **218**, 2035-2050, doi:10.1083/jcb.201810134 (2019).
312 Nishimura, K., Fukagawa, T., Takisawa, H., Kakimoto, T. & Kanemaki, M. An auxin-based degron system for the rapid depletion of proteins in nonplant cells. *Nat Methods* **6**, 917-922, doi:10.1038/nmeth.1401 (2009).
313 Simpson, J. C., Griffiths, G., Wessling-Resnick, M., Fransen, J. A., Bennett, H. & Jones, A. T. A role for the small GTPase Rab21 in the early endocytic pathway. *J Cell Sci* **117**, 6297-6311, doi:10.1242/jcs.01560 (2004).
314 Pellinen, T., Arjonen, A., Vuoriluoto, K., Kallio, K., Fransen, J. A. & Ivaska, J. Small GTPase Rab21 regulates cell adhesion and controls endosomal traffic of beta1-integrins. *J Cell Biol* **173**, 767-780, doi:10.1083/jcb.200509019 (2006).
315 Zhang, X., He, X., Fu, X. Y. & Chang, Z. Varp is a Rab21 guanine nucleotide exchange factor and regulates endosome dynamics. *J Cell Sci* **119**, 1053-1062, doi:10.1242/jcs.02810 (2006).
316 Junutula, J. R., De Maziere, A. M., Peden, A. A., Ervin, K. E., Advani, R. J., van Dijk, S. M., Klumperman, J. & Scheller, R. H. Rab14 is involved in membrane trafficking between the Golgi complex and endosomes. *Mol Biol Cell* **15**, 2218-2229, doi:10.1091/mbc.e03-10-0777 (2004).
317 Ullrich, O., Reinsch, S., Urbe, S., Zerial, M. & Parton, R. G. Rab11 regulates recycling through the pericentriolar recycling endosome. *J Cell Biol* **135**, 913-924 (1996).
318 Proikas-Cezanne, T., Gaugel, A., Frickey, T. & Nordheim, A. Rab14 is part of the early endosomal clathrin-coated TGN microdomain. *FEBS Lett* **580**, 5241-5246, doi:10.1016/j.febslet.2006.08.053 (2006).
319 Weimershaus, M., Mauvais, F. X., Saveanu, L., Adiko, C., Babdor, J., Abramova, A., Montealegre, S., Lawand, M., Evnouchidou, I., Huber, K. J., Chadt, A., Zwick, M., Vargas, P., Dussiot, M., Lennon-Dumenil, A. M., Brocker, T., Al-Hasani, H. & van Endert, P. Innate Immune Signals Induce Anterograde Endosome Transport Promoting MHC Class I Cross-Presentation. *Cell Rep* **24**, 3568-3581, doi:10.1016/j.celrep.2018.08.041 (2018).
320 Linford, A., Yoshimura, S., Nunes Bastos, R., Langemeyer, L., Gerondopoulos, A., Rigden, D. J. & Barr, F. A. Rab14 and its exchange factor FAM116 link endocytic recycling and adherens junction stability in migrating cells. *Dev Cell* **22**, 952-966, doi:10.1016/j.devcel.2012.04.010 (2012).

321 Kauppi, M., Simonsen, A., Bremnes, B., Vieira, A., Callaghan, J., Stenmark, H. & Olkkonen, V. M. The small GTPase Rab22 interacts with EEA1 and controls endosomal membrane trafficking. *J Cell Sci* **115**, 899-911 (2002).
322 Rodriguez-Gabin, A. G., Cammer, M., Almazan, G., Charron, M. & Larocca, J. N. Role of rRAB22b, an oligodendrocyte protein, in regulation of transport of vesicles from trans Golgi to endocytic compartments. *J Neurosci Res* **66**, 1149-1160, doi:10.1002/jnr.1253 (2001).
323 Mishra, A., Eathiraj, S., Corvera, S. & Lambright, D. G. Structural basis for Rab GTPase recognition and endosome tethering by the C2H2 zinc finger of Early Endosomal Autoantigen 1 (EEA1). *Proc Natl Acad Sci U S A* **107**, 10866-10871, doi:10.1073/pnas.1000843107 (2010).
324 Di Nardo, A. A., Fuchs, J., Joshi, R. L., Moya, K. L. & Prochiantz, A. The Physiology of Homeoprotein Transduction. *Physiol Rev* **98**, 1943-1982, doi:10.1152/physrev.00018.2017 (2018).
325 Prochiantz, A. & Di Nardo, A. A. Homeoprotein signaling in the developing and adult nervous system. *Neuron* **85**, 911-925, doi:10.1016/j.neuron.2015.01.019 (2015).
326 Spatazza, J., Di Lullo, E., Joliot, A., Dupont, E., Moya, K. L. & Prochiantz, A. Homeoprotein signaling in development, health, and disease: a shaking of dogmas offers challenges and promises from bench to bed. *Pharmacol Rev* **65**, 90-104, doi:10.1124/pr.112.006577 (2013).
327 Sagan, S., Burlina, F., Alves, I. D., Bechara, C., Dupont, E. & Joliot, A. Homeoproteins and homeoprotein-derived peptides: going in and out. *Curr Pharm Des* **19**, 2851-2862, doi:10.2174/1381612811319160002 (2013).
328 Rekaik, H., Blaudin de The, F. X., Fuchs, J., Massiani-Beaudoin, O., Prochiantz, A. & Joshi, R. L. Engrailed Homeoprotein Protects Mesencephalic Dopaminergic Neurons from Oxidative Stress. *Cell Rep* **13**, 242-250, doi:10.1016/j.celrep.2015.08.076 (2015).
329 Rekaik, H., Blaudin de The, F. X., Prochiantz, A., Fuchs, J. & Joshi, R. L. Dissecting the role of Engrailed in adult dopaminergic neurons--Insights into Parkinson disease pathogenesis. *FEBS Lett* **589**, 3786-3794, doi:10.1016/j.febslet.2015.10.002 (2015).
330 Blaudin de The, F. X., Rekaik, H., Peze-Heidsieck, E., Massiani-Beaudoin, O., Joshi, R. L., Fuchs, J. & Prochiantz, A. Engrailed homeoprotein blocks degeneration in adult dopaminergic neurons through LINE-1 repression. *EMBO J* **37**, doi:10.15252/embj.201797374 (2018).
331 Alvarez-Fischer, D., Fuchs, J., Castagner, F., Stettler, O., Massiani-Beaudoin, O., Moya, K. L., Bouillot, C., Oertel, W. H., Lombes, A., Faigle, W., Joshi, R. L., Hartmann, A. & Prochiantz, A. Engrailed protects mouse midbrain dopaminergic neurons against mitochondrial complex I insults. *Nat Neurosci* **14**, 1260-1266, doi:10.1038/nn.2916 (2011).
332 Sugiyama, S., Di Nardo, A. A., Aizawa, S., Matsuo, I., Volovitch, M., Prochiantz, A. & Hensch, T. K. Experience-dependent transfer of Otx2 homeoprotein into the visual cortex activates postnatal plasticity. *Cell* **134**, 508-520, doi:10.1016/j.cell.2008.05.054 (2008).
333 Torero Ibad, R., Rheey, J., Mrejen, S., Forster, V., Picaud, S., Prochiantz, A. & Moya, K. L. Otx2 promotes the survival of damaged adult retinal ganglion cells and protects against excitotoxic loss of visual acuity in vivo. *J Neurosci* **31**, 5495-5503, doi:10.1523/JNEUROSCI.0187-11.2011 (2011).

334 Minois, N., Carmona-Gutierrez, D. & Madeo, F. Polyamines in aging and disease. *Aging (Albany NY)* **3**, 716-732, doi:10.18632/aging.100361 (2011).
335 Miller-Fleming, L., Olin-Sandoval, V., Campbell, K. & Ralser, M. Remaining Mysteries of Molecular Biology: The Role of Polyamines in the Cell. *J Mol Biol* **427**, 3389-3406, doi:10.1016/j.jmb.2015.06.020 (2015).
336 Arruabarrena-Aristorena, A., Zabala-Letona, A. & Carracedo, A. Oil for the cancer engine: The cross-talk between oncogenic signaling and polyamine metabolism. *Sci Adv* **4**, eaar2606, doi:10.1126/sciadv.aar2606 (2018).
337 Handa, A. K., Fatima, T. & Mattoo, A. K. Polyamines: Bio-Molecules with Diverse Functions in Plant and Human Health and Disease. *Front Chem* **6**, 10, doi:10.3389/fchem.2018.00010 (2018).
338 Ramani, D., De Bandt, J. P. & Cynober, L. Aliphatic polyamines in physiology and diseases. *Clin Nutr* **33**, 14-22, doi:10.1016/j.clnu.2013.09.019 (2014).
339 Soulet, D., Covassin, L., Kaouass, M., Charest-Gaudreault, R., Audette, M. & Poulin, R. Role of endocytosis in the internalization of spermidine-C(2)-BODIPY, a highly fluorescent probe of polyamine transport. *Biochem J* **367**, 347-357, doi:10.1042/BJ20020764 (2002).
340 Soulet, D., Gagnon, B., Rivest, S., Audette, M. & Poulin, R. A fluorescent probe of polyamine transport accumulates into intracellular acidic vesicles via a two-step mechanism. *J Biol Chem* **279**, 49355-49366, doi:10.1074/jbc.M401287200 (2004).
341 Uemura, T., Stringer, D. E., Blohm-Mangone, K. A. & Gerner, E. W. Polyamine transport is mediated by both endocytic and solute carrier transport mechanisms in the gastrointestinal tract. *Am J Physiol Gastrointest Liver Physiol* **299**, G517-522, doi:10.1152/ajpgi.00169.2010 (2010).
342 van Veen, S., Martin, S., Van den Haute, C., Benoy, V., Lyons, J., Vanhoutte, R., Kahler, J. P., Decuypere, J. P., Gelders, G., Lambie, E., Zielich, J., Swinnen, J. V., Annaert, W., Agostinis, P., Ghesquiere, B., Verhelst, S., Baekelandt, V., Eggermont, J. & Vangheluwe, P. ATP13A2 deficiency disrupts lysosomal polyamine export. *Nature* **578**, 419-424, doi:10.1038/s41586-020-1968-7 (2020).
343 Klopper, T. H., Kienle, N., Fasshauer, D. & Munro, S. Untangling the evolution of Rab G proteins: implications of a comprehensive genomic analysis. *BMC Biol* **10**, 71, doi:10.1186/1741-7007-10-71 (2012).
344 Palm, W. Metabolic functions of macropinocytosis. *Philos Trans R Soc Lond B Biol Sci* **374**, 20180285, doi:10.1098/rstb.2018.0285 (2019).
345 Toshima, J. Y., Nishinoaki, S., Sato, Y., Yamamoto, W., Furukawa, D., Siekhaus, D. E., Sawaguchi, A. & Toshima, J. Bifurcation of the endocytic pathway into Rab5-dependent and -independent transport to the vacuole. *Nat Commun* **5**, 3498, doi:10.1038/ncomms4498 (2014).
346 Shimamura, H., Nagano, M., Nakajima, K., Toshima, J. Y. & Toshima, J. Rab5-independent activation and function of yeast Rab7-like protein, Ypt7p, in the AP-3 pathway. *PLoS One* **14**, e0210223, doi:10.1371/journal.pone.0210223 (2019).
347 Tebaldi, G., Pritchard, S. M. & Nicola, A. V. Herpes Simplex Virus Entry by a Nonconventional Endocytic Pathway. *J Virol* **94**, doi:10.1128/JVI.01910-20 (2020).
348 Castano-Rodriguez, C., Honrubia, J. M., Gutierrez-Alvarez, J., DeDiego, M. L., Nieto-Torres, J. L., Jimenez-Guardeno, J. M., Regla-Nava, J. A., Fernandez-Delgado, R., Verdia-Baguena, C., Queralt-Martin, M., Kochan, G., Perlman, S., Aguilella, V. M., Sola, I. & Enjuanes, L. Role of Severe Acute Respiratory Syndrome Coronavirus

Viroporins E, 3a, and 8a in Replication and Pathogenesis. *MBio* **9**, doi:10.1128/mBio.02325-17 (2018).
349 Quirin, K., Eschli, B., Scheu, I., Poort, L., Kartenbeck, J. & Helenius, A. Lymphocytic choriomeningitis virus uses a novel endocytic pathway for infectious entry via late endosomes. *Virology* **378**, 21-33, doi:S0042-6822(08)00294-8 [pii]
10.1016/j.virol.2008.04.046 (2008).
350 Rojek, J. M., Perez, M. & Kunz, S. Cellular entry of lymphocytic choriomeningitis virus. *J Virol* **82**, 1505-1517, doi:10.1128/JVI.01331-07 (2008).
351 Kunz, S. Receptor binding and cell entry of Old World arenaviruses reveal novel aspects of virus-host interaction. *Virology* **387**, 245-249, doi:10.1016/j.virol.2009.02.042 (2009).
352 Pasqual, G., Rojek, J. M., Masin, M., Chatton, J. Y. & Kunz, S. Old world arenaviruses enter the host cell via the multivesicular body and depend on the endosomal sorting complex required for transport. *PLoS Pathog* **7**, e1002232, doi:10.1371/journal.ppat.1002232 (2011).
353 Kunz, S. & de la Torre, J. C. Breaking the Barrier: Host Cell Invasion by Lujo Virus. *Cell Host Microbe* **22**, 583-585, doi:10.1016/j.chom.2017.10.014 (2017).
354 Raaben, M., Jae, L. T., Herbert, A. S., Kuehne, A. I., Stubbs, S. H., Chou, Y. Y., Blomen, V. A., Kirchhausen, T., Dye, J. M., Brummelkamp, T. R. & Whelan, S. P. NRP2 and CD63 Are Host Factors for Lujo Virus Cell Entry. *Cell Host Microbe* **22**, 688-696 e685, doi:10.1016/j.chom.2017.10.002 (2017).
355 Wu, Q. M., Liu, S. L., Chen, G., Zhang, W., Sun, E. Z., Xiao, G. F., Zhang, Z. L. & Pang, D. W. Uncovering the Rab5-Independent Autophagic Trafficking of Influenza A Virus by Quantum-Dot-Based Single-Virus Tracking. *Small* **14**, e1702841, doi:10.1002/smll.201702841 (2018).
356 Fan, J., Liu, X., Mao, F., Yue, X., Lee, I. & Xu, Y. Proximity proteomics identifies novel function of Rab14 in trafficking of Ebola virus matrix protein VP40. *Biochem Biophys Res Commun* **527**, 387-392, doi:10.1016/j.bbrc.2020.04.041 (2020).
357 Okai, B., Lyall, N., Gow, N. A., Bain, J. M. & Erwig, L. P. Rab14 regulates maturation of macrophage phagosomes containing the fungal pathogen Candida albicans and outcome of the host-pathogen interaction. *Infect Immun* **83**, 1523-1535, doi:10.1128/IAI.02917-14 (2015).
358 Mrozowska, P. S. & Fukuda, M. Regulation of podocalyxin trafficking by Rab small GTPases in 2D and 3D epithelial cell cultures. *J Cell Biol* **213**, 355-369, doi:10.1083/jcb.201512024 (2016).
359 Derossi, D., Joliot, A. H., Chassaing, G. & Prochiantz, A. The third helix of the Antennapedia homeodomain translocates through biological membranes. *J Biol Chem* **269**, 10444-10450 (1994).
360 Gehring, W. J. & Hiromi, Y. Homeotic genes and the homeobox. *Annu Rev Genet* **20**, 147-173, doi:10.1146/annurev.ge.20.120186.001051 (1986).
361 Chatelin, L., Volovitch, M., Joliot, A. H., Perez, F. & Prochiantz, A. Transcription factor hoxa-5 is taken up by cells in culture and conveyed to their nuclei. *Mech Dev* **55**, 111-117, doi:10.1016/0925-4773(95)00478-5 (1996).
362 Dom, G., Shaw-Jackson, C., Matis, C., Bouffioux, O., Picard, J. J., Prochiantz, A., Mingeot-Leclercq, M. P., Brasseur, R. & Rezsohazy, R. Cellular uptake of Antennapedia Penetratin peptides is a two-step process in which phase transfer

precedes a tryptophan-dependent translocation. *Nucleic Acids Res* **31**, 556-561, doi:10.1093/nar/gkg160 (2003).
363 Amblard, I., Dupont, E., Alves, I., Miralvès, J., Queguiner, I. & Joliot, A. Bidirectional transfer of Engrailed homeoprotein across the plasma membrane requires PIP2. *bioRxiv*, 2020.2001.2021.913566, doi:10.1101/2020.01.21.913566 (2020).
364 Beurdeley, M., Spatazza, J., Lee, H. H., Sugiyama, S., Bernard, C., Di Nardo, A. A., Hensch, T. K. & Prochiantz, A. Otx2 binding to perineuronal nets persistently regulates plasticity in the mature visual cortex. *J Neurosci* **32**, 9429-9437, doi:10.1523/JNEUROSCI.0394-12.2012 (2012).
365 Balayssac, S., Burlina, F., Convert, O., Bolbach, G., Chassaing, G. & Lequin, O. Comparison of penetratin and other homeodomain-derived cell-penetrating peptides: interaction in a membrane-mimicking environment and cellular uptake efficiency. *Biochemistry* **45**, 1408-1420, doi:10.1021/bi0518390 (2006).
366 Carlier, L., Balayssac, S., Cantrelle, F. X., Khemtemourian, L., Chassaing, G., Joliot, A. & Lequin, O. Investigation of homeodomain membrane translocation properties: insights from the structure determination of engrailed-2 homeodomain in aqueous and membrane-mimetic environments. *Biophys J* **105**, 667-678, doi:10.1016/j.bpj.2013.06.024 (2013).
367 Lee, E. J., Kim, N., Park, J. W., Kang, K. H., Kim, W. I., Sim, N. S., Jeong, C. S., Blackshaw, S., Vidal, M., Huh, S. O., Kim, D., Lee, J. H. & Kim, J. W. Global Analysis of Intercellular Homeodomain Protein Transfer. *Cell Rep* **28**, 712-722 e713, doi:10.1016/j.celrep.2019.06.056 (2019).
368 Amblard, I., Dupont, E., Alves, I., Miralves, J., Queguiner, I. & Joliot, A. Bidirectional transfer of homeoprotein EN2 across the plasma membrane requires PIP2. *J Cell Sci* **133**, doi:10.1242/jcs.244327 (2020).
369 Weber, M. M. & Faris, R. Subversion of the Endocytic and Secretory Pathways by Bacterial Effector Proteins. *Front Cell Dev Biol* **6**, 1, doi:10.3389/fcell.2018.00001 (2018).
370 Cossart, P. & Helenius, A. Endocytosis of viruses and bacteria. *Cold Spring Harb Perspect Biol* **6**, doi:10.1101/cshperspect.a016972 (2014).
371 Sherwood, R. K. & Roy, C. R. A Rab-centric perspective of bacterial pathogen-occupied vacuoles. *Cell Host Microbe* **14**, 256-268, doi:10.1016/j.chom.2013.08.010 (2013).
372 Starr, T., Ng, T. W., Wehrly, T. D., Knodler, L. A. & Celli, J. Brucella intracellular replication requires trafficking through the late endosomal/lysosomal compartment. *Traffic* **9**, 678-694, doi:10.1111/j.1600-0854.2008.00718.x (2008).
373 Isberg, R. R., O'Connor, T. J. & Heidtman, M. The Legionella pneumophila replication vacuole: making a cosy niche inside host cells. *Nat Rev Microbiol* **7**, 13-24, doi:10.1038/nrmicro1967 (2009).
374 Croxatto, A. & Greub, G. Early intracellular trafficking of Waddlia chondrophila in human macrophages. *Microbiology* **156**, 340-355, doi:10.1099/mic.0.034546-0 (2010).
375 Hackstadt, T., Scidmore, M. A. & Rockey, D. D. Lipid metabolism in Chlamydia trachomatis-infected cells: directed trafficking of Golgi-derived sphingolipids to the chlamydial inclusion. *Proc Natl Acad Sci U S A* **92**, 4877-4881 (1995).
376 Jeng, R. L., Goley, E. D., D'Alessio, J. A., Chaga, O. Y., Svitkina, T. M., Borisy, G. G., Heinzen, R. A. & Welch, M. D. A Rickettsia WASP-like protein activates the Arp2/3

complex and mediates actin-based motility. *Cell Microbiol* **6**, 761-769, doi:10.1111/j.1462-5822.2004.00402.x (2004).
377 Lambrechts, A., Gevaert, K., Cossart, P., Vandekerckhove, J. & Van Troys, M. Listeria comet tails: the actin-based motility machinery at work. *Trends Cell Biol* **18**, 220-227, doi:10.1016/j.tcb.2008.03.001 (2008).
378 Fine, K. L., Metcalfe, M. G., White, E., Virji, M., Karls, R. K. & Quinn, F. D. Involvement of the autophagy pathway in trafficking of Mycobacterium tuberculosis bacilli through cultured human type II epithelial cells. *Cell Microbiol* **14**, 1402-1414, doi:10.1111/j.1462-5822.2012.01804.x (2012).
379 Greub, G., Mege, J. L., Gorvel, J. P., Raoult, D. & Meresse, S. Intracellular trafficking of Parachlamydia acanthamoebae. *Cell Microbiol* **7**, 581-589, doi:10.1111/j.1462-5822.2004.00488.x (2005).
380 Bohlen, C. J. & Julius, D. Receptor-targeting mechanisms of pain-causing toxins: How ow? *Toxicon* **60**, 254-264, doi:10.1016/j.toxicon.2012.04.336 (2012).
381 Lin King, J. V., Emrick, J. J., Kelly, M. J. S., Herzig, V., King, G. F., Medzihradszky, K. F. & Julius, D. A Cell-Penetrating Scorpion Toxin Enables Mode-Specific Modulation of TRPA1 and Pain. *Cell* **178**, 1362-1374 e1316, doi:10.1016/j.cell.2019.07.014 (2019).
382 Ponnappan, N. & Chugh, A. Cell-penetrating and cargo-delivery ability of a spider toxin-derived peptide in mammalian cells. *Eur J Pharm Biopharm* **114**, 145-153, doi:10.1016/j.ejpb.2017.01.012 (2017).
383 Kerkis, A., Kerkis, I., Radis-Baptista, G., Oliveira, E. B., Vianna-Morgante, A. M., Pereira, L. V. & Yamane, T. Crotamine is a novel cell-penetrating protein from the venom of rattlesnake Crotalus durissus terrificus. *FASEB J* **18**, 1407-1409, doi:10.1096/fj.03-1459fje (2004).
384 Williams, J. M. & Tsai, B. Intracellular trafficking of bacterial toxins. *Current Opinion in Cell Biology* **41**, 51-56, doi:https://doi.org/10.1016/j.ceb.2016.03.019 (2016).
385 Chinnapen, D. J. F., Chinnapen, H., Saslowsky, D. & Lencer, W. I. Rafting with cholera toxin: endocytosis and trafficking from plasma membrane to ER. *FEMS microbiology letters* **266**, 129-137, doi:10.1111/j.1574-6968.2006.00545.x (2007).
386 Renard, H. F., Garcia-Castillo, M. D., Chambon, V., Lamaze, C. & Johannes, L. Shiga toxin stimulates clathrin-independent endocytosis of the VAMP2, VAMP3 and VAMP8 SNARE proteins. *J Cell Sci* **128**, 2891-2902, doi:10.1242/jcs.171116 (2015).
387 Torgersen, M. L., Skretting, G., van Deurs, B. & Sandvig, K. Internalization of cholera toxin by different endocytic mechanisms. *J Cell Sci* **114**, 3737-3747 (2001).
388 Sandvig, K., Grimmer, S., Iversen, T. G., Rodal, K., Torgersen, M. L., Nicoziani, P. & van Deurs, B. Ricin transport into cells: studies of endocytosis and intracellular transport. *International Journal of Medical Microbiology* **290**, 415-420, doi:https://doi.org/10.1016/S1438-4221(00)80055-7 (2000).
389 Spooner, R. A. & Lord, J. M. Ricin trafficking in cells. *Toxins* **7**, 49-65, doi:10.3390/toxins7010049 (2015).
390 DiRienzo, J. M. Uptake and processing of the cytolethal distending toxin by mammalian cells. *Toxins* **6**, 3098-3116, doi:10.3390/toxins6113098 (2014).
391 Morlon-Guyot, J., Méré, J., Bonhoure, A. & Beaumelle, B. Processing of Pseudomonas aeruginosa exotoxin A is dispensable for cell intoxication. *Infection and immunity* **77**, 3090-3099, doi:10.1128/IAI.01390-08 (2009).

392 Abrami, L., Bischofberger, M., Kunz, B., Groux, R. & van der Goot, F. G. Endocytosis of the anthrax toxin is mediated by clathrin, actin and unconventional adaptors. *PLoS Pathog* **6**, e1000792, doi:10.1371/journal.ppat.1000792 (2010).
393 Lemichez, E., Bomsel, M., Devilliers, G., van der Spek, J., Murphy, J. R., Lukianov, E. V., Olsnes, S. & Boquet, P. Membrane translocation of diphtheria toxin fragment A exploits early to late endosome trafficking machinery. *Molecular Microbiology* **23**, 445-457, doi:10.1111/j.1365-2958.1997.tb02669.x (1997).
394 Perret, P., Ahmadi, M., Riou, L., Bacot, S., Pecher, J., Poillot, C., Broisat, A., Ghezzi, C. & De Waard, M. Biodistribution, Stability, and Blood Distribution of the Cell Penetrating Peptide Maurocalcine in Mice. *Int J Mol Sci* **16**, 27730-27740, doi:10.3390/ijms161126054 (2015).
395 van Duijnhoven, S. M., Robillard, M. S., Nicolay, K. & Grull, H. Tumor targeting of MMP-2/9 activatable cell-penetrating imaging probes is caused by tumor-independent activation. *J Nucl Med* **52**, 279-286, doi:10.2967/jnumed.110.082503 (2011).
396 Oliveira-Mendes, B. B. R., Horta, C. C. R., do Carmo, A. O., Biscoto, G. L., Sales-Medina, D. F., Leal, H. G., Brandao-Dias, P. F. P., Miranda, S. E. M., Aguiar, C. J., Cardoso, V. N., de Barros, A. L. B., Chavez-Olortegui, C., Leite, M. F. & Kalapothakis, E. CPP-Ts: a new intracellular calcium channel modulator and a promising tool for drug delivery in cancer cells. *Sci Rep* **8**, 14739, doi:10.1038/s41598-018-33133-3 (2018).
397 Tiwari, P. M., Eroglu, E., Bawage, S. S., Vig, K., Miller, M. E., Pillai, S., Dennis, V. A. & Singh, S. R. Enhanced intracellular translocation and biodistribution of gold nanoparticles functionalized with a cell-penetrating peptide (VG-21) from vesicular stomatitis virus. *Biomaterials* **35**, 9484-9494, doi:10.1016/j.biomaterials.2014.07.032 (2014).
398 Jarver, P., Mager, I. & Langel, U. In vivo biodistribution and efficacy of peptide mediated delivery. *Trends Pharmacol Sci* **31**, 528-535, doi:10.1016/j.tips.2010.07.006 (2010).
399 Lakkadwala, S., Dos Santos Rodrigues, B., Sun, C. & Singh, J. Biodistribution of TAT or QLPVM coupled to receptor targeted liposomes for delivery of anticancer therapeutics to brain in vitro and in vivo. *Nanomedicine* **23**, 102112, doi:10.1016/j.nano.2019.102112 (2020).
400 Dos Santos Rodrigues, B., Lakkadwala, S., Kanekiyo, T. & Singh, J. Development and screening of brain-targeted lipid-based nanoparticles with enhanced cell penetration and gene delivery properties. *Int J Nanomedicine* **14**, 6497-6517, doi:10.2147/IJN.S215941 (2019).
401 Kho, K. W., Berselli, G. B. & Keyes, T. E. A Nanoplasmonic Assay of Oligonucleotide-Cargo Delivery from Cationic Lipoplexes. *Small* **17**, e2005815, doi:10.1002/smll.202005815 (2021).
402 Zuhorn, I. S., Bakowsky, U., Polushkin, E., Visser, W. H., Stuart, M. C., Engberts, J. B. & Hoekstra, D. Nonbilayer phase of lipoplex-membrane mixture determines endosomal escape of genetic cargo and transfection efficiency. *Mol Ther* **11**, 801-810, doi:10.1016/j.ymthe.2004.12.018 (2005).
403 ur Rehman, Z., Hoekstra, D. & Zuhorn, I. S. Mechanism of polyplex- and lipoplex-mediated delivery of nucleic acids: real-time visualization of transient membrane destabilization without endosomal lysis. *ACS Nano* **7**, 3767-3777, doi:10.1021/nn3049494 (2013).